PLACE IN RETURN BOX to remove this checkout from your record.

TO AVOID FINES return on or before date due.

MAY BE RECALLED with earlier due date if requested.

DATE DUE	DATE DUE	DATE DUE
	DAIL DOL	DAIL DOL
		:

2/05 p:/CIRC/DateDue.indd-p.1

THERMODYNAMIC AND KINETIC CHARACTERIZATION OF CHIRAL SEPARATIONS WITH β -CYCLODEXTRIN STATIONARY PHASE

Ву

Xiaoping Li

A DISSERTATION

Submitted to
Michigan State University
in partial fulfillment of the requirements
for the degree of

DOCTOR OF PHILOSOPHY

Department of Chemistry

2006

ABSTRACT

THERMODYNAMIC AND KINETIC CHARACTERIZATION OF CHIRAL SEPARATION WITH β-CYCLODEXTRIN STATIONARY PHASE

By

Xiaoping Li

Chiral separation by liquid chromatography using chiral stationary phases is the most popular approach in industry. In this dissertation, a series of coumarin related compounds is analyzed using a packed capillary β -cyclodextrin column with on-column laser-induced fluorescence detection.

In our approach for data analysis, the exponential modified Gaussian (EMG) model is employed. In order to validate this model, a three-dimensional stochastic simulation is first performed. Five methods are applied to extract the thermodynamic and kinetic information: "true" method, Statistical moment method, EMG method, Thomas method and Giddings method. Comparison of the accuracy relative to the "true" retention factors and "true" rate constants demonstrates that the EMG model provides similar results to the other models.

The experimental data are examined with the EMG model to observe the effect of mobile phase composition, temperature and pressure on the thermodynamics and kinetics of chiral separation. A polar-organic mobile phase composed of acetonitrile, methanol, acetic acid, and triethylamine is utilized.

Mobile phase composition affects the equilibration time, isotherm, retention, chiral selectivity, as well as the kinetic rate constants of the chiral separation. Both acid and amine modifiers can help to shorten the equilibration

time greatly. Acid modifier increases the linear isotherm range but decreases chiral selectivity. Amine modifier decreases retention and benefits chiral selectivity. Methanol decreases retention by hydrogen bonding. The mass transfer rate constant usually increases as the retention decreases. However, the second enantiomer often has a surprisingly faster mass transfer rate than the first enantiomer although it is more retained.

Temperature and pressure also affect retention, chiral selectivity, and kinetic rate constants. Temperature decreases retention and chiral selectivity for all compounds. Pressure decreases retention but does not significantly affect chiral selectivity. The changes in molar enthalpy are negative for all compounds, indicating an energetically favorable transfer from mobile to stationary phase. The changes in molar volume are positive for all compounds, indicating the compounds occupy more space in the stationary phase than in the mobile phase. No enthalpy-entropy compensation is achieved, hence different retention mechanisms are responsible for each compound.

In addition to chiral separation, a series of nitrogen-containing polycyclic aromatic hydrocarbons (N-PAHs) are investigated in a similar manner to observe the effects of mobile phase composition, temperature and pressure on an octadecylsilica column. The results demonstrate that the partition mechanism is dominant in methanol mobile phase but the adsorption mechanism is dominant in acetonitrile mobile phase. Another technique, fluorescence quenching, is also utilized to differentiate different types of N-PAHs with aliphatic amine quenchers. Aliphatic amines can selectively quench aza-PAHs over amino-PAHs.

To My Family...

ACKNOWLEDGEMENTS

First of all, I like to express my sincerest thanks to my advisor, Dr. Victoria L. McGuffin. Her profound knowledge and passion in science not only helped me though five years of graduate works, but also will encourage and lead me in my future careers. I would also like to thank all of my committee members, Dr. Jack Throck Watson, Dr. Merlin L. Bruening, Dr. Gregory L. Baker and Dr. Katharine C. Hunt, for their critical evaluations and suggestions.

To all of my group members: Dr. Samuel Howerton and Dr. Carl Newman are two excellent senior labmates. Their patience in teaching, dedication in research and humor in life help me through the toughest first few years. Rashad is my "same-year-buddy", who experienced every bit of graduate school life with me. It's so great to have such a company. Melissa and Amber are two sweetest "sisters" in the lab. Melissa always surprises me with her creativity, and Amber always impresses me with her smile. Thank you two for being my friend. I have no doubt that both of you will succeed in your future. Good luck to the youngest labmate, Kahsay, for his future graduate works as well. I am so blessed to have such a small but sweet group.

I would also like to thank my husband, Feng, for his love and encouragement. Without his love and company, the graduate school will be so much harder for me. To my parents, their love and support are the main sources of energy helped me through any difficult time. Thank you for always believing in me. Of course, thanks to all of my friends I got to know in these five years, you make my life in East Lansing so much colorful.

TABLE OF CONTENTS

LIST OF TABLES	ix
LIST OF FIGURES	xii
Chapter 1: Introduction and Background	1
1.1 Importance of Chiral Separation	1
1.2 Chiral Separation with Liquid Chromagraphic Methods	2 2
1.2.1 Indirect Methods	2
1.2.2 Direct Methods	2
1.3 Thermodynamic and Kinetic Theory	10
1.3.1 Thermodynamics	12
1.3.2 Kinetics	16
1.4 Methods for Thermodynamic and Kinetic Studies	18
1.4.1 Perturbation Methods	18
1.4.2 Shallow-Bed Methods	20
1.4.2 Chromatographic Methods	21 32
1.5 Previous Investigations of Chiral Separations	32 32
1.5.1 Inclusion-Type CSP	36
1.5.2 Brush-Type CSP 1.5.3 Amylose- and Cellulose-Type CSP	40
1.5.4 Protein-Type CSP	44
1.5.4 Protein-Type CSP 1.6 Conclusions	51
1.7 References	52
1.7 Reletelices	32
Chapter 2: Theoretical Evaluation of Methods for Extracting	
Retention Factors and Kinetic Rate Constants in	
Liquid Chromatography	56
2.1 Introduction	56
2.2 Computer Simulation Methods	57
2.3 Data Analysis Methods	58
2.3.1 True Extraction Method	58
2.3.2 Statistical Moment Extraction Method	60
2.3.3 EMG Model Extraction Method	62
2.3.4 Giddings Model Extraction Method	62
2.3.5 Thomas Model Extraction Method	63
2.4 Results and Discussion	64
3.4.1 Homogeneous Systems	64
3.4.2 Heterogeneous Systems	107
2.5 Conclusions	120
2.6 References	125

Chapter 3: Experimental Methods	127
3.1 Experimental Systems	127
3.1.1 Column Packing	127
3.1.2 Chromatographic System	128
3.2 Data Analysis	134
3.3 Conclusions	136
3.4 References	137
Chapter 4: Effect of Mobile Phase Composition to Chiral Separation	IS
With β-Cyclodextrin Stationary Phase	138
4.1 Introduction	138
4.2 Experimental Methods	139
4.2.1 Chemicals	139
4.2.2 Experimental System	140
4.3 Results and Discussion	140
4.3.1 Memory Effect	140
4.3.2 Two-Component Mobile Phase	145
4.3.3 Three-Component Mobile Phase	153
4.3.4 Four-Component Mobile Phase	161
4.4 Conclusions	175
4.5 References	177
Chapter 5: Effect of Temperature and Pressure to Chiral Separation	S
With β-Cyclodextrin Stationary Phase	179
5.1 Introduction	179
5.2 Experimental Methods	180
5.2.1 Chemicals	180
5.2.2 Experimental System	180
5.3 Results and Discussion	180
5.3.1 Thermodynamic Behavior	181
5.3.2 Kinetic Behavior	197
5.4 Conclusions	204
5.5 References	206
Chapter 6: Thermodynamic and Kinetic Characterization of Nitrogen-Containing Polycyclic Aromatic Hydrocarbons	
in Reversed-Phase Liquid Chromatography	207
6.1 Introduction	207
6.2 Experimental Methods	209
6.2.1 Chemicals	209
6.2.2 Experimental System	209
6.3 Results and Discussion	212
6.3.1 Methanol Mobile Phase	215

6.3.2 Acetonitrile Mobile Phase	236
6.4 Conclusions	243
6.5 References	246
Chapter 7: Spectroscopic Study of Nitrogen-Containing Polycyclic Aromatic Hydrocarbons by Fluorescence Quenching	c 249
7.1 Introduction	249
7.1.1 Nitrogen-Containing Polycyclic Aromatic Hydrocarb	ons
(N-PAHs)	249
7.1.2 Fluorescence Quenching	249
7.2 Experimental Methods	253
7.2.1 Chemicals	253
7.2.2 Fluorescence Quenching Measurements	253
7.2.3 Fluorescence Lifetime Measurements	258
7.3 Results and Discussion	259
7.3.1 Effect of Water	259
7.3.2 Effect of Amine Structure	260
7.3.3 Effect of Fluorophore Structure	268
7.4 Conclusions	274
7.5 References	276
Chapter 8: Conclusions and Future Directions	278
8.1 Theoretical Simulations	278
8.2 Chiral Separations	280
8.3 Characterization of Nitrogen-Containing Polycyclic Aromatic	
Hydrocarbons (N-PAHs)	284
9.5 References	286

LIST OF TABLES

Table 2.1:	Retention factors (k) with varying column length (L)	66
Table 2.2:	Kinetic rate constants from stationary to mobile phase (k_{ms}, s^{-1}) with varying column length (L)	67
Table 2.3:	Retention factors (k) with varying linear velocity (u ₀)	77
Table 2.4:	Kinetic rate constants from stationary to mobile phase (k_{ms}, s^{-1}) with varying linear velocity (u_0)	78
Table 2.5:	Retention factors (k) with varying stationary-phase diffusion coefficient (D _s)	86
Table 2.6:	Kinetic rate constants from stationary to mobile phase (k_{ms}, s^{-1}) with varying stationary-phase diffusion coefficient (D_s)	88
Table 2.7:	Retention factors (k) with varying interfacial mass transfer coefficient (α)	94
Table 2.8:	Kinetic rate constants from stationary to mobile phase (k_{ms}, s^{-1}) with varying interfacial mass transfer coefficient (α)	96
Table 2.9:	Retention factors (k) with varying equilibrium constants (K)	105
Table 2.10	: Kinetic rate constants from stationary to mobile phase (k _{ms} , s ⁻¹) with varying equilibrium constants (K)	106
Table 2.11	Different parameters for multiple interaction sites at the heterogeneous surface	109
Table 2.12	:Retention factors (k) along the column for equally distributed heterogeneous surface	112
Table 2.13	:Kinetic rate constants from stationary to mobile phase (k _{ms} , s ⁻¹) along the column for equally distributed heterogeneous surface	114
Table 2.14	Retention factors (k) along the column for unequally distributed heterogeneous surface	121

Table 2.15	:Kinetic rate constants from stationary to mobile phase (k _{ms} , s ⁻¹) along the column for unequally distributed heterogeneous surface	122
Table 4.1:	Retention time of 1 st warfarin enantiomer over successive days in a two-component mobile phase	149
Table 4.2:	Retention time of 1 st warfarin enantiomer over successive days in two-component and three-component mobile phases	155
Table 4.3:	Comparison of thermodynamic and kinetic behaviors of solutes at reference mobile phase composition	162
Table 4.4:	Effect of methanol concentration on thermodynamics	166
Table 4.5:	Effect of methanol concentration on kinetics	168
Table 4.6:	Effect of triethylamine (TEA) concentration on thermodynamics	169
Table 4.7:	Effect of triethylamine (TEA) concentration on kinetics	170
Table 4.8:	Effect of acetic acid concentration on thermodynamics when amine is present	172
Table 4.9:	Effect of acetic acid concentration on kinetics when amine is present	173
Table 4.10 :	: Effect of acetic acid concentration on thermodynamics and kinetics of warfarin without amine present	174
Table 5.1:	Retention factors for the coumarin-based solutes	182
Table 5.2:	Changes in molar enthalpy and molar volume for coumarin- based solutes	187
Table 5.3 :	Differential changes in molar enthalpy and molar entropy for the chiral coumarin-based solutes	194
Table 5.4 :	Co-elution temperature (T _{iso}) for the chiral coumarin-based solutes	198
Table 5.5 :	Kinetic rate constants for the coumarin-based solutes	200
Table 5.6 :	Activation energy for the coumarin-based solutes	203

Table 6.1:	Retention factors for N-PAHs in methanol mobile phase	216
Table 6.2:	Changes in molar enthalpy and molar volume for N-PAHs in methanol mobile phase	221
Table 6.3:	Rate constants for N-PAHs in methanol mobile phase	228
Table 6.4:	Activation energies and activation volumes for N-PAHs in methanol mobile phase	230
Table 6.5:	Thermodynamic data for N-PAHs in acetonitrile mobile phase	239
Table 6.6:	Kinetic data for N-PAHs in acetonitrile mobile phase	242
Table 7.1:	Stern-Volmer constants for pyrene with triethylamine in acetonitrile at room temperature with different water concentration (v/v) in the amine solution.	261
Table 7.2:	Stern-Volmer constants for pyrene with triethylamine in acetonitrile at room temperature with different water concentration (v/v) in the solvent	262
Table 7.3:	Stern-Volmer constants for PAHs and N-PAHs with three aliphatic amines in acetonitrile at room temperature	264
Table 7.4:	Stern-Volmer constants for alternant PAHs and aza-PAHs with diisopropylamine in acetonitrile at room temperature	270
Table 7.5 ·	Ionization potentials for the fluorophores (PAHs and N-PAHs)	273

LIST OF FIGURES

Figure 1.1:	(A) Structure of β -cyclodextrin. (B) Schematic diagram of the separation process with β -cyclodextrin stationary phase in 1) reversed-phase mode and 2) polar-organic phase mode.	5
Figure 1.2:	Schematic diagram of three-point model responsible for chiral separation.	8
Figure 1.3:	Energy coordinate diagram.	11
Figure 1.4:	Three typical adsorption isotherms. q: loading, c: concentration, t: time.	23
Figure 2.1:	Comparison of zone profiles with varying column length. From left to right, column length L = 1, 2, 4, 7, and 9 cm. Other simulation conditions: N = 5000 , t = 5.0×10^{-4} s, $D_m = 1.0 \times 10^{-5}$ cm ² /s, $D_s = 5.0 \times 10^{-8}$ cm ² /s, K = 1.0, $u_0 = 0.1$ cm/s, $R_m = 2.0 \times 10^{-3}$ cm, $d_s = 8.28 \times 10^{-4}$ cm, $\alpha = 1.0$.	69
Figure 2.2:	Comparison of zone profiles with varying linear velocity. From left to right, linear velocity u_0 = 0.5, 0.3, 0.2, 0.1, and 0.05 cm/s. Other simulation conditions: N = 5000, t = 5.0×10^{-4} s, D_m = 1.0×10^{-5} cm ² /s, D_s = 5.0×10^{-8} cm ² /s, K = 1.0, L = 8 cm, R_m = 2.0×10^{-3} cm, d_s = 8.28×10^{-4} cm, α = 1.0.	74
Figure 2.3:	Comparison of zone profiles at similar time with varying linear velocity. Peak (——) at L = 3 cm with u_0 = 0.05 cm/s, (– - – -) at L = 6 cm with u_0 = 0.1 cm/s, (– – –) at L = 18 cm with u_0 = 0.3 cm/s. Other simulation conditions: N = 5000, t = 5.0×10^{-4} s, D_m = 1.0×10^{-5} cm ² /s, D_s = 5.0×10^{-8} cm ² /s, K = 1.0, R_m = 2.0×10^{-3} cm, d_s = 8.28×10^{-4} cm, α = 1.0.	79
Figure 2.4:	Comparison of zone profiles (A) and statistical moments (B) with varying stationary-phase diffusion coefficient. (A) From left to right, stationary-phase diffusion coefficient $D_8 = 1.0 \times 10^{-8}$, 5.0×10^{-8} , 1.0×10^{-7} , 5.0×10^{-7} , and 1.0×10^{-8} cm ² /s. (B) First moment M_1 (\spadesuit), second moment M_2 (\blacksquare), third moment M_3 (\triangle), and skew M3/M2 ^{3/2} (*). Other simulation conditions: $N = 5000$, $t = 5.0 \times 10^{-4}$ s, $D_m = 1.0 \times 10^{-5}$ cm2/s, $u_0 = 0.1$ cm/s, $K = 1.0$, $L = 5$ cm, $R_m = 2.0 \times 10^{-3}$ cm, $R_m = 8.28 \times 10^{-4}$ cm, $R_m = 1.0$.	82

Figure 2.5:	Comparison of zone profiles (A) and statistical moments (B) with varying interfacial mass transfer coefficient. (A) Interfacial mass transfer coefficient $\alpha = 1$ (), 0.5 (), 0.1 () and 0.05 (). (B) First moment M_1 (\spadesuit), second moment M_2 (\blacksquare), third moment M_3 (\blacktriangle), and skew $M_3/M_2^{3/2}$ (*). Other simulation conditions: N = 5000, t = 5.0x10 ⁻⁴ s, D _m = 1.0x10 ⁻⁵ cm ² /s, D _s = 5.0x10 ⁻⁸ cm ² /s, u ₀ = 0.1 cm/s, K = 1.0, L = 6 cm, R _m = 2.0x10 ⁻³ cm, d _s = 8.28x10 ⁻⁴ cm.	91
Figure 2.6:	Comparison of zone profiles (A) and statistical moments (B) with varying equilibrium constant. (A) From left to right, equilibrium constant K = 1.0, 2.0, 5.0, and 10.0. (B) First moment M_1 (\spadesuit), second moment M_2 (\blacksquare), third moment M_3 (\triangle), and skew $M_3/M_2^{3/2}$ (*). Other simulation conditions: N = 5000, t = 5.0x10 ⁻⁴ s, $D_m = 1.0x10^{-5}$ cm ² /s, $D_s = 5.0x10^{-8}$ cm ² /s, $u_0 = 0.1$ cm/s, L = 2 cm, $R_m = 2.0x10^{-3}$ cm, $d_s = 8.28x10^{-4}$ cm, $\alpha = 1.0$.	98
Figure 2.7:	Comparison of zone profiles (A) and statistical moments (B) at similar time with varying equilibrium constant (K). (A) From left to right, $K = 5.0$ at $L = 2$ cm, $K = 2.0$ at $L = 4$ cm, $K = 1.0$ at $L = 6$ cm and $K = 0.5$ at $L = 8$ cm. (B) First moment M_1 (\spadesuit), second moment M_2 (\blacksquare), third moment M_3 (\triangle), and skew $M_3/M_2^{3/2}$ (*). Other simulation conditions: $N = 5000$, $t = 5.0 \times 10^{-4}$ s, $D_m = 1.0 \times 10^{-5}$ cm ² /s, $D_s = 5.0 \times 10^{-8}$ cm ² /s, $u_0 = 0.1$ cm/s, $R_m = 2.0 \times 10^{-3}$ cm, $d_s = 8.28 \times 10^{-4}$ cm, $\alpha = 1.0$.	101
Figure 2.8:	Comparison of zone profiles with equally distributed heterogeneous surface. From left to right, detector distance L = 0.5, 2, 5, and 7 cm. Other simulation conditions: N = 5000 , t = $5.0x10^{-4}$ s, $D_m = 1.0x10^{-5}$ cm ² /s, $u_0 = 0.1$ cm/s, $R_m = 2.0x10^{-3}$ cm, $d_s = 8.28x10^{-4}$ cm, $\alpha = 1.0$, P(1) conditions are given in Table 2.11.	110
Figure 2.9:	Comparison of zone profiles with unequally distributed heterogeneous surface. From left to right, detector distance L = 1, 5, 8, 15, and 20 cm. Other simulation conditions: N = 5000 , t = $5.0x10^{-4}$ s, $D_m = 1.0x10^{-5}$ cm ² /s, $u_0 = 0.1$ cm/s, $R_m = 2.0x10^{-3}$ cm, $d_s = 8.28x10^{-4}$ cm, $\alpha = 1.0$, P(2) conditions are given in Table 2.11.	116
Figure 2.10	:Comparison of skews among equally distributed (♠), unequally distributed (■) heterogeneous systems,	

	homogeneous system with D₅ equal to 1.0x10 ⁻⁷ cm²/s (▲) and homogeneous system with D₅ equal to 1.0x10 ⁻⁸ cm²/s (∗). For heterogeneous systems, simulation details as given in Figures 2.8 and 2.9. For homogeneous systems, simulation details are given in Figure 2.4.	118
Figure 3.1:	Schematic diagram of the experimental system for capillary liquid chromatography with one on-column laser-induced fluorescence detector for mobile phase study. I: injection valve, S: splitting tee, F: filter, PMT: photomultiplier tube, AMP: current to voltage amplifier.	129
Figure 3.2:	Schematic diagram of the experimental system for capillary liquid chromatography with four on-column laser-induced fluorescence detectors for temperature and pressure study. I: injection valve, S: splitting tee, R: restrictor, FOP: fiber-opti positioner, F: filter, PMT: photomultiplier tube, AMP: current to voltage amplifier	ic 132
Figure 4.1:	Structure of coumarin-based solutes	140
Figure 4.2:	Representative chromatograms of memory effect from acetic acid and triethylamine. Column: β-cyclodextrin. Solute: racemic warfarin. Mobile phase composition: acetonitrile:methanol (90%:10%) (A) original data before acid and amine modifier added; (B) acetic acid:triethylamine (0.30%:0.20%) added; (C) removal of acid and amine modifier at hour 4; (D) day 1; (E) day 3; (F) day 10.	143
Figure 4.3:	Representative chromatograms of memory effect from methanol. Column: β-cyclodextrin. Solute: racemic warfarin. Mobile phase composition: acetonitrile:methanol (90%:10%) after removal of pure methanol mobile phase at (A) day 1; (B) day 2; (C) day 3; (D) day 10	146
Figure 4.4:	Comparison of chromatograms in two-component mobile phase. Column: β-cyclodextrin. Solute: racemic warfarin. Mobile phase composition: acetonitrile:methanol (80%:20%) (A) day 2; (B) day 3; (C) day 6.	151
Figure 4.5:	Warfarin peak shape in the presence of acetic acid. Column: β-cyclodextrin. Mobile phase composition: acetonitrile:methanol:acid (90%:10%:0.30%). Warfarin concentration from highest to lowest: 8x10 ⁻⁴ M; 4x10 ⁻⁴ M; 2x10 ⁻⁴ M.	157
		. • •

rigure 4.0.	Column: β-cyclodextrin. Mobile phase composition: acetonitrile:methanol:amine (90%:10%:0.05%). Warfarin concentration from highest to lowest: 8x10 ⁻⁴ M; 4x10 ⁻⁴ M; 2x10 ⁻⁴ M; 5x10 ⁻⁵ M.	159
Figure 5.1:	Representative graph of the retention factor versus inverse temperature used to calculate the change in molar enthalpy. Mobile phase: acetonititrile:methanol:acetic acid:triethylamine 99%:1%:0.15%:0.1% (v/v/v), 1300 psi, Solutes: coumafury (♦), warfarin (♦), coumachlor (●), coumatetralyl (■), 4-hydroxycoumarin (▲). Other experimental details are given in the text.	е
Figure 5.2:	Representative graph of the retention factor versus pressure used to calculate the change in molar volume. Mobile phase acetonititrile:methanol:acetic acid:triethylamine 99%:1%:0.15%:0.1% (v/v/v), 293 K, Solutes: coumafuryl (♦), warfarin (♦), coumachlor (●), coumatetralyl (■), 4-hydroxycoumarin (▲). Other experimental details are given in the text.	
Figure 5.3:	Representative graph of the chiral selectivity versus inverse temperature used to calculate the chiral difference in molar enthalpy and molar entropy. Mobile phase: acetonititrile:methanol:acetic acid:triethylamine 99:1:0.15:0.1 (v/v/v/v), 1300 psi, Solutes: coumafuryl (♦), warfarin (♦), coumachlor (♠), coumatetralyl (■). Other experimental details are given in the text.	191
Figure 5.4:	Representative graph of the retention factor versus change is molar enthalpy used to observe enthalpy-entropy compensationabile phase: acetonititrile:methanol:acetic acid:triethylamine 99%:1%:0.15%:0.1% (v/v/v/v), 1300 psi.	tion.
Figure 5.5:	Representative graph of the kinetic rate constant versus invertemperature used to calculate the change in activation energy Mobile phase: acetonititrile:methanol:acetic acid:triethylamine 99%:1%:0.15%:0.1% (v/v/v/v), 1300 psi, Solutes: coumafury (♦), warfarin (♦), coumachlor (●), coumatetralyl (■). Other experimental details are given in the text.	у. е
Figure 6.1:	Structures of PAHs and N-PAHs for liquid chromatographic study.	210
Figure 6.2:	Representative chromatograms of 4-azapyrene in reversed-	

phase liquid chromatography. Column: polymeric

	octadecylsilica. Mobile phase: (A) methanol, 303 K, 2085 psi, 0.08 cm/s; (B) acetonitrile, 303 K, 2185 psi, 0.08 cm/s. Column: polymeric octadecylsilica. Other experimental details are given in the text.	213
Figure 6.3:	Representative graph of the retention factor versus inverse temperature used to calculate the change in molar enthalpy. Mobile phase: methanol, 2085 psi, 0.08 cm/s (——); acetonitrile, 2185 psi, 0.08 cm/s ($$). Solutes: 1-aminopyrene (\diamondsuit), 1-azapyrene (\spadesuit), 4-azapyrene (\spadesuit), benz[a]acridine (\blacksquare), dibenz[a,j]acridine (\blacktriangle). Other experimental details are given in the text.	218
Figure 6.4:	Representative graph of the retention factor versus pressure used to calculate the change in molar volume. Mobile phase: methanol, 283 K, 0.08 cm/s. Symbols defined in Figure 6.3. Other experimental details are given in the text.	225
Figure 6.5:	Representative graph of the rate constant (k_{ms}) versus inverse temperature used to calculate the activation energy. Mobile phase: methanol, 2085 psi, 0.08 cm/s (); acetonitrile, 2185 psi, 0.08 cm/s $()$. Symbols defined in Figure 6.3. Other experimental details are given in the text.	232
Figure 6.6:	Representative graph of the rate constant (k_{ms}) versus pressure used to calculate the activation volume. Mobile phase: methanol, 283 K, 0.08 cm/s. Symbols defined in Figure 6.3. Other experimental details are given in the text.	234
Figure 7.1:	Representative examples of alternant N-PAH and nonalterna N-PAH.	nt 250
Figure 7.1:	Structures of PAHs and N-PAHs for fluorescence quenching study.	254

CHAPTER 1

INTRODUCTION AND BACKGROUND

1.1 IMPORTANCE OF CHIRAL SEPARATIONS

Enantiomers are those pairs of molecular entities that are mirror images of each other and non-superimposable. The enantiomers have the same physical and chemical properties in an achiral environment and, thus, are difficult to Separation of chiral compounds has been of great interest in separate. academia and industry because of their prevalence and biological importance. The "building blocks" for the body, including proteins, nucleic acids and polysaccharides are composed of chiral biomolecules. Naturally, these biomolecules exist in only one of the two possible enantiomeric forms, demonstrating different responses to each enantiomer in drugs, foods, pesticides, wastes, and so on [1]. In previous years, the pharmaceutical industry suffered from failure to discriminate of the two enantiomers. Whereas one isomer may produce the expected therapeutic effect, the other may be inactive or, even worse, may produce unwanted side effects [2]. In 1992, the U.S. Food and Drug Administration (FDA) issued guidelines for development of stereoisomeric drugs. Not only the drugs, but also their metabolites, must be separated and analyzed individually. Only the therapeutically active isomer can be put on the market if the other isomer is detrimental. Thus, the separation of enantiomers is necessary and important.

1.2 CHIRAL SEPARATION WITH LIQUID CHROMATOGRAPHIC METHODS

Although chiral separations represent one group of the most complicated separations, great progress has been made ever since the extension of chiral separation to chromatography. Chromatographic methods can be divided into indirect methods, which utilize derivatizing agents, or direct methods, which utilize chiral mobile phases or chiral stationary phases.

1.2.1 Indirect Methods

In the indirect method, the racemic mixtures react with chiral reagents to form a pair of diastereomers. Because diastereomers possess different physiochemical properties, they can be separated in an achiral environment. The advantages of the indirect approach are the following: (1) less expensive, because conventional chromatographic columns can be used; (2) flexible, because various achiral columns and mobile phase conditions can be used; and (3) different selectivities can be achieved. On the other hand, the disadvantages of this method are: (1) long analysis time that includes sample preparation and verification of the derivatization chemistry; (2) inconvenience, specifically in preparative chromatography, when reversal of derivatization is needed to recover the pure enantiomers.

1.2.2 Direct Methods

Chiral high-performance liquid chromatography has proven to be one of the best methods for the direct separation of enantiomers [3]. Some optically pure chiral molecules are either added into the mobile phase (chiral additive) or attached to the stationary phase (chiral stationary phase, CSP). Both of these two methods are based on the formation of temporary diastereoisomers.

1.2.2.1 Chiral mobile phase additive

In this method, chiral separation is accomplished by the formation of a pair of transient diastereomeric complexes between racemic analytes and the chiral mobile phase additive. Chiral discrimination is due to differences in the stabilities of the diastereomeric complexes, solvation in the mobile phase, and/or binding of the complexes to the solid support. The more stable complex will be preferentially eluted and the less stable one will be eluted later. The three major approaches in the formation of diastereomeric complexes are transition metal ion complexes (ligand exchange), ion pairs, and inclusion complexes. Advantages of this technique are as follows [4]: (1) less expensive, conventional liquid chromatographic columns can be used; (2) a wide variety of possible additives are available; and (3) different selectivities from the chiral phases can be obtained by adding different additives. However, the disadvantage with this technique include: (1) need to synthesize optically pure additives, (2) inconvenience of the need to remove the chiral additive from the enantiomeric solutes for preparative applications; and (3) additives limit choice of detection system.

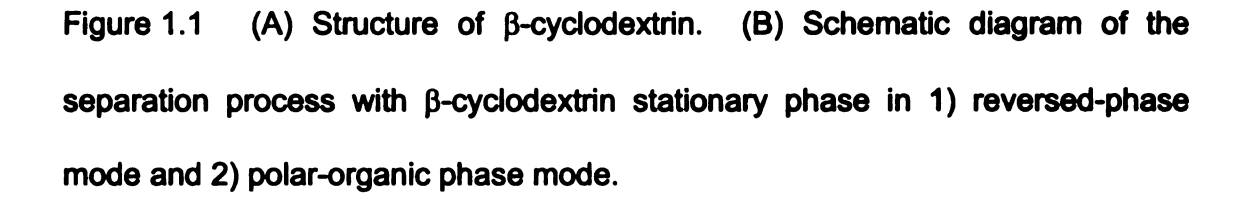
1.2.2.2 Chiral stationary phase (CSP)

Chiral separation by using chiral stationary phases (CSPs) is based on the formation of transient diastereomeric complexes between the enantiomers and the chiral molecule that is an integral part of the stationary phase. The more

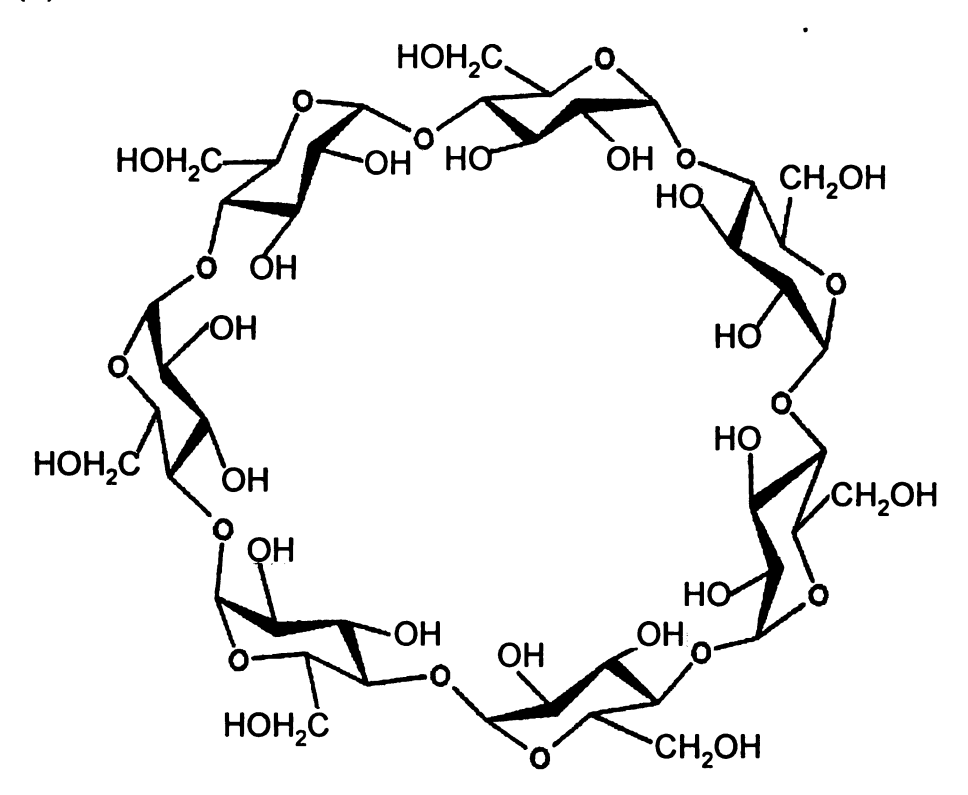
stable one will be preferentially retained and the less stable one will be eluted first. So far, the CSPs have been categorized under several different types including inclusion-type, brush-type, affinity-type, and also amylose- and cellulose-type CSPs.

1.2.2.2.1 Inclusion-type CSP

One of the most common examples of inclusion CSPs are the native and derivatized cyclodextrins. Cyclodextrins are cyclic oligosaccharides containing six or more D-glucose units connected through α -1,4-glycosidic bonds. The structure of β -cyclodextrin contains seven glucose units with 35 chiral centers. while α - and γ - cyclodextrins contain six and eight glucose units, respectively. The structure of β-cyclodextrin is shown in Figure 1.1A. In reversed-phase mode, the mobile phase is relatively more polar than the stationary phase, and mainly composed of water and acetonitrile or methanol. The hydroxyl groups of the cyclodextrin are oriented toward the exterior surface, which makes the interior of the cavity relatively nonpolar and hydrophobic. Consequently, solutes may enter the cavity and be retained by dispersion and hydrogen-bonding interactions. In the polar organic-phase mode, the mobile phase is mainly composed of acetronitrile and methanol. It is generally believed that the acetonitrile will enter the cavity, so the solute will be on top of the cyclodextrin cavity and be retained mainly by hydrogen bonding. The separation process is illustrated in Figure 1.1B. A naphthalene-related compound is illustrated as the model solute, because βcyclodextrin is known for separating two-ring compounds. In reversed-phase mode, the model solute is included into the cyclodextrin cavity; in polar-organic



(A)



(B)

1) In reversed-phase mode

2) In polar organic-phase mode

$$+ \bigvee_{z}^{x} \bigvee_{n \neq x}$$

phase mode, the acetonitrile is included into the cyclodextrin cavity, while the solute is only stay on top of the cyclodextrin cavity. These two processes are demonstrated in Figures 1.1B1 and 1.1B2, respectively.

1.2.2.2.2 Brush-type CSP

Brush CSPs distinguish themselves from other CSPs by having a small chiral molecule covalently bonded to the solid phase, usually silica. The organic groups of the chiral molecule remain directed away from the silica surface, appearing as bristles of a brush. Among the brush CSPs, the most widely known and commercially successful are those developed by Pirkle and coworkers. Most of the Pirkle-type CSPs emphasize electron donor-acceptor interactions of the nonbonding (n) and aromatic (π) type. Chiral separations are achieved by establishing three points of interaction between an enantiomer and the CSP (Figure 1.2), where at least one of these interactions is stereospecific [5]. Consequently, the other enantiomer is only able to sustain two points of interaction with the CSP and is less retained. Most separations with Pirkle-type CSPs are performed in the normal-phase mode, where a nonpolar mobile phase is utilized.

1.2.2.2.3 Amylose- and Cellulose-type CSP

Polysaccharides such as amylose and cellulose are naturally occurring, optically active polymers. Amylose is composed of glucose units connected with α -1,4-glycosidic bonds, and it adopts a helical structure in its native form. Cellulose is based on β -1,4-glycosidic bonds, and adopts a more linear structure. Native polysaccharides have long been known to exhibit chiral selectivity [6],

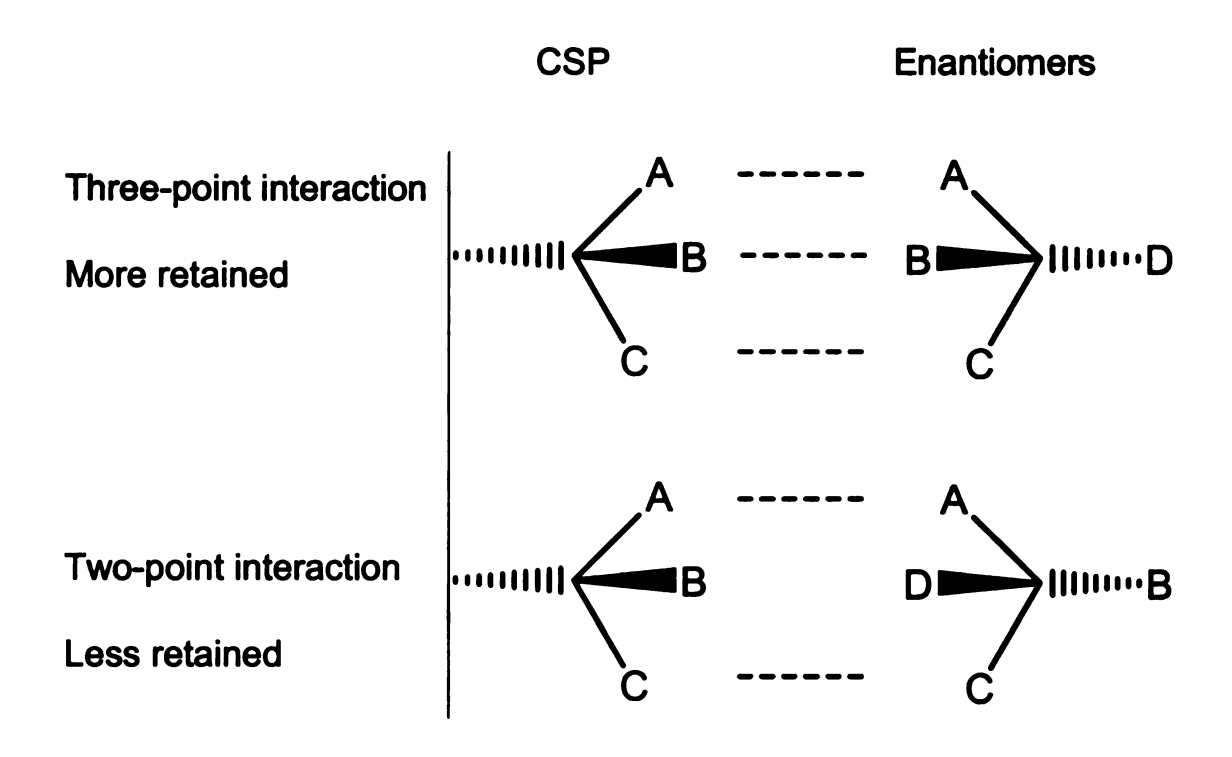


Figure 1.2 Schematic diagram of three-point model responsible for chiral separation.

however, their chiral resolving abilities are not sufficient for practical usage. Poor resolution and broad peaks are obtained due to nonstereoselective binding and slow mass transfer processes, and also because of slow diffusion through the polymer network. Comparatively, derivatized polysaccharide CSPs have much better chromatographic and enantiomeric properties than native polysaccharide CSPs, which has led to their successful commercialization. The chiral recognition mechanism for polysaccharide CSPs is generally thought to consist of cohesive attraction followed by steric fit of the chiral solute onto the chiral surface. The structural differences between amylose and cellulose are responsible for the difference in their retention mechanisms.

1.2.2.2.4 Affinity- type CSP (protein)

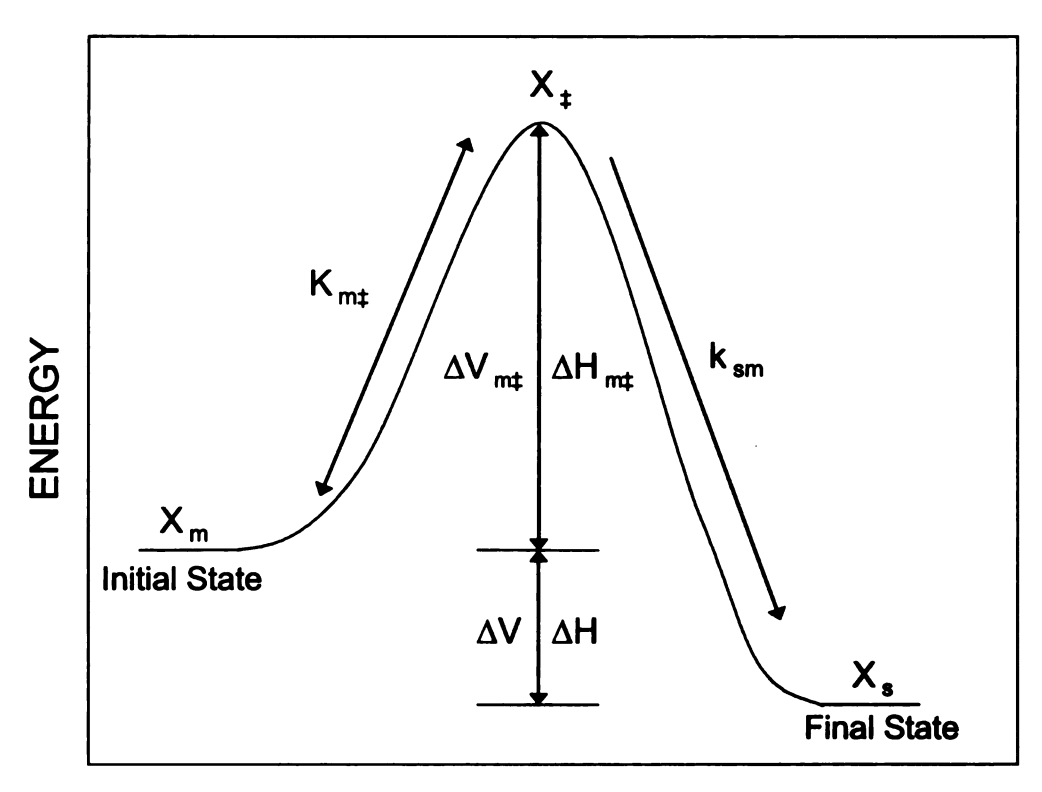
Proteins are naturally occurring, optically active polymers composed of L-amino acids. As a result, immobilized proteins on solid supports are capable of discriminating enantiomers. Protein-based CSPs are of special interest because of their unique enantioselective properties and wide applications. Chromatographic methods are distinguished on the basis of whether the proteins are soluble or immobilized, where the latter is known as affinity chromatography.

The most commonly used proteins are as follows: (1) albumins, such as human serum albumin and bovine serum albumin; (2) glycoproteins, such as α_1 -acid glycoprotein, ovomucoid, and avidin; (3) enzymes, such as cellobiohydrolase I, lysozyme, and pepsin; and (4) other miscellaneous proteins, such as β -lactoglobulin. Although protein CSPs are widely used, the elucidation of their retention mechanism is relatively difficult due to their complex structures.

These complex structures are the result of different amino acid sequences (primary structure) as well as different disulfide bridges, hydrogen bonding, and other types of intramolecular bonding (secondary and tertiary structure). Because of their structure, protein CSPs usually rely on different numbers or types of binding sites for discrimination of enantiomers. To retain the protein structure and avoid denaturation, most separations are performed in the reversed-phase mode.

1.3 THERMODYNAMIC AND KINETIC THEORY

When the retention process is considered as a chemical reaction, an energy-coordinate diagram (Figure 1.3) can be constructed to explain the thermodynamic and kinetic contributions. In this diagram, the solute transfers from the mobile phase (X_m) to the stationary phase (X_s) through a high-energy transition state (X_±). The thermodynamic parameters, e.g., the change in molar enthalpy (ΔH) and molar volume (ΔV), are characterized by the difference between the final and initial states. These thermodynamic quantities represent the weighted average of all of the available states in the heterogeneous stationary and mobile phases, respectively. The kinetic aspects of the retention event can be described by using transition-state theory. The transfer from mobile to stationary phase is characterized by a fast equilibrium between the mobile phase and transition state with pre-equilibrium constant K_{m±}, followed by a ratelimiting step between the transition state and the stationary phase with rate constant k_{em} . The kinetic parameters, e.g. the activation enthalpy (ΔH_{mt}) and activation volume (ΔV_{mt}), can be used to elucidate the kinetic description of the



REACTION COORDINATE

Figure 1.3 Energy coordinate diagram

retention event. For the transfer from stationary to mobile phase, the pre-equilibrium constant $K_{s\pm}$ and rate constant k_{ms} are used to determine the corresponding activation enthalpy ($\Delta H_{s\pm}$) and activation volume ($\Delta V_{s\pm}$). These kinetic quantities represent the weighted average of all available paths between the final and initial states. The derivation of these thermodynamic and kinetic quantities is described in the following sections.

1.3.1 Thermodynamics

Thermodynamics is the study of the system at steady state. At the microscopic level, steady-state conditions may be achieved in which the activity (or concentration) of the solute in the mobile and stationary phases (a_m and a_s, respectively) achieves a constant value

$$K = \frac{a_s}{a_-} = k\beta \tag{1.1}$$

where K is the equilibrium constant, k is the retention factor, and β is the phase ratio. The phase ratio is defined as the volume of the mobile phase divided by the volume of the stationary phase. The ratio of the equilibrium constants or retention factors for two solutes defines the selectivity (α)

$$\alpha = \frac{K_2}{K_1} = \frac{k_2}{k_1} \tag{1.2}$$

where the subscripts 1 and 2 denote the less and more retained solutes, respectively. This ratio may reflect the differences between chiral solutes (chiral selectivity in Chapter 4 and 5).

The equilibrium constant is related to the change in molar Gibbs free energy (ΔG) by

$$\ln K = \frac{-\Delta G}{RT} \tag{1.3}$$

where R is the gas constant and T is the absolute temperature. The selectivity for two solutes is correspondingly related as

$$\ln \alpha = \ln \frac{K_2}{K_1} = \frac{-\Delta \Delta G}{RT}$$
 (1.4)

where $\Delta\Delta G$ represents the difference in molar Gibbs free energy for chiral selectivity. The Gibbs free energy is related to the changes in molar enthalpy (ΔH) and molar entropy (ΔS) by the Gibbs-Helmholtz equation [7]

$$\Delta G = \Delta H - T \Delta S \tag{1.5}$$

By substitution, the retention factor can be related to the molar enthalpy and molar entropy as follows

$$\ln k = \ln K - \ln \beta = \frac{-\Delta H}{RT} + \frac{\Delta S}{R} - \ln \beta$$
 (1.6)

The change in molar enthalpy can be determined by graphing the natural logarithm of the retention factor versus inverse temperature at constant pressure. This will yield a slope that is related to the change in molar enthalpy, and an intercept that contains information about the change in molar entropy and the phase ratio. When the phase ratio is known, the molar entropy can be determined from the intercept. However, the phase ratio is often not known and accurate determination of the molar entropy is not possible. The phase ratio and the molar entropy must be independent of temperature for accurate determination of the molar enthalpy. The change in molar enthalpy will be positive for an endothermic transfer and negative for an exothermic transfer of

the solute from mobile to stationary phase. The change in molar entropy will be positive when there is a favorable dissipation of energy through an increase in the number or distribution of microstates. This most commonly occurs through a change in volume or concentration, leading to a change in configurational entropy, as the solute is transferred from the mobile to stationary phase. The selectivity for two solutes is correspondingly related as

$$\ln \alpha = \frac{-\Delta \Delta H}{RT} + \frac{\Delta \Delta S}{R} \tag{1.7}$$

Thus, a graph of the natural logarithm of the selectivity versus inverse temperature will yield from the slope and intercept the differential change in molar enthalpy ($\Delta\Delta H$) and molar entropy ($\Delta\Delta S$), respectively, associated with the chiral selectivity (Chapter 5).

From the definition of the molar enthalpy

$$\Delta H = \Delta E + P \Delta V \tag{1.8}$$

where ΔE is the change in molar internal energy, ΔV is the change in molar volume, and P is the pressure. Substitution of Equation 1.8 into Equation 1.6 yields

$$\ln k = \frac{-\Delta E}{RT} - \frac{P \Delta V}{RT} + \frac{\Delta S}{R} - \ln \beta$$
 (1.9)

The change in molar volume can be determined by graphing the natural logarithm of the retention factor versus pressure at constant temperature. This will yield a slope that is related to the change in molar volume, and an intercept that contains information about the molar internal energy, molar entropy, and phase ratio. These parameters must be independent of pressure for accurate

determination of the molar volume. The change in molar volume will be positive when the solute occupies a larger volume and negative when the solute occupies a smaller volume in the stationary phase than in the mobile phase.

To gain a greater understanding of the balance of thermodynamic contributions to solute retention, enthalpy-entropy compensation is very useful. For a pair or series of solutes that obey a linear free energy relationship [8], there exists a hypothetical temperature at which the relative changes in enthalpy and entropy are balanced and the net change in free energy is zero. By rearrangement of Equation 1.5, this compensation temperature (T_c) can be expressed as

$$T_{c} = \frac{\Delta \Delta H}{\Delta \Delta S} \tag{1.10}$$

At this temperature, the pair or series of solutes would co-elute and no separation would be achieved (α = 1.0). Hence, it is also called the isoselective temperature or iso-enantioselective temperature (T_{iso}) in chiral separations. A compensation temperature that is substantially greater than ambient temperature suggests that the retention mechanism is enthalpy-dominated, whereas a compensation temperature that is less than ambient temperature is entropy-dominated.

The compensation temperature can be determined from the slope of a graph of the change in molar enthalpy versus the change in molar entropy, both derived from Equation 1.6. However, for statistical reasons, a linear relationship may be observed between ΔH and ΔS even in the absence of enthalpy-entropy compensation [9]. Krug et al. [10] investigated different methods to identify true

enthalpy-entropy compensation that is not influenced by statistical artifacts. By means of Equation 1.6, the free energy at a specific temperature (T) can be related to the free energy at the compensation temperature (T_c) by

$$\Delta G = \Delta H \left(1 - \frac{T}{T_c} \right) + \frac{T \Delta G_{T_c}}{T_c}$$
 (1.11)

The retention factor can then be related to the free energy at the compensation temperature by

$$lnk = -\frac{\Delta H}{R} \left(\frac{1}{T} - \frac{1}{T_c} \right) + \frac{\Delta G_{Tc}}{RT_c} - ln\beta$$
 (1.12)

Thus, a graph of the natural logarithm of the retention factor versus the change in molar enthalpy may be used to evaluate enthalpy-entropy compensation. If compensation occurs, this graph will be linear and the slope can be used to calculate the compensation temperature. The compensation temperature may be used to compare the retention mechanisms for different solutes, different mobile phases, or different stationary phases. As discussed by Ranatunga et al. [11], if the compensation temperatures are identical, then the relative contributions of enthalpy and entropy to the overall free energy are the same for the two systems. However, if compensation temperatures are different, then the underlying retention mechanisms must be distinctly different.

1.3.2 Kinetics

Whereas thermodynamic information is vital, kinetic information provides a deeper understanding of the retention mechanism. If the retention process is treated as a first-order or pseudo-first-order reaction, k_{em} and k_{ms} are the corresponding rate constants for solute transfer from mobile to stationary phase

and from stationary to mobile phase, respectively. These are "lumped" rate constants, i.e., they comprise all contributions to the kinetic behavior including the sorption/desorption event, diffusion in the mobile and stationary phases, diffusion in pores and stagnant layers, interfacial resistance to mass transfer, etc. The rate constants, which reflect the kinetic behavior, are related to the retention factor, which reflects the thermodynamic behavior, by

$$k = \frac{k_{sm}}{k_{me}} \tag{1.13}$$

The detailed kinetic parameters can be elucidated by applying a combination of thermodynamic and transition-state theories. The rate constant k_{ms} is expressed by the Arrhenius equation as

$$k_{sm} = A_{mt} \exp\left(\frac{-\Delta E_{mt}}{RT}\right)$$
 (1.14)

where $A_{m\pm}$ is the pre-exponential factor and $\Delta E_{m\pm}$ is the activation energy for the transfer from mobile to stationary phase. By rearrangement,

$$\ln k_{sm} = \ln A_{mt} - \frac{\Delta E_{mt}}{RT}$$
 (1.15)

The activation energy can be determined by graphing the natural logarithm of the rate constant versus inverse temperature at constant pressure. This will yield a slope that is related to the activation energy, and an intercept that contains information about the pre-exponential factor. The activation energy represents the energetic barrier that must be overcome for the solute transfer from mobile to stationary phase.

By using classical thermodynamic relationships, the activation energy is given by

$$\Delta E_{mt} = \Delta H_{mt} + RT - P \Delta V_{mt}$$
 (1.16)

By substitution into Equation 1.15

$$\ln k_{sm} = \ln A_{mt} - \frac{\Delta H_{mt} + RT - P \Delta V_{mt}}{RT}$$
 (1.17)

The activation volume can be determined by graphing the natural logarithm of the rate constant versus pressure at constant temperature. This will yield a slope that is related to the activation volume, and an intercept that contains information about the activation enthalpy and pre-exponential factor. The activation enthalpy and pre-exponential factor must be independent of pressure for accurate determination of activation volume. The activation volume represents the volumetric barrier that must be overcome for the solute transfer from mobile to stationary phase. In a similar manner, the rate constant k_{ms} can be used to determine the activation energy (ΔE_{st}) and activation volume (ΔV_{st}) for the solute transfer from stationary to mobile phase. These kinetic quantities provide a detailed description of the energetic and volumetric requirements of the retention process that complement the thermodynamic description.

1.4 METHODS FOR THERMODYNAMIC AND KINETIC STUDIES

1.4.1 Perturbation Methods

Among the available methods for evaluation of thermodynamic and kinetic parameters, perturbation methods play an important role [12]. Perturbation methods represent the simplest approach, wherein the solute, mobile phase, and

stationary phase of interest are contained in a small, static cell. perturbation is applied to the equilibrium in order to alter the activity or concentration of the solute in the mobile and stationary phases. The perturbation may be achieved by rapidly changing conditions such as temperature, pressure, or dipole moment. After perturbation, the rate of relaxation of the system to the new conditions is monitored, followed by mathematical extraction of the equilibrium and rate constants. The advantage of the perturbation methods is their simplicity, where thermodynamic and kinetic behavior can be measured without interference from flow contributions. The measured rate constants consist of the sorption/desorption process and diffusional contributions to mass transfer. One of the limitations of these methods is that they require perturbation, during which the actual thermodynamic and kinetic behavior of the system is altered. Hence, the determined values of equilibrium and rate constants are neither those of the initial state nor of the final state after perturbation. In order to minimize the required perturbation, the equilibrium constant should be as close to unity as possible. This ensures the greatest change in activity or concentration for a given perturbation of the system. In addition, the perturbation must be applied uniformly to the entire system and with sufficient speed that it does not contribute to the observed kinetic behavior. Although these methods are very promising, their application to chromatographic systems has been relatively limited.

1.4.2 Shallow-Bed Method

The shallow-bed method can be considered as an intermediate between perturbation methods and chromatographic methods. In this method, the stationary phase particles are packed in an extremely short ("zero length") column. The experiments may be performed in two ways: sorption (uptake) or desorption (release) methods. In the sorption method, a mobile phase solution containing the solute flows through the shallow bed at a high linear velocity. The concentration of the solute in the effluent solution is nearly identical to that in the influent solution. If the linear velocity is sufficiently high, the stagnant diffusion layer surrounding the particle will be thin. Hence, the time required for diffusion through this layer will be small compared to the time required for the slow intraparticle processes. As a result, the intraparticle processes will determine the observed sorption rate. After a certain time, the flow is stopped and the amount of solute that has been sorbed is measured by eluting it out of the shallow bed. This measurement provides a single point on the sorption curve. This experiment is then repeated for varied sorption times to construct the complete sorption rate curve.

An alternative approach that is less time-consuming and labor-intensive is the desorption method. In this method, the shallow bed is pre-equilibrated by flow of a mobile phase solution containing the solute. To initiate the experiment, the flow is abruptly shifted to a solute-free mobile phase, which causes the solute to be desorbed from the bed. By detecting the eluted solute concentration as a function of time, the desorption curve can be constructed from a single

experiment. Specifically speaking, the concentration C(t) is a function of the instantaneous molecular desorption rate of the solute $(dn_i(t) / dt)$ and of the flow rate (F) as follows

$$C(t) = \frac{(dn_i(t)/dt)}{F}$$
 (1.18)

After integration, the desorption rate curve is constructed as

$$n_i(t) = F_0^t C(t) dt$$
 (1.19)

The desorption rate curve is then fit by nonlinear regression to different theoretical models, such as the linear driving force model and spherical diffusion model, to extract the rate constants [13-16].

1.4.3 Chromatographic Methods

Chromatographic methods are the most widely used methods for determining thermodynamic and kinetic behavior of the system. Chromatographic methods are dynamic with mobile phase flowing though the column at all times. In this way, the contribution of flow phenomena to the zone profile cannot be neglected. The two most common chromatographic methods are frontal and impulse methods.

1.4.3.1 Frontal method

In frontal analysis, the column is pre-equilibrated with the mobile phase. Then, a solution containing a known concentration of solute in the mobile phase is introduced continuously. As the solute sorbs onto the stationary phase, the column becomes saturated and the concentration of solute eluting from the column gradually increases, forming a characteristic breakthrough curve. The

mean position of the breakthrough curve can be related to the concentration and equilibrium constant of the solute as well as the sorption capacity of the column. The amount of solute sorbed is calculated from the breakthrough curve in order to derive a single point on the equilibrium isotherm. This process is repeated for progressively increasing concentrations of the solute to construct the complete isotherm. Three represented isotherm types are illustrated in Figure 1.4. Linear isotherm would produce a Guassian peak shape, Langmuir isotherm would produce a tailing peak shape, and Anti-Langmuir isotherm would produce a fronting peak shape.

To obtain kinetic information, theoretical breakthrough curves are numerically calculated for each concentration step. These theoretical curves use different values of the rate constant in the transport model, together with the equilibrium isotherm determined from the breakthrough data. The theoretical breakthrough curves are then compared to the experimental ones. The rate coefficient is determined in such a way that the best agreement is observed between the theoretical and experimental breakthrough curves. In this approach, it is assumed that the rate constant remains constant during each concentration step in the frontal analysis measurement and that this rate constant corresponds to the average concentration of each step [17].

1.4.3.2 Impulse method

The impulse method is generally performed by injecting a small volume of the solute onto the column. The elution of the solute zone is monitored by oncolumn or post-column detection. The retention factor and rate constants can be

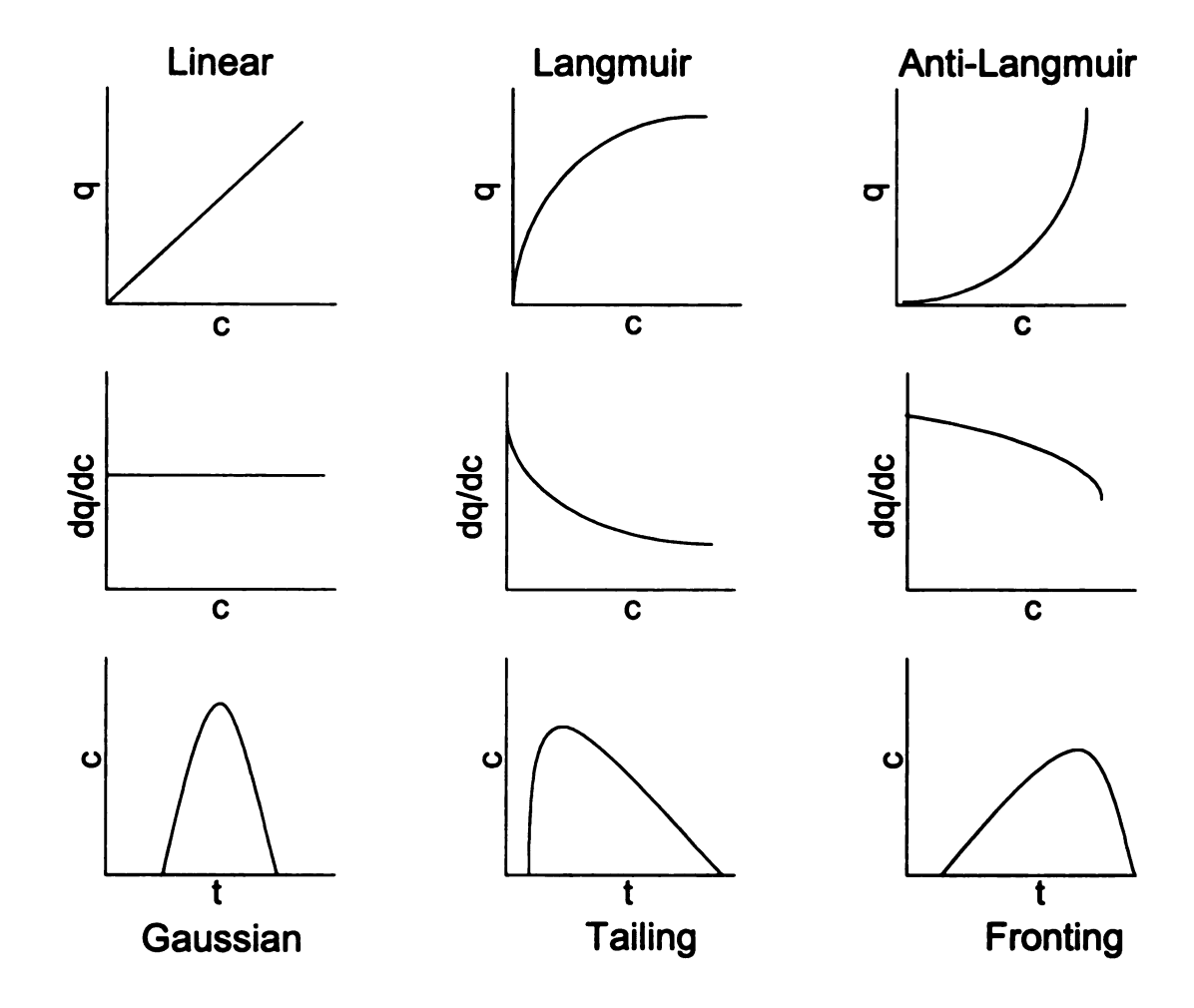


Figure 1.4 Three typical adsorption isotherms. q: loading, c: concentration, t: time.

extracted by any of the following models.

1.5.3.2.1 Plate-height model

In this model, the thermodynamic and kinetic parameters are determined from the mean and the broadening of the zone profile, respectively. The broadening or plate height may be determined in a variety of ways, but the most accurate is the statistical moments as they make no assumptions about the shape of the zone profile. The first and second statistical moments are calculated from the zone profile as

$$M_1 = \frac{\int C(t) t dt}{\int C(t) dt}$$
 (1.20)

$$M_{2} = \frac{\int C(t)(t - M_{1})^{2} dt}{\int C(t) dt}$$
 (1.21)

The first moment (M_1) represents the mean retention time. It can be directed related to the retention factor by

$$k = \frac{M_1 - t_0}{t_0} \tag{1.22}$$

where to is the elution time for a non-retained compound.

The method of calculating kinetic rate constants is derived by extrapolation of Giddings' work [18]. The plate height in the length domain (H_L) can be related to the second moment (M_2) in the time domain by

$$H_{L} = \frac{\sigma_{L}^{2}}{L} = \frac{M_{2}}{L} \left(\frac{u_{0}}{1+k}\right)^{2}$$
 (1.23)

where u_0 is the mobile-phase linear velocity. The mass transfer term (C_s) for slow kinetics in a system that exhibits a partition or adsorption mechanism is given by

$$C_{a} = \frac{2k}{(1+k)^{2}k_{am}}$$
 (1.24)

Thus,

$$k_{ms} = \frac{2 k u_0}{(1+k)^2 dH_1}$$
 and $k_{sm} = \frac{2 k^2 u_0}{(1+k)^2 dH_1}$ (1.25)

where dH_L is the contribution to plate height arising from slow mass transfer.

Miyabe and Guiochon have evaluated the plate height contributions to various mass transfer processes [18]. In their approach, the statistical moments can be further elucidated as

$$\mathbf{M_1} = \frac{\mathbf{L}}{\mathbf{u_0}} \delta_0 \tag{1.26}$$

$$M_2 = \frac{2L}{u_0} \left(\delta_{ax} + \delta_f + \delta_d \right) \tag{1.27}$$

where δ_0 is a dimensionless retention parameter, equal to 1 + k, and is given by

$$\delta_0 = \varepsilon + (1 - \varepsilon)(\varepsilon_p + \rho_p K) \tag{1.28}$$

The contributions to M_2 from axial dispersion (δ_{ax}), external mass transfer (δ_f), and intra-particle diffusion (δ_d), respectively, are given by

$$\delta_{\text{ax}} = \left(\frac{D_{\text{L}}}{u_0^2}\right) \delta_0^2 \tag{1.29}$$

$$\delta_{\rm f} = (1 - \varepsilon) \left(\frac{R_{\rm p}}{3k_{\rm f}} \right) \left(\varepsilon_{\rm p} + \rho_{\rm p} K \right)^2 \tag{1.30}$$

$$\delta_{d} = (1 - \varepsilon) \left(\frac{R_{p}^{2}}{15 D_{\bullet}} \right) (\varepsilon_{p} + \rho_{p} K)^{2}$$
(1.31)

where ε is the inter-particle void fraction, ε_p and ρ_p are the porosity and density of the packing material, R_p is the particle radius, D_L is the axial dispersion coefficient, k_f is the external mass transfer coefficient, D_e is the intra-particle diffusivity, and K is the equilibrium constant. Under conditions where the rate of sorption/desorption is negligibly small, the plate height can be written as

$$H = \left(\frac{M_2}{M_1^2}\right) \left(\frac{L}{2u_0}\right) = \frac{D_L}{u_0^2} + \frac{\delta_f}{\delta_0^2} + \frac{\delta_d}{\delta_0^2}$$
 (1.32)

The different parameters that are related to mass transfer processes can be estimated or calculated based on the above equations. For example, the external mass transfer coefficient, diffusion coefficient in the mobile phase, and pore diffusion coefficient can all be estimated, and the diffusion coefficient in the stationary phase can thus be calculated. More specific information on the foundations and application of this model can be found in the excellent review by Miyabe and Guiochon [18].

The plate-height model assumes that all contributions to variance, both symmetric and asymmetric, that are not directly attributable to fast processes such as axial dispersion arise from slow kinetics. There are several potential sources of error in this method. First, this method requires that the solute concentration be within the linear region of the isotherm, such that it does not contribute to the variance. Second, this method relies on the accurate calculation and subtraction of all fast mass transfer terms, which is difficult for packed columns in liquid chromatography. Empirical estimations of these

parameters will introduce errors. Moreover, any extra-column contributions to variance, including those from the injector, detector, connectors, etc., must be accurately calculated and subtracted. Again, there are no theoretical methods for the calculation of these parameters, so empirical estimations are necessary.

1.4.3.2.2 Exponentially modified Gaussian (EMG) model

Consider an incremental length of the chromatographic column. Zone broadening can arise from multiple paths, diffusion, and mass transfer processes that are fast relative to the time spent in the incremental length. These processes contribute to the symmetric broadening, which is described by a Gaussian function

$$C(t) = \frac{A}{\sqrt{2\pi}\sigma_g} \exp\left(-0.5\left(\frac{t - t_g}{\sigma_g}\right)^2\right)$$
 (1.33)

where A is the area, t_g is the retention time of the Gaussian component, and σ_g is the standard deviation of the Gaussian component.

In addition, zone broadening can arise from mass transfer processes that are slow relative to the time spent in the incremental length. These processes contribute to the asymmetric broadening. For a partition or adsorption mechanism that can be considered as a first-order or pseudo-first-order reaction, this contribution is given by an exponential function

$$C(t) = A \exp\left(\frac{-(t - t_g)}{\tau}\right)$$
 (1.34)

where τ is the standard deviation of the exponential component.

The zone profile observed at the end of the total column length is the convolution of the Gaussian and exponential contributions, i.e., the multiplication of the functions and integration within each incremental length. This convolution is given by the exponentially modified Gaussian (EMG) equation

$$C(t) = \frac{A}{2\tau} \exp\left(\frac{\sigma_g^2}{2\tau^2} + \frac{t_g - t}{\tau}\right) \left(erf\left(\frac{t - t_g}{\sqrt{2}\sigma_g} - \frac{\sigma_g}{\sqrt{2}\tau}\right) + 1 \right)$$
 (1.35)

where erf is an statistical error function. The zone profile is fit to the EMG equation by nonlinear regression to extract the regression parameters (A, t_g , σ_g , τ). From these parameters, the retention time t_r is calculated as

$$t_r = t_g + \tau \tag{1.36}$$

and the corresponding retention factor is calculated as

$$k = \frac{t_r - t_0}{t_0} \tag{1.37}$$

The method of calculating kinetic rate constants from the EMG model is derived by extrapolation of Giddings' work [19]. The mass transfer term for slow kinetics in the partition or adsorption mechanism is given by Equation 1.24. By rearrangement, the rate constants are given by

$$k_{ms} = \frac{2kt_0}{\tau^2}$$
 and $k_{sm} = \frac{2k^2t_0}{\tau^2}$ (1.38)

The EMG model assumes that all contributions to asymmetric broadening (τ) arise from slow kinetics. There are several potential sources of error in this method. First, this method requires that the solute concentration be within the linear region of the isotherm, such that it does not contribute to the asymmetry.

Second, any extra-column contributions to asymmetry must be minimized or eliminated. In practice, this is achieved by detection at several points along the chromatographic column and subtraction of the parameters determined at each detector [19]. It is noteworthy that the EMG method does not require *a priori* estimation, whether by theoretical or empirical means, of symmetric column or extra-column contributions to broadening.

1.4.3.2.3 Giddings model

By means of stochastic theory [14], Giddings derived a model suitable for theoretical treatment of the adsorption mechanism under first-order or pseudofirst-order conditions

$$C(x) = A\gamma \sqrt{\frac{k}{\sqrt{k}}} I_1(2\gamma \sqrt{kx}) \exp(-\gamma x - \gamma k)$$
 (1.39)

where γ is a dimensionless constant, equal to the product of the desorption rate constant (k_{ms}) and the elution time of a nonretained compound (t₀). After conversion from the time domain (t) to the retention factor domain (x), the zone profile is fit by nonlinear regression to Equation 1.39. From the regression parameters (A, k, γ), the corresponding retention factor and rate constants are calculated.

The Giddings model assumes that all contributions to symmetric and asymmetric broadening arise from slow kinetics. There are several potential sources of error in this method. First, this method requires that the solute concentration be within the linear region of the isotherm, such that it does not contribute to the broadening. Second, this method requires that column contributions from multiple paths and diffusion in the mobile and stationary

phases be negligible. Moreover, any extra-column contributions, including those from the injector, detector, connectors, etc., must also be negligible. Unlike the plate height and EMG methods, there is no *a posteriori* method to correct for these contributions.

1.4.3.2.4 Nonlinear chromatography models

All of the impulse methods described above are suitable for thermodynamic and kinetic measurements within the linear region of the isotherm. However, some mechanisms such as adsorption, ion exchange, and complexation have stationary phases with a limited number of sites that may be easily overloaded. Hence, it is desirable to be able to evaluate their behavior under nonlinear conditions.

A convenient method to extract thermodynamic and kinetic information from frontal profiles was reported by Thomas [20] and later modified for elution zone profiles by Wade et al. [21]. This model was derived for mechanisms that can be considered as second-order sorption and first-order desorption reactions under linear and nonlinear conditions. This theoretical model is given by

$$C(x) = \left(\frac{A\gamma}{KC_0}\right) \left(1 - \exp(-\gamma KC_0)\right) \left(\frac{\left(\sqrt{k/x} \ l_1(2\gamma\sqrt{kx})\right) \exp(-\gamma x - \gamma k)}{1 - T(\gamma k, \gamma x)(1 - \exp(-\gamma KC_0))}\right)$$
(1.40)

where

$$T(u,v) = e^{-v} \int_{0}^{u} e^{-t} I_{0}\left(\sqrt{2vt}\right) dt$$
 (1.41)

In this equation, γ is a dimensionless constant equal to the product of the desorption rate constant (k_{ms}) and the elution time of a nonretained compound (t_0), k is the retention factor, K is the equilibrium constant, and C_0 is the initial

concentration. After conversion from the time domain (t) to the retention factor domain (x), the zone profile is fit by nonlinear regression to Equation 1.41. From the regression parameters (A, k, γ , KC₀), the corresponding retention factor and rate constants are obtained.

The Thomas model assumes that all contributions to symmetric and asymmetric broadening arise from nonlinear isotherms and slow kinetics, which is a combination of mass transfer and sorption/desorption processes. There are several potential sources of error in this method. First, this method assumes the kinetics and the isotherm to be Langmuirian. Second, this method requires that column contributions from multiple paths and diffusion in the mobile and stationary phases be negligible. Moreover, any extra-column contributions, including those from the injector, detector, connectors, etc., must also be negligible. Unlike the statistical moment and EMG methods, there is no a posteriori method to correct for these contributions.

Other nonlinear chromatography models have been reviewed by Golshan-Shirazi and Guiochon [22,23]. Among those that provide both thermodynamic and kinetic information are the reaction-dispersive and transport-dispersive models. The reaction-dispersive model presumes that sorption/desorption kinetics are slow relative to the fast kinetics of mass transfer. The transport-dispersive model presumes that mass transfer kinetics are slow relative to the fast kinetics of sorption/desorption. These simplifications allow numerical solution of the general rate model for comparison of theoretical and experimental

zone profiles. Further information, including direct comparison of these models with the Thomas model, can be found in the previously published review [23].

1.5 PREVIOUS INVESTIGATIONS OF CHIRAL SEPARATIONS

1.5.1 Inclusion-Type CSP

Cyclodextrins were first immobilized to solid supports in 1978 [24]. Since then, extensive work has been done to improve the stability and versatility of cyclodextrinsilica CSPs, which made possible their commercialization in the 1980s. However, despite the large number of publications, only limited information is available on the thermodynamic characterization of these CSPs, and even less information is available on the kinetic characterization. Both thermodynamic and kinetic information are important for elucidation of the retention mechanism.

The earliest studies of temperature effects were focused on optimization of the separation process [25,26]. In these studies, lower temperature was shown to increase retention, due to stronger interactions between the solutes and the CSP, and also to increase enantioselectivity. A more detailed study of temperature was carried out by Cabrera and Lubda [27]. They separated two chiral pharmaceuticals, oxazepam and mephobarbital (Prominal), on native β-cyclodextrinsilica operated in the reversed-phase mode. A decrease in temperature caused an increase in retention factor for both solutes, however, it caused different effects on their enantioselectivity. The enantioselectivity was increased by reducing temperature for oxazepam, but increased by increasing temperature for mephobarbital. The van't Hoff plots were linear for both solutes

over the temperature range of 5 to 40 °C. From the thermodynamic data, the authors concluded that the differences in enantioselectivity were related to the enthalpy-controlled separation of oxazepam enantiomers ($\Delta\Delta H = -332$ cal/mol, $\Delta\Delta S = 55$ cal/mol) and the entropy-controlled separation of mephobarbital enantiomers ($\Delta\Delta H = 374$ cal/mol, $\Delta\Delta S = 419$ cal/mol). Morin et al. [28] also studied the effect of temperature on β-cyclodextrinsilica with a series of six imidazole derivatives. Over the temperature range of 20 to 55 °C, the van't Hoff plots for all solutes were linear at pH 7.0 and 7.5, but curved at pH 6.5, 8.0, and 8.5. The curved plots showed a minimum in the logarithm of the retention factor between 35 and 40 °C. The changes in molar enthalpy and entropy were determined from the van't Hoff plots. An enthalpy-entropy compensation analysis revealed that the retention mechanism was the same for all solutes at pH 7.0 and 7.5, and also the same for all solutes at pH 6.5, 8.0, and 8.5. From thermogravimetric analysis and differential scanning calorimetry, the authors speculated that a phase transition occurred at 43 °C between the ordered and disordered state of the cyclodextrin cavity at pH 6.5, 8.0, and 8.5, but not at pH 7.0 and 7.5. In the disordered state, a gain in freedom of the hydroxyl groups on each edge of the cyclodextrin cavity was obtained, with the minimum extent of hydrogen bond formation between them. In contrast, in the ordered state, a loss in freedom of the hydroxyl groups was obtained, with the maximum extent of hydrogen bond formation. As a result, the hydrophobic character, surface tension, and structure of the cyclodextrin cavity were all affected, thereby altering the retention mechanism.

Peyrin et al. [29] investigated the inclusion phenomena between βcyclodextrinsilica CSP and a series of dansyl amino acids with the salting-out agent sucrose. When the solute transfers from mobile to stationary phase. sucrose is displaced from the cyclodextrin cavity. With a simple physicochemical model, the number of displaced sucrose molecules can be determined, and the relative extent of solute inclusion can thus be calculated. The authors concluded that the L-enantiomers of the dansyl amino acids displaced a constant number of 1.9 sucrose molecules regardless of the R group. In contrast, the D-enantiomers displaced a larger number of sucrose molecules that decreased from 2.7 to 2.2 as the accessible surface area of the R group increased. Hence, the chiral recognition and enantioselectivity decreased with increasing size of the R group. The theoretical value of the accessible surface area that corresponded to no chiral resolution was 191 Å². It is noteworthy that the equivalent length of the R group (7.8 Å) is equal to the internal diameter of the native β -cyclodextrin cavity. The authors concluded that the inclusion process was largely dependent on steric hindrance. Temperature was also varied from 20 to 45 °C to observe the thermodynamic effects on enantioselectivity. The negative $\Delta\Delta H$ and $\Delta\Delta S$ values were determined from the linear van't Hoff plots, which indicated an enthalpycontrolled separation for all dansyl amino acids. The AAH and AAS values became less negative with increasing accessible surface area of the R group and more negative with increasing sucrose concentration. A similar approach was utilized by Guillaume et al. [30] using water as a surface tension modifier in the mobile phase. In this case, water was displaced when the dansyl amino acids were transferred to the β -cyclodextrin cavity. Similar results were concluded on the relative degrees of inclusion of the D- and L- enantiomers and the importance of steric effects in the chiral recognition mechanism.

The effect of pressure on the separation process with a βcyclodextrinsilica CSP was investigated by Ringo and Evans. With the positional isomers of nitrophenol as model solutes, a shift in retention with modest pressure change (300 bar) was observed and correlated to the change of partial molar volume for the complexation process [31]. The same method was applied to chiral separations with barbiturates, β-blockers, and anticoagulants as model solutes [32-34]. Most chiral compounds showed a dependence of the retention factor, enantioselectivity, and separation efficiency on pressure. The retention factor dependence reflected the statistical non-zero changes of molar volume for the complexation processes. The retention factors exhibited an increase or no change with pressure, and the change in molar volume was negative or negligible in the reversed-phase mode. However, in the polar-organic mode, the retention factors showed a decrease with pressure, and the change in molar volume was positive or negligible. The change in molar volume ranged from -12 to 17 cm³/mol. The enantioselectivity dependence reflected the unequal changes of molar volume between the enantiomers. Mephobarbital, metoprolol, and warfarin demonstrated a dependence of selectivity on pressure, with both positive and negative dependence observed. These pressure experiments provided insight into the differential volume of enantiomeric complexes formed with β-cyclodextrin.

Recently, Ching et al. [35,36] investigated both thermodynamic and kinetic behavior of derivatized β-cyclodextrinsilica CSPs. The equilibrium and kinetic constants for the chiral separation were obtained by moment analysis on the basis of the equilibrium-dispersive and transport-dispersive (solid-film linear driving force) models. The overall mass transfer coefficients, axial dispersion coefficients, and equilibrium constants were used to simulate the enantiomeric band profiles. Excellent correlation between simulated and experimental results confirmed the accuracy of the method as well as the results. The overall mass transfer coefficients were determined to be 58 and 73 min⁻¹ for S- and R-fluoxetine, respectively, and 669, 846, and 106 min⁻¹ for the co-eluted SRS- and SSR-nadolol, RRS-nadolol, and RSR-nadolol, respectively. These kinetic data indicate that mass transfer processes in the derivatized β-cyclodextrinsilica CSPs are relatively rapid.

1.5.2 Brush-Type CSP

Although there have been few systematic thermodynamic studies of Pirkle-type CSPs, temperature has been successfully utilized as an optimization tool. Mazzo et al. [37] optimized the chiral separation of an antihypertensive drug, MK-286, with an N-(3,5-dinitrobenzoyl)phenylglycine CSP. The retention factors and enantioselectivity increased with decreasing temperature, however, the peak broadening (plate height) also increased. Because of these concomitant changes, the resolution increased from 0.75 at room temperature to 1.25 at 0 °C. Although no thermodynamic parameters were reported here, it was probably an enthalpy-controlled process that facilitated separation at lower temperature.

Pescher et al. [38] optimized the separation of tertiary phosphine oxides with N-(3.5-dinitrobenzoyl) derivatives of phenylglycine, serine, and alanine as CSPs. They observed a similar effect of temperature, where the enantioselectivity with the phenylglycine CSP increased from 1.52 to 2.33 with a decrease in temperature from 50 to -15 °C. A nonlinear dependence of enantioselectivity on temperature was observed by Weaner and Hoerr [39]. They investigated a series of fatty acid esters and amide epoxides on an N-(3.5dinitrobenzoyl)phenylglycine CSP. While the enantioselectivity of the ester decreased rapidly above 0 °C, those of the amide reached a maximum at 10 °C and remained constant up to 40 °C. This behavior was attributed to the weak interaction forces between the ester and CSP, and to the relatively strong forces between the amide and CSP. Pirkle also observed some unusual temperaturedependent behavior [40]. In the separation of spirolactam enantiomers on an N-(3,5-dinitrobenzoyl)phenylglycine CSP, a nonlinear van't Hoff plot was obtained. The curvature of these plots was dependent on the concentration of 2-propanol in the mobile phase, which indicated a temperature-dependent interaction of 2propanol with the stationary phase or with the solute. However, the natural logarithm of enantioselectivity versus the inverse temperature gave a linear relationship, which indicated that this behavior affected both enantiomers equally and had little influence on the chiral recognition mechanism. Another example with the separation of N-(3,5-dinitrobenzoyl)-1-phenylethylamine enantiomers showed an initial decrease in enantioselectivity with a reduction of temperature, followed by an inversion of elution order and, subsequently, an increase in enantioselectivity [41]. The observed temperature effects showed a dependence on the type and concentration of organic modifier in the mobile phase.

Pirkle and Welch [42] systematically investigated the role of solvation on the of N-(2-naphthyl)alanine separation derivatives on N-(3.5dinitrobenzoyl)leucine CSP. In general, both retention and enantioselectivity decreased with increasing mobile phase polarity in both normal- and reversedphase modes. The van't Hoff plots, obtained over a temperature range of 0 to 90 °C, were used to evaluate the thermodynamic changes in molar enthalpy and entropy as a function of mobile phase composition. Under all conditions, the changes in molar enthalpy and entropy were negative as were the differential changes ($\Delta\Delta H$ and $\Delta\Delta S$) for each pair of enantiomers. The enthalpy and entropy changed in a similar manner with the polarity of the mobile phase, which indicated that the highly exothermic sorption was accompanied by a correspondingly large loss in entropy. The authors noted that this behavior is analogous to enthalpy-entropy compensation, as discussed previously. steric effects of the organic modifier were further investigated by Blackwell et al. [43]. Their detailed study used linear, branched, and cyclic alcohols (ranging in size from ethanol to octanol) in the normal-phase mode with amide derivatives of 1-phenylethylamine as model solutes. The enantioselectivity varied slightly (1.15 1.35) as a function of the modifier structure for an N-(3.5dinitrobenzoyl)phenylglycine CSP. The enantioselectivity was higher and varied more greatly (1.53 – 2.44) with modifier structure for an N-(3,5-dinitrobenzoyl)-4amino-1,2,3,4-tetrahydrophenanthrene (Whelk-O) CSP. For both CSPs, the

smallest selectivities were observed for 1-hexanol and cyclohexanol. The greatest selectivities were observed for bulky modifiers, such as 2-propanol, 2-butanol, and 2-methyl-2-propanol. The greater selectivities were the result of a dramatic increase in retention of the second enantiomer. Based on detailed thermodynamic measurements, the authors suggested that the bulky modifiers cannot penetrate into the tight complex formed between the second enantiomer and the CSP. They also suggested that chiral separations giving large enantioselectivity ($\alpha > 2$), such as those with the Whelk-O CSP, were not consistent with the classical three-point interaction model of Dalgliesh [44] (Figure 1.3). These separations exhibited a wide range of selectivities, were not well described by linear solvation energy relationships, and did not exhibit consistent enthalpy-entropy compensation behavior with varying modifier structure.

Thermodynamic studies can also be used to examine the nature of the surface for covalently bonded CSPs. Pirkle and Readnour [45] designed a chromatographic system utilizing π -basic CSPs with a series of π -acidic solutes, bis-(2,4-dinitrophenyl)- α , ω -diaminoalkanes (bis-DNPs). The number of methylene groups in the bis-DNPs was varied in order to influence their ability to interact with the CSP. The enthalpy of sorption, determined from van't Hoff plots, was expected to be maximized (most negative) when the length of the bis-DNPs matched the distance between strands of the stationary phase. By using this approach, the authors found maximum enthalpy when the number of methylene groups was equal to five. For CSPs having different surface coverage (0.36 to

1.36 µmol/m²), maximum enthalpy occurred with the same number of methylene groups, but with different maximum enthalpy values. These interesting results suggested that the strands were not randomly distributed on the silica surface, but clustered with similar distributions of interstrand distances. The surface coverage thus affected the size of the cluster rather than the average distance between clusters.

1.5.3 Amylose- and Cellulose-Type CSP

The temperature dependence of chiral discrimination was investigated by Smith et al. [46]. Two analogues of Cromakalim, a potassium channel activator, were separated on cellulose derivatized with tris(3,5-dimethylphenylcarbamate) (Chiralcel-OD) over the temperature range from 0 to 42 °C. Although the two analogs differ only by replacement of a benzoyl group with an n-pentanoyl group, they showed different temperature dependence. The benzoyl enantiomers exhibited an increasing trend in resolution with increasing temperature, whereas the n-pentanoyl enantiomers had a decreasing trend. The van't Hoff plots were linear for all enantiomers, from which the changes in molar enthalpy and entropy were determined. A large difference was observed for ΔΔH (1.929 and 4.265 kJ/mol for the benzovl and n-pentanovl enantiomers, respectively), but relatively small difference for $\triangle\triangle$ S (10.3 and 13.6 J/mol K, respectively). isoenantioselective temperature, which is analogous to the enthalpy-entropy compensation temperature, also differed greatly (-86 and 41 °C, respectively). Hence, the benzoyl enantiomers exhibited an entropy-dominated separation, whereas the n-pentanoyl enantiomers had an enthalpy-dominated separation.

The authors concluded that increased temperature should be beneficial for any chiral separation that predominantly involves π -type electron donor-acceptor interactions and, conversely, that decreased temperature should be beneficial for separations that predominantly involve hydrogen bonding interactions. This general conclusion was confirmed by Kuesters and Spoendlin [47] for the separation of rolipram and a series of structurally related compounds on the same Chiralcel-OD CSP over the temperature range from 10 to 60 °C. These aromatic compounds showed an unusual entropy-dominated separation with $\Delta\Delta H$ of 1.62 kJ/mol and $\Delta\Delta S$ of 5.72 J/mol K for rolipram, similar to the entropy-dominated separation of the benzoyl analog discussed above. More enthalpy-dominated separations were observed by Mesplet et al. [48] for some phosphoramidate derivatives of anti-HIV nucleosides.

A detailed mechanistic investigation was undertaken by O'Brien et al. [49] with a diol intermediate for a leukotriene D₄ antagonist separated on cellulose derivatized with tris(4-methylbenzoate) (Chiralcel-OJ). A nonlinear van't Hoff plot was observed over the temperature range of 5 to 50 °C for both retention factor and selectivity. At low temperature, the enantioselectivity was entropy-controlled with positive values for $\Delta\Delta H$ and $\Delta\Delta S$, but at high temperature, it was enthalpy-controlled with negative values for $\Delta\Delta H$ and $\Delta\Delta S$. This temperature dependence was very unusual. In general, the entropy contribution (T $\Delta\Delta S$) should tend to increase with increasing temperature and overcome the enthalpy contribution ($\Delta\Delta H$), thereby changing the separation mechanism from enthalpy-dominated to entropy-dominated with increasing temperature. The unusual temperature

dependence observed by O'Brien et al. suggested a phase transition in the CSP. The transition observed in the van't Hoff plots occurred at a temperature of approximately 18 °C, where a conformational change in the stationary phase was confirmed by infrared spectroscopy and differential scanning calorimetry. The thermodynamic behavior was also examined for different mobile phase compositions in the normal-phase mode. With an increase in concentration of the organic modifier, 2-propanol, an increase in $\Delta\Delta H$ was observed, accompanied by an increase in $\Delta\Delta S$. These two effects cancelled each other by means of enthalpy-entropy compensation and resulted in a negligible change in molar free energy. This explained why an increase in the concentration of 2propanol had virtually no effect on enantioselectivity. The authors suggested that the loss of interaction energy for the more retained R-enantiomer relative to the S-enantiomer with increasing 2-propanol concentration was balanced by a relative increase in the space available for the R-enantiomer when it entered the stationary phase. This was indicative of a swelling of the cellulose CSP with increasing 2-propanol concentration. The kinetic behavior was also evaluated by means of the plate-height method. Reduced plate height is calculated the plate height divided by the particle size. For the more retained R-enantiomer, the reduced plate height was large at temperatures up to 10 °C, but showed a sharp decrease above 15 °C. However, for the S-enantiomer, the reduced plate height showed a gradual decrease over the entire temperature range of 5 to 50 °C. These data suggested that slow mass transfer processes occurred for the Renantiomer at lower temperatures. This behavior was attributed to the relatively

slow inclusion of the R-enantiomer at low temperature, where the cellulose chains are rigid.

In closely related studies, Wang et al. [50-52] have also reported some unusual temperature effects with polysaccharide CSPs. They separated the enantiomers of dihydropyrimidinone (DHP) acid and its methyl ester on both amylose and cellulose derivatized with tris(3,5-dimethylphenylcarbamate) (Chiralpak-AD and Chiralcel-OD). A nonlinear van't Hoff plot was observed for R- and S-DHP acid on Chiralpak-AD, but a linear relationship was observed on Chiralcel-OD. Moreover, the van't Hoff plots obtained with Chiralpak-AD upon cyclic heating and cooling between 5 and 50 °C were not superimposable. This suggested an irreversible, thermally induced conformational change of Chiralpak-AD at approximately 30 °C. Solid-state NMR was utilized to verify and to characterize this conformation change. Booth and Wainer [53] investigated the separation of mexiletine and a series of structurally related solutes on Chiralpak-AD CSP. Although a nonlinear van't Hoff plot was observed for one solute (which was subsequently eliminated), linear van't Hoff plots were observed for all others over the temperature range from 0 to 30 °C. The change in molar enthalpy was, thus, constant and negative for these solutes. An enthalpyentropy compensation plot of ln k versus -∆H was then constructed. The data for these solutes fell into two distinct groups, with linearity observed within each This linearity was indicative of an enthalpy-entropy compensation group. phenomenon within that group of solutes. The two groups had different compensation temperatures and, hence, different retention mechanisms. It was

interesting to note that one group contained the solutes with hydroxyl substituents, while the other group contained all other solutes.

The frontal analysis method has been utilized by Guiochon et al. [54,55] to elucidate thermodynamics and mass transfer kinetics. The sorption isotherms of Troeger's base were determined on a microcrystalline cellulose triacetate CSP over a temperature range of 30 to 60 °C. Whereas the S-enantiomer exhibited a Langmuir isotherm, the R-enantiomer could best be described by a quadratic equation for an S-shaped isotherm. The sorption enthalpies of both enantiomers increased with increasing temperature. The mass transfer kinetics for the S-enantiomer was studied by two different models, the equilibrium-dispersive and transport-dispersive (solid-film linear driving force) models. The two approaches gave almost identical results. The mass transfer rate constant was determined to be around 7-11 min⁻¹ for concentration steps from 0 to 3.2 g/L of Troeger's base.

1.5.4 Protein-Type CSP

Loun and Hage [56,57] have systematically investigated the chiral separation mechanism of a human serum albumin (HSA) CSP by using warfarin as a model solute. From frontal analysis, it was found that both enantiomers have a single type of binding site in the same area of HSA. Temperature-dependent measurements of the equilibrium constant, obtained over the range from 4 to 45 °C, enabled the calculation of specific thermodynamic parameters. Although the changes in molar free energy were similar for R- and S-warfarin (-7.5 and -7.7 kcal/mol, respectively, at 37 °C), the contributions from molar enthalpy and entropy were different. The R-enantiomer had a smaller

contribution than the S-enantiomer from the enthalpy change (-3.5 and -5.6 kcal/mol, respectively), but a larger contribution from the entropy change (13 and 7 cal/mol K, respectively). The larger entropy change for R-warfarin indicated that more solvent molecules were released during the binding, while the larger enthalpy change for S-warfarin indicated stronger interaction during the binding. This is consistent with a model in which R-warfarin interacts with amino acid residues deep within the binding pocket of HSA mainly by hydrophobic interactions, whereas S-warfarin interacts with residues at or near the outer rim of the binding site mainly by polar interactions. The effect of mobile phase was investigated by increasing the concentration of the polar organic modifier, 2propanol, in aqueous phosphate buffer. Concomitantly, the retention factor for Rwarfarin decreased, but that for S-warfarin increased. This result provided further support for the authors' suggestion that R-warfarin interacted by nonpolar interaction, while S-warfarin interacted by polar interaction. From elution analysis, the plate height model was utilized to study the band broadening processes and to measure sorption/desorption kinetics. With an increase in temperature, both the sorption and desorption rate constants increased, while the equilibrium constant decreased. The faster kinetics resulted in a decrease in plate height and an increase in column efficiency. The measurement of mass transfer kinetics at different temperatures allowed the calculation of activation energy, activation enthalpy, and activation entropy. Although the activation energy was similar for R- and S-warfarin (10.8 and 11.5 kcal/mol, respectively, at 37 °C), the contributions from activation enthalpy and entropy were different. The R-

enantiomer had a larger activation enthalpy (10.5 and 1.9 kcal/mol), but a smaller activation entropy (-0.9 and 31 cal/mol K) than the S-enantiomer. The large positive activation enthalpy for R-warfarin indicated more bonds breaking than forming during the complex-formation process, whereas the more negative activation entropy for S-warfarin indicated a higher degree of order. These results also corresponded well with the retention model presented previously. In this way, thermodynamic and kinetic information help to elucidate specific retention and separation mechanisms. Similar experiments were performed for another chiral solute, tryptophan, by Yang and Hage [58-60]. Both D- and Ltryptophan had a single type of binding site but, unlike the warfarin enantiomers, they were in different areas of HSA. The strength of L-tryptophan binding was enthalpy-dominated, while D-tryptophan was entropy-dominated. Consequently, L-tryptophan showed greater changes when varying the temperature, pH, ionic strength, and modifier concentration of the mobile phase. These changes were predominantly due to changes in the equilibrium constant, but also to changes in the moles of binding sites (phase ratio). From kinetic studies, L-tryptophan showed much greater broadening and, hence, slower kinetics than D-tryptophan. The primary contribution was the much lower desorption rate of L-tryptophan from the HSA phase.

Fornstedt et al. systematically investigated another type of protein CSP, immobilized cellobiohydrolase I (CBH I), with some β-andrenergic blocking agents as chiral solutes [61-64]. The sorption isotherms for both R- and S-propranolol fit well to the bi-Langmuir model. One of the contributions was the

same for both enantiomers, whereas the other was different. The common contribution was considered to be the nonchiral (Type I) interaction, while the other was the chirally selective (Type II) interaction. It was suspected that the chirally selective interaction involved the formation of ion pairs on this CSP. Thus, the saturation capacity of the Type II sites was lower because of the limited number of ionic sites. As a result, the enantioselectivity decreased with an increase in solute concentration and eventually vanished when the nonchiral interactions became predominant. Also, due to the ionic nature of the chirally selective sites, retention behavior was pH dependent. At pH 4.7, the retention times of both enantiomers decreased with increasing temperature from 5 to 55 °C. However, at pH 5.5, the retention time of the more retained S-propranolol increased, while that of R-propranolol decreased with increasing temperature. Thus, at this pH, an unusual increase in chiral selectivity was observed with an increase in temperature. Detailed thermodynamic parameters were determined at this pH to try to explain this phenomenon. The changes in molar enthalpy and entropy on Type I sites were calculated as -1.1 kcal/mol and 0.1 cal/mol K, respectively. On Type II sites, R-propranolol had negative changes in molar enthalpy and entropy at -1.9 kcal/mol and -2.6 cal/mol K, respectively, whereas S-propranolol had positive changes at 1.6 kcal/mol and 11.6 cal/mol K, respectively. The authors attributed the large positive entropy change to a considerable decrease in the organization of water molecules around the chiral (Type II) sites in the protein CSP. The positive enthalpy change suggested that this disorganization was associated with weakening of the hydrogen bonding of

water molecules. The endothermic interaction for the S-enantiomer and exothermic interaction for the R-enantiomer accounted for the unusual temperature-dependent behavior. Peak tailing was observed at both low and high concentration of solutes. At low concentration, the Type II sites were within the linear range of the isotherm. The tailing observed was a result of slow heterogeneous mass transfer kinetics. At high concentration, the Type II sites were saturated and no longer within the linear range. As a result, the more pronounced tailing observed was a combination of heterogeneous thermodynamics and heterogeneous kinetics. The transport-dispersive model using the solid-film linear driving force model with homogenous kinetics failed to account for the pronounced peak tailing, while the same model with heterogeneous kinetics accounted well. For example, a sorption rate constant of 10.000 min⁻¹ and desorption rate constant of 18 min⁻¹ were determined for best fit to the experimental zone profile produced with 100 µL of 0.36 mM propranolol. The rate constants were found to be concentration dependent. With higher concentrations of 1.02 and 1.55 mM propranolol, the sorption rate constant was decreased to 90 and 60 min⁻¹, respectively, when the desorption rate constant was held constant at 18 min⁻¹.

Some other interesting thermodynamic studies have been performed on other types of protein CSPs. Gilpin et al. [65] separated tryptophan enantiomers on a bovine serum albumin CSP at varying temperatures and pH. For D-tryptophan, the van't Hoff plot was reasonably linear over the temperature range from 0.5 to 45 °C. However, for L-tryptophan, a nonlinear plot was observed with

a maximum value at approximately 20 – 24 °C. The authors noted that the initial increase in the retention factor of L-tryptophan with temperature is thermodynamically inconsistent with a simple retention mechanism, where binding occurs at a fixed number of specific sites with a constant, negative change in molar enthalpy. They speculated that the observed nonlinearity may be due to an increase in the number of binding sites due to gross changes in protein surface orientation or an increase in the binding energy due to induced conformational changes of the protein. These changes are apparently not consequential for D-tryptophan, which does not have a specific binding site with BSA.

Amyloglucosidase was immobilized onto the silica support by Strandberg et al. [66]. Both retention and enantioselectivity increased with column temperature. The ionic strength of the mobile phase and the concentration of the organic modifier, 2-propanol, both affected the chiral selectivity. The pH value of the mobile phase affected the charges on the CSP and the solute, thereby influencing their interactions. A pH above the isoelectric point of the protein CSP introduced more electrostatic interaction between the positively charged solute and the negatively charged protein. The thermodynamic results indicated that the interaction could be enthalpy- or entropy-dominated, depending on the mobile phase composition. An inversion of elution order was observed for enantiomers of mosapride on an α_1 -acid glycoprotein CSP with the change of temperature and pH [67]. A linear van't Hoff plot was obtained at lower pH (4.2), but a nonlinear plot was obtained at higher pH (7.4). Thermodynamic results

showed the separation was enthalpy-dominated at lower pH, but entropy-dominated at higher pH.

A vancomycin-based CSP was used to separate a series of dansyl amino acids in the temperature range of 0 to 28 °C [68]. Linear van't Hoff plots were obtained for all enantiomers. However, their thermodynamic parameters were distinguished in two groups, where the first group had a more negative ΔH with smaller molecular size (e.g., dansyl valine and leucine) and the second group had a much less negative ΔH with a larger molecular size (e.g., dansyl Enthalpy-entropy compensation was observed for the chiral tryptophan). compounds within the same group, indicating a similar retention mechanism. The size of the solute affected their retention and chiral recognition by affecting the hydrophobic interaction and steric hindrance with the CSP. Berthod et al. [69] observed linear van't Hoff plots on four macrocyclic glycopeptide CSPs with 71 chiral compounds, which indicated that no conformational transitions were observed for these CSPs. Most chiral separations were enthalpy-controlled with a few exceptions, depending on the mobile phase composition and the solute structure as well. Enthalpy-entropy compensation was observed in most cases.

In summary, protein CSPs have a much complex structure than those CSPs containing only small chiral molecules. Temperature and pH are the most important parameters that control retention and separation behavior in this type of CSP. Broader peaks are usually observed due to the slow mass transfer kinetics. More investigations need to be performed to find ways to increase mass transfer kinetics and enable higher column efficiency for protein CSPs.

1.6 CONCLUSIONS

Chiral separation is an important issue in both academia and industry. Although great efforts have been made to separate enantiomers with various methods or CSPs, the mechanisms for the chiral separation process still remain unclear. Thus, the goal of this thesis is to investigate the detailed thermodynamic and kinetic information concerned with β-cyclodextrin chiral stationary phase. At first, the method to extract thermodynamic and kinetic information will be evaluated in Chapter 2. Then the detailed mobile phase effect (Chapter 4) and temperature and pressure effects (Chapter 5) will be discussed. Such investigations will lead to a better understanding of the retention and separation process in chiral separation.

1.7 REFERENCES

- [1] S. Ahuja, Chiral separations: Application and technology, American Chemical Society, Washington, DC, 1997
- [2] G. Blaschke, H.P. Kraft, K. Fickentscher and F. Kohler, Arneiz.-Forsch., 29 (1979) 1640.
- [3] G. Subramanian, Chiral separation techniques: A practical approach, Wiley-VCH, 2001
- [4] G. Subramanian, A practical approach to chiral separations by liquid chromatography, Wiley-VCH, 1994
- [5] C.E. Dalgliesh, J. Chem. Soc. 137 (1952) 3940-3942.
- [6] M. Kotake, T. Sakan, N. Nakamura, S. Senoh, J. Am. Chem. Soc. 73 (1951) 2973-2974.
- [7] P.W. Atkins, Physical Chemistry, 6th Ed; W. H. Freeman: New York, NY, 1997.
- [8] J. Leffler, E. Grunwald, Rates and Equilibria of Organic Reactions; Wiley: New York, NY, 1963.
- [9] R.R. Krug, W.G. Hunter, R.A. Grieger, J. Phys. Chem. 80 (1976) 2335-2341.
- [10] R.R. Krug, W.G. Hunter, R.A. Grieger, J. Phys. Chem. 80 (1976) 2341-2351.
- [11] R. Ranatunga, M.F. Vitha, P.W. Carr, J. Chromatogr. A 946 (2002) 47-49.
- [12] C.F. Bernasconi, Relaxation Kinetics; Academic Press: New York, NY, 1976.
- [13] D. Gowanlock, R. Bailey, F.F. Cantwell, J. Chromatogr. A 726 (1996) 1-23.
- [14] J. Li, L.M. Litwinson, F.F. Cantwell, J. Chromatogr. A 726 (1996) 25-36.
- [15] J. Li, F.F. Cantwell, J. Chromatogr. A 726 (1996) 37-44.
- [16] R. Bujalski, F.F. Cantwell, J. Chromatogr. A 1048 (2004) 173-181.
- [17] K. Miyabe, G. Guiochon, J. Separ. Sci. 26 (2003) 155-173.

- [18] J.C. Giddings, Dynamics of Chromatography; Marcel Dekker: New York, NY, 1965.
- [19] S.B. Howerton, V.L. McGuffin, Anal. Chem. 75 (2003) 3539-3548.
- [20] H.C. Thomas, J. Am. Chem. Soc. 66 (1944) 1664-1666.
- [21] J.L. Wade, A.F. Bergold, P.W. Carr, Anal. Chem. 59 (1987) 1286-1295.
- [22] S. Golshan-Shirazi, G. Guiochon, J. Chromatogr. 603 (1992) 1-11.
- [23] G. Guiochon, J. Chromatogr. A 965 (2002) 129-161.
- [24] A. Harada, M. Furue, S. Nozakura, J. Polym. Sci., Part A: Polym. Chem. 16 (1978) 189-196.
- [25] W.L. Hinze, T.E. Riehl, D.W. Armstrong, W. DeMond, A. Alak, T. Ward, Anal. Chem. 57 (1985) 237-242.
- [26] H.Y. Aboul-Enein, M.R. Islam, S.A. Bakr, 11 (1988) 1485-1493.
- [27] K. Cabrera, D. Lubda, J. Chromatogr. A 666 (1994) 433-438.
- [28] N. Morin, Y.C. Guillaume, E. Peyrin, J.C. Rouland, Anal. Chem. 70 (1998) 2819-2826.
- [29] E. Peyrin, Y.C. Guillaume, A. Ravel, Anal. Chem. 72 (2000) 1263-1267.
- [30] Y.C. Guillaume, J. F. Robert, C. Guinchard, Talanta 55 (2001) 263-269.
- [31] M.C. Ringo, C.E. Evans, Anal. Chem. 69 (1997) 643-649.
- [32] M.C. Ringo, C.E. Evans, J. Phys. Chem. B 101 (1997) 5525-5530.
- [33] M.C. Ringo, C.E. Evans, Anal. Chem. 69 (1997) 4964-4971.
- [34] M.C. Ringo, C.E. Evans, J. Microcolumn Sep. 10 (1998) 647-652.
- [35] X. Wang, C.B. Ching, Sep. Sci. Technol. 37 (2002) 2567-2586.
- [36] H.W. Yu, C.B. Ching, Chromatographia 54 (2001) 697-702.
- [37] D.J. Mazzo, C.J. Lindemann, G.S. Brenner, Anal. Chem. 58 (1986) 636-638.
- [38] P. Pescher, M. Caude, R. Rosset, A. Tambute, J. Chromatogr. 371 (1986) 159-175.
- [39] L.E. Weaner, D.C. Hoerr, J. Chromatogr. 437 (1988) 109-119.

- [40] W.H. Pirkle, J. Chromatogr. 558 (1991) 1-6.
- [41] W.H. Pirkle, P.G. Murray, J. High. Resolut. Chromatogr. 16 (1993) 285-288.
- [42] W.H. Pirkle, C.J. Welch, J. Liq. Chromatogr. 14 (1991) 2027-2042.
- [43] J.A. Blackwell, R.E. Waltermire, R.W. Stringham, Enantiomer 6 (2001) 353-367.
- [44] C.E. Dalgliesh, J. Chem. Soc. 137 (1952) 3940-3942.
- [45] W.H. Pirkle, R.S. Readnour, Anal. Chem. 63 (1991) 16-20.
- [46] R.J. Smith, D.R. Taylor, S.M. Wilkins, J. Chromatogr. A 697 (1995) 591-596.
- [47] E. Kuesters, C. Spoendlin, J. Chromatogr. A 737 (1996) 333-337.
- [48] N. Mesplet, Y. Saito, P. Morin, L.A. Agrofoglio, J. Chromatogr. A 983 (2003) 115-124.
- [49] T. O'Brien, L. Crocker, R. Thompson, K. Thompson, P.H. Toma, D.A. Conlon, B. Feibush, C. Moeder, G. Bicker, N. Grinberg, Anal. Chem. 69 (1997) 1999-2007.
- [50] F. Wang, T. O'Brien, T. Dowling, G. Bicker, J. Wyvratt, J. Chromatogr. A 958 (2002) 69-77.
- [51] F. Wang, T. Dowling, D. Ellison, J. Wyvratt, J. Chromatogr. A 1034 (2004) 117-123.
- [52] F. Wang, R.M. Jr. Wenslow, T.M. Dowling, K.T. Mueller, I. Santos, J. M. Wyvratt, Anal. Chem. 75 (2003) 5877-5885.
- [53] T.D. Booth, I.W. Wainer, J. Chromatogr. A 741 (1996) 205-211.
- [54] P. Rearden, P. Sajonz, G. Guiochon, J. Chromatogr. A 813 (1998) 1-9.
- [55] A. Seidel-Morgenstern, G. Guiochon, Chem. Eng. Sci. 48 (1993) 2787-2797.
- [56] B. Loun, D.S. Hage, Anal. Chem. 66 (1994) 3814-3822.
- [57] B. Loun, D.S. Hage, Anal. Chem. 68 (1996) 1218-1225.
- [58] J. Yang, D.S. Hage, J. Chromatogr. A 645 (1993) 241-250.
- [59] J. Yang, D.S. Hage, J. Chromatogr. A 725 (1996) 273-285.

- [60] J. Yang, D.S. Hage, J. Chromatogr. A 766 (1997) 15-25
- [61] T. Fornstedt, G. Zhong, Z. Bensetiti, G. Guiochon, Anal. Chem. 68 (1996) 2370-2378.
- [62] T. Fornstedt, P. Sajonz, G. Guiochon, J. Am. Chem. Soc. 119 (1997) 1254-1264.
- [63] T. Fornstedt, G. Goetmar, M. Andersson, G. Guiochon, J. Am. Chem. Soc. 121 (1999) 1164-1174.
- [64] G. Goetmar, T. Fornstedt, G. Guiochon, Anal. Chem. 72 (2000) 3908-3915.
- [65] R.K. Gilpin, S. E. Ehtesham, R.B. Gregory, Anal. Chem. 63 (1991) 2825-2828.
- [66] A. Strandberg, A. Nystrom, S. Behr, A. Karlsson, Chromatographia 50 (1999) 215-222.
- [67] A. Karlsson, A. Skoog, K. Ohlen, J. Biochem. Biophys. Methods 54 (2002) 347-356.
- [68] I. Slama, E. Jourdan, A. Villet, C. Grosset, A. Ravel, E. Peyrin, Chromatographia 58 (2003) 399-404.
- [69] A. Berthod, B.L. He, T.E. Beesley, J. Chromatogr. A 1060 (2004) 205-214.

CHAPTER 2

THEORETICAL EVALUATION OF METHODS FOR EXTRACTING RETENTION FACTORS AND KINETIC RATE CONSTANTS IN LIQUID CHROMATOGRAPHY

2.1 INTRODUCTION

The importance of kinetics in separation science has been recognized since the pioneering work of Giddings [1-5]. While thermodynamics governs the separation strength and selectivity, kinetics governs the extent of zone broadening and asymmetry, all of which affect the resolution. Thermodynamic processes have been studied for many years, but comparatively, kinetic processes have not been fully elucidated. A detailed understanding of kinetic behavior is essential to identify the rate-limiting processes so that separation speed may be increased without sacrificing resolution. For a better understanding of kinetic behavior, accurate measurement of the kinetic rate constants is required.

The different methods for extracting thermodynamic and kinetic information have been discussed in Chapter 1.5. To the best of our knowledge, there have been no studies dedicated to the validation and comparison of experimental methods for extracting kinetic rate constants. For this purpose, stochastic simulation can be of great benefit [6-11]. Stochastic simulations are based on the migration of individual molecules by the sequential application of independently defined transport processes (Markov chain). The fundamental equations of motion used to describe these transport processes require few, if any, assumptions that limit their general applicability. Stochastic simulation

models have shown excellent correspondence with macroscopic kinetic models [12,13]. All of the simulation parameters are specified, so the associated retention factors and kinetic rate constants can be easily calculated or extracted to serve as the "true" values. These true values can be used to compare the values from all other methods to validate the accuracy of the experimental methods.

The goals of this research are as follows: (1) to perform stochastic simulations under different conditions in liquid chromatography systems with homogeneous or heterogeneous stationary phases, (2) to compare the generated zone profiles under different conditions, (3) to extract retention factors and kinetic rate constants by using different theoretical models, and (4) to compare the different methods with respect to their accuracy, advantages, and limitations.

2.2 COMPUTER SIMULATION METHOD

A three-dimensional stochastic simulation was written in the FORTRAN 90 programming language. This simulation has been described in detail elsewhere [14-17]. This program incorporates algorithms for the processes of diffusion, laminar convection, and retention. The molecules can interact with a homogeneous or heterogeneous stationary phase by a partition (absorption) mechanism. These processes are repeated for each molecule at each time increment until the total simulation time is reached.

The input parameters required for the simulation are divided into three categories. The system parameters describe properties of the mobile and

stationary phases, as well as the spatial dimensions of the system to be simulated. These include the radius of the mobile phase (R_m) , depth of the stationary phase (d_s) , column length (L), linear velocity (u_0) , etc. The molecular parameters describe attributes of the molecules, such as the diffusion coefficients in the mobile (D_m) and stationary (D_s) phases, and the distribution coefficient between the two phases (K). The computational parameters describe certain constraints that are required for the simulation, such as the number of molecules (N), time increment (t), and total simulation time (T). To initialize the simulation, the molecules are distributed in a statistically random manner entirely in either the mobile or stationary phase.

The results of the simulation are output as the time distribution of molecules at specific distances or, correspondingly, as the distance distribution of molecules at specific times. The statistical moments of the molecular distribution are calculated in time units for simulations at specified distances (or in length units at specified times). In addition to these numerical output parameters, the molecular population is summed in discrete segments of time and then connected in a continuous zone profile for graphical display or for zone profile fitting by the different models.

2.3 DATA ANALYSIS METHODS

2.3.1 "True" Extraction Method

In the partition process, the solute molecules are distributed between the mobile and stationary phases. The rate of distribution between these two phases can be treated as a pseudo-first-order reaction. Under these conditions, the

distribution can be described by a simple kinetic model of reversible reactions. To determine the rate constants, the number of molecules in each phase is recorded as a function of simulation time. The mass transfer rate constants from the mobile to stationary phase (k_{sm}) and from the stationary to mobile phase (k_{ms}) are determined by fitting the data to the kinetic equation for a first-order reversible reaction

$$\frac{N_{m}}{N} = \frac{[k_{ms} + k_{sm} \exp(-(k_{sm} + k_{ms})T)]}{k_{sm} + k_{ms}}$$
(2.1)

where N_m is the number of molecules in the mobile phase, N is the total number of molecules, and T is the time elapsed in the simulation. The rate constants determined in this manner will be called the "true" kinetic rate constants. Furthermore, the ratio of the kinetic rate constants defines the retention factor (k),

$$k = \frac{k_{sm}}{k_{ms}} = \frac{\overline{N_s}}{\overline{N_m}}$$
 (2.2)

which is equal to the ratio of the number of molecules in the stationary phase to those in the mobile phase at equilibrium ($\overline{N_s}$ and $\overline{N_m}$, respectively). The retention factor determined in this manner will be called the "true" retention factor. Three repetitive simulations with 10,000 molecules are performed for each set of simulation conditions. Rate constants are then determined by nonlinear regression of the data to Equation 2.1. The three values are then averaged to obtain the rate constants and their standard deviations. Similarly, the retention factor and its standard deviation are determined by Equation 2.2.

2.3.2. Statistical Moment Extraction Method

Statistical moment method is parallel to the plate height method. In this method, all of the moments are directly obtained from the molecular zone profiles.

These statistical moments are calculated in the time domain as

$$M_1 = N^{-1} \sum_{i=1}^{N} T_i \tag{2.3}$$

$$M_2 = N^{-1} \sum_{i=1}^{N} (T_i - M_1)^2$$
 (2.4)

$$M_3 = N^{-1} \sum_{i=1}^{N} (T_i - M_1)^3$$
 (2.5)

where T_i is the arrival time of an individual molecule (i) at the specified distance and N is the total number of molecules. The first moment (M₁) is the mean retention time. It can be related to the retention factor by

$$k = \frac{M_1 - t_0}{t_0} \tag{2.6}$$

where t_0 is the elution time for a non-retained compound, which is calculated from the column length (L) and the mobile-phase linear velocity (u_0).

As discussed in Chapter 1.5, the method of calculating kinetic rate constants from moment analysis is derived by extrapolation of Giddings' work [1]. The plate height in the length domain (H_L) can be related to the second moment (M_2) in the time domain by

$$H_{L} = \frac{\sigma_{L}^{2}}{L} = \frac{M_{2}}{L} \left(\frac{u_{0}}{1+k}\right)^{2}$$
 (2.7)

The mass-transfer term (C_s) for slow kinetics in a system that exhibits a partition mechanism is given by

$$C_{s} = \frac{2k}{(1+k)^{2}k_{ms}}$$
 (2.8)

Thus,

$$k_{ms} = \frac{2ku_0}{(1+k)^2 dH_L}$$
 and $k_{sm} = \frac{2k^2u_0}{(1+k)^2 dH_L}$ (2.9)

where dH_L is the contribution to plate height arising from slow mass transfer, and is calculated by

$$dH_{L} = H_{L} - A - B_{m} / u_{0} - B_{s} / u_{0} - C_{m} u_{0}$$
 (2.10)

The terms for multiple paths (A), diffusion in the mobile phase (B_m), diffusion in the stationary phase (B_s), and resistance to mass transfer in the mobile phase (C_m) are calculated from the Golay equation for an open tubular column as

$$A=0 ag{2.11}$$

$$B_{m} = 2\gamma_{m}D_{m} \tag{2.12}$$

$$B_{S} = 2\gamma_{S}D_{S}k \tag{2.13}$$

$$C_{m} = \frac{\left(1 + 6k + 11k^{2}\right)R_{m}^{2}}{24(1+k)^{2}D_{m}}$$
(2.14)

where γ_m is the obstruction factor in the mobile phase, which is unity for an open tubular column, and γ_s is the obstruction factor in the stationary phase, which is unity for a uniform surface.

This method relies on the accurate calculation and subtraction of all fast mass transfer terms, which include A, B_m , B_s , and C_m . These corrections are

relatively simple for these simulations in open tubular columns, but more difficult in experimental systems, especially those in packed columns. The equations for A and C_m terms in packed beds are largely empirical and cannot provide accurate values [1,18-21].

2.3.3. EMG Model Extraction Method

EMG model is the convolution of the Gaussian and exponential contributions as described by the following equation

$$C(t) = \frac{A_0}{2A_3} \exp\left(\frac{A_2^2}{2A_3^2} + \frac{A_1 - t}{A_3}\right) \left(\operatorname{erf}\left(\frac{t - A_1}{\sqrt{2}A_2} - \frac{A_2}{\sqrt{2}A_3}\right) + 1 \right)$$
 (2.15)

where erf is an statistical error function. The zone profile is fit to the EMG equation by nonlinear regression (PeakFit, Jandel Scientific) to extract the relevant parameters, A_0 , A_1 , A_2 , and A_3 . From these parameters, the retention time t_r is calculated as

$$t_r = A_1 + A_3$$
 (2.16)

The corresponding retention factor is calculated as

$$k = \frac{t_r - t_0}{t_0} \tag{2.17}$$

where t_0 is the elution time for a non-retained compound, which is calculated from the column length (L) and the mobile-phase linear velocity (u_0). The rate constants are calculated by

$$k_{ms} = \frac{2kt_0}{A_3^2}$$
 and $k_{sm} = \frac{2k^2t_0}{A_3^2}$ (2.18)

2.3.4. Giddings Model Extraction Method

Concentration, C(x), in the Giddings model is expressed as

$$C(x) = A\gamma \sqrt{\frac{k}{x}} I_1(2\gamma \sqrt{kx}) exp(-\gamma x - \gamma k)$$
 (2.19)

where γ is a dimensionless constant, equal to the product of the desorption rate constant (k_{sm}) and the elution time of a nonretained compound (t_0). After conversion from the time domain (t) to the retention factor domain (x), the zone profile is fit by nonlinear regression (PeakFit, Jandel Scientific). From the regression parameters (A, k, γ), the corresponding retention factor and rate constants are calculated.

2.3.5. Thomas Model Extraction Method

Concentration, C(x), in the Thomas equation is given by

$$C(x) = \frac{a_0}{a_2 a_3} \left(1 - \exp\left(-\frac{a_3}{a_2}\right) \right) \left(\frac{\sqrt{\frac{a_1}{x}} I_1 \left(\frac{2\sqrt{a_1 x}}{a_2}\right) \exp\left(\frac{-x - a_1}{a_2}\right)}{1 - T\left(\frac{a_1}{a_2}, \frac{x}{a_2}\right) \left(1 - \exp\left(-\frac{a_3}{a_2}\right)\right)} \right)$$
(2.20)

where

$$T(u,v) = e^{-v} \int_{0}^{u} e^{-t} I_{0}(\sqrt{2vt}) dt$$
 (2.21)

and I_0 and I_1 are modified Bessel functions of the first kind. After conversion from the time domain to the retention factor domain (denoted as x), the zone profile is fit by nonlinear regression (PeakFit, Jandel Scientific). The fitting parameters that are incorporated in the Thomas model are the area (a_0), position (a_1), width

 (a_2) , and distortion (a_3) . From the definition of the parameters in the Thomas model, the retention factor is simply the position parameter a_1

$$k = a_1 \tag{2.22}$$

The kinetic rate constants are related to the width parameter a2

$$k_{ms} = \frac{1}{a_2 t_0}$$
 and $k_{sm} = \frac{k}{a_2 t_0} = \frac{a_1}{a_2 t_0}$ (2.23)

2.4. RESULTS AND DISCUSSION

2.4.1. Homogenous Systems

In a homogeneous system, there is only one type of interaction site in each simulation system. The simulation conditions are varied with respect to the column length (L), linear velocity (u_0), stationary-phase diffusion coefficient (D_0), interfacial mass transfer coefficient (α) [39], and equilibrium constant (K). For each set of conditions, the four different theoretical methods are applied to extract the retention factors and kinetic rate constants. The retention factors reflect the thermodynamic or equilibrium behavior, whereas the rate constants reflect the kinetic behavior of the system.

2.4.1.1. Effect of column length on equilibrium and kinetic processes

To elucidate the effect of column length, the molecular distribution is examined at values of 1, 2, 4, 5, 7, and 9 cm. The simulation conditions are chosen with linear velocity of 0.1 cm/s, equilibrium constant of 1.0, mobile-phase diffusion coefficient of 1.0×10^{-5} cm²/s, and stationary-phase diffusion coefficient of 5.0×10^{-8} cm²/s. Other simulation parameters are specified in the figure legends.

The retention factors and kinetic rate constants are extracted by using the true kinetic method with Equations 2.1 and 2.2. An average value for the square of the correlation coefficient (R²) of 0.96 indicates the good quality of the nonlinear regression. Extracted values for retention factors and rate constants along the column length are summarized in Tables 2.1 and 2.2, respectively. Since the true kinetic method only deals with the number of molecules in each phase, it is independent of the column length. The retention factors are constant at 1.004, and the kinetic rate constants from stationary to mobile phase are constant at 0.203 s⁻¹ along the column.

When retention factors and kinetic rate constants are compared between the different methods, the concept of steady state (equilibrium) needs to be considered. The true kinetic method helps to describe the overall kinetic behavior in terms of the characteristic time τ

$$\tau = \frac{1}{k_{sm} + k_{ms}} \tag{2.24}$$

which represents the time required for the number of molecules in the mobile phase (N_m) to reach 1 – (1/e) of the number at equilibrium ($\overline{N_m} = N/(1+k)$). It will usually require at least 20 to 50 τ for the chromatographic system to reach steady state. In this case where $k_{ms} = k_{em} = 0.203 \text{ s}^{-1}$, approximately 50 to 120 s are needed for steady state achievement, which corresponds to a mean zone distance of 2.5 to 6 cm. Among the six column lengths, the zone profiles achieved after 4 cm should have reached steady state.

Table 2.1 Retention factors (k) with varying column length (L).^a

L	1 cm	2 cm	4 cm*	5 cm*	7 cm*	9 cm*
True	1.004 ± 0.007					
Moment	0.994	0.991	1.008	1.004	1.004	1.004
EMG	N/A	1.184	1.066	1.040	1.022	1.011
Giddings	N/A	0.918	0.989	0.991	0.996	0.996
Thomas	N/A	2.364	1.258	1.160	1.076	1.052

^a Simulation conditions given in Figure 2.1.

N/A Not available

* Steady state achieved

Table 2.2 Kinetic rate constants from stationary to mobile phase $(k_{ms}, \, s^{-1})$ with varying column length (L).^a

L Model	1 cm	2 cm	4 cm*	5 cm*	7 cm*	9 cm*
True	0.203 ± 0.003	0.203 ± 0.003	0.203 ± 0.003	0.203 ± 0.003	0.203 ± 0.003	0.203 ± 0.003
Moment	0.182	0.187	0.177	0.184	0.186	0.181
EMG	N/A	0.0846	0.127	0.157	0.199	0.232
Giddings	N/A	0.216	0.175	0.177	0.177	0.172
Thomas	N/A	0.162	0.170	0.174	0.175	0.170

^a Simulation conditions given in Figure 2.1.

N/A Not available

* Steady state achieved

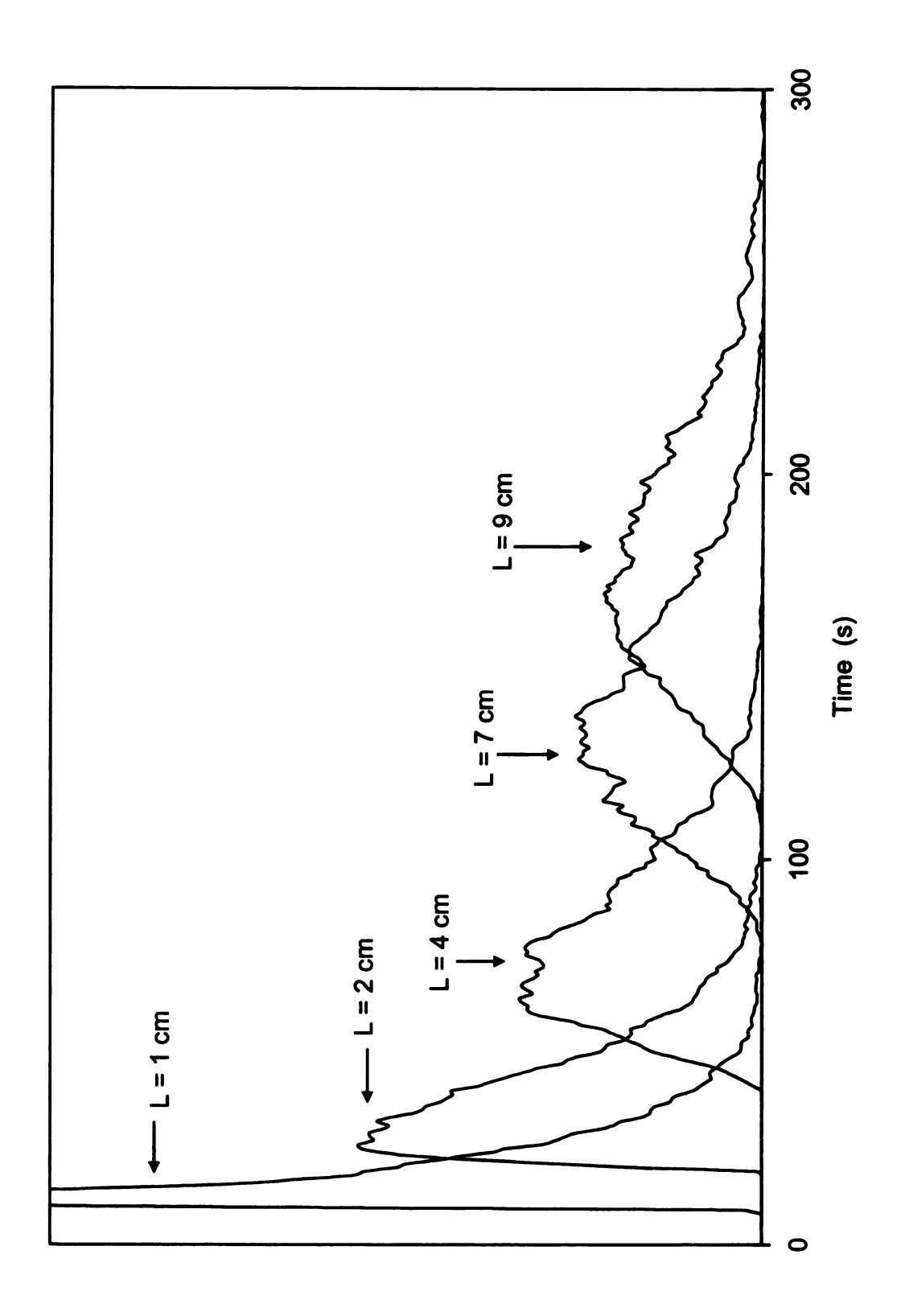
The zone profiles at each column length are illustrated and compared in Figure 2.1. The zone profile at 1 cm is highly asymmetric. It has a narrow central region with a long exponential tail, which makes it appear bimodal. The reason for this appearance is the non-equilibrium nature at 1-cm column length. There are two populations of molecules present: One population has no opportunity to interact with the stationary phase, but travels only in the mobile phase; these molecules compose the narrow central zone profile. The other population has already interacted with the stationary phase; these molecules compose the long exponential tail. The zone profile at 2 cm is still highly asymmetric, but seems to lose the bimodal character as more molecules interact with the stationary phase. The zone profiles at 4, 7, and 9 cm are all slightly asymmetric, similar to the profiles usually seen in chromatography. The asymmetry decreases, but the broadening of the zone profile increases continuously along the column. These phenomena have direct effects on the retention factor and kinetic rate constants, as discussed below.

The retention factors and kinetic rate constants from stationary to mobile phase with the different methods are summarized in Tables 2.1 and 2.2. Theoretically, the retention factor is given by

$$k = \frac{KV_S}{V_m}$$
 (2.25)

where $V_m = \pi R_m^2 L$ and $V_s = \pi (d_s^2 + 2 R_m d_s) L$. For these simulations, the phase ratio (V_m/V_s) has been carefully calculated and set as 1.0. Hence, a retention factor of 1.0 is expected and is verified by the results of the true kinetic method. In Table 2.1, the statistical moment method gives constant and

Figure 2.1: Comparison of zone profiles with varying column length. From left to right, column length L = 1, 2, 4, 7, and 9 cm. Other simulation conditions: N = 5000, t = $5.0x10^{-4}$ s, $D_m = 1.0x10^{-5}$ cm²/s, $D_s = 5.0x10^{-8}$ cm²/s, K = 1.0, $u_0 = 0.1$ cm/s, $R_m = 2.0x10^{-3}$ cm, $d_s = 8.28x10^{-4}$ cm, $\alpha = 1.0$.



accurate values along the column. Even the zone profile at the first column length can be used to calculate a retention factor that is similar to the expected value. However, non-constant values are observed for the EMG, Giddings and Thomas models. None of the three models is able to fit the zone profile at the first column length accurately because of its bimodal shape. However, for all subsequent lengths, all models can fit the zone profiles well. Their statistical parameters indicating the quality of the fitting, R² and F, are similar to each other. Table 2.1 clearly demonstrates a decreasing trend for retention factors along the column length from both EMG and Thomas models, and an increasing trend from Giddings model. However, the retention factors from the EMG and Giddings models are closer to the expected value of 1.0 than those from the Thomas model. When comparing the different methods to extract retention factors, it may be concluded that the statistical moment method is independent of the zone profile. The statistical moment method is not a regression approach and makes no assumptions about the zone profile. It is also independent of the column length and the associated achievement of steady-state conditions. However, the EMG, Giddings, and Thomas models are dependent on the zone profile and column length. It is noteworthy that all of these methods yield retention factors that are similar to the true kinetic value.

With respect to the kinetic behavior in Table 2.2, the rate constants from stationary to mobile phase are relatively constant along the column length for the statistical moment model. For the EMG model, an increasing trend in rate constant is observed along the column. Before steady state is reached, the

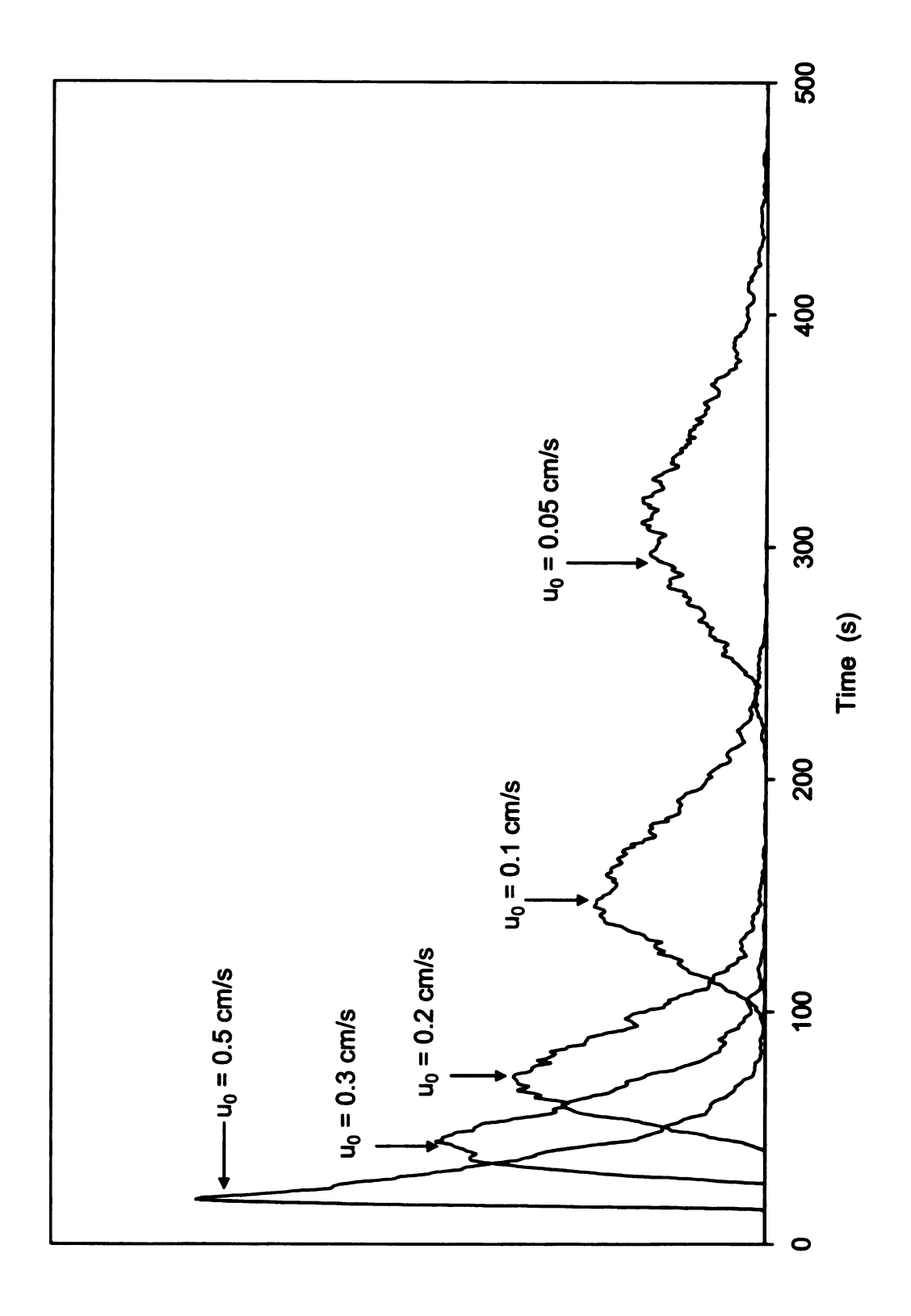
kinetic rate constant is more than 50% smaller than the true value. After the steady state condition has been reached, the kinetic rate constant begins to approach and even surpass the true value. The reason for the increasing trend along the column length derives from the EMG method itself. This method only deals with the exponential tail of the zone profile. As the zone profile progresses along the column, it evolves from a highly asymmetric zone profile to a more symmetric Gaussian zone profile. In other words, the ratio of exponential variance and column length (τ^2/L) decreases along the column length. As the rate constants are inversely related to τ^2/L (Equation 2.18), they increase along the column length. The reason that the final value is larger than the true kinetic value also derives from the limitations of the EMG method. As the zone profile approaches a Gaussian shape, where the ratio of τ/σ is less than 0.4, the EMG model cannot be used to extract reliably the exponential variance [22]. The rate constants calculated under these conditions are statistically inaccurate. The closest value to the true kinetic rate constant is observed at 7 cm, which corresponds to 50 to 60 r. The kinetic rate constants from the Giddings and Thomas models are similar and relatively constant along the column, especially after steady state achievement. The constant values derive from the nature of the statistical moment, Giddings, and Thomas methods. All of these methods deal with the total variance of the zone profile, which increases linearly along the column. As the kinetic rate constants are directly related to the ratio of total variance and column length (Equations 2.9 and 2.23), they remain constant along the column length. Although the statistical moment, Giddings, and Thomas models give constant rate constants, their values are slightly different. Those from the statistical moment model are about 10% smaller than the true values, whereas those from Giddings and Thomas models are 15% smaller. When comparing the different methods to extract kinetic rate constants, the EMG model strongly depends on the zone profile, column length, and the associated achievement of steady-state conditions. However, the statistical moment, Giddings, and Thomas models are much more independent. It is noteworthy that all of these methods yield rate constants that are similar to the true kinetic value.

2.4.1.2. Effect of linear velocity on equilibrium and kinetic processes

To elucidate the effect of linear velocity, the molecular distribution is examined at values of 0.05, 0.1, 0.2, 0.3, and 0.5 cm/s. These velocities include the common range in practical application of liquid chromatography. The simulation conditions are chosen with equilibrium constant of 1.0, mobile-phase diffusion coefficient of 1.0x10⁻⁵ cm²/s, and stationary-phase diffusion coefficient of 5.0x10⁻⁸ cm²/s. Other simulation parameters are specified in the figure legends.

Figure 2.2 shows the simulated zone profiles at varying velocities with a single column length of 8 cm. The zone profile at the highest velocity is detected in the shortest time with a highly asymmetric zone profile, whereas the zone profile at the lowest velocity is detected in the longest time with a fairly Gaussian zone profile. With decreasing velocity, the zone profile gradually changes from asymmetric to Gaussian. At the same time, retention time increases. These trends are identical with those discussed above for increasing column length. In

Figure 2.2: Comparison of zone profiles with varying linear velocity. From left to right, linear velocity $u_0=0.5,\ 0.3,\ 0.2,\ 0.1,\ and\ 0.05\ cm/s$. Other simulation conditions: $N=5000,\ t=5.0x10^{-4}\ s,\ D_m=1.0x10^{-5}\ cm^2/s,\ D_s=5.0x10^{-8}\ cm^2/s,\ K=1.0,\ L=8\ cm,\ R_m=2.0x10^{-3}\ cm,\ d_s=8.28x10^{-4}\ cm,\ \alpha=1.0.$



other words, decreasing the linear velocity should have the same effect as increasing the column length.

The retention factors calculated by using the different methods are summarized in Table 2.3. The retention factors from the true kinetic method are constant and statistically equivalent (0.999 – 1.004) at different velocities. The retention factors from the statistical moment model give very accurate and constant values at every velocity. In contrast, the retention factors from the EMG and Thomas models clearly show an increasing trend with increasing linear velocity, while those from the Giddings model show a decreasing trend. Those determined at the lowest velocity are most accurate and closest to the expected value of 1.0, according to Equation 2.25. Again, the EMG model yields a more accurate value than the Giddings and Thomas models.

The true kinetic rate constants extracted at different velocities are constant and statistically equivalent (0.194 – 0.203 s⁻¹), as shown in Table 2.4. In other words, the change in velocity should have no effect, theoretically, on the kinetic processes. A similar amount of time should be required for each system to reach steady state. However, the column length where steady-state conditions are achieved will be different at each velocity. For example, the simulation with 0.1 cm/s linear velocity will achieve steady state at a column length of 4 cm, but the simulation with 0.5-cm/s velocity will achieve steady state at a column length of 20 cm, approximately 5 times longer. If molecules spend the same amount of time on the column, the zone profile they achieve should be identical as long as the kinetic processes remain constant. Figure 2.3 shows the simulated zone

Table 2.3 Retention factors (k) with varying linear velocity (u₀).^a

u ₀	0.05 cm/s*	0.1 cm/s*	0.2 cm/s*	0.3 cm/s	0.5 cm/s
True	1.001 ± 0.012	1.004 ± 0.007	0.999 ± 0.011	1.002 ± 0.005	1.002 ± 0.012
Moment	1.003	1.005	1.004	1.003	1.004
EMG	1.007	1.016	1.025	1.028	1.138
Giddings	0.994	0.999	0.984	0.955	N/A
Thomas	1.022	1.047	1.098	1.280	N/A

^a Simulation conditions given in Figure 2.2.

N/A Not available

* Steady state achieved

Table 2.4 Kinetic rate constants from stationary to mobile phase (k_{ma}, s^{-1}) with varying linear velocity (u_0) .

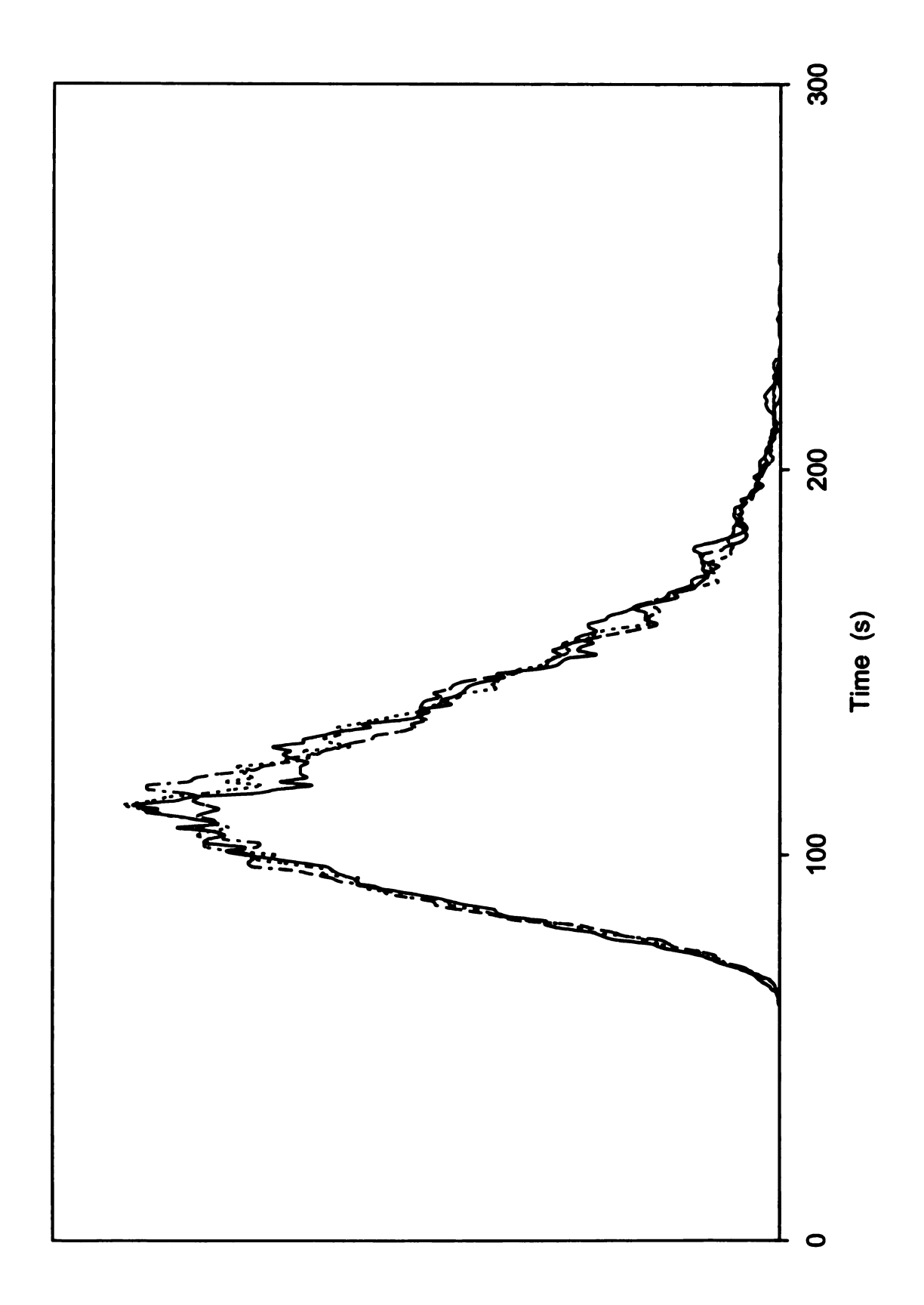
u ₀	0.05 cm/s*	0.1 cm/s*	0.2 cm/s*	0.3 cm/s	0.5 cm/s
True	0.200 ± 0.003	0.203 ± 0.003	0.197 ± 0.001	0.195 ± 0.001	0.194 ± 0.003
Moment	0.175	0.183	0.184	0.179	0.175
EMG	0.289	0.224	0.171	0.137	N/A
Giddings	0.181	0.175	0.187	0.193	N/A
Thomas	0.180	0.174	0.183	0.184	N/A

^a Simulation conditions given in Figure 2.2.

N/A Not available

* Steady state achieved

Figure 2.3: Comparison of zone profiles at similar time with varying linear velocity. Peak (----) at L = 3 cm with u_0 = 0.05 cm/s, (----) at L = 6 cm with u_0 = 0.1 cm/s, (---) at L = 18 cm with u_0 = 0.3 cm/s. Other simulation conditions: N = 5000, t = 5.0x10⁻⁴ s, D_m = 1.0x10⁻⁵ cm²/s, D_s = 5.0x10⁻⁸ cm²/s, K = 1.0, R_m = 2.0x10⁻³ cm, d_s = 8.28x10⁻⁴ cm, α = 1.0.



profiles at three different velocities (u_0) , detected at different column lengths (L), but the ratios of L/u_0 are constant. Their zone profiles are identical to each other, as discussed above. This further demonstrates that decreasing the linear velocity has the same effect as increasing the column length.

The kinetic rate constants from the other methods are also summarized in Table 2.4. The rate constants from the statistical moment, Giddings, and Thomas methods have a relatively constant value at all velocities, approximately 10% smaller than the true value. However, those from the EMG model continually decrease with increasing linear velocity. The range of values includes the true kinetic rate constant. Again, the trends from the EMG model are related to the asymmetric zone profile at the highest linear velocity and the Gaussian zone profile at the lowest velocity. Overall, these trends in kinetic rate constants are the same as discussed above when varying the column length.

2.4.1.3. Effect of stationary-phase diffusion coefficient on equilibrium and kinetic processes

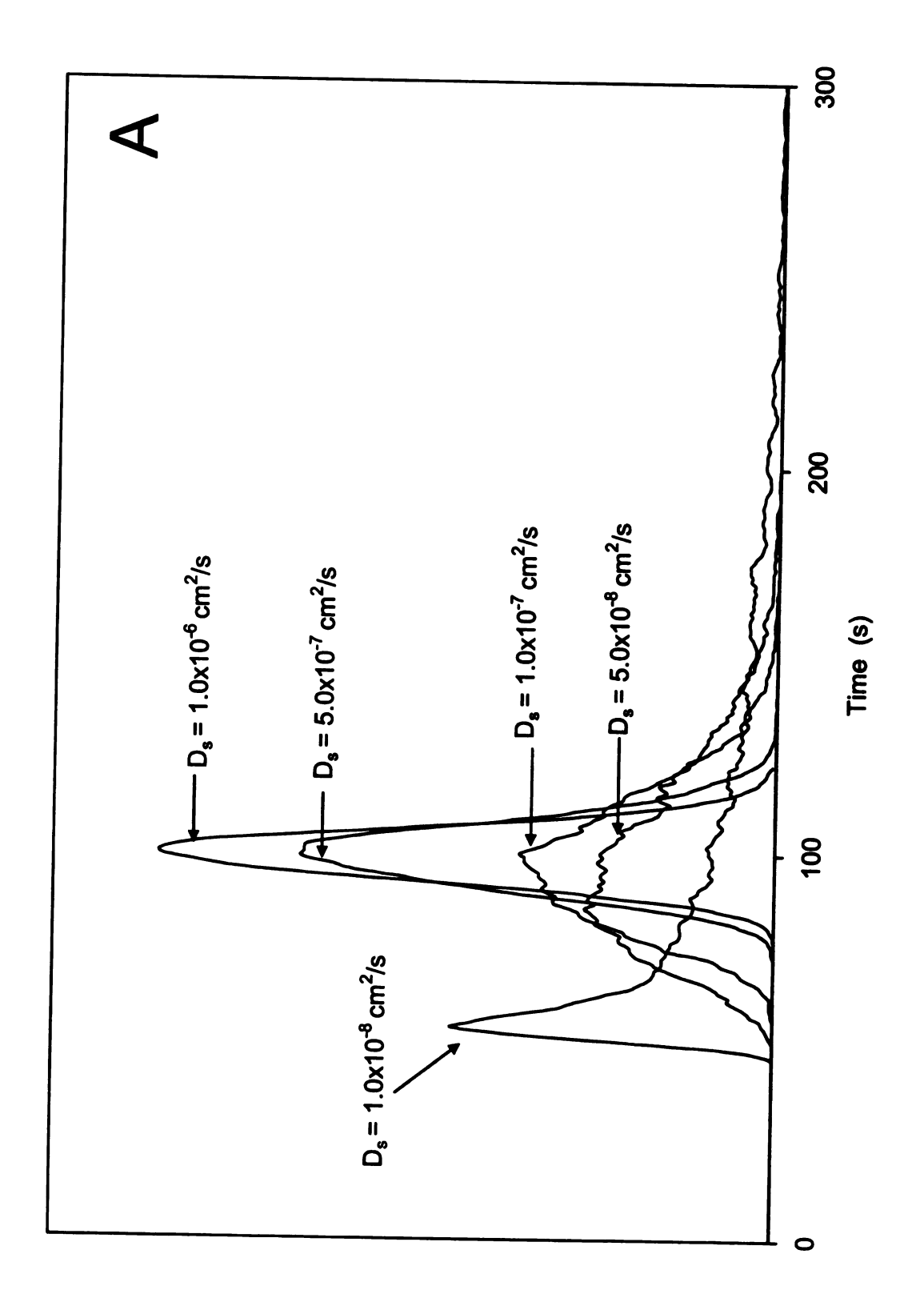
Molecules will have very similar diffusion coefficients in the mobile phase, typically 1.0×10^{-5} cm²/s in liquid chromatography. However, the diffusion coefficient in the stationary phase can vary greatly, given the wide variety of phases that are available. To elucidate the effect of stationary-phase diffusion coefficient, the molecular distribution is examined at values of 1.0×10^{-6} , 5.0×10^{-7} , 1.0×10^{-7} , 5.0×10^{-8} , and 1.0×10^{-8} cm²/s. For each diffusion coefficient, the column length is individually selected to ensure achievement of steady-state conditions $(30-75 \tau)$. The simulation conditions are chosen with linear velocity of 0.1 cm/s,

equilibrium constant of 1.0, and mobile-phase diffusion coefficient of 1.0x10⁻⁵ cm²/s. Other simulation parameters are specified in the figure legends.

For a clear comparison, the zone profiles for different diffusion coefficients are compared at a single column length (5 cm) in Figure 2.4A. The zone profile with the largest stationary-phase diffusion coefficient (1.0x10⁻⁶ cm²/s) is a narrow and symmetric Gaussian zone profile. With decreasing diffusion coefficient, the zone profiles evolve gradually to broader and more asymmetric shapes. The zone profile with the smallest stationary-phase diffusion coefficient (1.0x10⁻⁸ cm²/s) has not reached steady state vet at column length of 5 cm. But the asymmetric character of the zone profile can be clearly seen by its extremely long tail. The statistical moments associated with each zone profile are compared in Figure 2.4B as well. The first moment for all of the zone profiles is virtually the same, and is independent of stationary-phase diffusion coefficient. However, the second moment increases in a linear manner and the third moment increases in a quadratic manner as the stationary-phase diffusion coefficient decreases. Hence the skew, which is the ratio M₃/M₂^{3/2}, increases in a squareroot manner with decreasing diffusion coefficient, indicating a more asymmetric zone profile.

The retention factors are summarized in Table 2.5. The true kinetic method gives accurate and statistically equivalent retention factors (0.994 – 1.004) for different diffusion coefficients. The retention factors from the statistical moment method are all within 1.5% error, those from the EMG model within 3.0% error, and those from the Giddings model within 3.5% error. However, those

Figure 2.4: Comparison of zone profiles (A) and statistical moments (B) with varying stationary-phase diffusion coefficient. (A) From left to right, stationary-phase diffusion coefficient $D_8 = 1.0 \times 10^{-8}$, 5.0×10^{-8} , 1.0×10^{-7} , 5.0×10^{-7} , and 1.0×10^{-8} cm²/s. (B) First moment M_1 (\spadesuit), second moment M_2 (\blacksquare), third moment M_3 (\triangle), and skew $M_3/M_2^{3/2}$ (*). Other simulation conditions: N = 5000, $t = 5.0 \times 10^{-4}$ s, $D_m = 1.0 \times 10^{-5}$ cm²/s, $u_0 = 0.1$ cm/s, K = 1.0, L = 5 cm, $R_m = 2.0 \times 10^{-3}$ cm, $d_8 = 8.28 \times 10^{-4}$ cm, $\alpha = 1.0$.



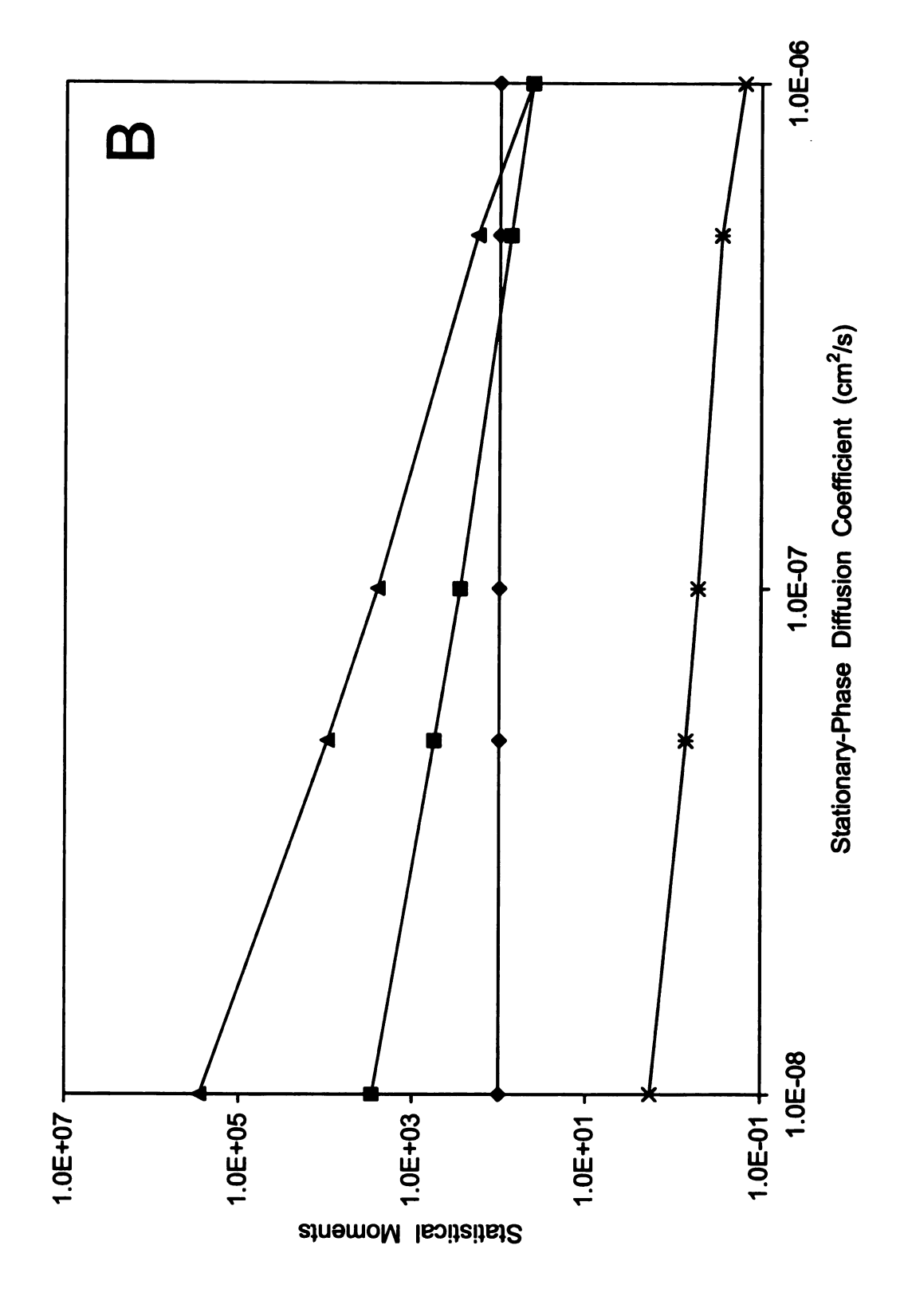


Table 2.5 Retention factors (k) with varying stationary-phase diffusion coefficient (D_s).^a

D _s	1.0x10 ⁻⁶ cm ² /s	5.0x10 ⁻⁷ cm²/s	1.0x10 ⁻⁷ cm ² /s	5.0x10 ⁻⁸ cm²/s	1.0x10 ⁻⁸ cm ² /s
True	0.999 ± 0.003	0.994 ± 0.007	0.997 ± 0.005	1.004 ± 0.007	0.996 ± 0.019
Moment	1.004	1.007	1.002	1.005	0.986
EMG	1.006	1.015	1.020	1.028	1.000
Giddings	1.015	1.002	0.997	0.990	0.966
Thomas	1.016	1.018	1.051	1.103	1.093
L	0.5 cm (65 τ)	1 cm (75 τ)	3 cm (50 τ)	6 cm (50 τ)	18 cm (30 τ)

^a Steady state achieved for all systems at the specified column length (L).

Other simulation conditions given in Figure 2.4.

from the Thomas model can have errors as high as 10%, especially for the smallest diffusion coefficients. It may be concluded that the moment, EMG, and Giddings models are relatively more accurate than the Thomas model in extracting retention factors.

The kinetic rate constants from stationary to mobile phase are summarized in Table 2.6. As shown for the true kinetic method, the rate constants decrease proportionally with the stationary-phase diffusion coefficient. This behavior is expected when the stationary-phase diffusion coefficient is substantially smaller than the mobile-phase diffusion coefficient and, therefore, dominates mass transfer processes [38]. Accordingly, when comparing the extracted kinetic rate constants from the three models with the true kinetic method, the largest error is found for the largest diffusion coefficient of 1.0x10⁻⁶ cm²/s. For the statistical moment method, this error arises from the assumptions of the model in Equation 2.10. When the diffusion coefficients in the mobile and stationary phases are comparable, both processes contribute to the observed rate constant. Under these conditions, the mass transfer term in the stationary phase is not the only source of "slow" kinetics, and the kinetic rate constant calculated from the C_s term alone will not be correct. When the C_m term is considered in Equation 2.10, the kinetic rate constant determined with the statistical moment method is 2.349 s⁻¹, rather than 3.626 s⁻¹, for the simulation with stationary-phase diffusion coefficient 1.0x10⁻⁶ cm²/s. This value is notably smaller than the true kinetic method (3.241 s⁻¹), suggesting that mobile-phase diffusion does not contribute wholly to slow mass transfer processes. For

Table 2.6 Kinetic rate constants from stationary to mobile phase (k_{ms}, s⁻¹) with varying stationary-phase diffusion coefficient (D_s).^a

D _s	1.0x10 ⁻⁶ cm ² /s	5.0x10 ⁻⁷ cm²/s	1.0x10 ⁻⁷ cm ² /s	5.0x10 ⁻⁸ cm ² /s	1.0x10 ⁻⁸ cm ² /s
True	3.241 ± 0.060	1.906 ± 0.043	0.411 ± 0.008	0.203 ± 0.003	0.041 ± 0.002
Moment	3.626	1.702	0.370	0.183	0.037
EMG	3.875	1.898	0.392	0.179	0.034
Giddings	2.289	1.374	0.348	0.180	0.037
Thomas	2.284	1.365	0.345	0.176	0.036
L	0.5 cm (65 τ)	1 cm (75 τ)	3 cm (50 τ)	6 cm (50 τ)	18 cm (30 τ)

^a Steady state achieved for all systems at the specified column length (L).

Other simulation conditions given in Figure 2.4.

stationary-phase diffusion coefficients smaller than 1.0x10⁻⁶ cm²/s, the kinetic rate constants from the statistical moment method have constant error of approximately –10%. For the EMG, Giddings, and Thomas models, a different source of error arises because these models do not work well for Gaussian zone profiles, i.e., for the largest diffusion coefficient of 1.0x10⁻⁶ cm²/s. With decreasing diffusion coefficient, the rate constants from the EMG model have more negative error, whereas those from the Giddings and Thomas models have less negative error. When comparing the different methods to extract rate constants, it is noteworthy that all four models provide values that are reasonably close to the true kinetic values, which vary over a range of two orders of magnitude. This indicates the inherent reliability of all models.

2.4.1.4. Effect of interfacial mass transfer on equilibrium and kinetic processes

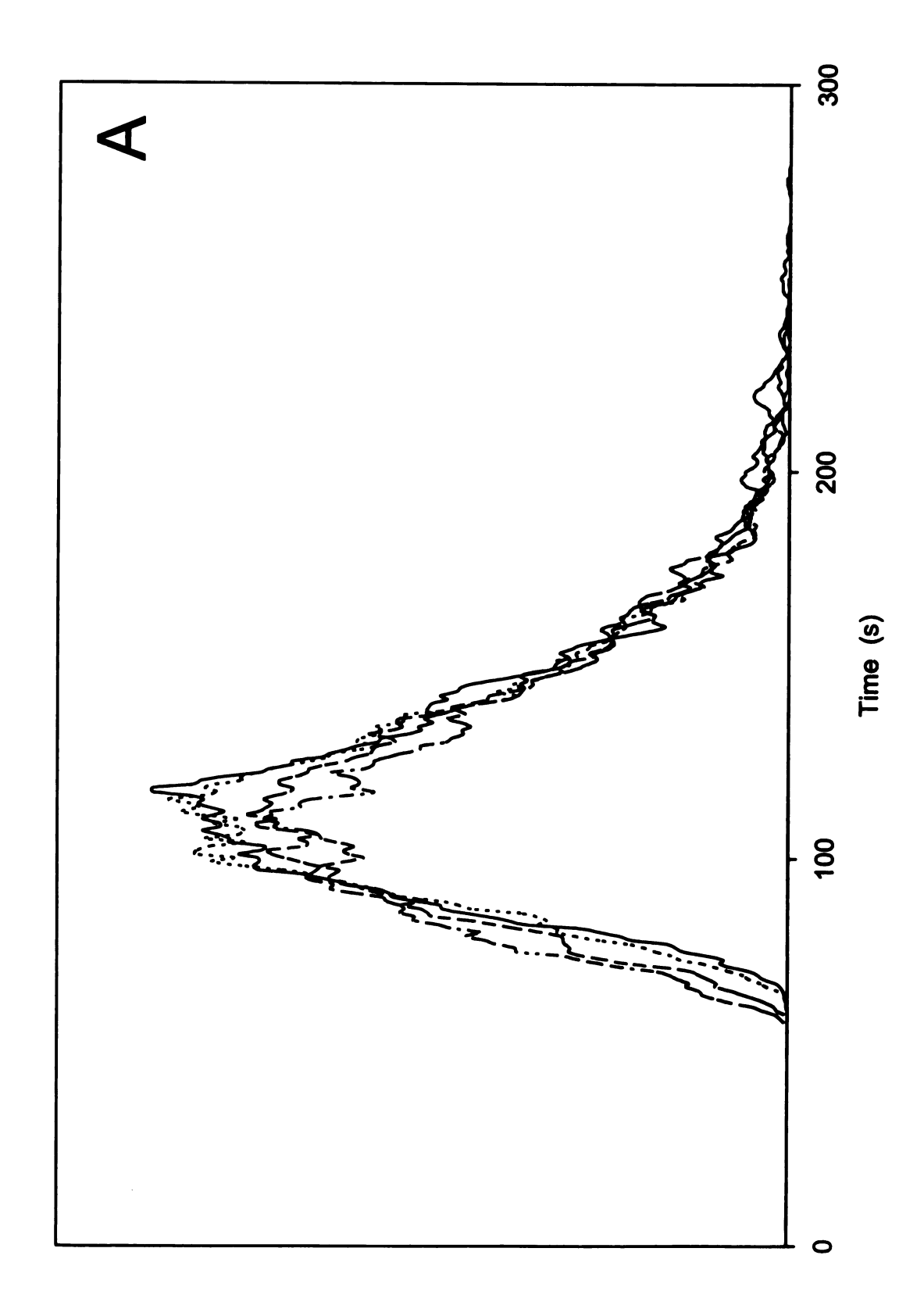
In these studies, the simulation approach is extended to consider resistance to mass transfer at the interface between the mobile and stationary phases. This resistance is associated with an energetic barrier for the kinetic transfer between mobile and stationary phases. Not every collision is sufficiently energetic to overcome this barrier. To represent the efficiency of collisional mass transfer, the interfacial mass transfer coefficient α is introduced. This coefficient is varied as 1.0, 0.5, 0.1, and 0.05 to represent 100%, 50%, 10%, and 5% efficient mass transfer, respectively. The simulation conditions are chosen with linear velocity of 0.1 cm/s, equilibrium constant of 1.0, mobile-phase diffusion coefficient of 1.0x10⁻⁵ cm²/s, stationary-phase diffusion coefficient of 5.0x10⁻⁸

cm²/s, and column length of 6 cm, where steady-state conditions should have been achieved. Other simulation parameters are specified in the figure legends.

The simulated zone profiles for different interfacial mass transfer coefficients are compared in Figure 2.5A. When the interfacial mass transfer coefficient is decreased from 1.0 to 0.5, the zone profile does not appear to change significantly. However, when the coefficient is further decreased to 0.1 and 0.05, the zone profile begins to show slightly more broadness and tailing. These changes can be seen from the comparison of statistical moments in Figure 2.5B. The first statistical moment is independent of the interfacial mass transfer coefficient α , whereas the second and third moment are dependent upon α . Decreasing α will increase both the second and third moments, but the third moment will be affected more greatly. As a result, the skew will increase slightly as well, which indicates a more asymmetric zone profile.

The retention factors with varying interfacial mass transfer coefficient α are summarized in Table 2.7. The true kinetic method gives accurate and statistically equivalent values for the retention factor (0.997 – 1.008) with varying interfacial mass transfer coefficient. For the other four methods, a slightly decreasing and increasing trend in retention factor is observed with decreasing interfacial mass transfer coefficient. The errors introduced in extracting the retention factor are within 1% for the statistical moment model, 3% for the EMG model, 2% for the Giddings model, and 10% for the Thomas model. Comparing the three models, the statistical moment, EMG, and Giddings models give more accurate results than the Thomas model.

Figure 2.5: Comparison of zone profiles (A) and statistical moments (B) with varying interfacial mass transfer coefficient. (A) Interfacial mass transfer coefficient $\alpha = 1$ (——), 0.5 (----), 0.1 (----) and 0.05 (----). (B) First moment M_1 (\spadesuit), second moment M_2 (\blacksquare), third moment M_3 (\triangle), and skew $M_3/M_2^{3/2}$ (*). Other simulation conditions: N = 5000, $t = 5.0 \times 10^{-4}$ s, $D_m = 1.0 \times 10^{-5}$ cm²/s, $D_s = 5.0 \times 10^{-8}$ cm²/s, $u_0 = 0.1$ cm/s, K = 1.0, L = 6 cm, $R_m = 2.0 \times 10^{-3}$ cm, $d_s = 8.28 \times 10^{-4}$ cm.



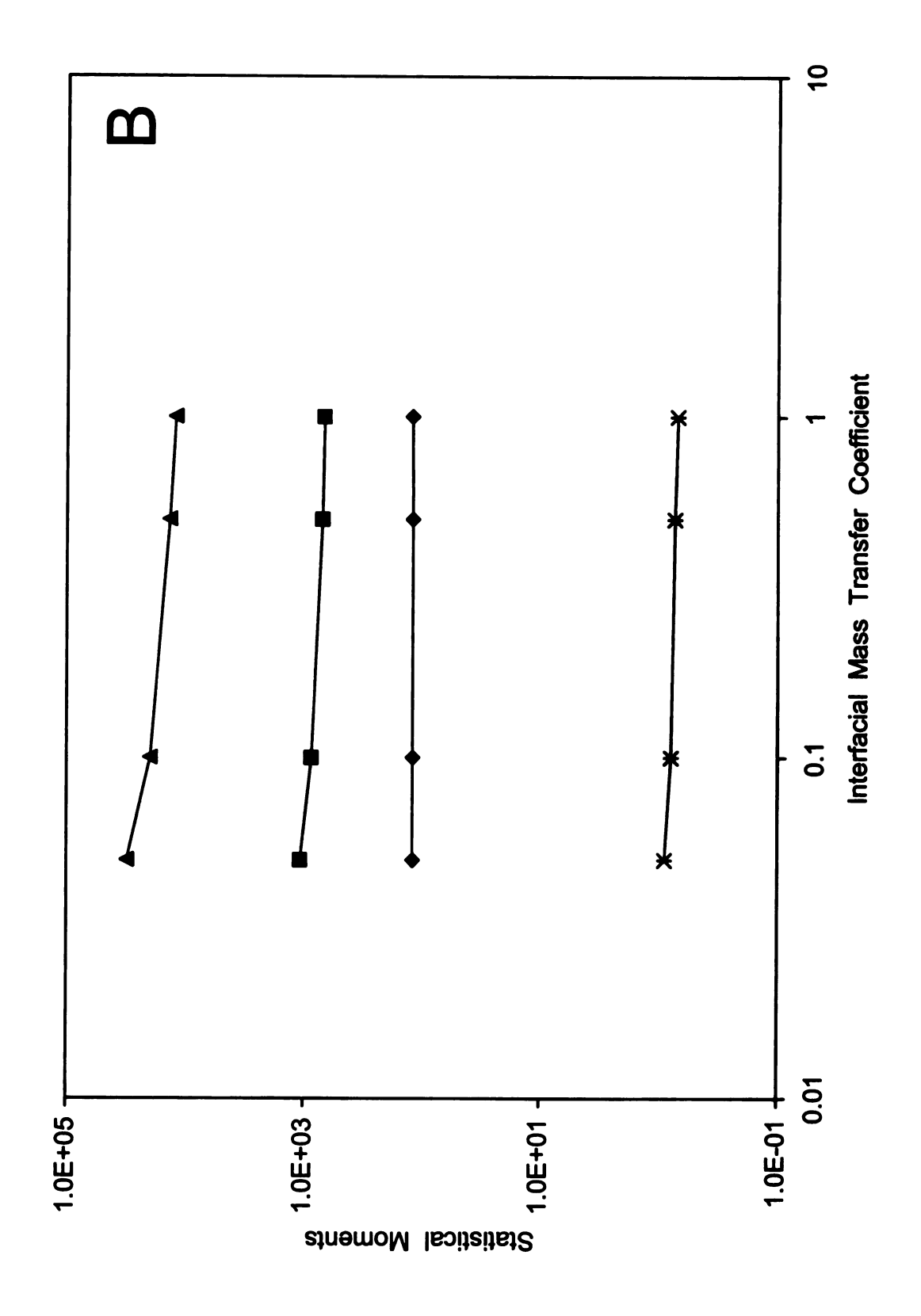


Table 2.7 Retention factors (k) with varying interfacial mass transfer coefficient (α) .

α Model	1.0	0.5	0.1	0.05
True	1.004 ± 0.007	0.997 ± 0.001	1.003 ± 0.006	1.008 ± 0.019
Moment	1.005	0.999	0.991	0.998
EMG	1.028	1.018	0.995	1.005
Giddings	0.990	0.983	0.990	0.985
Thomas	1.103	1.092	0.990	1.016

^a Simulation conditions given in Figure 2.5.

The kinetic rate constants with varying α are summarized in Table 2.8. From the true kinetic method, it is apparent that a decrease in α will decrease the kinetic rate constants. This is consistent with observing the most tailing zone profile for the smallest value of α in Figure 2.5A. This decreasing trend can be easily observed from the moment, Giddings and Thomas models, but more difficult to observe from the EMG model. Again, this behavior is strongly affected by the achievement of steady-state conditions, which corresponds to different column lengths for different simulation conditions. When the interfacial mass transfer coefficient α is equal to 1.0, the four models give comparable results in extracting rate constants. However, when α decreases to 0.1 and 0.05, the moment, Giddings, and Thomas models give more accurate results than the EMG model.

2.4.1.5. Effect of equilibrium constant on equilibrium and kinetic processes

The equilibrium constant governs the molecular distribution between the mobile and stationary phases in liquid chromatography. Different mobile phase composition, stationary phase structure, temperature, and pressure will all affect the equilibrium constant of a specific solute. Within the same system, different solutes will have different equilibrium constants as well. To elucidate the effect of the equilibrium constant, the molecular distribution is examined at values of 0.5, 1.0, 2.0, 5.0, and 10.0. For each value of the equilibrium constant, the column length is individually selected to insure achievement of steady-state conditions $(40 - 130 \tau)$. The simulation conditions are chosen with linear velocity of 0.1

Table 2.8 Kinetic rate constants from stationary to mobile phase (k_{ms} , s^{-1}) with varying interfacial mass transfer coefficient (α).^a

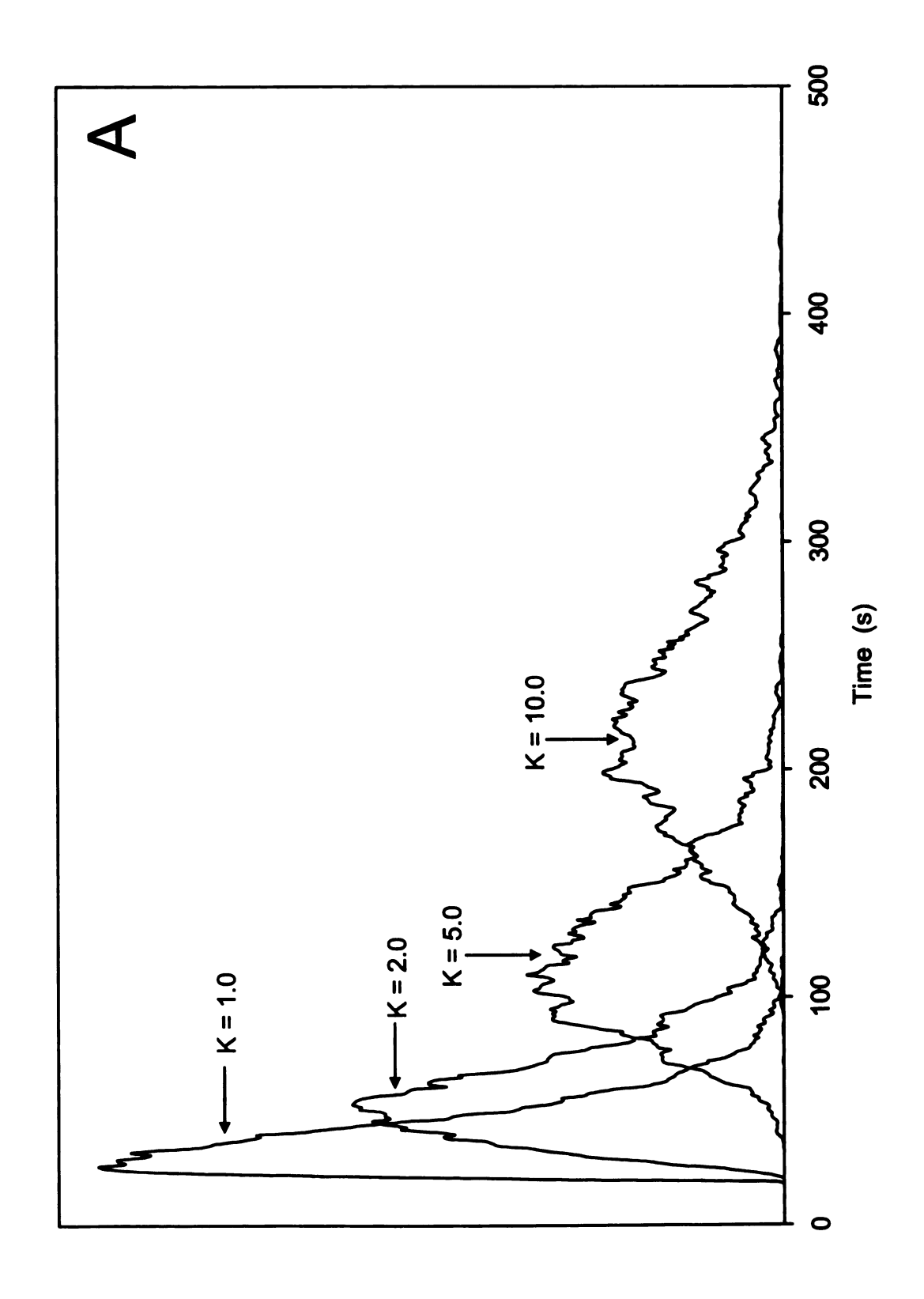
α Model	1.0	0.5	0.1	0.05
True	0.203 ± 0.003	0.183 ± 0.002	0.143 ± 0.004	0.113 ± 0.002
Moment	0.183	0.176	0.143	0.114
EMG	0.179	0.183	0.173	0.119
Giddings	0.180	0.178	0.139	0.116
Thomas	0.176	0.175	0.139	0.115

^a Simulation conditions given in Figure 2.5.

cm/s, mobile-phase diffusion coefficient of 1.0×10^{-5} cm²/s, and stationary-phase diffusion coefficient of 5.0×10^{-8} cm²/s. Other simulation parameters are specified in the figure legends.

For a clear comparison, the peak shapes for different equilibrium constants are compared at a single column length (2 cm) in Figure 2.6A. With increasing equilibrium constant, the zone profiles take longer time to elute and become broader. The statistical moments associated with each simulated zone profile are also graphed in Figure 2.6B. With the increase of equilibrium constant, all three statistical moments will increase accordingly. However, the skew decreases greatly, which indicates less tailing for zone profiles associated with a larger equilibrium constant. In part, this decrease in tailing results from the longer time spent on the column with an increase in equilibrium constant. From the previous discussion of both column length and linear velocity, tailing decreases when more time is spent on the column. To eliminate this effect and consider only the innate effect of the equilibrium constant, another graph with the simulated zone profiles at similar time is shown in Figure 2.7A, where the ratio of column length and the individual flow rate (L(1+k)/u₀) remains constant. The associated statistical moments are shown in Figure 2.7B. After spending a similar time on the column, all the zone profiles reach the same distance along the column, which is illustrated by their similar first statistical moments. However, the second and third moments increase with an increase in equilibrium constant. The second moment increases at a greater rate than the third moment, which

Figure 2.6: Comparison of zone profiles (A) and statistical moments (B) with varying equilibrium constant. (A) From left to right, equilibrium constant K = 1.0, 2.0, 5.0, and 10.0. (B) First moment M_1 (\spadesuit), second moment M_2 (\blacksquare), third moment M_3 (\triangle), and skew $M_3/M_2^{3/2}$ (*). Other simulation conditions: N = 5000, t = 5.0×10^{-4} s, $D_m = 1.0 \times 10^{-5}$ cm²/s, $D_s = 5.0 \times 10^{-8}$ cm²/s, $u_0 = 0.1$ cm/s, L = 2 cm, $R_m = 2.0 \times 10^{-3}$ cm, $d_s = 8.28 \times 10^{-4}$ cm, $\alpha = 1.0$.



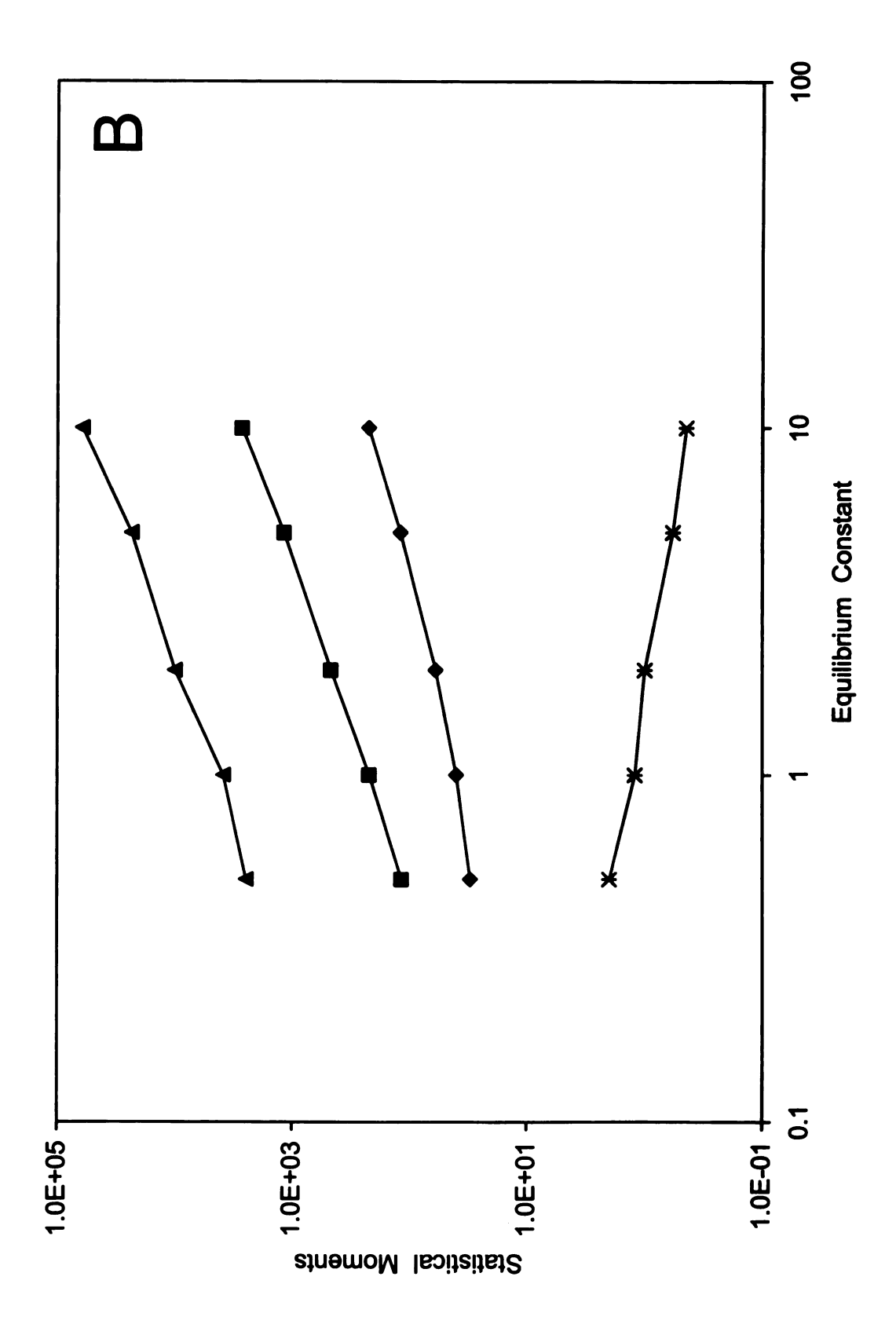
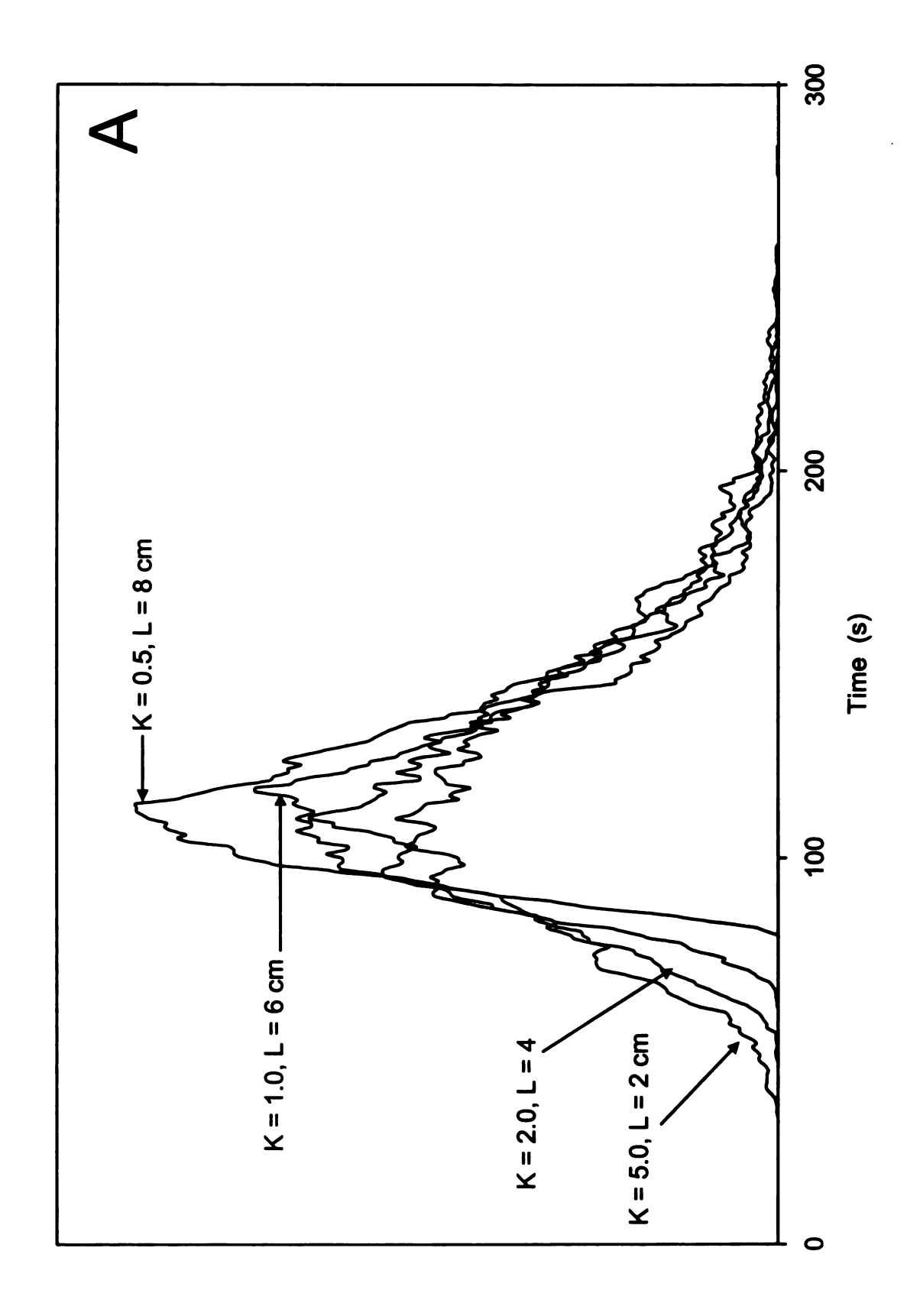
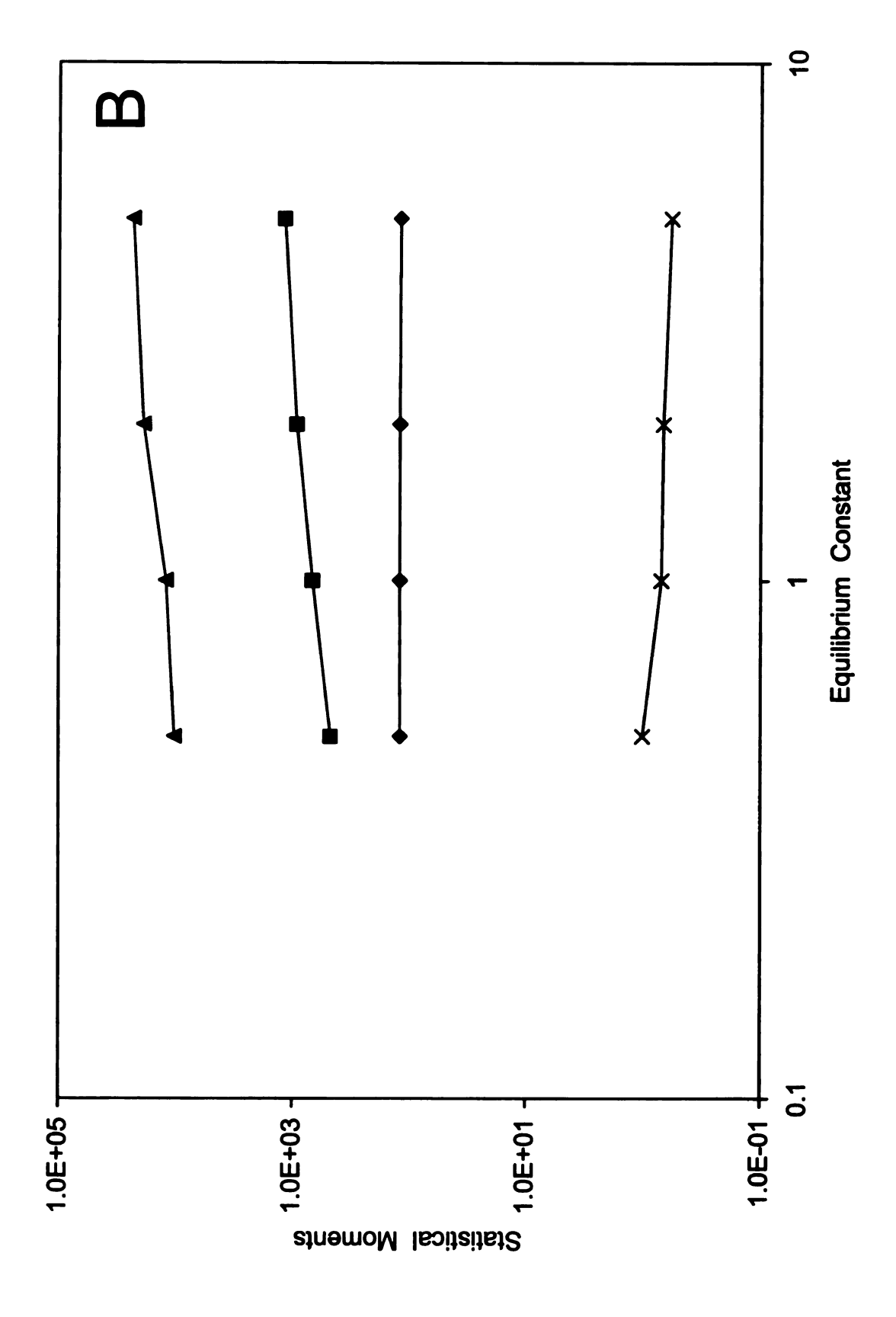


Figure 2.7: Comparison of zone profiles (A) and statistical moments (B) at similar time with varying equilibrium constant (K). (A) From left to right, K = 5.0 at L = 2 cm, K = 2.0 at L = 4 cm, K = 1.0 at L = 6 cm and K = 0.5 at L = 8 cm. (B) First moment M_1 (\spadesuit), second moment M_2 (\blacksquare), third moment M_3 (\triangle), and skew $M_3/M_2^{3/2}$ (*). Other simulation conditions: N = 5000, t = 5.0x10⁻⁴ s, D_m = 1.0x10⁻⁵ cm²/s, D_s = 5.0x10⁻⁸ cm²/s, u₀ = 0.1 cm/s, R_m = 2.0x10⁻³ cm, d_s = 8.28x10⁻⁴ cm, α = 1.0.





results in a slight decrease of the skew. In other words, the simulated zone profiles become broader, but more symmetric with higher equilibrium constant.

The retention factors associated with various equilibrium constants are summarized in Table 2.9. The true kinetic method yields accurate values, according to Equation 2.25. While the statistical moment, EMG, and Giddings models give results that are consistent with the true value within 3% error, the Thomas model can introduce errors as high as 20%. Thus, the statistical moment, EMG, and Giddings models are more accurate than the Thomas model in extracting retention factors.

The kinetic rate constants associated with various equilibrium constants are summarized in Table 2.10. Considerable discrepancy is observed among the results from the five methods. In the true kinetic method, the rate constant from stationary to mobile phase increases with increasing values of the equilibrium constant. In the statistical moment method, the rate constant remains relatively constant, whereas in the EMG, Giddings and Thomas models, the rate constant decreases with increasing equilibrium constant. It is difficult to draw conclusions about which model provides the most accurate results. Even the true kinetic model gives poor fit of the simulation data to the single exponential decay with increasing equilibrium constant. For example, the correlation coefficient R² decreases from 0.97 to 0.89 as K increases from 0.5 to 10. This makes the true kinetic results unreliable for comparison to the other methods.

Table 2.9 Retention factors (k) with varying equilibrium constants (K).^a

K Model	0.5	1.0	2.0	5.0	10.0
True	0.500 ± 0.003	1.004 ± 0.007	2.026 ± 0.011	4.995 ± 0.058	9.952 ± 0.154
Moment	0.500	1.005	1.995	4.937	10.287
EMG	0.498	1.028	2.016	4.990	10.187
Giddings	0.491	0.990	1.955	4.696	10.031
Thomas	0.493	1.103	2.104	6.599	12.009
L	9 cm (40 τ)	6 cm (50 τ)	3 cm (53 τ)	0.5 cm (48 τ)	0.3 cm (130 τ)

^a Steady state achieved for all systems at the specified column length (L). Other simulation conditions are given in Figure 2.6.

Table 2.10 Kinetic rate constants from stationary to mobile phase (k_{ms}, s⁻¹) with varying equilibrium constants (K).^a

K	0.5	1.0	2.0	5.0	10.0
True	0.194 ± 0.010	0.203 ± 0.003	0.196 ± 0.005	0.264 ± 0.017	0.375 ± 0.016
Moment	0.176	0.183	0.182	0.182	0.181
EMG	0.212	0.179	0.200	0.125	0.128
Giddings	0.184	0.180	0.183	0.177	0.156
Thomas	0.184	0.183	0.181	0.167	0.151
L	9 cm (40 τ)	6 cm (50 τ)	3 cm (53 τ)	0.5 cm (48 τ)	0.3 cm (130 τ)

^a Steady state achieved for all systems at the specified column length (L).

Other simulation conditions are given in Figure 2.6.

2.4.2. Heterogeneous Systems

In the simulation of homogeneous systems, the asymmetry tends to decrease and eventually disappear as molecules travel along the column. In other words, all zone profiles will eventually approach a Gaussian shape if given enough time and distance. However, in many of our experimental studies, persistent peak tailing has been observed that increases with column length [23-26]. Giddings attributed the kinetic origin of tailing to a heterogeneous surface with different types of sites, where one site is relatively scarce and with a high energy [27]. Weiss used a theoretical approach to conclude that persistent tailing can only occur if there exists a random distribution of first-order rate constants or an infinite number of interaction sites [28,29]. In each case, a heterogeneous surface is implicated as a contributing cause of persistent tailing. Hence, it is instructive to study the effect of multiple interaction sites on the zone profiles as well as the thermodynamic and kinetic behavior.

For these simulations of heterogeneous systems, five interaction sites are chosen to have different equilibrium constants and stationary-phase diffusion coefficients. The parameters are chosen based on previous experimental measurements for fatty acids in reversed-phase liquid chromatography. For example, we may consider a C₁₈ fatty acid to have contributions to the retention mechanisms in which 10, 12, 14, 16, and 18 carbon atoms are inserted into the stationary phase. The corresponding equilibrium constants and stationary-phase diffusion coefficients are chosen based on the experimentally measured retention factors and rate constants for the fatty acids. The natural logarithm of the

equilibrium constants and stationary-phase diffusion coefficients increases linearly with carbon number. The probability for each site is either kept constant or varied individually as well. The specific information for different simulation parameters is listed in Table 2.11.

2.4.2.1. Equally distributed multiple sites for heterogeneous surface

In the system with equally distributed sites, the probability for each of the five sites is maintained constant at 0.2. This is a simple system with straightforward physical meaning; the fraction of different surface sites is equally weighted. Representative zone profiles are shown at varying column lengths in Figure 2.8. The first zone profile at 0.5 cm has not yet reached steady state, but steady state should have been achieved for all subsequent zone profiles. As the simulated zone profiles travel along the column, their broadness increases, but their asymmetry decreases in the same manner as for a homogeneous surface.

The retention factor for a heterogeneous surface may be calculated as the sum of the retention factor at each interaction site multiplied by its probability. A calculated retention factor of 6.33 is expected for equally distributed multiple sites under these conditions (Table 2.11). The true kinetic method gives an accurate result of 6.263, as shown in Table 2.12. Among the other four methods, the statistical moment method provides an accurate result before and after steady state has been achieved. The EMG model gives a slightly smaller retention factor before steady state. It reaches a maximum value immediately after steady state, followed by a decreasing trend along the column length tending toward the true value. The Giddings model shows an increasing trend, and the

Table 2.11 Different parameters for multiple interaction sites at the heterogeneous surface.^a

Site	#1	#2	#3	#4	#5
D _s	1.0x10 ⁻⁶	3.0x10 ⁻⁷	1.0x10 ⁻⁷	3.0x10 ⁻⁸	1.0x10 ⁻⁸
К	0.56	1.29	3.12	7.88	18.8
P (1)	0.200	0.200	0.200	0.200	0.200
P (2)	0.583	0.253	0.105	0.042	0.017

^a P(1) is the probability selected for equally distributed sites, while P(2) is the probability selected for unequally distributed sites.

Figure 2.8: Comparison of zone profiles with equally distributed heterogeneous surface. From left to right, detector distance L=0.5, 2, 5, and 7 cm. Other simulation conditions: N=5000, $t=5.0x10^{-4}$ s, $D_m=1.0x10^{-5}$ cm²/s, $u_0=0.1$ cm/s, $R_m=2.0x10^{-3}$ cm, $d_s=8.28x10^{-4}$ cm, $\alpha=1.0$, P(1) conditions are given in Table 2.11.

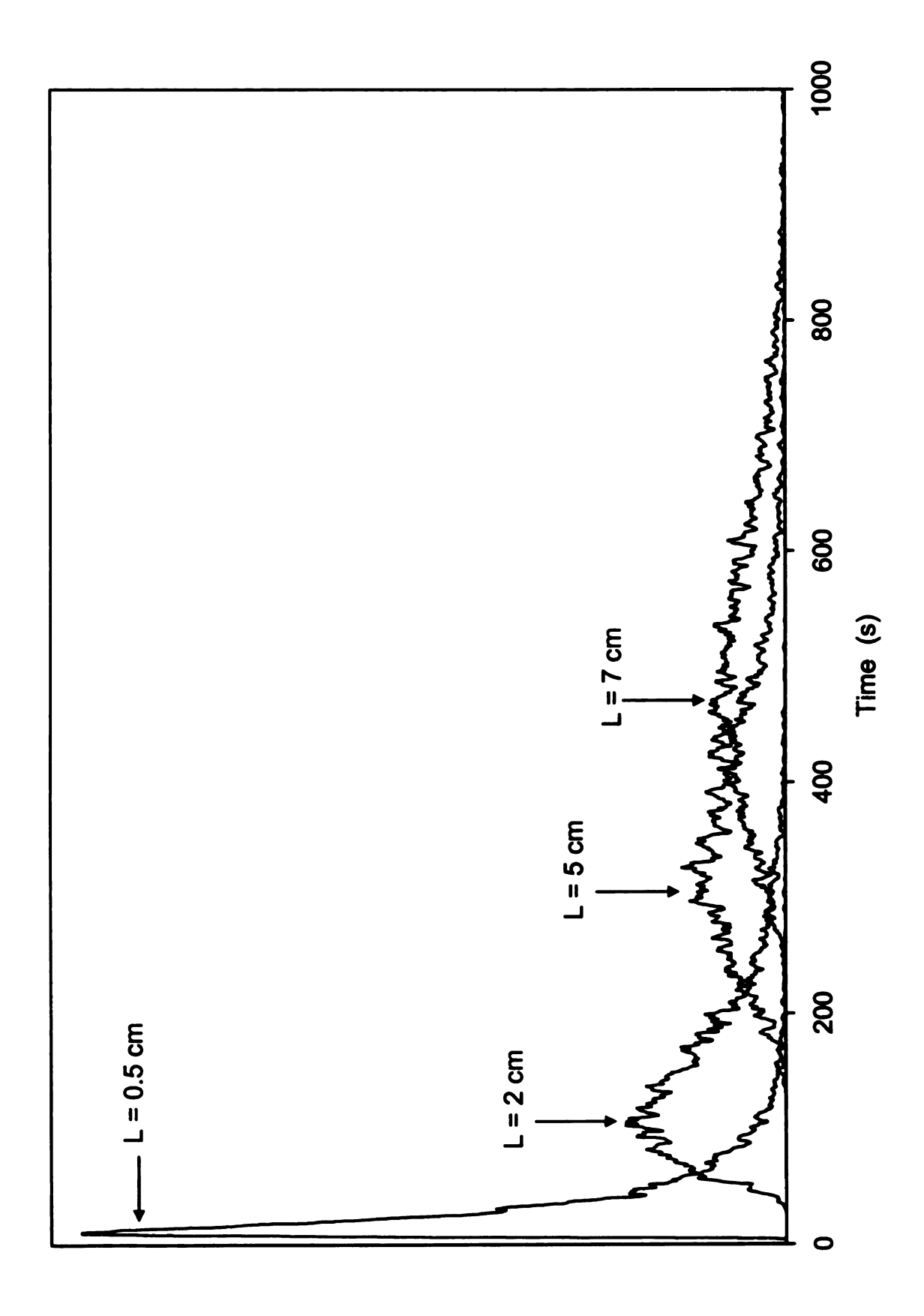


Table 2.12 Retention factors (k) along the column for equally distributed heterogeneous surface.^a

Model	0.5 cm	2 cm*	5 cm*	7 cm*
Calculated	6.33	6.33	6.33	6.33
True	6.263 ± 0.062	6.263 ± 0.062	6.263 ± 0.062	6.263 ± 0.062
Moment	6.35	6.35	6.32	6.36
EMG	5.06	6.55	6.42	6.44
Giddings	3.55	5.82	6.13	6.24
Thomas	17.10	8.68	7.25	7.02

^a Simulation conditions given in Figure 2.8.

^{*} Steady state achieved

Thomas model shows a decreasing trend toward the true value. The Thomas model has much larger error (35%) than the statistical moment (0.5%), EMG (3%), and Giddings (8%) models.

The kinetic rate constants are summarized in Table 2.13. The statistical moment, EMG, Giddings, and Thomas models all give similar results at steady state, but deviate significantly from the true kinetic method. The reliability of the true kinetic method is in doubt. This method assumes first-order or pseudo-first-order kinetics of transfer between the mobile and stationary phases, which is clearly not the case for heterogeneous surfaces. Accordingly, the square of the correlation coefficient (R²) for regression to the single exponential decay is relatively low at 0.89. In this case, the statistical moment, EMG, Giddings and Thomas models are more reliable in extracting kinetic rate constants than the true kinetic method. The rate constant from stationary to mobile phase for this system is around 0.05 s⁻¹, which is only slightly larger than the value 0.04 s⁻¹ observed in Table 2.6 for the homogeneous system with the smallest stationary-phase diffusion coefficient (1.0x10⁻⁸ cm²/s).

2.4.2.2. Unequally distributed multiple sites for heterogeneous surface

In the system with unequally distributed sites, the probability of each site is chosen to be exponentially distributed. It is well known that the retention factor is exponentially related to the free energy (ΔG) of transfer between the mobile and stationary phases [1]. Thus, the physical meaning for this particular system is that the probability of each site is inversely proportional to the interaction energy. This yields increasingly smaller populations of higher energy sites.

Table 2.13 Kinetic rate constants from stationary to mobile phase (k_{ms}, s⁻¹) along the column for equally distributed heterogeneous surface.^a

L Model	0.5 cm	2 cm*	5 cm*	7 cm*
True	0.254 ± 0.004	0.254 ± 0.004	0.254 ± 0.004	0.254 ± 0.004
Moment	0.055	0.052	0.053	0.051
EMG	0.094	0.043	0.054	0.059
Giddings	0.197	0.065	0.056	0.052
Thomas	2.176	0.062	0.055	0.051

^a Simulation conditions given in Figure 2.8.

^{*} Steady state achieved

Representative zone profiles at varying column length are compared in Figure 2.9. The first zone profile at 1.0 cm has not yet reached steady state, but steady state should have been achieved for all subsequent zone profiles. These zone profiles show more asymmetry than those from the equally distributed heterogeneous system in Figure 2.8. However, the extent of asymmetric tailing still decreases along the column. In other words, the heterogeneous system with unequally distributed sites does not successfully produce permanent tailing. But it does increase the tailing and maintain the tailing longer than the heterogeneous system with equally distributed sites. This can be clearly seen in Figure 2.10, in which the unequally distributed heterogeneous system has more skew than the equally distributed heterogeneous system. For comparison, the skew of two homogeneous systems with stationary-phase diffusion coefficients of 1.0×10^{-7} cm²/s and 1.0×10^{-8} cm²/s are also shown in Figure 2.10. heterogeneous systems show more skew than the homogeneous system with D. equal to the median value of 1.0x10⁻⁷ cm²/s. But the unequally distributed heterogeneous system has comparable skew to the homogeneous system with D_s equal to the smallest value of 1.0x10⁻⁸ cm²/s before 8 cm, and only slightly larger skew thereafter. This behavior is interesting, given that the probability for the smallest value of D_s in the unequally distributed system is as small as 0.017. However, this 1.7% distribution site clearly dominates the resultant zone profiles.

Based on the retention factors and probabilities given in Table 2.11, a calculated retention factor of 1.63 is expected for unequally distributed multiple sites under these conditions. The retention factors derived from the different

Figure 2.9: Comparison of zone profiles with unequally distributed heterogeneous surface. From left to right, detector distance L = 1, 5, 8, 15, and 20 cm. Other simulation conditions: N = 5000, t = 5.0×10^{-4} s, $D_m = 1.0 \times 10^{-5}$ cm²/s, $u_0 = 0.1$ cm/s, $R_m = 2.0 \times 10^{-3}$ cm, $d_s = 8.28 \times 10^{-4}$ cm, $\alpha = 1.0$, P(2) conditions are given in Table 2.11.

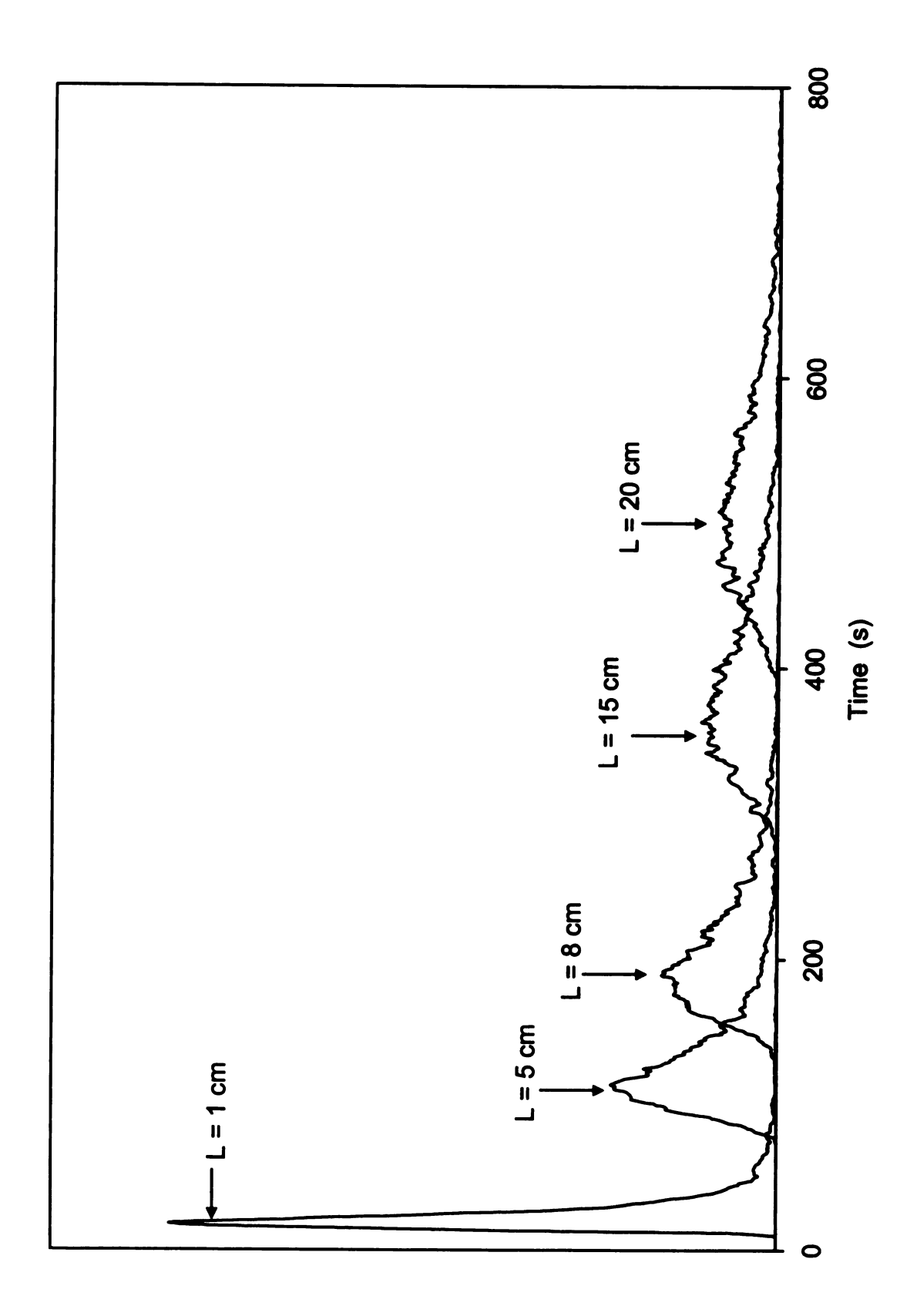
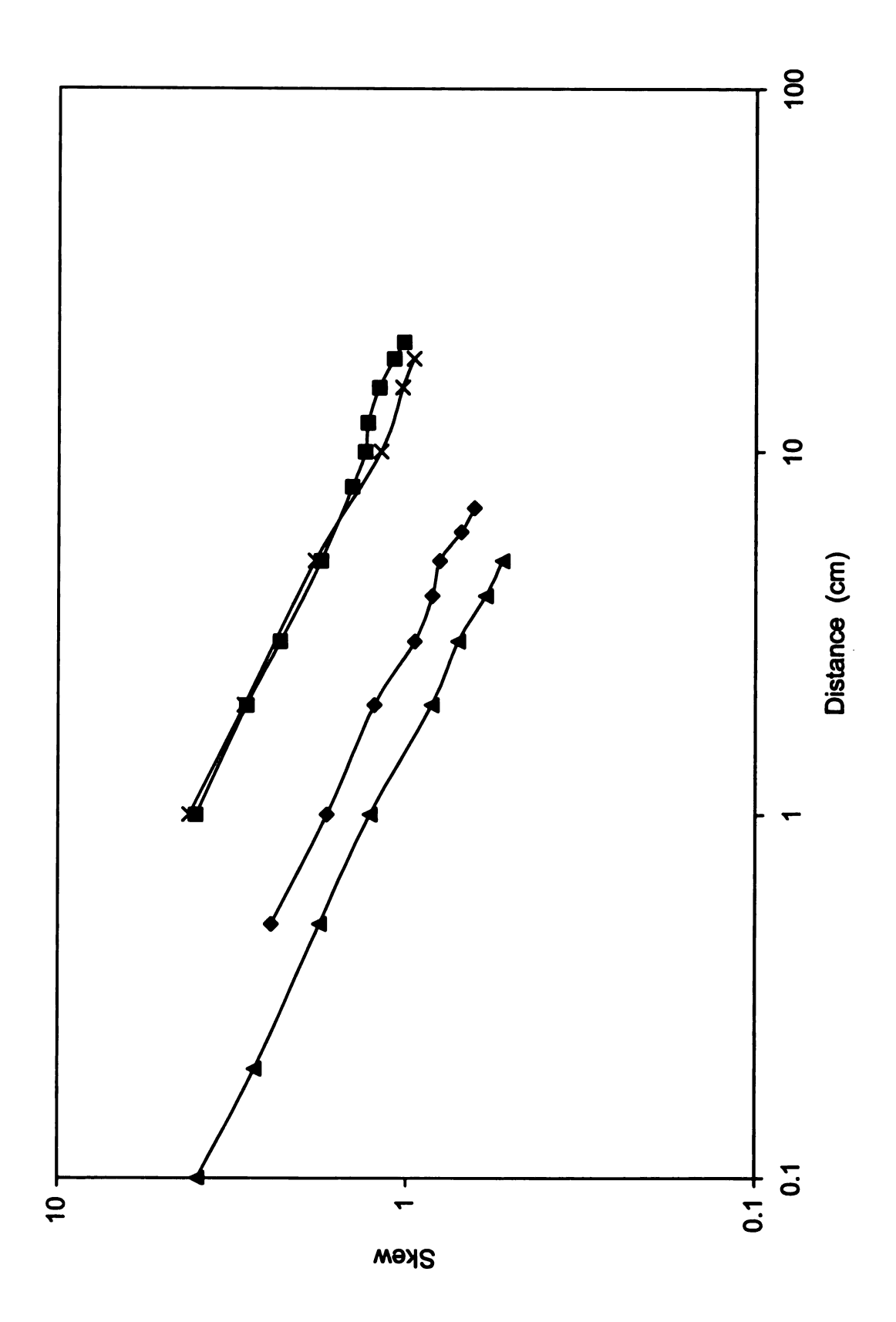


Figure 2.10: Comparison of skews among equally distributed (\spadesuit), unequally distributed (\blacksquare) heterogeneous systems, homogeneous system with D_s equal to 1.0×10^{-7} cm²/s (\triangle) and homogeneous system with D_s equal to 1.0×10^{-8} cm²/s (\star). For heterogeneous systems, simulation details as given in Figures 2.8 and 2.9. For homogeneous systems, simulation details are given in Figure 2.4.



methods are compared in Table 2.14. The true kinetic method gives an accurate value at 1.613. The statistical moment method gives accurate and reliable results before and after steady state has been achieved. The EMG method is relatively accurate (1% error) after steady state, followed by the Giddings model (13% error), and the Thomas method produces the largest errors (30% error).

The kinetic rate constants are summarized in Table 2.15. The accuracy of the true kinetic method is still unreliable because of the first-order kinetic model. All the other methods have comparable results, but still deviate from the true kinetic method. Again, the statistical moment, EMG, Giddings and Thomas models are more reliable in extracting the kinetic rate constant than the true method. The rate constant for this system is around 0.12 s⁻¹, which is higher than that of the equally distributed sites, which is around 0.05 s⁻¹. But this rate constant is intermediate between that for the two homogeneous systems with the smallest stationary-phase diffusion coefficients of 1.0x10⁻⁸ and 3.0x10⁻⁸ cm²/s.

Based on the simulated results above for the two heterogeneous systems, peak tailing is still considered to be a complicated phenomenon that requires further investigation. In contrast to Giddings' original proposition, it appears that one scarce, high-energy site is not sufficient to cause persistent tailing. Indeed, the five sites demonstrated herein are also not sufficient. According to Weiss' work, more sites are needed to cause persistent tailing.

2.5. CONCLUSIONS

This study is the first to validate and compare the accuracy of different experimental methods for extracting retention factors and kinetic rate constants

Table 2.14 Retention factors (k) along the column for unequally distributed heterogeneous surface.^a

Model	1 cm	5 cm*	8 cm*	15 cm*	20 cm*
Calculated	1.63	1.63	1.63	1.63	1.63
True	1.613 ± 0.001	1.613 ± 0.001	1.613 ± 0.001	1.613 ±	1.613 ± 0.001
Moment	1.63	1.62	1.63	1.63	1.63
EMG	1.36	1.60	1.65	1.65	1.64
Giddings	1.10	1.43	1.48	1.55	1.57
Thomas	2.23	2.14	2.17	1.97	1.89

Simulation conditions given in Figure 2.9.

Steady state achieved

Table 2.15 Kinetic rate constants from stationary to mobile phase (k_{ms}, s⁻¹) along the column for unequally distributed heterogeneous surface.^a

L	1 cm	5 cm*	8 cm*	15 cm*	20 cm*
True	0.800 ±	0.800 ± 0.006	0.800 ± 0.006	0.800 ± 0.006	0.800 ± 0.006
Moment	0.124	0.134	0.126	0.125	0.124
EMG	0.351	0.151	0.116	0.117	0.131
Giddings	0.706	0.260	0.201	0.159	0.145
Thomas	0.685	0.266	0.213	0.168	0.150

^a Simulation conditions given in Figure 2.9.

^{*} Steady state achieved

with the stochastic simulation method. In this simulation, the effects of column length, linear velocity, stationary-phase diffusion coefficient, interfacial mass transfer coefficient, and equilibrium constant have been evaluated. Overall, the retention factors are the most reliable from the statistical moment method, relatively reliable from the EMG and Giddings models, and exhibit the greatest error from the Thomas model. For the kinetic rate constants, the different parameters that influence mass transport appear to have different effects on the relative accuracy of the different methods. When increasing the column length, rate constants from the statistical moment, Giddings, and Thomas models are quite constant while those from the EMG model increase. Decreasing the linear velocity has the same effect as increasing the column length. After spending a similar amount of time on the column, the same zone profiles are achieved. When decreasing the stationary-phase diffusion coefficient or decreasing the interfacial mass transfer coefficient, rate constants for all models decrease and the zone profiles become broader with more asymmetry. In all of these simulations, the rate constants from the statistical moment, EMG, Giddings, and Thomas models are all similar to the true kinetic value. However, when increasing the equilibrium constant, the rate constants deviate from the true kinetic data for all models. This deviation may arise from poor fit of the simulation data to the single exponential decay in the true kinetic method.

Heterogeneous surfaces with equally or unequally distributed interaction sites are also generated to compare the kinetic rate constants with different methods. While the statistical moment, EMG, Giddings, and Thomas models

yield comparable results, significant deviation is observed from the true kinetic method due to poor fit in the true kinetic method. In these cases, the statistical moment, EMG, Giddings, and Thomas models may be more reliable in extracting kinetic rate constants. It is apparent that tailing of zone profiles is a transient phenomenon for homogeneous surfaces and for heterogeneous surfaces with a limited number of interaction sites. But the tailing can be maintained longer and stronger with unequally distributed heterogeneous surfaces.

2.6 REFERENCES

- [1] J.C. Giddings, Dynamics of Chromatography, Marcel Dekker, New York, NY, 1960.
- [2] J.C. Giddings, J. Chromatogr. 2 (1959) 44-52.
- [3] J.C. Giddings, J. Chem. Phys. 31 (1959) 1462-1467.
- [4] J.C. Giddings, J. Chromatogr. 3 (1960) 443-453.
- [5] J.C. Giddings, J. Chromatogr. 5 (1961) 61-67.
- [6] S. Golshan-Shirazi, G. Guiochon, in: F. Dondi, G. Guiochon (Eds.), Theoretical Advancement in Chromatography and Related Separation Techniques, Kluwer, Amsterdam, 1992, 61–92.
- [7] J.C. Giddings, H. Eyring, J. Phys. Chem. 59 (1955) 416-421.
- [8] J.C. Giddings, J. Chem. Phys. 26 (1957)169-173.
- [9] D.A. McQuarrie, J. Chem. Phys. 38 (1963) 437-445.
- [10] F. Dondi, M. Remelli, J. Phys. Chem. 90 (1986) 1885-1891.
- [11] C.P. Woodbury, J. Chromatogr. Sci. 32 (1994) 339-348.
- [12] A. Felinger, A. Cavazzini, F. Dondi, J. Chromatogr. A 1043 (2004) 149-157.
- [13] A. Cavazzini, F. Dondi, A. Jaulmes, C. Vidal-Madjar, A. Felinger, Anal. Chem. 74 (2002) 6269-6278.
- [14] V.L. McGuffin, P. Wu, J. Chromatogr. A 722 (1996) 3-17.
- [15] D.L. Hopkins, V.L. McGuffin, Anal. Chem. 70 (1998) 1066-1075.
- [16] P.E. Krouskop, V.L. McGuffin, J. Chromatogr. A 959 (2002) 49-64.
- [17] V.L. McGuffin, P.E. Krouskop, D.L. Hopkins, American Chemical Society (2000) Chapter 4, 37-66.
- [18] C. Horvath, H.J. Lin, J. Chromatogr. 126 (1976) 401-420.
- [19] C. Horvath, H.J. Lin, J. Chromatogr. 149 (1978) 43-70
- [20] A.M. Lenhoff, J. Chromatogr. 384 (1987), 285-299.
- [21] K. Miyabe, G. Guiochon, J. Sep. Sci. 26 (2003) 155-173.

- [22] S.B. Howerton, C. Lee, V.L. McGuffin, Anal. Chim. Acta, 478 (2003) 99-110.
- [23] V.L. McGuffin, C. Lee, J. Chromatogr. A 987 (2003) 3-15.
- [24] S.B. Howerton, V.L. McGuffin, Anal. Chem. 75 (2003) 3539-3548.
- [25] S.B. Howerton, V.L. McGuffin, J. Chromatogr. A 1030 (2004) 3-12.
- [26] V.L. McGuffin, S.B. Howerton, X. Li, J. Chromatogr. A 1073 (2005) 63-73.
- [27] J.C. Giddings, Anal. Chem. 35 (1963) 1999-2002.
- [28] G.H. Weiss, Sep. Sci. Technol. 16 (1981) 75-80.
- [29] G.H. Weiss, Sep. Sci. Technol. 17 (1982-1983) 1609-1622.

CHAPTER 3

EXPERIMENTAL METHODS

3.1 EXPERIMENTAL SYSTEM

3.1.1 Column Packing

In order for the quantification of thermodynamics and kinetics, capillary columns are employed throughout the study. A well-behaved column is crucial for our research. In this section, the methods for column packing are described.

An optically transparent, fused-silica capillary is used for the column (200µm i.d., Polymicro Technologies). With 5-µm particles, the number of particles
across the column is around 40. The number of particles across the column is
important because a larger number of particles across the column results in a
minimization of wall effects, which contribute to asymmetrical tailing (*vide infra*).
The column detection window needs to be made before packing by burning off
the polyimide coating. The columns are terminated by quartz wool frits that
prevent leakage of the stationary phases from the packed column.

The stationary phase used in chiral separation are native β -cyclodextrin (Cyclobond I 2000, Astec) characterized by a 5.2- μ m particle size, 0.89-mL/g pore size, and 305-m²/g surface area. In order to pack the stationary phase, the slurry method is utilized [1]. Columns prepared by this method have very uniform packing across the diameter and along the length. This method involves suspension of the stationary phase in a solvent that prevents immediate precipitation. For the β -cyclodextrin stationary phase, methanol is chosen as the solvent. Once suspended, the material is transferred to a stainless steel

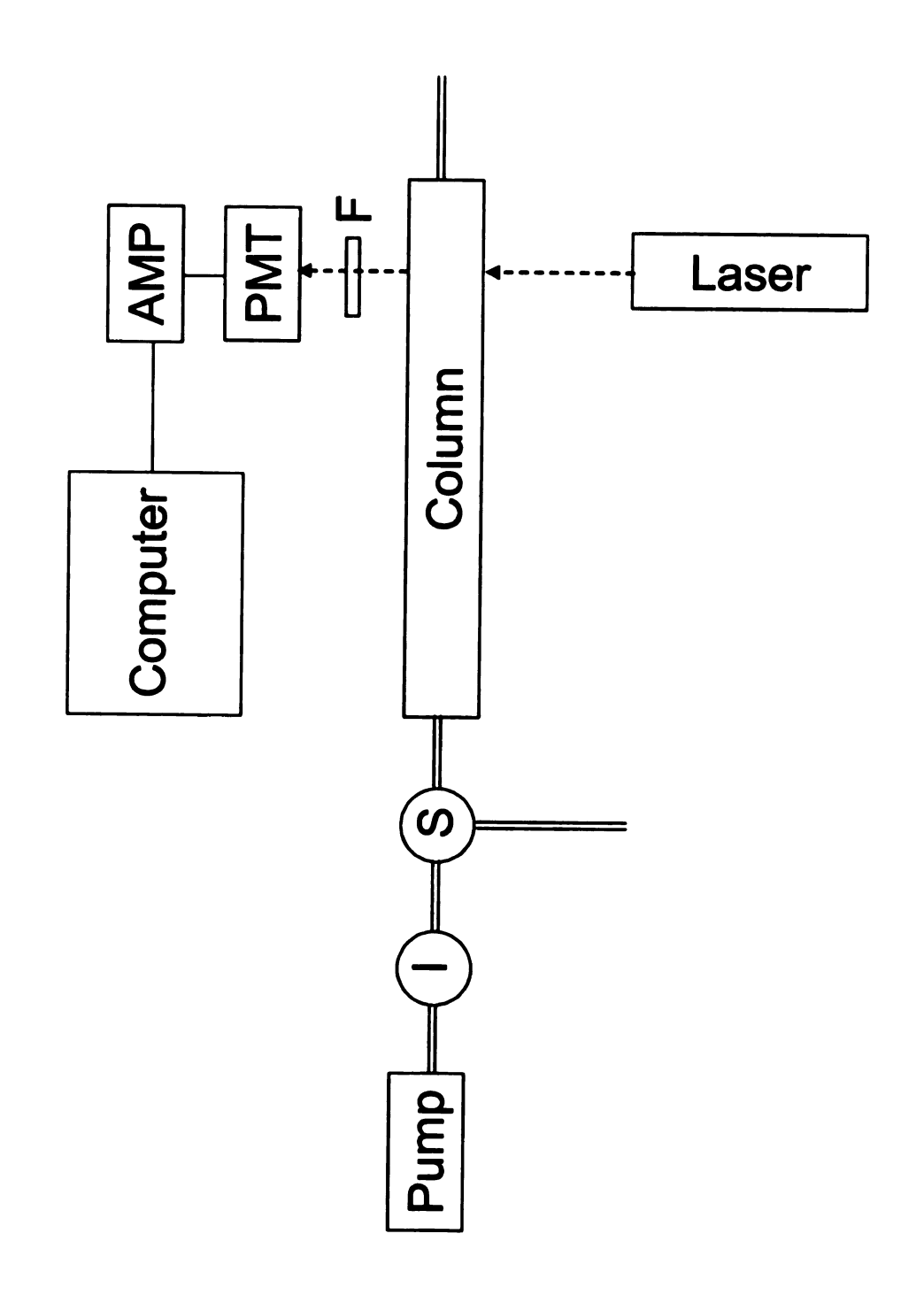
reservoir that is connected in series with a single-piston reciprocating pump (Model 114M, Beckman Instruments) and a fused-silica capillary. The reservoir is pressurized rapidly, thus injecting the stationary phase into the open capillary. The highest pressure at 4000 psi packs the column in a matter of minutes. The highest pressure is maintained for three hours and lowered to 1500 psi gradually. The pressure is maintained at 1500 psi overnight. This lower pressure allows the packed bed to compress, thus removing any voids that could be left during the initial packing step. The column has a plate height (H) of 99 µm and reduced plate height (h) of 19.03.

3.1.2 Chromatographic System

3.1.2.1 One detector system for the mobile phase study

As illustrated in Figure 3.1, this system is used for the mobile-phase study (Chapter 4). The solutes are separated on a capillary liquid chromatography system. The mobile phases are delivered by a single-piston reciprocating pump (Model 114M, Beckman Instruments), operated in the constant-pressure mode. The pump allows for the mobile phase to be supplied continuously without the need for depressurization during the refill cycle. After injection (Model ECI4W1, Valco Instruments), the samples are split between the column and a fused-silica capillary (50-µm i.d., Polymicro Technologies) that served as a splitter. The length of the splitter is varied to change the amount of sample that is introduced into the column so as to prevent an overload of the stationary phase. Under normal conditions, the injection volume is around 15 nL.

Figure 3.1 Schematic diagram of the experimental system for capillary liquid chromatography with one on-column laser-induced fluorescence detector for mobile phase study. I: injection valve, S: splitting tee, F: filter, PMT: photomultiplier tube, AMP: current to voltage amplifier.



The polyimide coating is removed from the capillary column at 99-cm length to facilitate on-column detection by laser-induced fluorescence. A helium-cadmium laser (Model 3074-20M, Melles Griot) provides excitation at 325 nm. The fluorescence emission is isolated by a liquid filter (1% aqueous NaNO₃) and two interference filters (420 nm, S10-410-F, Corion), and is detected by a photomultiplier tube (Centronic Model Q4249BA, Bailey Instruments). The resulting photocurrent is amplified, converted to the digital domain (Model PCI-MIO-16XE-50, National Instruments), and stored by a user-defined program (Labview v5.1, National Instruments).

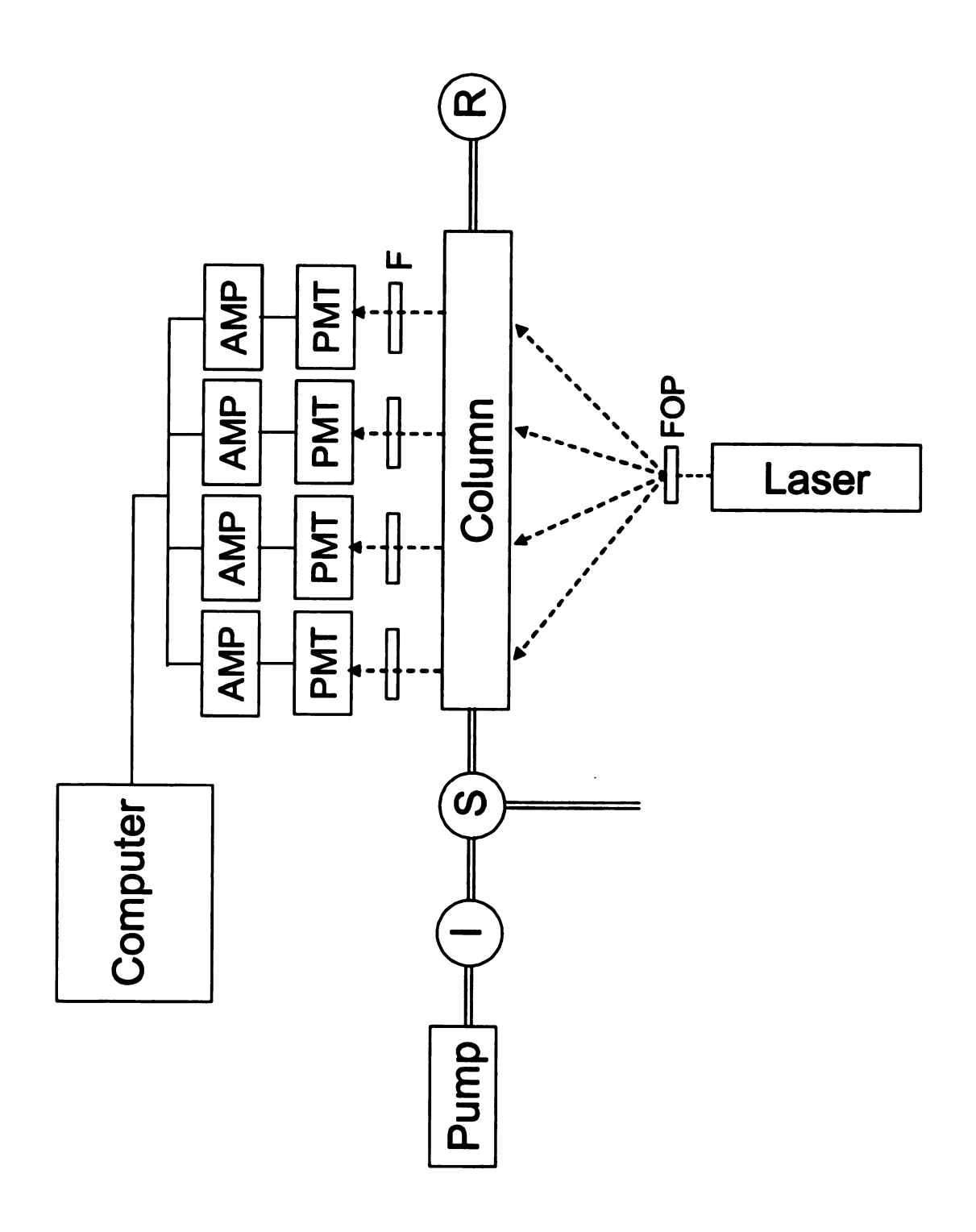
3.1.2.2 Four-detector system for temperature and pressure study

As illustrated in Figure 3.2, this system is used for the temperature and pressure study (Chapter 5 and 6). The design and validation of this system were conducted by Dr. Shu-hui Chen [2]. There are three major differences between this system and the system discussed in 3.1.2.1.

At the end of the column, another capillary (20-μm i.d., Polymicro Technologies) is attached to serve as restrictor. The length of the restrictor is reduced as the inlet pressure is decreased in order to maintain a constant pressure drop along the column of (~10 psi/cm). By reducing the length of the restrictor and splitter proportionally, the split ratio could be maintained at a constant value.

The injector, splitter, column, and restrictor are all housed within a cryogenic oven (Model 3300, Varian Associates) that maintains a constant

Figure 3.2 Schematic diagram of the experimental system for capillary liquid chromatography with four on-column laser-induced fluorescence detectors for temperature and pressure study. I: injection valve, S: splitting tee, R: restrictor, FOP: fiber-optic positioner, F: filter, PMT: photomultiplier tube, AMP: current to voltage amplifier.



temperature (± 0.1 K) through the use of liquid nitrogen aspiration and resistive heating coils.

Four detector windows are available for this system to monitor solute zone profiles along the column. The laser beam is carried via UV-grade optical fibers (100 µm, Polymicro Technologies) to four locations along the column where the polyimide coating has been removed. The laser power at each location is balanced using fiber optic positioners and a fluorophore at the inception of each experiment. At each location, the fluorescence is collected orthogonal to the incident beam by optical fibers (500 µm, Polymicro Technologies) and is transmitted to a photomultiplier tube (Model R760, Hamamatsu), which has a 420-nm interference filter (S10-420-F, Corion). The resulting photocurrent is amplified using a gain of 100 nA/V and a time constant of 10 ms. The signal is then converted to the digital domain (PCI-MIO-16XE-50, National Instruments) and stored by a user-defined program (Labview v5.1, National Instruments). The acquisition rate of the program can be manually adjusted, and is typically set between 1 and 4 Hz.

3.2 DATA ANALYSIS

After collection, the zone profile for each solute is extracted from the chromatogram. Each profile is fit by nonlinear regression to the exponentially modified Gaussian (EMG) equation by using a commercially available program (Peakfit v4.14, SYSTAT Software). The EMG equation is chosen because the statistics of fit are better than for any other model that has been demonstrated to have physical meaning. Specifically speaking, the statistical fit parameter R²

from the EMG model is usually higher than that from the Thomas [3,4] or Giddings [5] models. The residuals from the EMG model are more random and smaller than those from the Thomas or Giddings models as well. The EMG model has already been validated for extracting thermodynamic and kinetic information by the simulation works in Chapter 2. The EMG equation is the convolution of Gaussian and exponential functions, with the resulting form

$$C(t) = \frac{A}{2\tau} \exp\left[\frac{\sigma^2}{2\tau^2} + \frac{t_g - t}{\tau}\right] \left[\operatorname{erf}\left(\frac{t - t_g}{\sqrt{2}\sigma} - \frac{\sigma}{\sqrt{2}\tau}\right) + 1 \right]$$
 (2.1)

where C(t) is the concentration as a function of time, A is the peak area, t_q is the retention time of the Gaussian component, σ is the standard deviation of the Gaussian component, τ is the exponential component, and erf is an statistical error function. Symmetrical zone broadening, which arises from diffusion and mass transfer processes that are fast relative to the separation time, is quantified by σ . Asymmetrical broadening, which arises from volumetric sources (i.e., injectors, unions, etc.), electronic sources (i.e., amplifiers, etc.), nonlinear isotherm, and diffusion and mass transfer processes that are slow relative to the separation time, is quantified by τ . By deliberate design of the system, the asymmetrical broadening from volumetric and electronic sources can be minimized and kept small relative to those from slow mass transfer processes. The nonlinear isotherm contribution to asymmetric broadening can be totally eliminated by injecting solutes at sufficiently low concentrations. Thus, the slow mass transfer will dominate the asymmetrical broadening. The resultant fitting

parameters of the EMG equation are used to calculate thermodynamic and kinetic values [6] as discussed in Chapters 1.4 and 2.3.3.

3.3 CONCLUSIONS

In order to accurately characterize the liquid chromatographic process, both a judiciously designed experimental system and an accurate data analysis method are necessary. This chapter describes the system as well as the mathematic function for analysis.

3.4 REFERENCES

- [1] J.C. Gluckman, A. Hirose, V.L. McGuffin, M. Novotny, Chromatographia 17 (1983) 303-309.
- [2] S.-H. Chen, in Chemistry, Michigan State University, East Lansing, Michigan 1993
- [3] H.C. Thomas, J. Am. Chem. Soc. 66 (1944) 1664-6.
- [4] J. L. Wade, A.F. Bergold, P.W. Carr, Anal. Chem. 59 (1987) 1286-95.
- [5] J. C. Giddings, Dynamics of Chromatography; Marcel Dekker: New York, NY, 1965.
- [6] S.B. Howerton, V.L. McGuffin, Anal. Chem. 75 (2003) 3539-48.

CHAPTER 4

EFFECT OF MOBILE PHASE COMPOSITION TO CHIRAL SEPARATIONS WITH β-CYCLODEXTRIN STATIONARY PHASE

4.1. INTRODUCTION

In liquid chromatography, once a specific stationary phase is chosen, mobile phase composition is the factor that will most significantly affect the separation. With native cyclodextrin CSPs, reversed-phase separation is the most popular and successfully used mobile phase [1,2]. Many publications are available on the effect of mobile phase composition in the reversed-phase mode [3-16]. Systematic studies have been performed on the effect of organic modifier type, modifier concentration, buffer type, buffer concentration and ionic strength. More recently, polar-organic phase separation has also become widely utilized. Armstrong et al. [17] first utilized polar-organic mobile phases with native Bcyclodextrin CSP to separate some β-blocker pharmaceuticals. Since then, many other enantiomers have been separated in the polar-organic mode [18-21]. However, limited information is available on the effect of polar-organic mobile phase composition, especially detailed and systematic characterization studies. Notably, there have been investigations of mobile phase effects on β-blockers [22] and amino acids [23]. In these studies, the thermodynamic effects on retention factor and chiral selectivity are carefully investigated, however, the kinetic effects on mass transfer rates are usually overlooked. Both thermodynamic and kinetic information are equally important for elucidation of the retention mechanism.

In addition to the effect of mobile phase composition, the memory effect is another interesting issue that needs to be addressed. The existence of memory effects with acid and amine modifiers has been demonstrated with polysaccharide columns by Stringham et al. [24,25]. In their work, acids and amines showed persistent effects after their removal, indicating strong interaction with the polysaccharide CSP. However, there has been no report on these effects with cyclodextrin CSPs. Considering that cyclodextrin has the same building blocks (glucose units) as polysaccharides, the memory effect is worthy of investigation.

4.2. EXPERIMENTAL METHODS

4.2.1 Chemicals

As depicted in Figure 4.1, five coumarin-based solutes are chosen based on their structural similarities. Warfarin is a well-known pharmaceutical compound that serves as an anti-coagulant. It inhibits the synthesis of clotting factors, thus preventing blood clot formation. Coumachlor, coumafuryl, and coumatetrally are three anti-coagulant pesticides to kill rodents. They take effect by blocking vitamin K-dependent synthesis of the blood clotting substance prothrombin, thus causing wide-spread internal bleeding [26]. All four compounds are chiral and they are marketed in racemic form. The chirality of these compounds arises from the sp^3 – alpha carbon. Another achiral compound, 4-hydroxycoumarin, is an important intermediate for coumarin-related pharmaceuticals. It is a subunit contained in all four chiral compounds, thus, a separate view of this particular group to the retention process is possible. The

Figure 4.1 Structure of coumarin-based solutes.

$$\begin{array}{cccc} & & & & & & \\ & & & & \\ & & & & \\ & & & \\ & & & \\ & & & \\ & & & \\ & & & \\ & & & \\ & & & \\ & & & \\ & & & \\ & & & \\ &$$

4-Hydroxycoumarin

solutes are obtained from Sigma-Aldrich as solids and are dissolved in high-purity acetonitrile (Burdick and Jackson, Baxter Healthcare) to yield standard solutions at 10⁻⁴ M. Nitromethane is used as non-retained marker and is added to each solution at a concentration at 15% (v/v). High purity acetonitrile, methanol (Burdick and Jackson, Baxter Healthcare), acetic acid (Sigma-Aldrich), and triethylamine (Sigma-Aldrich) are used for mobile phase preparation.

4.2.2 Experimental System

The solutes are separated on a capillary liquid chromatography system as illustrated in Figure 3.1. The silica packing (Cyclobond I 2000, Astec) is characterized by a 5.2- μ m particle size, 0.89-mL/g pore volume, and 305-m²/g surface area, reacted with β -cyclodextrin at a bonding density of 0.39 μ mol/m². The data are analyzed by exponentially modified Gaussian (EMG) function, as described in Chapters 1.4.3.2.2 and 2.3.3.

4.3. RESULTS AND DISCUSSION

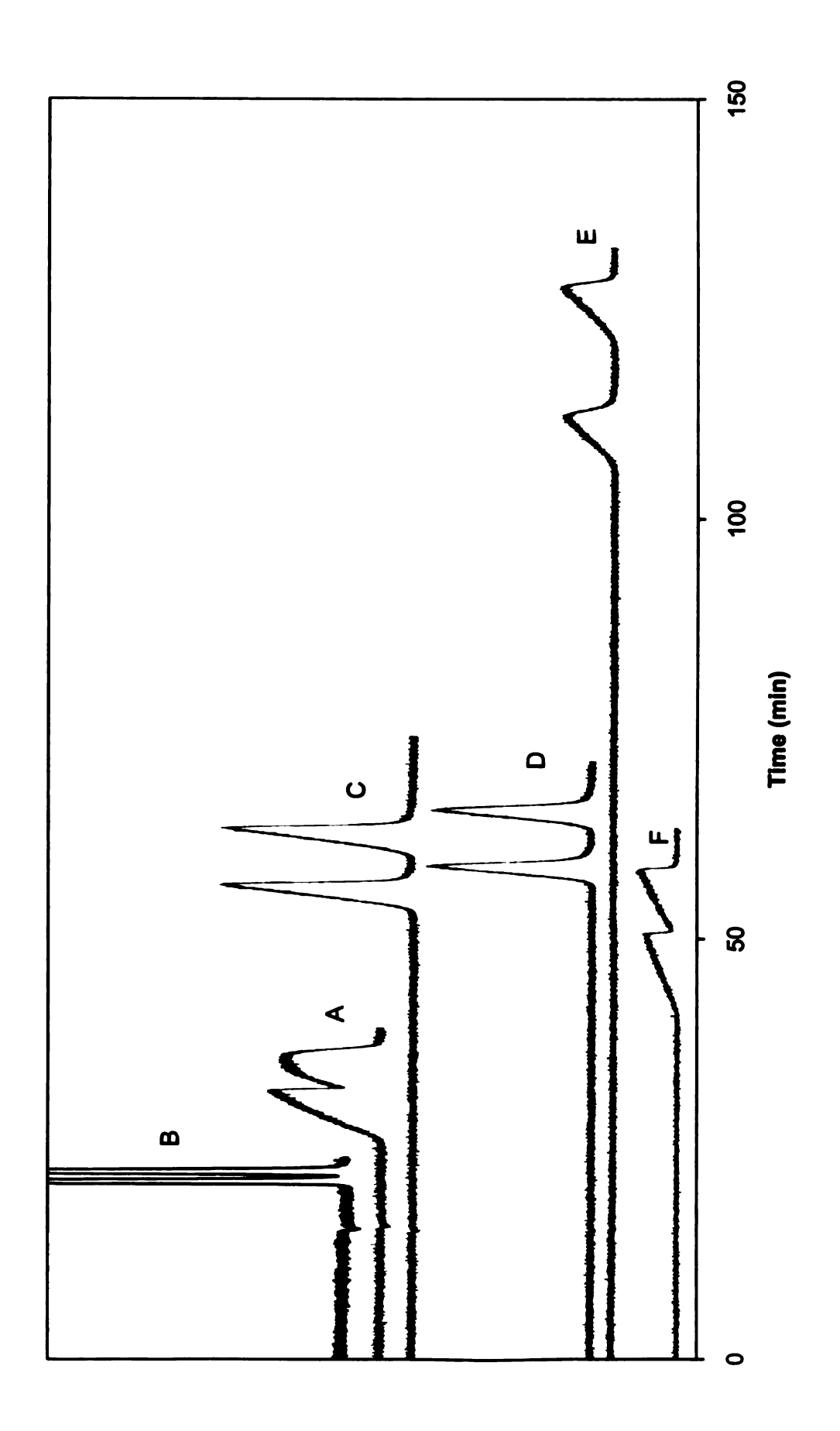
4.3.1. Memory Effect

In the first series of experiments, warfarin is utilized as the solute to investigate memory effects on a β -cyclodextrin CSP. Two polar-organic mobile phase compositions are used: the first mobile phase contains only acetonitrile and methanol at a 90%:10% ratio by volume; the second mobile phase contains acetonitrile and methanol (90%:10%) together with acetic acid (0.30%) and triethylamine (0.20%) modifiers. Warfarin is initially injected at the first mobile phase composition. This result serves as the "original" retention data (t_r) for comparison when acid and amine are not present in the mobile phase. Then the

second mobile phase is introduced with another warfarin injection. Finally, the first mobile phase is switched back, and warfarin is injected over successive days to monitor the peak shape and retention time. Representative chromatograms are illustrated in Figure 4.2. The original peaks have a broad and fronting shape. with a retention time of approximately 35 min (Figure 4.2A). When acid and amine are added to the mobile phase, the elution time of warfarin is greatly reduced and the peak shape becomes narrow and Gaussian (Figure 4.2B). When acid and amine are subsequently removed from the mobile phase, the retention time of warfarin increases, with increased peak broadening as well (Figures 4.2C and 4.2D), until 3 days later when the retention time reaches a maximum (Figure 4.2E). Thereafter, the retention time begins to decrease and the peak shape becomes broader and more fronting (Figure 4.2F). But even after 10 days, the retention time does not return to the original value shown in Figure 4.2A. These data indicate two possibilities: either a memory effect of the acid and amine exists in the cyclodextrin CSP, or the equilibration time for the acetonitrile:methanol mobile phase is extremely long. The second possibility can also be considered as the existence of a memory effect of methanol.

In the approach used by Stringham et al. [24,25] to remove the memory effect of acid or amine on a polysaccharide CSP, the column was washed with alcohols or water. Since methanol is already a component of the polar-organic mobile phase, methanol alone is used herein to remove any possible memory effect of acid or amine. The β-cyclodextrin column is washed with methanol for one day, then the mobile phase is switched back to acetonitrile:methanol

Figure 4.2 Representative chromatograms of memory effect from acetic acid and triethylamine. Column: β-cyclodextrin. Solute: racemic warfarin. Mobile phase composition: acetonitrile:methanol (90%:10%) (A) original data before acid and amine modifier added; (B) acetic acid:triethylamine (0.30%:0.20%) added; (C) removal of acid and amine modifier at hour 4; (D) day 1; (E) day 3; (F) day 10.

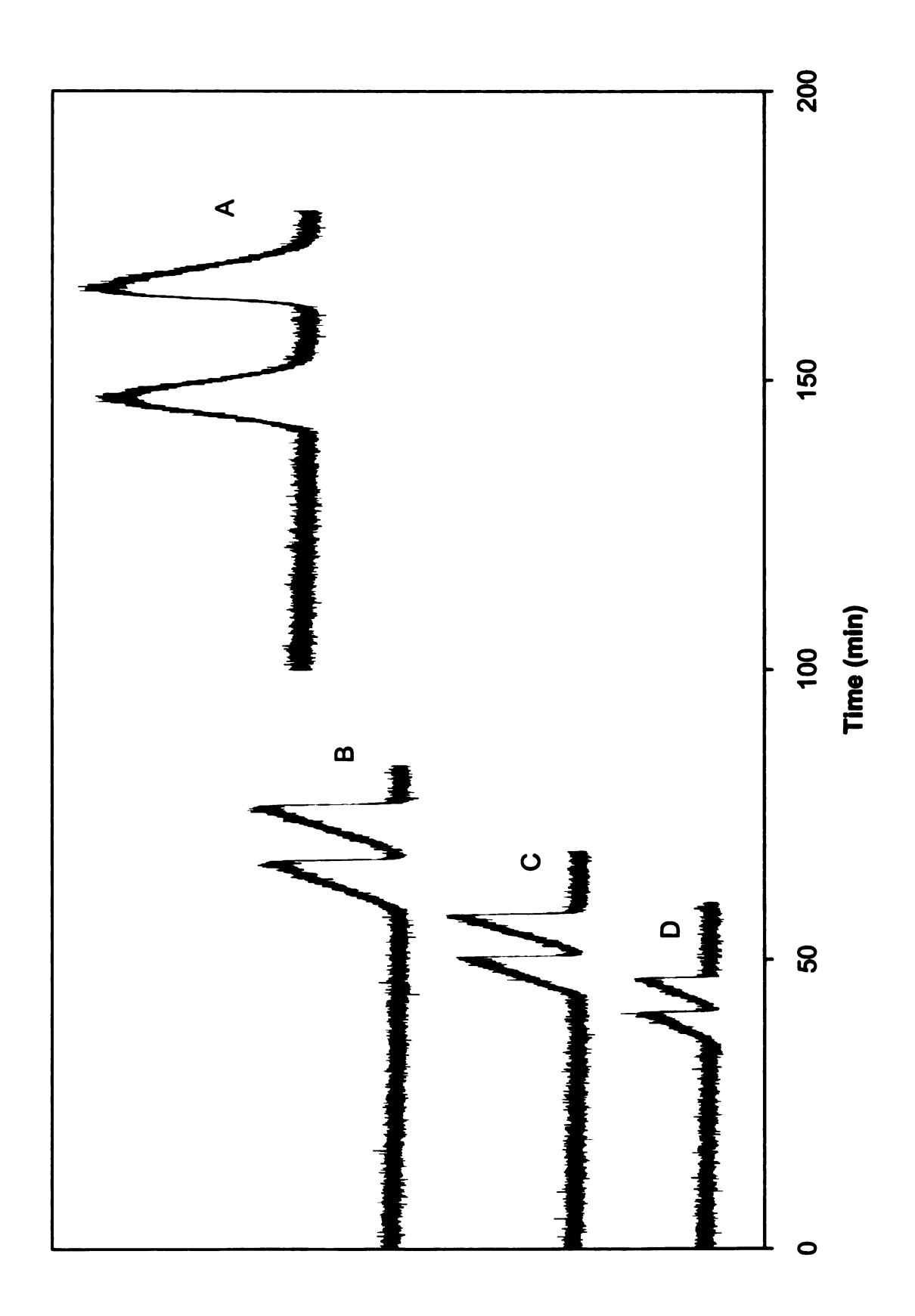


(90%:10%), followed by the injection of warfarin over successive days. Representative chromatograms are shown in Figure 4.3. After one day, the retention time for warfarin is extremely long at around 150 min (Figure 4.3A). Moreover, the peak shape is tailing instead of fronting as seen previously in Figure 4.2. After two days, the retention time is reduced to around 65 min with a fronting peak shape (Figure 4.3B). The retention time of warfarin continues to decrease over several days, but does not return to the original value even after 10 days (Figure 4.3D). However, these retention times are closer to the original values than those obtained after removal of acid and amine (Figure 4.2). These data indicate that washing with methanol provides some improvement, but cannot completely eliminate the memory effect of acid or amine. On the contrary, methanol itself exhibits an even stronger memory effect over short periods of time (e.g., less than 1 day). These results suggest that more detailed investigation of the effect of the individual components in the polar-organic mobile phase is warranted. Prior to these experiments, the β-cyclodextrin column is washed with pure acetonitrile for several weeks to remove any residual memory effect of the previous mobile phases.

4.3.2. Two-Component Mobile Phase

In these experiments, acetonitrile and methanol are the only components in the mobile phase, no acid or amine is added. The percent of methanol is varied at 3%, 5%, 10%, 15%, and 20%. Each composition of the mobile phase is maintained for several days in order to observe the rate of achievement of equilibrium conditions.

Figure 4.3 Representative chromatograms of memory effect from methanol. Column: β-cyclodextrin. Solute: racemic warfarin. Mobile phase composition: acetonitrile:methanol (90%:10%) after removal of pure methanol mobile phase at (A) day 1; (B) day 2; (C) day 3; (D) day 10.



The retention time of warfarin over successive days is reported in Table 4.1. Using the second day as an example, the retention time decreases as the mobile phase composition changes from 3% to 10% methanol. From 10% to 20% methanol, however, the retention time shows an increasing trend. For each composition, the retention time is not stable even after several days. Interestingly, the trends in retention time over days are not the same for each concentration. At lower concentrations (3% and 5%) of methanol, the retention time decreases over successive days. At higher concentrations (15% and 20%), the retention time increases over successive days. At an intermediate concentration of 10% methanol, the retention time shows an initial decrease followed by an increase. By careful observation, the trend over successive days is noted to be the same as the trend for the next higher concentration of methanol. Using 3% methanol mobile phase as an example, the retention time of warfarin increases over successive days, and retention time also increases when changing from 3% to 5% methanol. Using 15% methanol as an example, the retention time of warfarin decreases over successive days, and retention time also decreases when changing from 15% to 20% methanol. These observations suggest that methanol may accumulate on the β-cyclodextrin column. While a low concentration of methanol can compete with the solute warfarin and serve as a displacing agent to decrease its retention time, higher concentrations may build up a layer of methanol on the cyclodextrin surface. This layer can serve as a partitioning medium and can increase retention time because the effective volume of the stationary phase increases with increasing methanol concentration.

Table 4.1 Retention time of 1st warfarin enantiomer over successive days in a two-component mobile phase

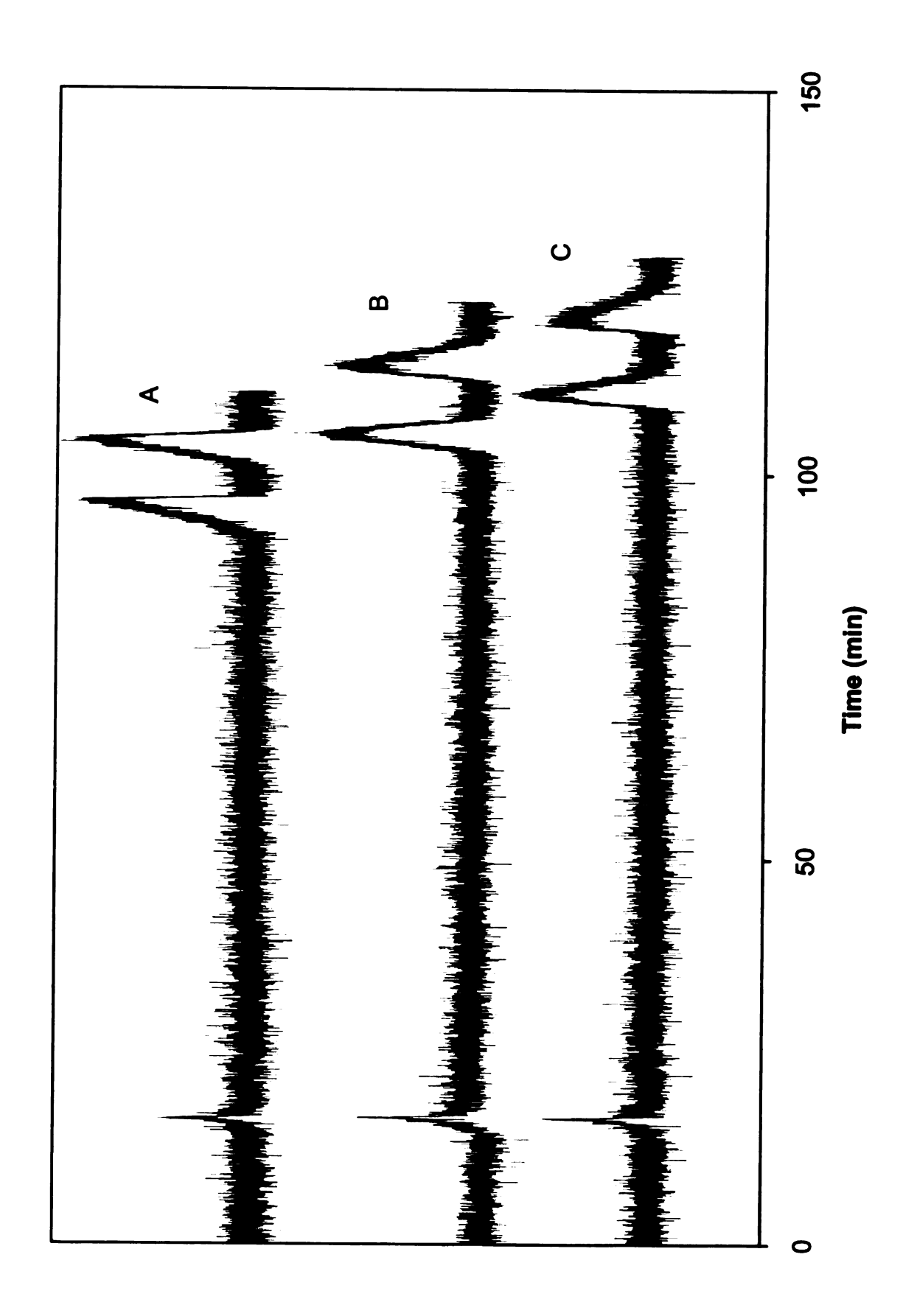
Mobile Phase		Retention	Time (min)	
Composition (acetonitrile:methanol)	Day 1	Day 2	Day 3	Day 4
97%:3%	183.5	174.8	174.1	N/Aª
95%:5%	93.4	81.3	76.1	N/A
90%:10%	28.1	22.9	27.8	31.6
85%:15%	N/A	48.0	50.9	55.3
80%:20%	100.3	96.1	105.4	108.3

a not available

Another interesting observation is the change in warfarin peak shape with concentration of methanol. At concentrations of 3% to 15% methanol, all the peaks are fronting. At 20% methanol, however, different peak shapes appear over successive days as shown in Figure 4.4. The peaks on the second day are fronting (Figure 4.4A), those on the third day are slightly tailing (Figure 4.4B), while those on the sixth day are strongly tailing (Figure 4.4C). This change in peak shape suggests a change in the interaction between warfarin and the cyclodextrin CSP. A tailing shape is usually considered as a sign of a Langmuir or BET type I isotherm, where there exists a limited number of interaction sites on the stationary phase. As the concentration of solute increases, these sites become completely occupied and the remaining solute molecules are not retained. A fronting shape usually suggests an anti-Langmuir or BET type III isotherm, where there is weak interaction between the solute and stationary phase. As the concentration of solute increases, it has stronger interactions with other solute molecules bonded to the stationary phase than with the stationary phase alone. It is certainly possible that the retention mechanism changes with increasing methanol concentration due to the formation of a methanol layer, as discussed above. However, it is also possible that a single mechanism exists with a more complicated isotherm, such as BET type V, which combines the features and behavior of the BET type I and III isotherms. More detailed studies are needed to elucidate the underlying reason for the change in peak shape with methanol concentration.

150

Figure 4.4. Comparison of chromatograms in two-component mobile phase. Column: β-cyclodextrin. Solute: racemic warfarin. Mobile phase composition: acetonitrile:methanol (80%:20%) (A) day 2; (B) day 3; (C) day 6.



4.3.3 Three-Component Mobile Phase

In these experiments, acetic acid or triethylamine is added to an acetonitrile:methanol (90%:10%) mobile phase to prepare a three-component mobile phase. The retention time, equilibration time, peak shape, and isotherm effect are compared for the different mobile phase conditions.

4.3.3.1 Retention Time and Equilibration Time Investigation

As in the previous study, warfarin is injected over successive days to observe the trends in retention time and equilibration time. Three different mobile phase compositions are reported. The first mobile phase is a two-component mobile phase containing acetonitrile and methanol (90%:10%). The second mobile phase added 0.30% acetic acid to the first mobile phase, while the third mobile phase added 0.20% triethylamine to the first mobile phase.

The retention time of warfarin measured over successive days at each mobile phase composition is reported in Table 4.2. The average retention time, standard deviation, and percent relative standard deviation (RSD) are reported as well. In the two-component mobile phase, equilibrium is not reached even after four days, which can be discerned from the large RSD of 13%. In fact, the retention time is still changing even after one week (results not shown). When acid or amine modifier is added to the mobile phase, equilibrium is reached much faster (one day or less) and the RSD is reduced to 1 - 2%. This indicates that acid or amine modifier can help greatly to shorten the equilibration time of the mobile phase.

Table 4.2 can also be used to compare the retention time for different mobile phase compositions. When compared to the two-component mobile phase, the addition of 0.30% acetic acid modifier does not have a significant effect upon retention time, which increases only slightly. On the contrary, the addition of 0.20% triethylamine modifier greatly shortens the retention time. The suspected reasons for this behavior will be discussed in the next section.

4.3.3.2. Peak Shape and Isotherm Investigation

As the mobile phase composition is changed, not only do the retention time and equilibration time change, but also the peak shape. Unusual fronting and tailing shapes are frequently encountered, as discussed in Sections 4.3.1 and 4.3.2. Since these peak shapes are usually associated with nonlinear isotherms, this possibility is examined by injecting warfarin at different concentrations ranging from 5×10^{-5} to 8×10^{-4} M.

As discussed previously, fronting peaks are observed in the two-component mobile phase composition with acetonitrile:methanol (90%:10%). But when both acid and amine modifiers are added, symmetric Gaussian peaks are observed. To determine which modifier is responsible for the Gaussian peak shape, two different mobile phases are investigated. One contains 0.30% acetic acid modifier and the other contains 0.05% triethylamine modifier. Representative chromatograms of warfarin are illustrated in Figures 4.5 and 4.6. With acid modifier alone, the retention time is virtually unchanged and the peak shape is Gaussian until the highest warfarin concentration (8x10⁻⁴ M), where the retention time decreases slightly and is accompanied by slight tailing. This

Table 4.2 Retention time of 1st warfarin enantiomer over successive days in two-component and three-component mobile phases

Mobile Phase	Re	etention	Time (n	nin)			
Composition (acetonitrile:methanol:	Day	Day	Day	Day	Average	St.	% RSDª
acid:amine)	1	2	3	4			
90%:10%:0%:0%	28.1	22.9	27.8	31.6	27.6	3.7	13
90%:10%:0.30%:0%	28.6	29.1	28.9	N/A ^b	28.9	0.3	1
90%:10%:0%:0.20%	12.3	12.3	11.9	N/A	12.2	0.3	2

a % RSD = (Average / St. Dev.) x 100 %

b Not available

suggests that a linear isotherm is obtained in the mobile phase with acid modifier over most of the solute concentration range in this study. However, with amine modifier alone, fronting peaks are observed even at the lowest warfarin concentration. The solutes become more retained and the peaks become more asymmetric with increasing concentration. Although the maxima are shifted to longer retention time, all the peaks for the first enantiomer appear to arise from the same initial position. The peaks for the second enantiomer do not arise from the same initial position, but are shifted to longer retention time with increasing warfarin concentration. This behavior is indicative of a competitive nonlinear isotherm, where both enantiomers are competing for the same adsorption sites on the cyclodextrin CSP.

The change in peak shape with mobile phase composition is interesting and informative. Fronting peaks are observed when no modifier or only amine modifier is present in the mobile phase. As noted above, fronting shape is usually indicative of an anti-Langmuir or BET type III isotherm. When no acid or amine modifier is present, the methanol may accumulate on the cyclodextrin surface, as discussed above. This may be the reason why warfarin cannot interact directly with cyclodextrin, but tends to interact with other warfarin molecules. When triethylamine is present, it has a tendency to interact with the acidic hydroxyl group on warfarin (pK_a = 4.5) to facilitate its elution, which corresponds to the much shorter retention time. However, triethylamine probably cannot compete with and displace warfarin from the cyclodextrin sites or from the sites where the solute molecules interact with each other, thus it does not affect

Figure 4.5 Warfarin peak shape in the presence of acetic acid. Column: β-cyclodextrin. Mobile phase composition: acetonitrile:methanol:acid (90%:10%:0.30%). Warfarin concentration from highest to lowest: $8x10^{-4}$ M; $4x10^{-4}$ M; $2x10^{-4}$ M.

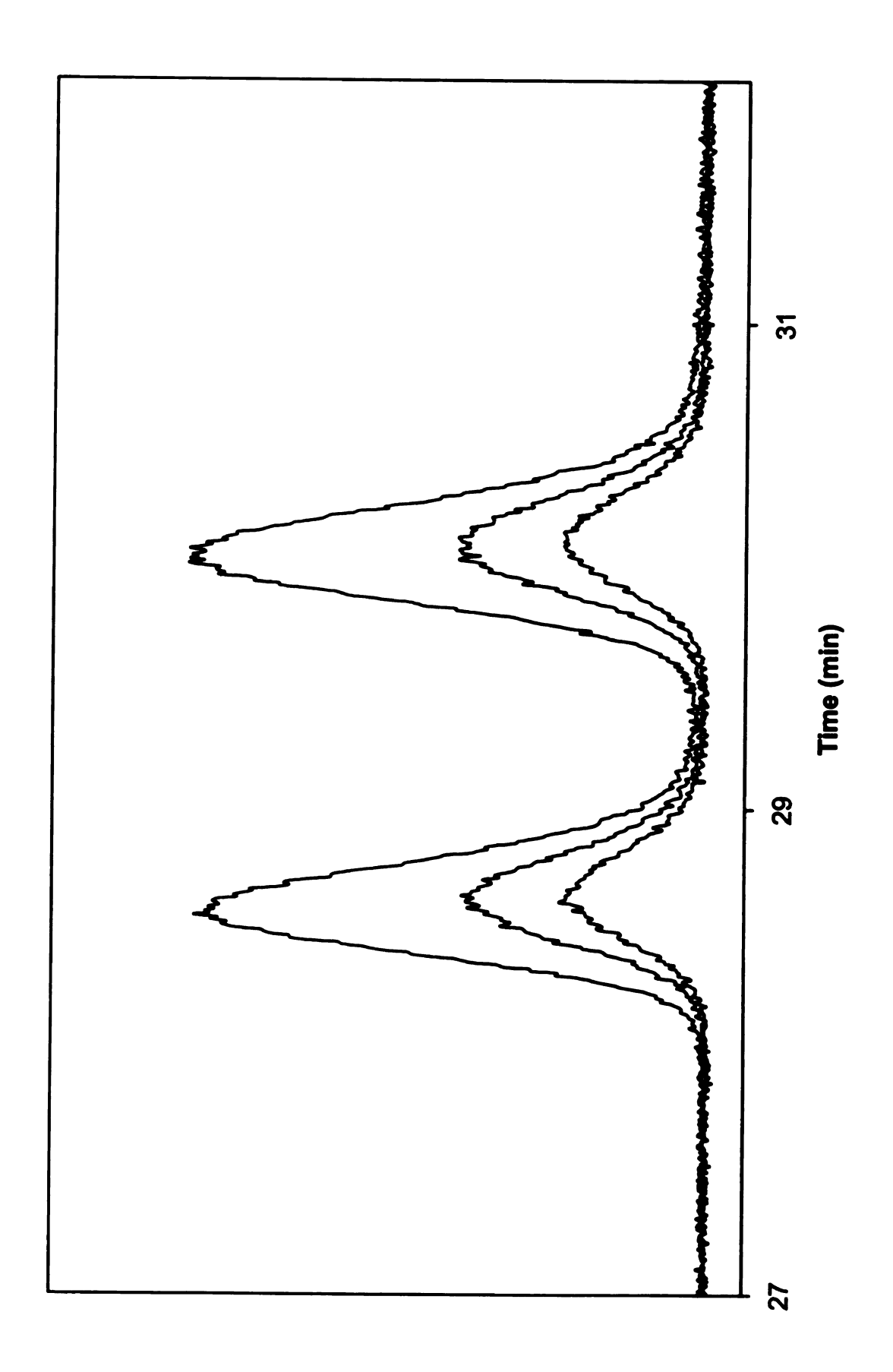
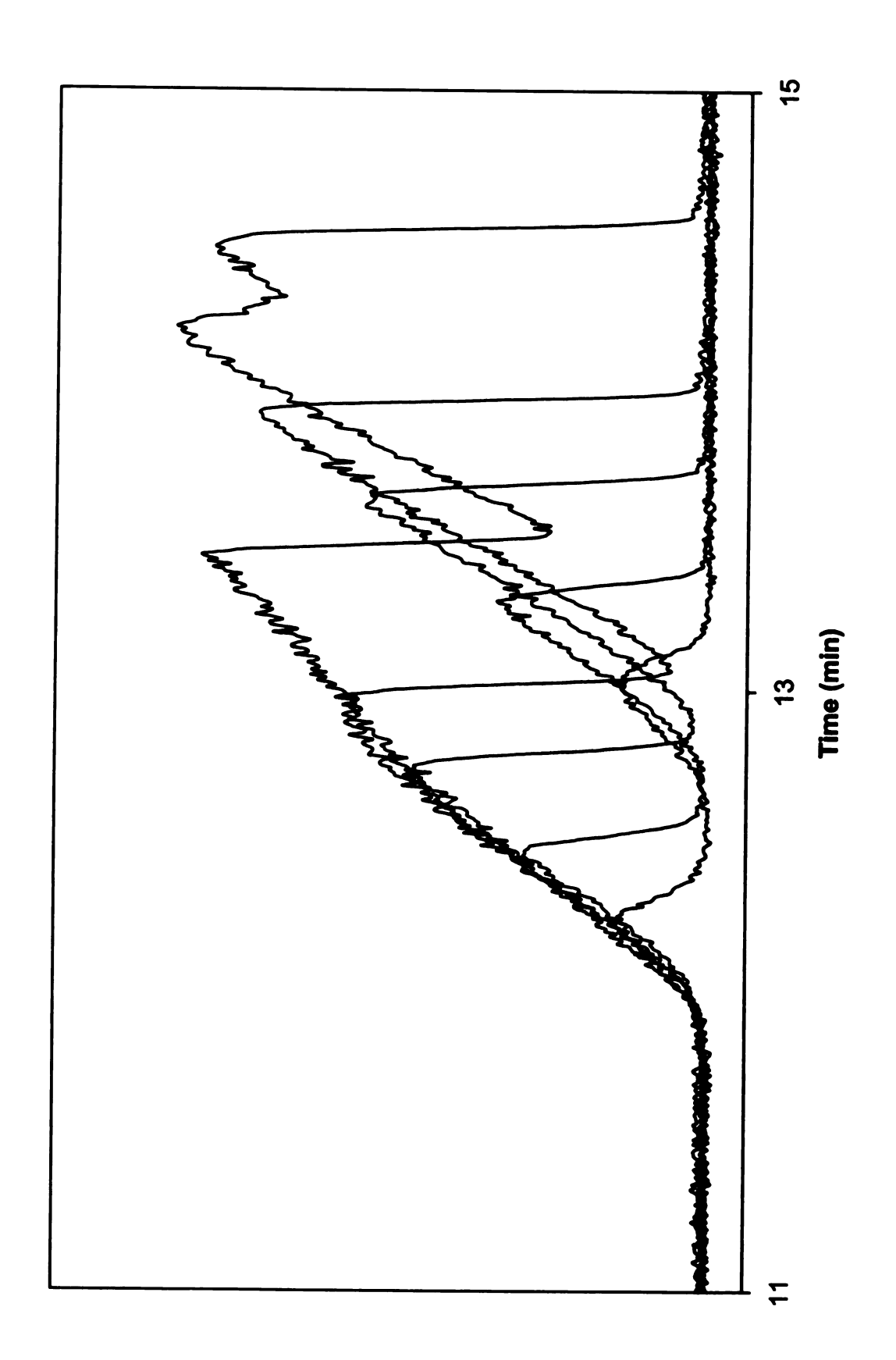


Figure 4.6 Warfarin peak shape in the presence of triethylamine. Column: β -cyclodextrin. Mobile phase composition: acetonitrile:methanol:amine (90%:10%:0.05%). Warfarin concentration from highest to lowest: $8x10^{-4}$ M; $4x10^{-4}$ M; $2x10^{-4}$ M; $1x10^{-4}$ M; $5x10^{-5}$ M.



the fronting shape. In contrast, acetic acid (pK_a = 4.76) can effectively compete and replace warfarin and methanol from similar sites on cyclodextrin. In this manner, the linear range of the isotherm is increased and the fast acid-base kinetics improve the peak shape.

4.3.4. Four-Component Mobile Phase

When all four components are present in the mobile phase, the peak shapes are within the linear isotherm range to provide reasonable thermodynamic and kinetic information. Thus, as the concentration of each mobile phase component is changed, a detailed examination of its individual effect on the thermodynamic and kinetic behavior of the coumarin-based solutes is possible. The mobile phase composition of acetonitrile:methanol:acid:amine (99%:1%:0.15%:0.10%) is chosen as the reference composition, from which all variations are measured. Methanol is varied at 0%, 1%, 3%, and 5%; acetic acid is varied at 0.05%, 0.10%, 0.15%, 0.20%, and 0.30%; triethylamine is varied at 0.05%, 0.10%, 0.15%, and 0.20%.

4.3.4.1. Comparison of Solutes

At the reference mobile phase composition, the retention factor, chiral selectivity, and rate constants are reported in Table 4.3. The trend in retention factor has a close relationship with the solute structure in Figure 4.1. As generally believed, retention in the polar-organic mode with the β -cyclodextrin CSP is mainly due to hydrogen bonding. The achiral compound, 4-hydroxycoumarin, has the largest retention factor due to its strong intermolecular hydrogen bonding with the stationary phase. The interactions of two sites, the

Comparison of thermodynamic and kinetic behaviors of solutes at reference mobile phase composition^a Table 4.3

O optide	Retention Factor	n Factor	Chiral	Desorption R	Desorption Rate Constant	Adsorption R	Adsorption Rate Constant
	ጁ	Ŕ	Selectivity	k _{ms1} (s ⁻¹)	k _{ms2} (s ⁻¹)	k _{sm1} (s ⁻¹)	k _{sm2} (s ⁻¹)
Warfarin	1.06	1.39	1.31	23	30	25	42
Coumachlor	1.11	1.41	1.26	20	24	22	8
Coumafuryl	0.82	0.98	1.19	33	46	27	45
Coumatetralyl	2.87	3.05	1.06	7	11	20	33
4-Hydroxy- coumarin	3.52	γ/N	V	0.5	N/A	1.7	Y/N

Mobile phase composition, acetonitrile:methanol:acetic acid:amine (99%:1%:0.15%:0.10%)

Not available

۵

hydroxyl and carboxyl groups of 4-hydroxycoumarin, contribute predominantly to the retention. The relatively planar structure of 4-hydroxycoumarin facilitates the simultaneous interaction of both sites with the hydroxyl groups on the rim of All of the chiral solutes have smaller retention than 4cvclodextrin. hydroxycoumarin because of the bulky groups inserted between the hydroxyl and carboxyl groups, which block their simultaneous interaction. warfarin, and coumachlor have a similar structure but differ slightly in one substituent on the chiral carbon. For coumafuryl, the oxygen of the furan ring has the ability to hydrogen bond with the hydroxyl group. Due to this intramolecular hydrogen bonding, the intermolecular hydrogen bonding of the hydroxyl group with the stationary phase is decreased. Thus, coumafuryl has the smallest retention factor. By replacement of the furan ring with a benzene ring, warfarin and coumachlor do not have the same intramolecular hydrogen bonding as coumafuryl. Thus, they have slightly larger, but similar retention factors due to their similar structures. Coumatetralyl has a much larger retention factor than the other three chiral solutes. The hydroxyl group can also form intramolecular hydrogen bonds with the carbonyl group, which is present in coumafuryl, warfarin, and coumachlor, but not present in coumatetralyl. Thus, coumatetralyl has the least intramolecular hydrogen bonding and, hence, the largest intermolecular hydrogen bonding with the stationary phase. Moreover, the substituent group of coumatetralyl is relatively nonpolar, which enhances its interaction with the nonpolar cyclodextrin cavity. All of these effects contribute to its largest retention factor among the chiral compounds.

Chiral selectivity, also summarized in Table 4.3, can help to explain the difference between the two enantiomers and their interactions with the cyclodextrin CSP. Under all conditions, warfarin has the largest chiral selectivity. around 1.30. Courachlor has a slightly smaller chiral selectivity, around 1.25. due to the chlorine group on the benzene ring. The aromatic substituents of warfarin and coumachlor have the ability to draw the molecule to hydrogen bond closer to the chiral center by interacting with the cyclodextrin cavity. In fact, the chlorine group on coumachlor further enhances this process and weakens the much stronger hydrogen bonding interaction of the carboxyl group in the cyclic ester. The presence of chlorine enhances retention, but not the chirally selective interaction of hydrogen bonding. Thus, the chiral selectivity of coumachlor is actually less than that of warfarin. Coumafuryl has a chiral selectivity around 1.20. Again, this is related to the smaller chirally selective interaction of hydrogen bonding, as discussed above. Coumatetralyl has the least selectivity among all the chiral molecules at around 1.05. This is related to the different structure of coumatetralyl. Its chiral carbon is within a ring structure, which restricts motion and makes it more difficult to discriminate between the two enantiomers. Also, the substituents on the chiral carbon do not have hydrogenbonding ability. These substituents are relatively nonpolar, and have a better chance to interact with the cavity of cyclodextrin. In other words, the groups with stronger inclusion effects contribute more greatly to retention, but are not chirally selective.

The kinetic rate constants also have a direct relationship with the solute structure. The rate constants for 4-hydroxycoumarin are one to two orders-ofmagnitude smaller than those of the chiral molecules, as shown in Table 4.3. Because of the two strong and simultaneous hydrogen bonding sites, the adsorption and desorption processes for 4-hydroxycoumarin on the cyclodextrin surface are extremely slow. For the chiral solutes, the restricted accessibility of the hydrogen bonding sites also influences their rates of mass transfer. In general, the longer the solutes are retained, the smaller are their rate constants. However, within each chiral pair, the second enantiomer has a higher rate of mass transfer than the first enantiomer, even though it is more retained. This behavior suggests that the chiral and achiral selective sites have different kinetic contributions, with the chiral sites having surprisingly higher mass transfer rates. Warfarin, coumachlor, coumatetralyl, and 4-hydroxycoumarin all have a higher adsorption rate (k_{em}) than desorption rate (k_{me}). Hence, the limiting mass transfer process is from stationary to mobile phase for these solutes. However, for coumafuryl, the limiting mass transfer process is from mobile to stationary phase.

4.3.4.2. Effect of Methanol

The effect of methanol on thermodynamics is shown in Table 4.4. As mentioned previously, methanol is able to hydrogen bond with the β -cyclodextrin CSP. Thus, as the concentration of methanol is increased from 0% to 5%, the retention factor of all solutes is decreased. The decrease in retention factor for all chiral compounds is similar at 44% to 48%. However, the decrease in retention factor for 4-hydroxycoumarin is the largest at 55%, which suggests that

Table 4.4 Effect of methanol concentration on thermodynamics^a

%	_	Warfarin	_		Coumachlor	ъ	Ŏ	Coumafuryl	<u> </u>	<u> </u>	Coumatetralyl	Jýle I	4-Hydroxy- coumarin	
Methanol	<u>δ</u>	δ _o	م	<u> 7</u>	৵	ಶ	گ	8	ಶ	k ₁	۲۶	¤	*	
%0	1.27	1.66	1.31	1.26	1.59	1.26	0.98	1.15	1.18	3.30	3.53	1.07	4.49	
1%	1.06	1.39	1.31	1.11	1.41	1.26	0.82	96.0	1.19	2.87	3.05	1.06	3.52	
3%	0.78	1.02	1.30	0.79	66.0	1.25	0.61	0.73	1.20	2.17	2.26	20.	2.59	
2%	0.68	0.87	1.28	0.71	0.87	1.23	0.54	0.64	1.20	1.85	1.88	1.02	2.02	
2	Other mehile phase composition	90040		ı		octic sciditiothylomine (0.45%:0.10%)) ocimol	0.45%.0	100%					

Other mobile phase composition, acetic acid:triethylamine (0.15%:0.10%)

k₁ and k₂ are retention factors for the first and second enantiomers

۵

 α is chiral selectivity

ပ

methanol is affecting 4-hydroxycoumarin more than the other compounds. This behavior also supports the previous discussion of the strong hydrogen bonding interaction between 4-hydroxycoumarin and the stationary phase. The effect of methanol concentration on chiral selectivity is relatively small. Warfarin, coumachlor, and coumatetrally show a slight decrease, but coumafuryl shows a slight enhancement. The effect of methanol on kinetics is shown in Table 4.5. As the concentration of methanol is increased, all the solutes show an increase in the desorption rate constant for transfer from stationary to mobile phase (k_{ma}). But the adsorption rate constant for transfer from mobile to stationary phase is relatively constant. In other words, because methanol acts as a displacing agent, it influences the desorption rate rather than the adsorption rate.

4.3.4.3. Effect of Triethylamine

Tables 4.6 and 4.7 demonstrate the effect of triethylamine on thermodynamics and kinetics when the acetic acid concentration is held constant at 0.15%. As the concentration of triethylamine is increased from 0.05% to 0.20%, the retention factor of all solutes is decreased. However, chiral selectivities are simultaneously increased for warfarin, coumachlor, and coumatetralyl. As noted above, it is most likely that triethylamine is interacting with the acidic hydroxyl group of the solute molecules. As these interactions do not directly involve the chiral center, they are probably decreasing the achiral interactions such that the chiral selectivities are actually enhanced. As the concentration of triethylamine is increased, the rate constants for mass transfer (k_{ms} and k_{sm}) are increased as well. This indicates that triethylamine increases

Table 4.5 Effect of methanol concentration on kinetics^a

							:										4	
8		War	Warfarin			Coumachlor	achlor			Coumafuryl	afuryi		S	Coumatetralyl	etraly	_	Hydroxy-	-xxo
% Methanol												,					coumarin	arin
	Kms1 ^b	Kms2 ^b	Kemato	K _{sm2} c	Kanst 1	Kms2	K a	k _{sm2}	Kans 1	Kms2	Kem1 Ksm2		Kms1	k _{ms2}	K _{sm1}	K _{sm2}	K _{ms1}	K _{sm1}
	(s ⁻¹)	(s-1)	(s ⁻¹) (s ⁻¹) (s ⁻¹)	(s ⁻¹)	(s ⁻¹)	(s ⁻¹)	(s ⁻¹)	(s ⁻¹)	(s ⁻¹)	(s ⁻¹)	(s ⁻¹)	(s ⁻¹)	(s ⁻¹)	(s ⁻¹)	(s ⁻¹)	(s ⁻¹)	(s^{-1})	(s ⁻¹)
%0	19	23	24	38	17	21	21	33	8	8	33	39	7	=	22	39	0.4	8.
1%	23	99	25	42	20	24	22	श्र	33	46	27	45	7	+	20	33	0.5	1.7
3%	90	42	23	42	23	33	18	32	61	62	37	46	œ	41	17	32	6.0	2.3
2%	33	47	22	41	28	36	20	31	73	95	39	36	N/A°	¥ ¥	A N	¥ W	1.2	2.4
8	Other mobile phase composition	eda elic		Citio		Ocetic acid-triothylamina () 45% () 40%				15%:0	10%							

Other mobile phase composition, acetic acid:triemyramine (0.15%:0.10%)

kms1 and kms2 are desorption mass transfer rate constants from stationary to mobile phase for the first and second

enantiomers

Kem1 and Km2 are adsorption mass transfer rate constants from mobile to stationary phase for the first and second

enantiomers

not available

Effect of triethylamine (TEA) concentration on thermodynamics^a Table 4.6

% <u>п</u>	_	Warfarin		Š	oumachlor	ō	Ŏ	Coumafuryl	-	Š	Coumatetralyl	Ķ	4-Hydroxy- coumarin
<u> </u>	K ₁ b	k ₂ b	ၓ	۲۶	\$	ಶ	κι	8	ಶ	k,	끃	ಶ	¥
0.05%	1.26	1.62	1.28	1.40	1.74	1.24	1.09	1.30	1.20	3.77	3.92	40.1	4.41
0.10%	1.06	1.39	1.31	1.11	1.41	1.26	0.82	0.98	1.19	2.87	3.05	1.06	3.52
0.15%	0.95	1.26	1.34	0.95	1.21	1.28	0.71	0.84	1.19	2.51	2.68	1.07	2.79
0.20%	0.81	1.09	1.35	08.0	1.03	1.29	0.58	0.68	1.18	2.17	2.33	1.07	2.43
	Other m	Ariolo phe	Other mobile phase composition	Poeition	Softoni	trile-met	i Podet	acetonitrile.methanol.acetic acid (00%.1%.0 15%)	1 /00%	10.01	K		

Other mobile phase composition, acetonitrile:methanol:acetic acid (99%:1%:0.15%)

k₁ and k₂ are retention factors for the first and second enantiomers

 α is chiral selectivity

Table 4.7 Effect of triethylamine (TEA) concentration on kinetics^a

																	4	
		War	Warfarin			Coumachlor	achlor		-	Coumafuryl	afuryl		O	Coumatetralyl	tetraly		Hydroxy-	oxy-
% TEA																	coumarin	arin
	Kasto	K _{m82} 0	Kem1 Kem2	K _{sm2} c	Kms1	K _{ms2}	Kem1 Kem2	K _{sm2}	Kms1	K _{ms2}	Kem1 Ksm2	K _{sm2}	Kms1	Kms2 Ksm1 Ksm2	Ksm1	K _{sm2}	K _{ms1}	K _{sm1}
	(s ⁻¹)	(s ⁻¹)	(s ⁻¹)	(s ⁻¹) (s ⁻¹)	(s^{-1})	(s ⁻¹)	(s ⁻¹)	(s ⁻¹)	(s ⁻¹)	(s ⁻¹)	(s ⁻¹)	(s ⁻¹)	(s ⁻¹)	(s ⁻¹)	(s ⁻¹)	(s-1)	(s ⁻¹)	(s ⁻¹)
0.05%	13	19	16	31	5	4	4	24	23	32	25	42	က	9	12	24	0.4	1.5
0.10%	23	30	25	42	20	24	22	क्ष	33	46	27	45	7	=	20	33	0.5	1.7
0.15%	36	43	8	22	98	88	53	46	39	65	28	22	9	13	25	35	0.7	6.1
0.20%	37	28	90	63	88	37	34	88	55	114	32	78	18	30	39	20	0.9	2.2
	therm	Other mobile phase composition	7986	Januari Tanana	1 .	acetonitrile:methanol:acetic acid (99%:1%:0 15%)	ile.me		l'acetic	, priod	,- %00,	18.01	5%)					

Other mobile phase composition, acetonitrile:methanol:acetic acid (99%:1%:0.15%)

kms1 and kms2 are desorption mass transfer rate constants from stationary to mobile phase for the first and second enantiomers

kems and kma2 are adsorption mass transfer rate constants from mobile to stationary phase for the first and second enantiomers

both adsorption and desorption rates for all solutes, but the desorption rate increases faster.

4.3.4.4. Effect of Acetic Acid

Tables 4.8 and 4.9 demonstrate the effect of acetic acid on thermodynamics and kinetics when the amine concentration is held constant at 0.10%. As the concentration of acetic acid is increased from 0.05% to 0.20%, the retention factor of all chiral solutes increases. However, a further increase from 0.20% to 0.30% actually decreases the retention factor for warfarin, coumachlor, and coumatetralyl. Coumafuryl shows a continual increase over the concentration range. On the contrary, 4-hydroxycoumarin shows a continual decrease with an increase in acid concentration. While the acid serves as a displacing agent for 4-hydroxycoumarin, it may have a different effect for the chiral solutes. It is noteworthy that the chiral selectivity decreases for the chiral solutes, which suggests that acetic acid may be interacting with chiral selective sites of the stationary phase. The rate constants for mass transfer (k_{ms} and k_{em}) decrease for the chiral solutes, but are relatively constant for the achiral solute, 4-hydroxycoumarin.

To understand this behavior more fully, a three-component mobile phase is examined to determine whether acetic acid acts in the same manner without the amine. Table 4.10 shows the effect of acetic acid on thermodynamics and kinetics of a single solute, warfarin, when no amine is present. The data in this table are used as a direct comparison to those in Tables 4.8 and 4.9. Interestingly, the trends in retention are completely opposite and suggest a

Effect of acetic acid concentration on thermodynamics when amine is present^a Table 4.8

Acetic	>	Warfarin		ర	Coumachlor	<u></u>	Ŏ	Coumafuryl	5	8	Coumatetralyl	lyle	4-Hydroxy-coumarin
Acid	4.	3%	త	<u>*</u>	\$	8	72	쪼	ಶ	조	য়	ಶ	*
0.05%	0.86	1.19	1.38	0.79	1.05	1.33	0.57	0.72	1.25	2.66	2.83	1.07	3.73
0.10%	1.00	1.35	1.35	0.98	1.27	1.29	0.73	0.87	1.20	2.81	2.99	1.07	3.56
0.15%	1.06	1.39	1.31	1.11	1.41	1.26	0.82	0.98	1.19	2.87	3.05	1.06	3.52
0.20%	1.08	1.40	1.29	1.15	4.	1.25	0.91	1.07	1.18	2.97	3.13	1.05	3.46
0.30%	0.97	1.23	1.26	1.13	1.38	1.22	9.94	1.10	1.17	2.97	3.09	2.5	3.44

Other mobile phase composition, acetonitrile:methanol:triethylamine (99%:1%:0.10%)

k₁ and k₂ are retention factors for the first and second enantiomers

α is chiral selectivity

Effect of acetic acid concentration on kinetics when amine is present^a Table 4.9

															i		4	
% A cotio		Warfarin	farin		.	Coumachlor	chlor	-	•	Coumafuryl	afuryl		O	Coumatetralyl	tetraly		Hydroxy-	oxy-
Acid Acid																	coumarin	arin
	Kms1 ^D	Km82	Kms2 Kem1 Ksm2	K _{sm2} ^c	Kms1	K _{ms2}	Kema	Kem2	Kms1	kms2	Kem 1	K _{sm2}	Kms1	K _{ms2}	Ksm1	K _{sm2}	Kms1	K _{sm1}
	(s ⁻¹)	(s ⁻¹) (s ⁻¹)	(s ⁻¹)	(s ⁻¹)	(s ⁻¹)	(s ⁻¹)	(s^{-1})	(s ⁻¹)										
0.05%	37	22	32	2	24	37	19	33	88	20	33	36	6	14	23	39	0.3	1.3
0.10%	25	35	25	47	21	52	24	32	8	27	22	23	œ	12	22	35	0.5	1.8
0.15%	23	30	25	42	20	24	22	8	33	46	27	45	7	1-	20	33	0.5	1.7
0.20%	21	27	23	38	16	21	19	30	37	53	8	22	7	9	19	31	0.5	1.7
0.30%	20	26	19	32	4	19	19	56	88	39	56	43	က	ω	15	26	0.5	1.7
]. -]:						┥,	7	7000		1				

Other mobile phase composition, acetonitrile:methanol:triethylamine (99%:1%:0.10%)

kms1 and kms2 are desorption mass transfer rate constants from stationary to mobile phase for the first and second enantiomers

kem1 and kms2 are adsorption mass transfer rate constants from mobile to stationary phase for the first and second enantiomers

Effect of acetic acid concentration on thermodynamics and kinetics of warfarin without amine present^a. **Table 4.10**

);;));;	٤.		·		Ť,	,	
	<u>ک</u>	, &	ິ ຮ	K _{ms1} (S')	K _{ms2} (S ')	K _{sm1} (S ')	K _{sm2} (S')
0.05%	2.60	2.96	1.137	2	9	13	16
0.10%	1.71	1.93	1.132	80	8	13	16
0.15%	1.20	1.36	1.128	11	13	13	17
0.20%	76.0	1.09	1.125	12	15	12	16
0.30%	0.75	0.84	1.118	19	25	14	21

Other mobile phase composition, acetonitrile:methanol (99%:1%)

k₁ and k₂ are retention factors for the first and second enantiomers

 α is chiral selectivity

ပ

kms1 and kms2 are desorption mass transfer rate constants from stationary to mobile phase for the first and second ס

enantiomers

Kem1 and Kms2 are adsorption mass transfer rate constants from mobile to stationary phase for the first and second

enantiomers

difference in mechanism. When the amine is absent, an increase in the acetic acid concentration alone decreases the retention factor of warfarin. Under these conditions, acetic acid probably behaves as a displacing agent for the acidic solute. When triethylamine is present in the mobile phase, the acetic acid tends to interact with the amine first to minimize the amine effect. That is why the retention factor of the chiral solutes increases initially for 0.05% to 0.20% acid in Table 4.8. But for acid concentration in range of 0.20% to 0.30%, where the amine has been completely consumed, the system behaves in the same manner as acid present alone and the retention factor decreases. The chiral selectivity exhibits the same trend and decreases regardless of whether triethylamine is present. This behavior indicates that acetic acid is interacting with the chirally selective sites of the stationary phase. Thus, as the retention factor is decreased, chiral selectivity is reduced as well. Although both acid and amine can affect retention, they are actually interacting with different positions of the stationary phase or with the solutes. The acid interacts with chiral selective sites, whereas the amine interacts with achiral selective sites. As to the kinetics, in the absence of amine, acetic acid serves only to increase the desorption mass transfer rates (k_{ms}) , but not the adsorption rates (k_{sm}) .

4.4 CONCLUSIONS

In this study, the effect of mobile phase composition on thermodynamics and kinetics of chiral separation is examined. Mobile phase composition affects the equilibration time, retention time, as well as peak shape. Both acid and amine modifier shorten the equilibration time greatly from weeks to one day or

less. Whereas the acetic acid modifier can increase the linear isotherm range and ensure a Gaussian peak shape, the triethylamine modifier can dramatically decrease the retention time while still enhancing chiral selectivity. In fourcomponent mobile phases, the elution order of all solutes is strongly dependent on the hydrogen bonding ability between the solutes and the stationary phase. The kinetic rate constants typically decrease with an increase in retention factor. For the chiral solutes, the second enantiomer has a surprisingly higher mass transfer rate than the first enantiomer although it is more retained. This behavior suggests a difference in the kinetic contributions for chiral and achiral selective sites. In a four-component mobile phase, methanol can hydrogen bond with the stationary phase, thus decreasing retention and increasing the kinetics for all solutes. Triethylamine decreases retention, but enhances chiral selectivity, but acetic acid increases retention and reduces chiral selectivity. Both acid and amine modifiers increase adsorption and desorption rate constants. When both acid and amine are present in the mobile phase, they tend to interact with each other and complicate the separation process.

4.5 REFERENCES

- [1] W.L. Hinze, T.E. Riehl, D.W. Armstrong, W. DeMond, A. Alak, T. Ward, Anal. Chem. 57 (1985) 237-242
- [2] H.Y. Aboul-Enein, M.R. Islam, S.A. Bakr, J. Liq. Chromatogr. 11 (1988) 1485-1493
- [3] D.W. Armstrong, G.L. Bertrand, K.D. Ward, T.J. Ward, H.V. Secor, J.I. Seeman, Anal. Chem. 62 (1990), 332-338
- [4] K. Fujimura, T. Ueda, T. Ando, Anal. Chem. 55 (1983) 446-450
- [5] K.G. Feitsma, J. Bosman, B.F.H. Drenth, R.A. De Zeeuw, J. Chromatogr. 333 (1985) 59-68
- [6] C.A. Chang, Q. Wu, D.W. Armstrong, J. Chromatogr. 354 (1986) 454-458
- [7] C.A. Chang, Q. Wu, M.P. Eastman, J. Chromatogr. 371 (1986), 269-282
- [8] J.I. Seeman, H.V. Secor, D.W. Armstrong, K.D. Timmons, T.J. Ward, Anal. Chem. 60 (1988) 2120-2127
- [9] P. Macaudiere, M. Caude, R. Rosset, A. Tambute, J. Chromatogr. 450 (1988) 255-269
- [10] I.Z. Atamna, G.M. Muschik, H.J. Issaq, J. Chromatogr. 499 (1990) 477-488
- [11] J.T. Andersson, G. Kaiser, Fresenius' Zeitschrift fuer Analytische Chemie 334 (1989) 749-751
- [12] S. Li, W.C. Purdy, J. Chromatogr. 543 (1991) 105-112
- [13] C.A. Chang, H. Ji, G. Lin, J. Chromatogr. (1990) 522 143-152
- [14] S. Piperaki, A. Perakis, M. Parissi-Poulou, J. Chromatogr. A 660 (1994) 339-350
- [15] R.J. Soukup, R.V. Rozhkov, R.C. Larock, D.W. Armstrong, Chromatographia 61 (2005) 219-224
- [16] X. Han, T. Yao, Y. Liu, R.C. Larock, D.W. Armstrong, J. Chromatogr. A 1063 (2005) 111-120
- [17] D.W. Armstrong, S. Chen, C. Chang, S. Chang, J. Liq. Chromatogr. 15 (1992), 545-556

- [18] S.C. Chang, G.L. Reid, S. Chen, C.D. Chang, D.W. Armstrong, TrAC, Trends Anal. Chem. 12 (1993) 144-153
- [19] C. Pham-Huy, B. Radenen, A. Sahui-Gnassi, J. Claude, J. Chromatogr. B, 665 (1995) 125-132
- [20] J. Zukowski, M. Pawlowska, M. Nagatkina, D.W. Armstrong, J. Chromatogr. 629 (1993) 169-179
- [21] E. Lipka, V. Glacon, G. Mackenzie, D. Ewing, C. Len, D. Postel, M. Vaccher, J. Bonte, C. Vaccher, Anal. Lett. 37 (2004) 385-398
- [22] M.W. Matchett, S.K. Branch, T.M. Jefferies, Chirality 8 (1996) 126-130
- [23] S. Chen, T. Ward, Chirality 16 (2004) 318-330
- [24] R.W. Stringham, K.G. Lynam, B.S. Lord, Chirality 16 (2004) 493-498
- [25] Y.K. Ye, B. Lord, R.W. Stringham, J. Chromatogr. A 945 (2002) 139-146
- [26] S.E. Hygnstrom, D.R. Virchow, Controlling rats, Ed. Wildlife Management University of Nebraska-Lincoln, 2001

CHAPTER 5

EFFECT OF TEMPERATURE AND PRESSURE TO CHIRAL SEPARATIONS WITH β-CYCLODEXTRIN STATIONARY PHASE

5.1. INTRODUCTION

As demonstrated in Chapter 4, the effect of mobile phase composition is important to the thermodynamics and kinetics of chiral separation. In this chapter, temperature and pressure effects are illustrated to quantitate more detailed thermodynamic and kinetic information.

In previous research, temperature studies are utilized most for thermodynamic characterization. However, most of the investigations were in reversed-phase mode [1,2]. Cabrera et al. [3] reported the different temperature effects on chiral selectivity on two pharmaceuticals, oxazapam and prominal. Morin et al. [4] reported van't Hoff plots at different mobile phase compositions. A change in the retention mechanism was accompanied by a change in pH value. Pressure effects are also utilized for thermodynamic characterization. Most investigations have been carried out by the Evans group with positional isomers [5] and a few barbiturate chiral compounds [6-8]. Compared to the thermodynamic characterizations, kinetic characterizations on β-cyclodextrin stationary phase are limited.

Thus, the goal here is to conduct a systematic investigation on chiral separation, to observe temperature and pressure effects on both thermodynamic and kinetic behavior, to report specific thermodynamic and kinetic parameters, and to elucidate chiral separation mechanisms.

5.2 EXPERIMENTAL METHODS

5.2.1 Chemicals

As depicted in Figure 4.1, five coumarin-related solutes are chosen as model compounds: warfarin, coumachlor, coumafuryl, coumatetralyl and 4-hydroxycoumarin. The solutes are obtained from Sigma-Aldrich as solids and dissolved in high-purity acetonitrile (Burdick and Jackson, Baxter Healthcare) to yield standard solutions at 10⁻⁴ M. Nitromethane is used as non-retained marker and is added to each solution at a concentration at 15% (v/v). High purity acetonitrile, methanol (Burdick and Jackson, Baxter Healthcare), acetic acid (Sigma-Aldrich), and triethylamine (Sigma-Aldrich) are used for mobile phase preparation.

5.2.2 Experimental System

The solutes are separated on a capillary liquid chromatography system as illustrated in Figure 3.2. The silica packing (Cyclobond I 2000, Astec) is characterized by a 5.2-μm particle size, 0.89-mL/g pore volume, and 305-m²/g surface area, reacted with β-cyclodextrin at a bonding density of 0.39 μmol/m². The temperatures for these experiments are 273, 278, 283, 288 and 293 K. The inlet pressures for these experiments are 1200, 1800, 2400, 3000 and 3600 psi. These values correspond to the average pressure of 700, 1300, 1900 and 3100 psi. The data are analyzed by exponentially modified Gaussian (EMG) function, as described in Chapters 1.4.3.2.2. and 2.3.3.

5.3 RESULTS AND DISCUSSION

In Chapter 4, the mobile phase effect on chiral separation with β-cyclodextrin stationary phase has been carefully investigated. A standard mobile phase composition is chosen at 99:1:0.15:0.1 (acetontrile:methanol:acetic acid:triethylamine). In this chapter, all of the investigations are carried out in this standard mobile phase composition.

5.3.1 Thermodynamic Behavior

5.3.1.1 Retention Factor

Retention factors for all compounds are reported in Table 5.1. The retention follows the same general order as in Chapter 4 for coumafuryl, warfarin, coumachlor, coumatetralyl, and 4-hydroxycoumarin. Their retention orders are greatly affected by their hydrogen-bonding abilities. Coumafuryl has the greatest intra-molecular hydrogen bonding, thus the least inter-molecular hydrogen bonding between solute and stationary phase. Warfarin and coumachlor have similar retention factors, smaller intra-molecular hydrogen bonding, and slightly larger inter-molecular hydrogen bonding. Coumatetralyl has even less intra-hydrogen bonding ability. Finally, 4-hydroxycoumaim has the largest inter-molecular hydrogen bonding because of the free hydroxyl group, free carboxyl group, and its relatively planar structure.

The effects of temperature and pressure on retention are demonstrated in Table 5.1. Retention factors for all the solutes decrease dramatically with an increase in temperature. With an increase in pressure, the retention factors

Table 5.1: Retention factors for the coumarin-based solutes.

Solute	283	3 K ^a	303	3 Kª	700	psi ^b	3100) psi ^b
Colute	k₁ ^c	k ₂ ^c	k ₁	k ₂	k ₁	k ₂	k ₁	k ₂
Coumafuryl	0.85	1.00	0.59	0.68	0.72	0.84	0.66	0.76
Warfarin	1.07	1.42	0.76	0.96	0.92	1.19	0.85	1.09
Coumachlor	1.07	1.35	0.70	0.86	0.89	1.11	0.80	1.01
Coumatetralyl	3.20	3.39	2.11	2.18	2.60	2.73	2.44	2.55
4-Hydroxy- coumarin	4.89	N/A ^d	4.15	N/A	4.59	N/A	4.29	N/A

^a Retention factor (k) calculated at P = 1300 psi

b Retention factor calculated at T = 293 K

 $^{^{\}text{c}}$ $\,$ $\,$ k_1 and k_2 are retention factors for the first and second enantiomers

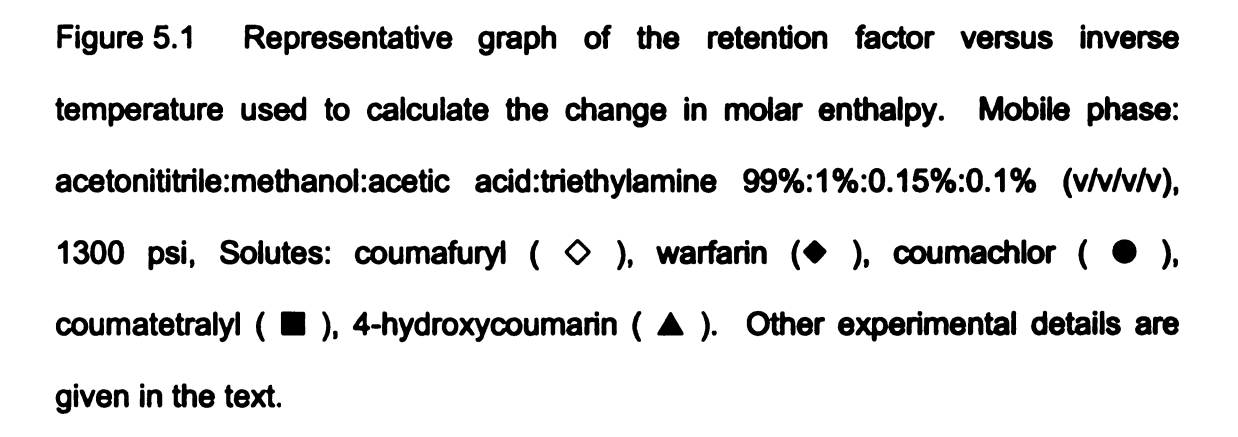
^d Not available

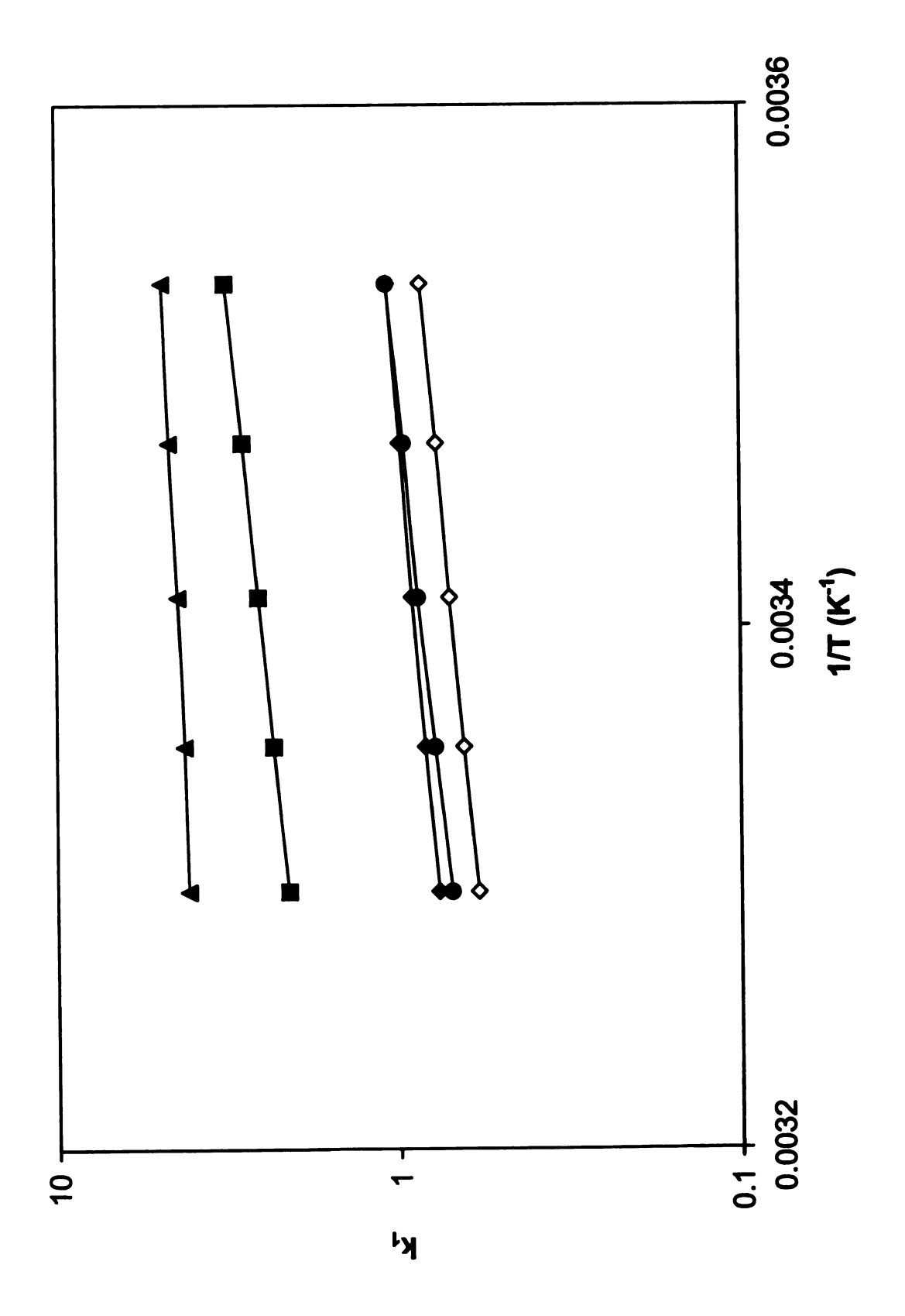
decrease as well. The detailed reasons for these phenomena are discussed below.

5.3.1.2 Molar Enthalpy

A representative graph of the logarithm of the retention factor versus the inverse temperature (van't Hoff plot) is shown in Figure 5.1. The graph for each solute is linear ($R^2 = 0.993 - 0.999$) with a positive slope. A linear graph indicates that the change in molar enthalpy is constant, which suggests that there is no significant change in retention mechanism and no phase transition over the temperature range of 283 - 303 K. A positive slope is indicative of a negative change in molar enthalpy, which suggests that the transfer from mobile to stationary phase is an enthalpically favorable process. The change in molar enthalpy is calculated from the slope of this graph according to Equation 1.6 and is reported in Table 5.2. The standard deviation is coming from linear regression.

Although 4-hydroxycoumarin is the most retained solute among the coumarin series, it has the least negative change in molar enthalpy. In other words, the energy between the solutes and stationary phase is the smallest. If the van't Hoff plots were extrapolated to calculate the intercepts, 4-hydroxycoumarin has the largest intercept. A large intercept usually implies that the change in molar entropy for 4-hydroxycoumarin is larger or, alternatively, that the phase ratio 4-hydroxycoumarin experienced by is smaller. 4-Hydroxycoumarin has multiple positions for inter-molecular hydrogen bonding with cyclodextrin. Every hydrogen bonding process will displace solvent molecules from the cyclodextrin and introduce a change in molar entropy. Thus,





the more interaction sites, the more solvent molecules are displaced, and the higher the change in molar entropy. In addition, the smaller size and the relatively planar structure of 4-hydroxycoumarin facilitate its binding with cyclodextrin with more possible configurations, which could potentially increase the change in molar entropy as well. The phase ratio 4-hydroxycoumarin experienced by might be different from that of the other chiral molecules, depending on the adsorption sites. For example, if 4-hydroxycoumarin can access unreacted silanol sites on the silica surface due to its small size, whereas others cannot, then the phase ratio for 4-hydroxycoumarin is different.

When the changes in molar enthalpy are compared between the two enantiomers, the second enatiomer always has a more negative change in molar enthalpy than that of the first enantiomer. This difference indicated that the second enantiomer is more enthalpically favorable in the transfer from mobile to stationary phase.

When the changes in molar enthalpy are compared among all chiral solutes in Table 5.2, no apparent trend can be found. In the reversed-phase separation with octadecylsilica stationary phase, the change in molar enthalpy is usually more negative as the retention factor increases. However, this trend is not observed for cyclodextrin column with our series of compounds. This behavior suggests that the change in molar entropy is an important parameter for retention, and the trend of the change in molar entropy is not consistent with the trend of retention. When we take a close look at warfarin and coumachlor, they have similar structures and similar retention at ambient temperature, but their

Table 5.2 Changes in molar enthalpy and molar volume for coumarin-based solutes

Solute	ΔH ₁ ^a (kcal/mol)	ΔH₂ ^a (kcal/mol)	ΔV ₁ ^b (cm³/mol)	ΔV ₂ ^b (cm ³ /mol)
Coumafuryl	-3.21 ± 0.04	-3.33 ± 0.03	13.8 ± 0.5	15 ± 1
Warfarin	-2.91 ± 0.07	-3.28 ± 0.07	14 ± 1	13 ± 1
Coumachlor	-3.65 ± 0.09	-3.8 ± 0.1	16 ± 2	15 ± 2
Coumatetralyl	-3.54 ± 0.02	-3.78 ± 0.02	11 ± 1	11 ± 1
4- Hydroxycoumarin	-1.5 ± 0.1	N/A ^c	18 ± 2	N/A

^a Molar enthalpy (ΔH) for the first and second enantiomer calculated at P = 1300 psi

b Molar volume (ΔV) for the first and second enantiomer calculated at T = 293 K

^c Not available

changes in molar enthalpy are surprisingly different from each other. Coumachlor has a more negative molar enthalpy than warfarin. Although both compounds have a similar response to mobile phase composition, their differences in the change of molar enthalpy enable their separation with the change of temperature. At lower temperature, warfarin will elute before coumachlor, while at higher temperature, the elution order will be reversed.

5.3.1.3 Molar Volume

A representative graph of the logarithm of the retention factor versus pressure is shown in Figure 5.2. The graph for each solute is linear ($R^2 = 0.98 - 0.99$) with a negative slope. A negative slope is indicative of a positive change in molar volume, which suggests that the solute occupies more volume in the stationary phase than in the mobile phase. The change in molar volume is calculated from the slope of this graph according to Equation 1.9, and reported in Table 5.2. The standard deviation is coming from linear regression.

In reversed-phase separations with cyclodextrin stationary phase, the solute will be included into the cyclodextrin cavity, where a negative change in molar volume is usually observed. In the polar-organic mode as described here, the change in molar volume is positive, which is a clear sign that no inclusion occurs. The change in molar volume is the smallest for coumatetralyl, larger and statistically similar for warfarin, coumachlor and coumafuryl, and largest for 4-hydroxycoumarin. Coumatetralyl has the most rigid structure, which might partly explain its smallest change in molar volume in the coumarin series. When the changes in molar volume are compared for the two enantiomers, they are

Figure 5.2 Representative graph of the retention factor versus pressure used to calculate the change in molar volume. Mobile phase: acetonititrile:methanol:acetic acid:triethylamine 99%:1%:0.15%:0.1% (v/v/v/v), 293 K, Solutes: coumafuryl (♦), warfarin (♦), coumachlor (●), coumatetralyl (■), 4-hydroxycoumarin (▲). Other experimental details are given in the text.

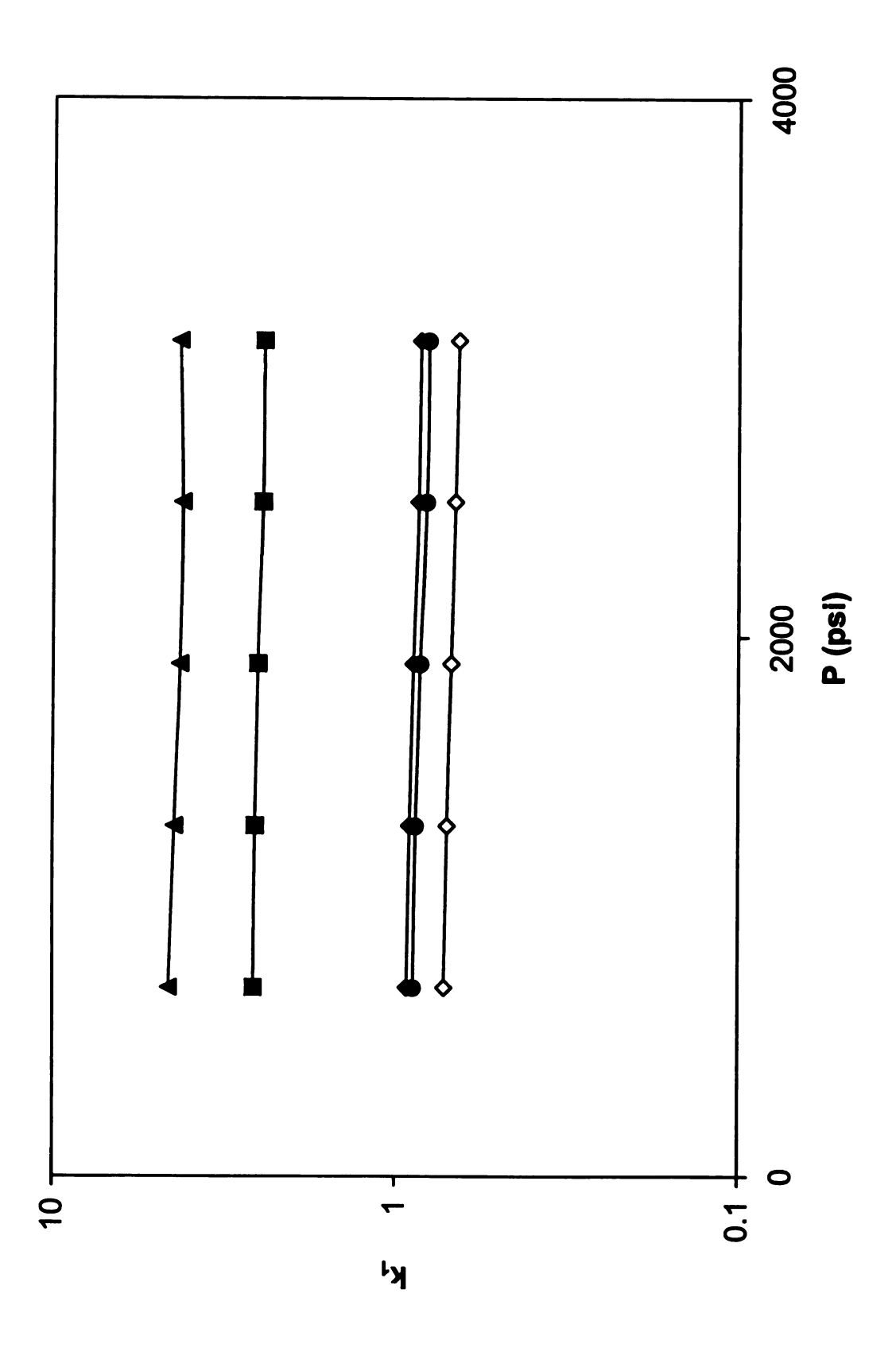
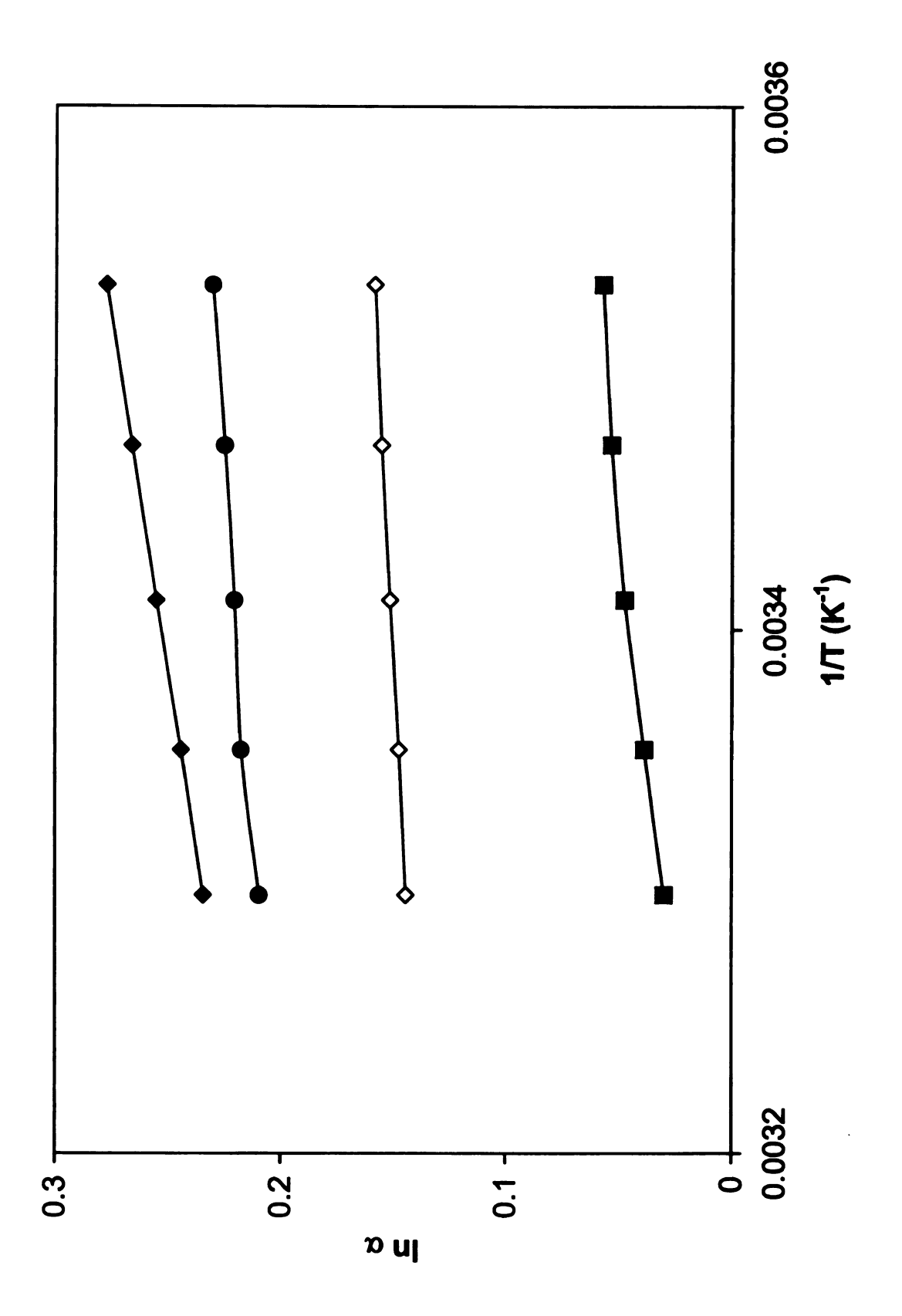


Figure 5.3. Representative graph of the chiral selectivity versus inverse temperature used to calculate the chiral difference in molar enthalpy and molar entropy. Mobile phase: acetonititrile:methanol:acetic acid:triethylamine 99%:1%:0.15%:0.1% (v/v/v/v), 1300 psi, Solutes: coumafuryl (♦), warfarin (♦), coumachlor (●), coumatetralyl (■). Other experimental details are given in the text.



statistically similar. This indicates that pressure will have a similar effect on both enantiomers, and chiral selectivity will not be significantly affected by pressure.

5.3.1.4 Chiral Difference in Molar Enthalpy and Molar Entropy

A representative graph of the logarithm of the chiral selectivity versus the inverse temperature is shown in Figure 5.3. The graph for each chiral solute is linear ($R^2 = 0.982 - 0.997$) with a positive slope. Positive slope is indicative of a negative differential change in molar enthalpy for the enantiomer.

The differential change in molar enthalpy and molar entropy are calculated from Equation 1.7, and are reported in Table 5.3. The standard deviation is coming from linear regression. Because the mobile phase is an achiral environment, the two enantiomers will have the same molar enthalpy and molar entropy in the mobile phase. Thus, the differential change in molar enthalpy is solely concerned with the chiral interactions with the stationary phase. The difference in molar enthalpy is negative, which indicates that the second enantiomer is enthalpically more favorable in the stationary phase. The difference is molar entropy is also negative, which indicates that the first enantiomer is actually entropically more favorable in the stationary phase. This is the first indication that the chiral separation of the coumarin-based solutes is an enthalpy-controlled process.

5.3.1.5 Enthalpy-Entropy Compensation

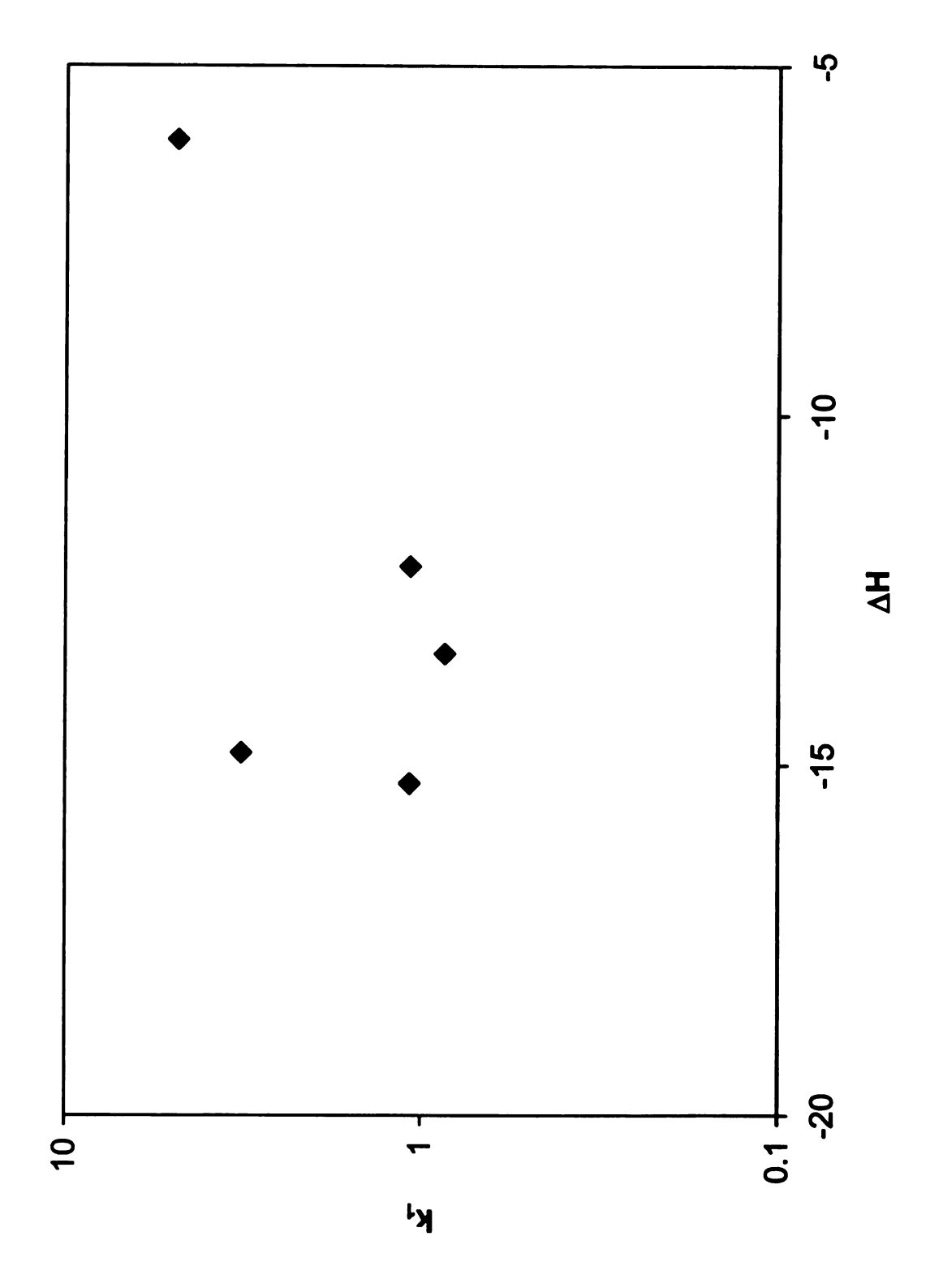
A graph of the natural logarithm of retention factor versus the change in molar enthalpy is shown in Figure 5.4. Each point represents one of the coumarin-based solute. The scattering of these points clearly shows that no

Table 5.3 Differential changes in molar enthalpy and molar entropy for the chiral coumarin-based solutes

Solute	ΔΔH ^a (kcal/mol)	ΔΔS ^a (cal/mol K)
Coumafuryl	- 0.122 ± 0.005	- 0.12 ± 0.02
Warfarin	- 0.369 ± 0.002	- 0.751 ± 0.005
Coumachlor	- 0.17 ± 0.02	- 0.14 ± 0.05
Coumatetralyl	- 0.23 ± 0.02	- 0.71 ± 0.08

^a Chiral differences in molar enthalpy ($\Delta\Delta H$) and molar entropy ($\Delta\Delta S$) calculated at P = 1300 psi

Figure 5.4 Representative graph of the retention factor versus change in molar enthalpy used to observe enthalpy-entropy compensation. Mobile phase: acetonititrile:methanol:acetic acid:triethylamine 99%:1%:0.15%:0.1% (v/v/v/v), 1300 psi



enthalpy-entropy compensation is achieved. Different retention mechanisms are, thus, responsible for the retention of the individual solutes.

The co-elution temperatures, T_{iso} , are also calculated from Equation 1.10 and reported in Table 5.4. The values are higher than ambient temperature, which suggests that the separation of all chiral solutes is an enthalpy-driven reaction. A different T_{iso} for all solutes is another sign that enthalpy-entropy compensation does not occur. But the T_{iso} values are similar for coumafuryl and coumachlor, and for warfarin and coumatetralyl. This suggests that the retention mechanism is similar for these pair of solutes. The T_{iso} values for coumafuryl and coumachlor are significantly greater than those for warfarin and coumatetralyl. For coumafuryl and coumachlor, $\Delta\Delta H$ mainly controls their chiral separation. But for warfarin and coumatetralyl, $\Delta\Delta S$ plays a more important role for their chiral separation.

5.3.2. Kinetic Behavior

While thermodynamics can elucidate the steady-state information and is concerned with the change between the initial (mobile phase) and final (stationary phase) states, it does not fully explain the retention mechanism. By considering a transition state, the pseudo-first-order rate constants, activation energies, and activation volumes can be calculated with the equations developed above. These values help to quantify the kinetic aspects of mass transfer between the mobile and stationary phases as a function of solute structure. These data provide information about the retention mechanism that would not be available from thermodynamic data alone.

Table 5.4 Co-elution temperature (T_{iso}) for the chiral coumarin-based solutes

Chiral Solute	T _{iso} (K)
Coumafuryl	1000 ± 170
Warfarin	491 ± 4
Coumachlor	1200 ± 460
Coumatetralyl	320 ± 46

5.3.2.1 Rate Constants

Representative kinetic rate constants, including the desorption rate constant k_{ms} and the adsorption rate constant k_{em}, are summarized in Table 5.5. As noted previously, 4-hydroxycoumarin has notably smaller kinetic rate constants than the other chiral molecules due to its small size and multiple positions for strong hydrogen bonding. When the chiral solutes are compared, the kinetic rate constants decrease as the retention factors increase. But for each chiral pair, the second eluted enantiomer always has a surprisingly higher mass transfer rate constant than the first enantiomer. This variation might be attributed to the different contribution from chiral selective sites and achiral selective sites. The kinetic rate constants generally show an increasing trend with an increase in temperature.

5.3.2.2 Activation Energy

A representative graph of the logarithm of the desorption rate constants versus the inverse temperature is illustrated in Figure 5.5. The standard deviation is coming from linear regression. The rate constant for 4-hydroxycoumarin is relatively constant with temperature, so it is not included in the graph. The graph for each chiral solute is linear, ($R^2 = 0.942 - 0.999$) with a negative slope, which indicates a positive change in activation energy. The activation energy is calculated from the slope of this graph according to Equation 1.15, and is shown in Table 5.6. The activation energy for the transfer from stationary phase to transition state (ΔE_{st}) is larger than that from mobile phase to the transition state (ΔE_{mt}). These data indicate that it is easier for the solutes to

Table 5.5. Kinetic rate constants for the coumarin-based solutes

		283	3 K ^a			303	3 Kª	
Solute	k _{ms1} d	k _{ms2} d	k _{sm1} e	k _{sm2} e	k _{me1}	k _{ms2}	K _{em1}	K _{em2}
	(s ⁻¹)							
Coumafuryl	13	12	11	12	33 b	39 ^b	23 ^b	32 ^b
Warfarin	8	8	8	11	18	26	13	25
Coumachlor	7	7	8	10	15°	30	12 ^b	26
Coumatetralyl	2	4	7	13	3	14	9°	31
4-Hydroxy- coumarin	0.05	N/A ^f	0.23	N/A	0.03	N/A	0.14	N/A

^a Kinetic rate constants calculated at P = 1300 psi

^b Kinetic rate constants calculated at T = 293 K

^c Kinetic rate constants calculated at T = 298 K

k_{ms1} and k_{ms2} are desorption mass transfer rate constants from stationary to mobile phase for the first and second enantiomers

 $^{^{\}rm e}$ $k_{\rm sm1}$ and $k_{\rm ms2}$ are adsorption mass transfer rate constants from mobile to stationary phase for the first and second enantiomers

f Not available

Figure 5.5 Representative graph of the kinetic rate constant k_{ms1} versus inverse temperature used to calculate the change in activation energy. Mobile phase: acetonititrile:methanol:acetic acid:triethylamine 99%:1%:0.15%:0.1% (v/v/v/v), 1300 psi, Solutes: coumafuryl (\diamondsuit), warfarin (\diamondsuit), coumachlor (\blacksquare), coumatetralyl (\blacksquare). Other experimental details are given in the text.

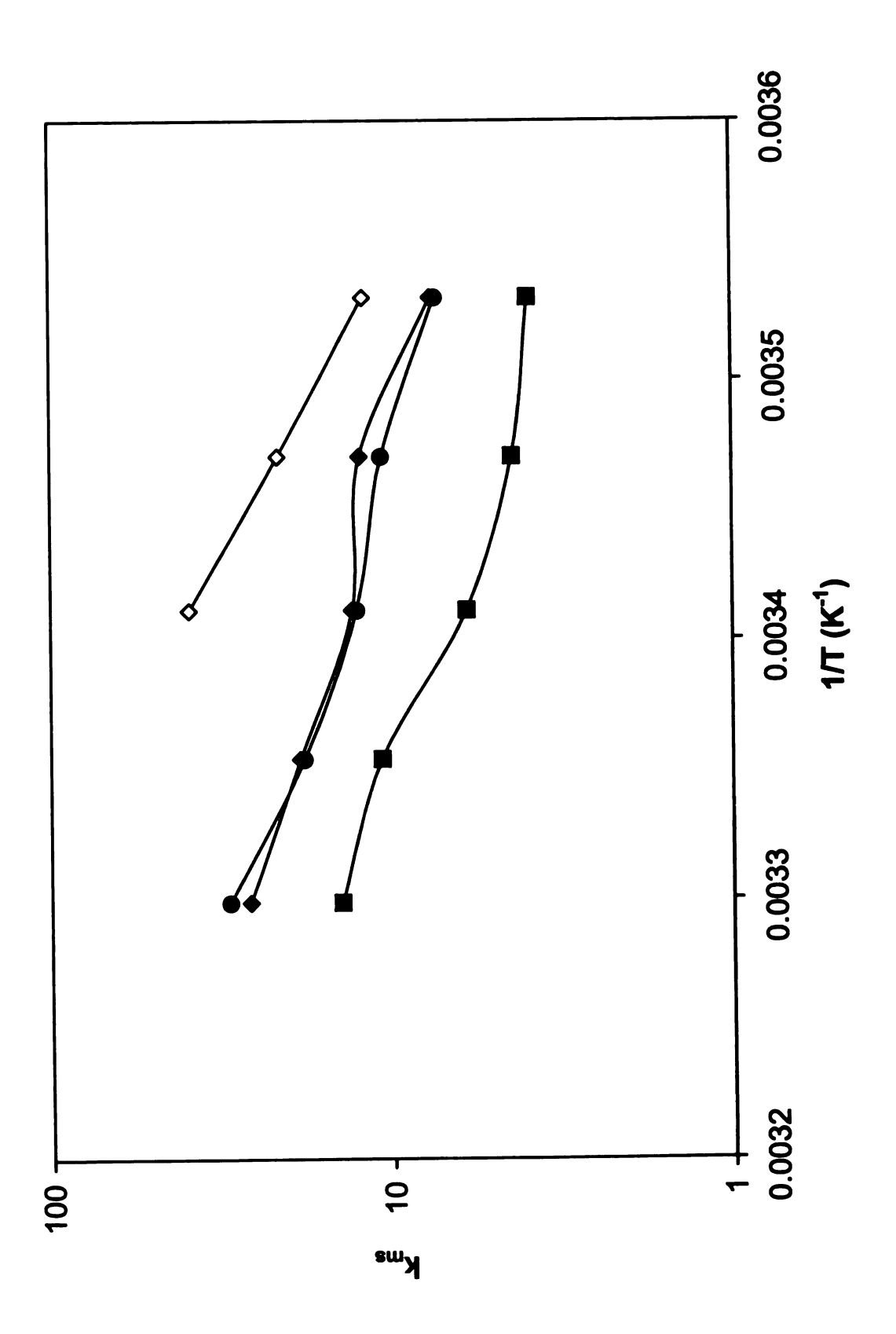


Table 5.6 Activation energy for the coumarin-based solutes

Solute	ΔE _{m‡1} ª (kcal/mol)	ΔE _{m‡2} ª (kcal/mol)	ΔE _{s‡1} ^b (kcal/mol)	ΔE _{st2} ^b (kcal/mol)
Coumafuryl	N/A	16.3 ± 0.4	N/A	19.6 ± 0.4
Warfarin	3.6 ± 0.8	7 ± 1	6.5 ± 0.8	10 ± 1
Coumachlor	4.5 ± 0.8	8 ± 1	8.0 ± 0.9	11 ± 1
Coumatetralyl	5 ± 2	8 ± 2	9 ± 2	12 ± 2
4-Hydroxy- coumarin	N/A ^c	N/A	N/A	N/A

- ^a $\Delta E_{m\pm 1}$ and $\Delta E_{m\pm 2}$ are the activation energy from mobile to transition state for the first and second enantiomers calculated at P = 1300 psi
- $^{\rm b}$ $\Delta E_{\rm s \pm 1}$ and $\Delta E_{\rm s \pm 2}$ are the activation energy from stationary to transition state for the first and second enantiomers calculated at P = 1300 psi
- ^d Not available

enter the stationary phase than to exit. A comparison between the two enantiomers demonstrates that the second enantiomer always has higher activation energy than the first enantiomer. Thus, the energy diagram can be constructed as follows: both enantiomers start in the mobile phase at the same energy state, then the second enantiomer needs to overcome an even higher activation energy ($\Delta E_{m\ddagger}$) than the first enantiomer, but finally reaches a lower energy state in the stationary phase than the first enantiomer.

5.4 CONCLUSIONS

In this study, the thermodynamic and kinetic behavior is examined with the β -cyclodextrin stationary phase in polar-organic mode. Increasing temperature from 283 to 303 K decreases the retention for all solutes dramatically. The change in molar enthalpy can be calculated through the slope of the van't Hoff plot. 4-Hydroxycoumarin has the largest retention, but the least negative change of molar enthalpy. For the chiral solutes, the trend of their change in molar enthalpy doesn't always match the trend of their retention. Apparently, the change in molar entropy takes an important role in the separation. The second enantiomer has a more negative change in molar enthalpy than the first enantiomer, indicating an enthalpically more favorable process for the second enantiomer. But the second enantiomer does not experience an entropically favorable process in the transfer, which can be seen from the negative chiral difference in molar entropy ($\Delta\Delta$ S). All the separations are enthalpically controlled. But there is no enthalpy-entropy compensation observed with five model solutes. Increasing pressure decreases the retention for all solutes. The positive change

in molar volume indicates no inclusion happened in this mobile phase. As for kinetics, increasing temperature increases kinetic rate constants. Activation energies are positive for chiral solutes, with the second enantiomer having higher activation energy than the first enantiomer.

5.5 References

- [1] W.L. Hinze, T.E. Riehl, D.W. Armstrong, W. DeMond, A. Alak, T. Ward, Anal. Chem. 57 (1985) 237-242.
- [2] H.Y. Aboul-Enein, M.R. Islam, S.A. Bakr, 11 (1988) 1485-1493.
- [3] K. Cabrera, D. Lubda, J. Chromatogr. A 666 (1994) 433-438.
- [4] N. Morin, Y.C. Guillaume, E. Peyrin, J.C. Rouland, Anal. Chem. 70 (1998) 2819-2826.
- [5] M.C. Ringo, C.E. Evans, Anal. Chem. 69 (1997) 643-649.
- [6] M.C. Ringo, C.E. Evans, J. Phys. Chem. B 101 (1997) 5525-5530.
- [7] M.C. Ringo, C.E. Evans, Anal. Chem. 69 (1997) 4964-4971.
- [8] M.C. Ringo, C.E. Evans, J. Microcolumn Sep. 10 (1998) 647-652.

CHAPTER 6

THERMODYNAMIC AND KINETIC CHARACTERIZATION OF NITROGEN-CONTAINING POLYCYCLIC AROMATIC HYDROCARBONS IN REVERSED-PHASE LIQUID CHROMATOGRAPHY

6.1. INTRODUCTION

Polycyclic aromatic hydrocarbons (PAHs) are a class of compounds that present a recognized health hazard. As a result, many studies have been conducted to investigate the biological and chemical properties of these substances [1-3]. When formed at elevated temperatures, PAHs may contain substituent moieties that alter their toxicity. Two substitutions that lead to highly toxic analogues involve the exchange of a carbon atom with nitrogen to form an azaarene, and the replacement of a hydrogen atom with an amino or nitro group. These solutes are collectively known as nitrogen-containing polycyclic aromatic hydrocarbons (N-PAHs). N-PAHs are commonly found in fossil fuels and their derivatives, although some may also form during combustion processes.

Relative to their parent PAHs, N-PAHs are more soluble in aqueous environments. Increased water solubility results in an increased potential for harm. For example, 1-aminopyrene demonstrates a fifty-fold increase in mutagenic activity when compared to that of the parent PAH, pyrene [4]. Similarly, azaarenes demonstrate increased carcinogenicity when compared to their parent PAHs [5-7].

Studies have been carried out to determine the presence of N-PAHs in fossil fuels [8-12], coal substitutes [13], lake sediment [14], urban aerosols [15],

as well as in the degradation products of polymers [16]. In order to identify and differentiate N-PAHs, many investigators have used chromatographic techniques because of their high resolving power. These techniques have included gas [12,17,18], thin layer [19], supercritical fluid [20], and liquid chromatography [8-11,16,17,21-26]. In nearly all instances, the chromatographic applications have focused upon the optimization of the separation or upon qualitative and quantitative analysis, rather than a detailed examination of the molecular contributions to retention. The most noteworthy study by Colin et al. [21] examined the retention of 26 mono-substituted and 5 di-substituted aza-PAHs in reversed-phase liquid chromatography as a function of the mobile and stationary phase compositions. They reported that the aza-PAHs are separated on the basis of carbon number with aqueous methanol mobile phases and octadecylsilica stationary phases, whereas the position of the nitrogen atom(s) has a greater effect with aqueous tetrahydrofuran or acetonitrile mobile phases and octylsilica stationary phases. They observed dramatic tailing, which was attributed to interactions with unreacted silanol groups and/or the slow equilibrium between the neutral and protonated forms of the aza-PAHs. Although these observations suggest unusual thermodynamic and kinetic behavior, to the best of our knowledge, no results of quantitative explorations of this behavior have been published.

To overcome this dearth of information, the thermodynamics and kinetics of retention for a series of N-PAHs are presented herein. Using theory and methodology developed in Chapter 1, the retention factors and rate constants for

the N-PAHs are determined as a function of temperature and pressure. The effect of mobile phase is examined by using methanol as a model of protic solvents and acetonitrile as a model of aprotic solvents. From the retention factors, the changes in molar enthalpy and molar volume are quantitated. From the rate constants, the activation energy and activation volume are quantitated. This analysis provides insight into the retention mechanism of N-PAHs in reversed-phase liquid chromatography.

6.2. EXPERIMENTAL METHODS

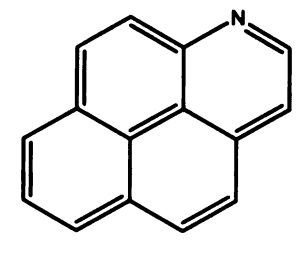
6.2.1 Chemicals

As depicted in Figure 6.1, five N-PAHs are chosen to study the effect of nitrogen position, ring number, and annelation structure on the thermodynamics and kinetics of retention. 1-Aminopyrene (Sigma-Aldrich), 1-azapyrene, 4-azapyrene, benz[a]acridine, and dibenz[a,j]acridine (Institüt für PAH Forschung) are obtained as solids and dissolved in high-purity methanol and acetonitrile (Burdick and Jackson, Baxter Healthcare) to yield standard solutions at a concentration of 10⁻⁴ M. A nonretained marker, 4-hydroxymethyl-7-methoxycoumarin, is added to each solution at a concentration of 10⁻⁴ M.

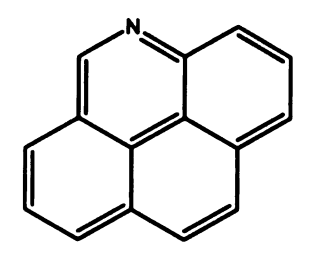
6.2.2 Experimental System

The solutes are separated on a capillary liquid chromatography system that has been described in Figure 3.2. The mobile phases are methanol and acetonitrile, and the stationary phase is polymeric octadecylsilica. The silica packing is characterized by a 5.5-μm particle size, 190-Å pore size, and 240-m²/g surface area (IMPAQ 200, PQ Corp.), and reacted with trifunctional



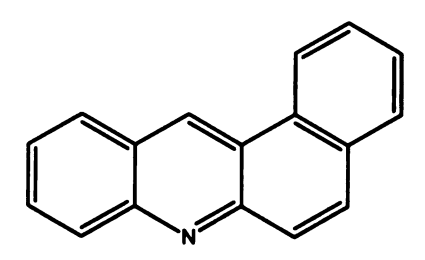


1-azapyrene

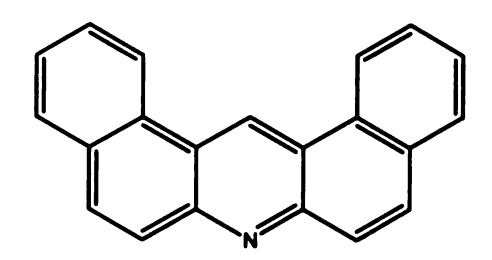


4-azapyrene

1-aminopyrene



benz(a)acridine



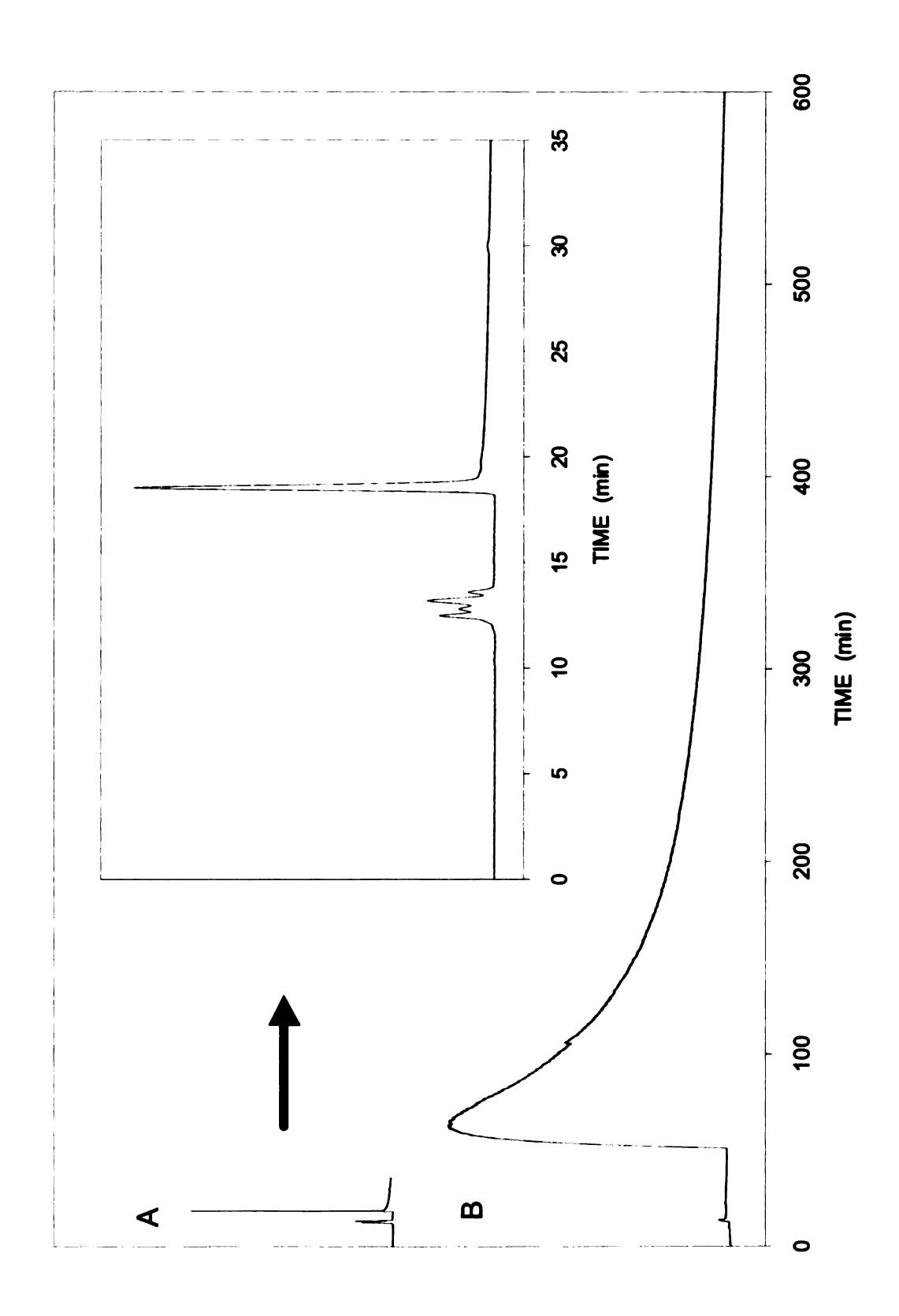
dibenz(a,j)acridine

octadecylsilane to produce a polymeric phase with bonding density of 5.4 μmol/m². Although this stationary phase is not commercially available, it may be considered representative of high-density, polymeric octadecylsilica phases. The column has a plate height (H) of 15 µm, reduced plate height (h) of 2.73, total porosity (ε_T) of 0.84, and flow resistance parameter (ϕ) of 500. The column is operated at a nominal flow rate of 1.05 µL/min, linear velocity (v) of 0.055 cm/s, and reduced velocity (v) of 2.75. The temperatures for these experiments are 283, 288, 293, 298 and 303 K for methanol, and 298, 303, 308, 313, and 323 K for acetonitrile. The inlet pressures for the methanol experiments are 1000. 1750, 2500, 3250 and 4000 psi. These values correspond to average pressures of 585, 1335, 2085, 2835, and 3585 psi, respectively, which were calculated assuming a linear pressure drop along the column. The inlet pressure for the acetonitrile experiments was 2500 psi, which corresponds to an average pressure of 2175 psi, which was calculated assuming a linear pressure drop along the column. The data were analyzed using the exponentially modified Gaussian (EMG) and the Thomas (NLC) equations, which are described in Section 2.3.3 and 2.3.4

6.3. RESULTS AND DISCUSSION

Based on previous experience with the parent PAHs [27,28], the EMG function was chosen for regression of the N-PAH zone profiles in initial studies. The zone profiles in methanol mobile phase, shown in Figure 6.2A, are similar to those observed in previous studies. The overall quality of fit is high, exhibiting random residuals and large values for the square of the correlation coefficient (R²)

Figure 6.2 Representative chromatograms of 4-azapyrene in reversed-phase liquid chromatography. Column: polymeric octadecylsilica. Mobile phase: (A) methanol, 303 K, 2085 psi, 0.08 cm/s; (B) acetonitrile, 303 K, 2185 psi, 0.08 cm/s. Column: polymeric octadecylsilica. Other experimental details are given in the text.



> 0.98) and F-statistic (F > 1000). However, the zone profiles in acetonitrile mobile phase, shown in Figure 6.2B, are quite different and demonstrate a much higher degree of asymmetry. This asymmetry may arise from a change in retention mechanism from partition to either adsorption or mixed-mode partition and adsorption. As a result, the zone profiles in acetonitrile were analyzed by using the Thomas model, which was thought to be more appropriate for the adsorption mechanism. However, the Thomas model failed to produce any improvement in the quality of fit ($R^2 > 0.95$, F > 1000). Moreover, the zone profiles did not change as a function of concentration, which suggests that the isotherm is linear rather than nonlinear. Consequently, the EMG model was used throughout this study to provide consistency in the thermodynamic and kinetic results.

6.3.1 Methanol Mobile Phase

6.3.1.1 Thermodynamic Behavior

6.3.1.1.1 Retention Factor

Representative values of the retention factor for the N-PAHs in methanol mobile phase are summarized in Table 6.1. The retention factors for the N-PAHs are notably smaller than those for the parent PAHs on the same stationary phase [27,28]. 1-Aminopyrene, 1-azapyrene, and 4-azapyrene have retention factors that are smaller by 73%, 38%, and 43%, respectively, than pyrene (k = 0.84 at 303 K). Similarly, the retention factor for benz[a]acridine is 60% smaller than that for benz[a]anthracene (k = 1.46 at 303 K). This decreased retention is due to the increased polarity of the N-PAHs relative to that of the PAHs. Because the

Table 6.1 Retention factors for N-PAHs in methanol mobile phase.

Solute	k	8	k	b
Solute	288 K	303 K	585 psi	3585 psi
1-Aminopyrene	0.35	0.23	0.35	0.35
1-Azapyrene	0.94	0.52	0.95	0.94
4-Azapyrene	0.78	0.48	0.79	0.78
Benz[a]acridine	1.03	0.58	0.97	1.03
Dibenz[a,j]acridine	3.26	1.52	2.96	3.26

^a Retention factor (k) calculated at P = 3585 psi

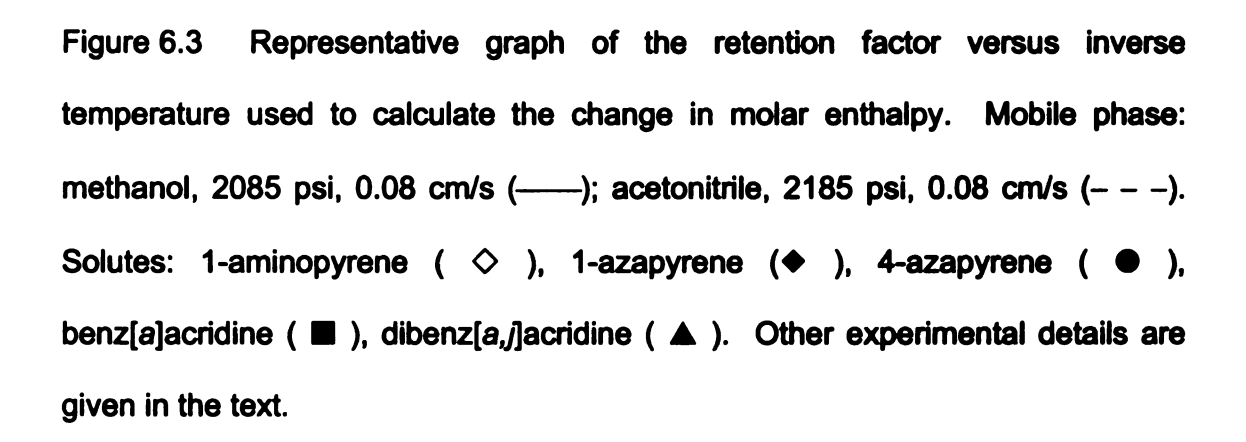
^b Retention factor calculated at T = 288 K

partition mechanism is governed by differences in relative solubility in the polar mobile phase and nonpolar stationary phase [29], the more polar N-PAHs are less retained. It is noteworthy that the trends in retention factor for the N-PAHs are the same as those identified previously for the PAHs. Retention increases with the number of aromatic rings [27] and decreases with more condensed annelation structure [28] or length-to-breadth ratio [30]. These trends are consistent with the partition mechanism.

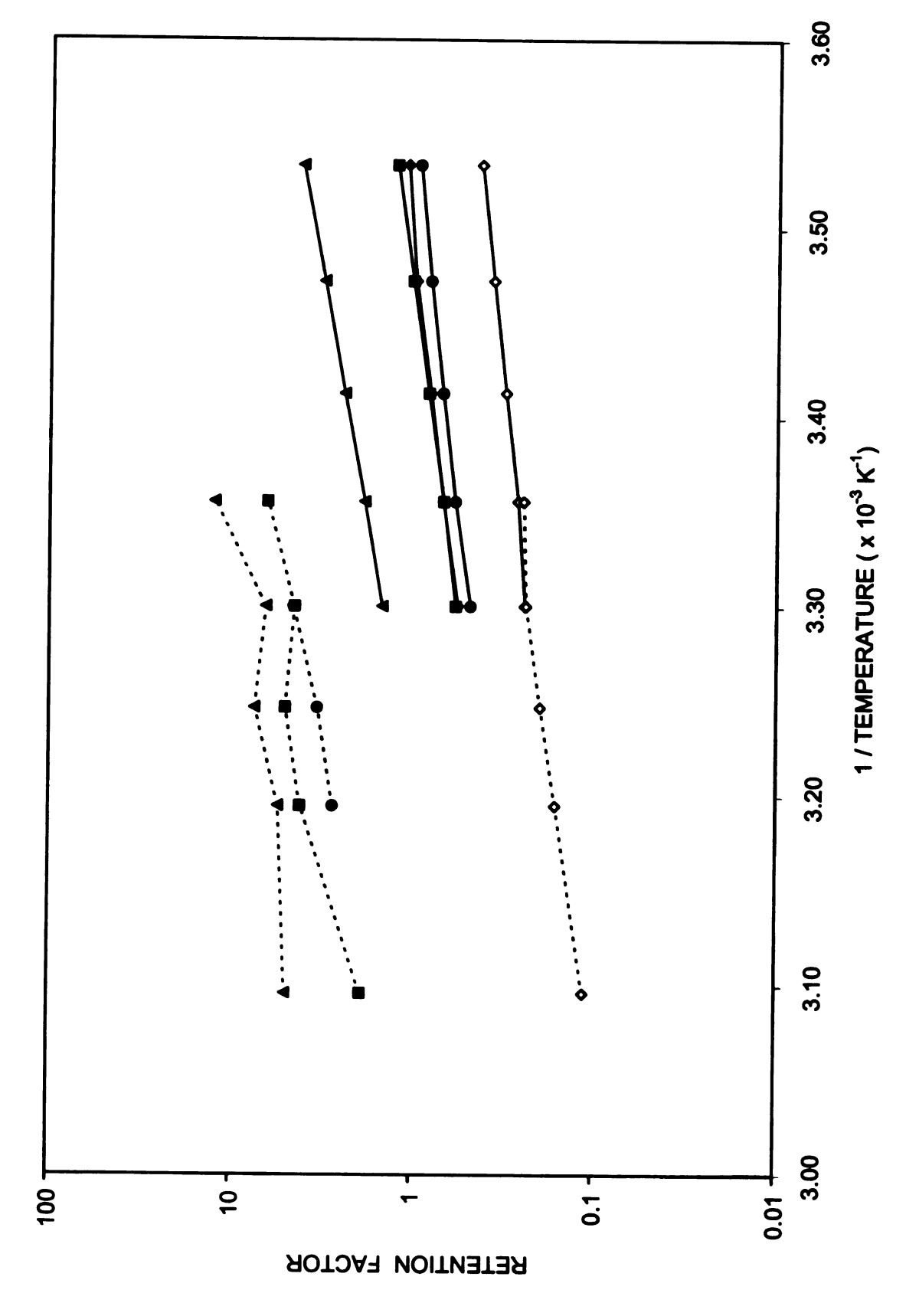
As shown in Table 6.1, the retention factor for all solutes decreases significantly (34 - 53%) with increasing temperature. The retention factor increases slightly (6 - 10%) with increasing pressure for benz[a]acridine and dibenz[a,j]acridine, but remains statistically invariant for the amino- and azapyrenes. The reasons for this behavior are discussed below in further detail.

6.3.1.1.2 Molar Enthalpy

A representative graph of the logarithm of the retention factor versus the inverse temperature (van't Hoff plot) is shown in Figure 6.3. The data for the methanol mobile phase are represented using solid lines. The graph for each solute is linear ($R^2 = 0.986 - 0.999$) and the slope is positive. A linear graph indicates that the change in molar enthalpy is constant, which suggests that there is no significant change in retention mechanism over the temperature range of 283 - 303 K. A positive slope is indicative of a negative change in molar enthalpy, which suggests that the transfer from mobile to stationary phase is enthalpically favorable. The change in molar enthalpy is calculated from the slope of Figure 6.3, according to Equation 1.6.







As shown in Table 6.2, the changes in molar enthalpy are the least negative for 1-aminopyrene, are comparable for 1-azapyrene and 4-azapyrene, and become progressively more negative for benzíalacridine dibenz[a,/]acridine. These changes in molar enthalpy follow the same trends as observed for the parent PAHs [27,28]. These trends indicate that the change in molar enthalpy becomes more negative with increasing ring number and with less condensed annelation structure. The reasons for these trends have been discussed previously [28] and may be attributed to the depth to which each PAH can penetrate into the stationary phase. The proximal regions, where the alkyl group is bound to the silica surface, are highly ordered with all trans carboncarbon bonds. As the distance from the surface increases there are more gauche bonds and greater disorder [31,32]. The more condensed PAHs, such as pyrene, probe only the distal regions, whereas less condensed PAHs, such as benz[a]anthracene, can penetrate more deeply into the ordered regions of the stationary phase. Consequently, the change in molar enthalpy becomes more negative the farther the PAH penetrates into the stationary phase.

When compared to the molar enthalpy of the parent PAH, pyrene (ΔH = 4.4 kcal/mol [28]), the change in molar enthalpy is 0.6 kcal/mol more negative for 1-aminopyrene and 1.2 – 1.3 kcal/mol more negative for the azapyrenes on the same stationary phase. Interactions with the octadecyl groups are relatively similar for these solutes. Hence, the differences may arise from interactions with silanol groups, either on the silica surface or on incompletely reacted and hydrolyzed molecules of the trifunctional octadecylsilane [21,33]. The PAHs

Table 6.2 Changes in molar enthalpy and molar volume for N-PAHs in methanol mobile phase.

Solute	ΔH (kcal/mol) ^a	ΔV (mL/mol) ^b
1-Aminopyrene ^c	-5.0 ± 0.2	-2 ± 2
1-Azapyrene	-5.7 ± 0.3	-0.1 ± 4
4-Azapyrene	-5.6 ± 0.2	-2 ± 5
Benz[a]acridine	-6.6 ± 0.1	-7 ± 1
Dibenz[<i>a,j</i>]acridine	-8.9 ± 0.1	-11 ± 1

^a Molar enthalpy (ΔH) calculated at P = 2085 psi

b Molar volume (△V) calculated at T = 288 K, except as otherwise noted

^c Molar volume calculated at T = 283 K

interact very weakly with the silanol sites by hydrogen bonding through the aromatic (π) system. The nitrogen atom imparts a more basic character to the N-PAHs, relative to that of the parent PAHs, and this feature allows for stronger interaction with the acidic silanol sites [34,35]. This interaction is stronger than a simple hydrogen bond, but not as strong as proton transfer [35]. The amine group is less basic than the aza group, as evidenced by the acid-base equilibrium constants of aniline (p K_a = 4.63) and pyridine (p K_a = 5.25) [36]. Thus, the change in molar enthalpy for 1-aminopyrene is expected to be less than that for the azapyrenes, as observed in Table 6.2. The molar enthalpy for 4azapyrene is less than that for 1-azapyrene because diffusion through the octadecyl groups to the silanol sites is more facile along the short axis than along the long axis of the molecule. It is also evident that the change in molar enthalpy for benz[a]acridine is 0.5 kcal/mol less negative than that for the parent PAH, benz[a]anthracene ($\Delta H = 7.1$ kcal/mol [28]). Given the position of the nitrogen atom, diffusion must occur along the long axis of the molecule in order to bind with the silanol groups. This is much less favorable for the linear structure of benz[a]acridine than for the condensed structure of the azapyrenes. Similar steric effects are expected for dibenz[a,/]acridine, whose molar enthalpy is 6.9 kcal/mol less negative than the structurally similar five-ring PAH, picene [28].

Although there have been no published studies on the thermodynamics of retention for N-PAHs in reversed-phase liquid chromatography, supporting evidence is provided from other separation techniques. Woodrow and Dorsey examined the partitioning of acridine in micellar electrokinetic chromatography

[37]. They report an enthalpy of transition between the alkyl group of the surfactant and water as -6.75 kcal/mol for acridine. Matzner and Bales examined the retention of acridine on silica in aqueous media [38,39]. They report an enthalpy of transition between silica and water as -8.05 kcal/mol. These results support our suggestion that the more negative values of enthalpy for the four-ring N-PAHs relative to that of their parent PAHs are due to interactions with the silica surface.

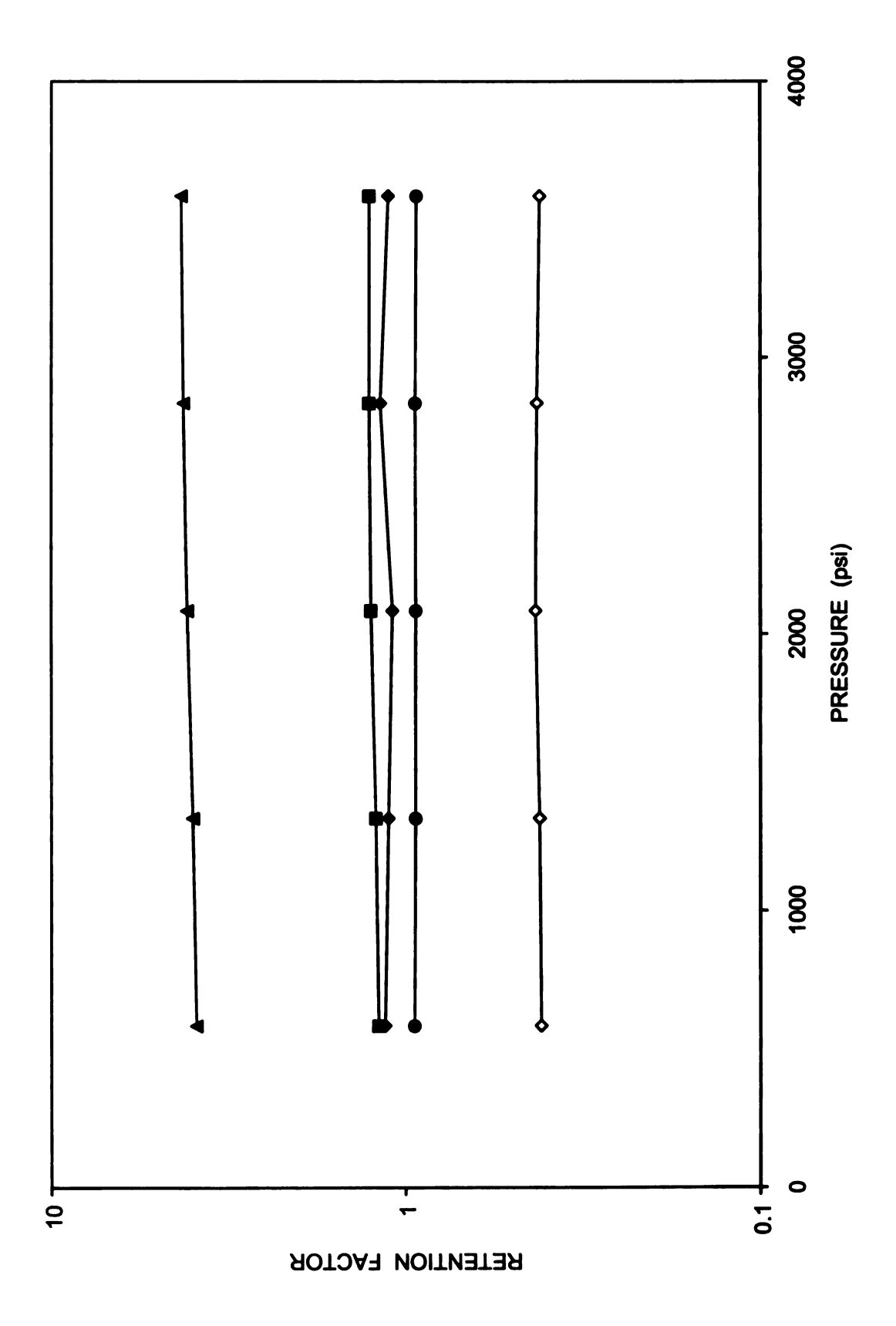
Finally, it is important to note that the retention factors for the N-PAHs are smaller than those of the parent PAHs, even though the changes in molar enthalpy are more negative. There are two potential reasons for this phenomenon. First, there may be a significant entropic effect that offsets the enthalpic contributions to retention. For example, Matzner and Bales report values for the entropy term (TΔS) as –5.09 kcal/mol compared with the enthalpy term of –8.05 kcal/mol for adsorption of acridine on silica [38,39]. Second, the phase ratio for the silanol sites may be very small relative to that of the octadecyl groups because of the high bonding density (5.4 μmol/m²). According to Equation 1.6, either a significant change in the entropy term or the phase ratio would allow the retention factors for the N-PAHs to remain smaller than those of the parent PAHs, despite the greater changes in molar enthalpy. As both of these contributions are contained in the intercept of the van't Hoff plot, they are difficult to distinguish by chromatographic methods alone.

6.3.1.1.3 Molar Volume

A representative graph of the logarithm of the retention factor versus pressure is shown in Figure 6.4. Although the graph for each N-PAH is linear, the square of the correlation coefficient is highly variable ($R^2 = 0.594 - 0.998$) because of the small influence of pressure on retention. It should be noted that the smallest correlation coefficients are exhibited by the azapyrenes, which are affected the least by changes in pressure. The slope of the graph is positive for all solutes, which is indicative of a negative change in molar volume. This suggests that the solute occupies less volume in the stationary phase than in the mobile phase. The change in molar volume is calculated from the slope of this graph, according to Equation 1.9.

As shown in Table 6.2, 1-aminopyrene, 1-azapyrene, and 4-azapyrene have values that are statistically indistinguishable and close to zero. In contrast, benz[a]acridine and dibenz[a,]acridine exhibit changes in molar volume that are statistically nonzero, with the four-ring N-PAH demonstrating a less negative change in molar volume than the five-ring analogue. The values for the azapyrenes and benz[a]acridine are similar to those for the parent PAHs, pyrene (2.3 mL/mol) and benz[a]anthracene (8.4 mL/mol) [28]. As noted previously, these changes in molar volume may be attributed to the depth that each PAH can penetrate into the stationary phase [27,28]. The more condensed PAHs, such as pyrene, probe only the distal regions, whereas less condensed PAHs, such as benz[a]anthracene, can penetrate more deeply into the ordered region

Figure 6.4 Representative graph of the retention factor versus pressure used to calculate the change in molar volume. Mobile phase: methanol, 283 K, 0.08 cm/s. Symbols defined in Figure 6.3. Other experimental details are given in the text.



of the stationary phase. Consequently, the change in molar volume becomes more negative the farther the PAH penetrates into the stationary phase.

6.3.1.2 Kinetic Behavior

Although the thermodynamic data demonstrate the steady-state aspects of chromatographic behavior, they do not fully explain the retention mechanism. Using the equations and methods developed in Section 1.4.2, the pseudo-first-order rate constants, activation energies, and activation volumes were calculated. These values help to quantify the kinetic aspects of mass transfer between the mobile and stationary phases as a function of solute structure. These data provide information about the retention mechanism that would not be available from thermodynamic data alone.

6.3.1.2.1 Rate Constants

Representative values of the rate constants, calculated using Equation 1.38, are summarized in Table 6.3. 1-Aminopyrene undergoes the highest rate of transfer, followed by 4-azapyrene, benz[a]acridine, and dibenz[a,j]acridine. 1-Azapyrene has the lowest rate of transfer, with rate constants that are one order-of-magnitude less than 4-azapyrene and two orders-of-magnitude less than 1-aminopyrene. The rate-limiting step for 1-aminopyrene, 1-azapyrene, 4-azapyrene, and benz[a]acridine is the transfer from mobile to stationary phase, because the retention factor ($k = k_{sm}/k_{ms}$) is less than unity. In contrast, the rate-limiting step for dibenz[a,j]acridine is the transfer from the stationary to the mobile phase, since the retention factor is greater than unity.

Table 6.3 Rate constants for N-PAHs in methanol mobile phase.

ajrijo	k _{ms} (s ⁻¹) ^a	S ⁻¹) a	k _{sm} (s ⁻¹) ^a	s ⁻¹) a	k _{ms} (s ⁻¹) ^b	s ⁻¹) ^b	K _{sm} (k _{sm} (s ⁻¹) ^b
	288 K	303 K	288 K	303 K	585 psi	3585 psi	585 psi	3585 psi
1-Aminopyrene	149	675	52	154	351	149	124	52
1-Azapyrene	0.7	4	0.7	2	0.8	0.7	0.7	2.0
4-Azapyrene	18	62	14	30	14	18	11	14
Benz[a]acridine	14	80	14	47	18	14	17	14
Dibenz[<i>a,j</i>]acridine	9	49	21	75	6	9	27	21

Rate constants from stationary to mobile phase (k_{ms}) and from mobile to stationary phase (k_{em}) calculated at P = 3585

psi

^b Rate constants calculated at T = 288 K

The rate constants for the four-ring N-PAHs are notably smaller than those for their parent PAHs on the same stationary phase [28]. 1-Aminopyrene, 1-azapyrene, and 4-azapyrene have rate constants that are smaller by 71%, 99.8%, and 97%, respectively, than pyrene (k_{ms} = 2300 s⁻¹ at 303 K). Similarly, the rate constant for benz[a]acridine is 91% smaller than that for benz[a]anthracene (k_{ms} = 850 s⁻¹ at 303 K). In contrast, the rate constant for the five-ring N-PAH, dibenz[a,j]acridine, is more comparable to that for the five-ring PAH, picene [27]. These results suggest that 1-azapyrene is most greatly affected, 4-azapyrene and benz[a]acridine are moderately affected, and dibenz[a,j]acridine is relatively unaffected by the slow kinetics of adsorption at silanol sites.

As shown in Table 6.3, the rate constants for all solutes increase significantly (240 – 720% for k_{me}) with increasing temperature. This behavior is a consequence of the increased diffusion coefficients and the enhanced fluidity of the stationary phase. As more kinetic energy is imparted, the alkyl chains become more labile and can more readily undergo rotation of the carbon-carbon bonds from the *trans* to *gauche* conformation. In fact, an order-disorder phase transition has been reported previously for this stationary phase at approximately 318 K. The rate constants decrease significantly (58% for k_{me}) with increasing pressure for 1-aminopyrene, but decrease only slightly or remain invariant for the other solutes. This behavior is a consequence of the compression of the alkyl chains, which impedes diffusion into and out of the stationary phase.

Activation energies and activation volumes for N-PAHs in methanol mobile phase. Table 6.4

Solute	ΔΕ _{s‡} (kcal/mol) ^a	ΔΕ _{mt} (kcal/mol) ^a	ΔV _{s‡} (mL/mol) ^b	ΔV _{m‡} (mL/mol) ^b
1-Aminopyrene ^c	21±1	16±1	97 ± 20	99 ± 18
1-Azapyrene	24 ± 2	18±2	47 ± 48	47 ± 44
4-Azapyrene	19±1	14 ± 1	5±6	6±7
Benz[a]acridine	21±3	14±3	58 ± 36	51 ± 36
Dibenz[a,]acridine	25±1	16±1	49±15	38 ± 16

Activation energies from stationary phase to transition state (ΔE_{ct}) and from mobile phase to transition state (ΔE_{mt}) calculated at P = 2835 psi Activation volumes from stationary phase to transition state (ΔV_{xt}) and from mobile phase to transition state (ΔV_{mt}) calculated at T = 288 K, except as otherwise noted

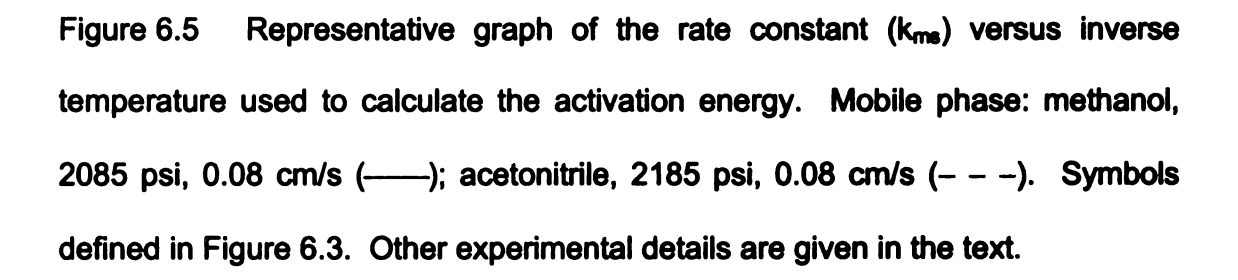
^c Activation volumes calculated at T = 283 K

6.3.1.2.2 Activation Energy

A representative graph of the logarithm of the rate constant versus the inverse temperature is shown in Figure 6.5. The data for the methanol mobile phase are represented using solid lines. The graph for each solute is linear ($R^2 = 0.968 - 0.995$) and the slope is negative. A negative slope is indicative of a positive energy barrier. The activation energy is calculated from the slope of this graph, according to Equations 1.15. As shown in Table 6.4, the activation energies are positive for all solutes. The activation energy for the transfer from stationary phase to transition state (ΔE_{st}) is greater than that from mobile phase to transition state (ΔE_{mt}). These data indicate that it is easier for the solutes to enter the stationary phase than to exit. The energy barriers ΔE_{st} and ΔE_{mt} seem to be similar for all solutes and, indeed, there is no statistically significant difference. These values are comparable to those reported previously for the parent PAHs [28].

6.3.1.2.3 Activation Volume

A representative graph of the natural logarithm of the rate constant versus pressure is shown in Figure 6.6. The activation volume is calculated from the slope of this graph, according to Equations 1.17. As shown in Table 6.4, 1-aminopyrene has the largest activation volume while those of the other solutes are somewhat smaller. The values for the azapyrenes appear to be similar to those for the parent PAH, pyrene ($\Delta V_{s\pm} = 47 \pm 7$ mL/mol, $\Delta V_{m\pm} = 43 \pm 7$ mL/mol) [28]. However, the activation volumes for many of the N-PAHs are statistically indistinguishable from zero, given the small effect of pressure and the



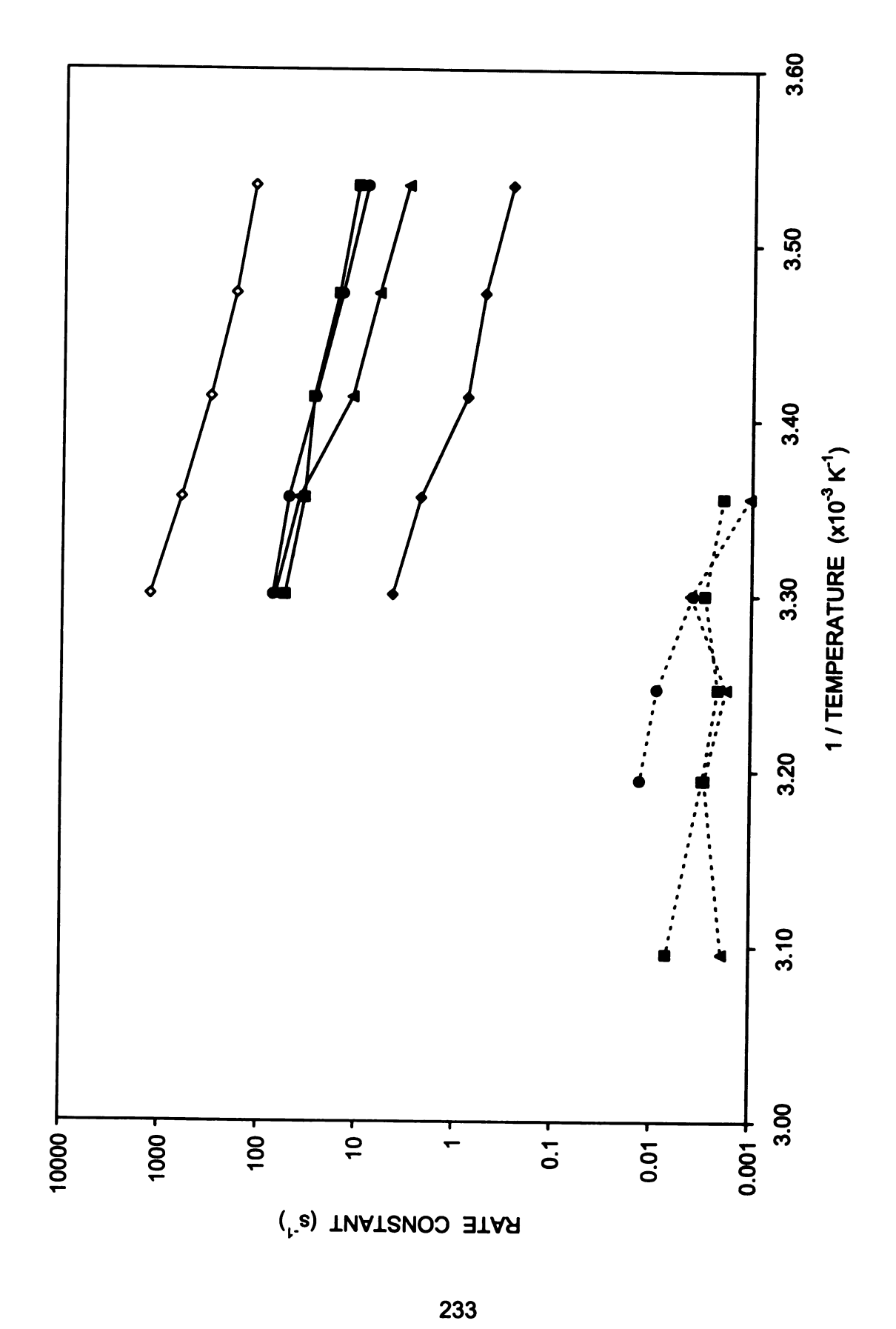


Figure 6.6 Representative graph of the rate constant (k_{ms}) versus pressure used to calculate the activation volume. Mobile phase: methanol, 283 K, 0.08 cm/s. Symbols defined in Figure 6.3. Other experimental details are given in the text.

correspondingly large standard deviation. Hence, no definitive conclusions can be drawn about the volumetric barrier for these solutes.

6.3.2 Acetonitrile Mobile Phase

In the previous study, the N-PAHs showed evidence of a partition mechanism on the octadecylsilica stationary phase, similar to that of the parent PAHs, with some additional contributions that are attributable to adsorption. The methanol mobile phase used for this study is able to form hydrogen bonds with the N-PAHs and thereby inhibit their ability to adsorb at silanol sites. At the same time, methanol can form hydrogen bonds with the silanol sites to displace or compete with the N-PAHs. By these two mechanisms, the protic mobile phase can reduce interactions of the N-PAHs with silanol sites. Therefore, it is beneficial to examine the effect of an aprotic solvent such as acetonitrile, which cannot undergo such hydrogen-bonding interactions, on the combined partition-adsorption mechanism.

The effect of temperature on the thermodynamic and kinetic behavior of the N-PAHs in the methanol mobile phase is significant (Tables 6.1 and 6.3), so that a large temperature range is also warranted in acetonitrile. A higher range of temperatures (293 to 333 K) is selected because of the greater retention and asymmetry of the zone profiles in acetonitrile (Figure 6.2). In contrast, the effect of pressure on the thermodynamic and kinetic behavior is very small in the methanol mobile phase (Tables 6.1 and 6.3). Hence, the study in acetonitrile is conducted at a single average pressure of 2185 psi.

6.3.2.1 Thermodynamic Behavior

6.3.2.1.1 Retention Factor

Representative values of the retention factor for the N-PAHs in acetonitrile mobile phase are summarized in Table 6.5. As shown, 1-aminopyrene is eluted first, followed by 4-azapyrene, benz[a]acridine, and dibenz[a,j]acridine. 1-Azapyrene is the most strongly retained solute and it exhibited such severe asymmetry that it was excluded from the quantitative thermodynamic and kinetic studies.

When compared to the results with the methanol mobile phase (Table 6.1), all solutes demonstrate an increase in retention factor in acetonitrile. Given that acetonitrile is less polar than methanol, the retention factor would be expected to decrease if the partition mechanism were predominant. Thus, the observed increase in retention factor suggests that the adsorption mechanism is contributing more greatly to retention in acetonitrile than in methanol. The increase is slight (4%) for 1-aminopyrene but very substantial (320 – 850%) for the aza-PAHs, which is consistent with the relative basicity of amine and aza groups, as discussed previously. In fact, the retention factors for the four-ring aza-PAHs are markedly larger than those for the parent PAHs [27,28], which suggests that the adsorption mechanism is predominant for these solutes in acetonitrile.

6.3.2.1.2 Molar Enthalpy

A representative graph of the logarithm of the retention factor versus the inverse temperature is shown in Figure 6.3. The data for the acetonitrile mobile

phase are represented using dashed lines. It is evident that the retention data for 1-aminopyrene are nearly collinear in the acetonitrile and methanol mobile phases. This suggests that there is no significant difference in the retention mechanism for this solute. In contrast, the retention factors for the aza-PAHs are approximately an order-of-magnitude greater in acetonitrile than in methanol. Although the graph for each N-PAH is linear, the square of the correlation coefficient is highly variable (R² = 0.724 – 0.986) because of the high degree of asymmetry and resulting uncertainty in the retention factor. It should be noted that the smallest correlation coefficients are exhibited by the aza-PAHs, which have the greatest asymmetry. The slope of the graph is positive, which is indicative of a negative change in molar enthalpy and suggests that the transfer from mobile to stationary phase is enthalpically favorable. The change in molar enthalpy is calculated from the slope of graph in Figure 6.3, according to Equation 1.6.

As shown in Table 6.5, the changes in molar enthalpy are the least negative for 1-aminopyrene and dibenz[a,j]acridine, and become progressively more negative for benz[a]acridine and 4-azapyrene. This order does not show the trends expected for the partition mechanism, i.e., more negative changes in molar enthalpy with increasing ring number and less condensed annelation structure. Rather, this order is consistent with the hydrogen bonding strength and steric effects at silanol groups, as discussed previously for the methanol mobile phase. The changes in molar enthalpy for the four-ring N-PAHs are slightly more negative in acetonitrile than in methanol. 1-Aminopyrene, 4-

Table 6.5 Thermodynamic data for N-PAHs in acetonitrile mobile phase.

Solute	k	a	ΔН *
Solute	303 K	313 K	(kcal/mol)
1-Aminopyrene	0.24	0.16	6.3 ± 0.7
4-Azapyrene	4.55	2.74	10 ± 1
Benz[a]acridine	4.48	4.15	8 ± 2
Dibenz[a,j]acridine	6.43	5.49	6 ± 2

Retention factor (k) and change in molar enthalpy (ΔH) calculated at P = 2185
 psi

azapyrene, and benz[a]acridine exhibit values that are 1.3, 3.7, and 1.7 kcal/mol more negative in acetonitrile than in methanol (Table 6.2). This change in molar enthalpy is consistent with the greater role of adsorption in the aprotic solvent, particularly for azapyrene. In contrast, the value for dibenz[a,j]acridine is 2.8 kcal/mol less negative in acetonitrile than in methanol. This suggests that the partition mechanism is still relatively important for this solute, such that the less polar mobile phase, acetonitrile, competes more effectively than methanol with the nonpolar stationary phase.

Although there are small but important differences, it is noteworthy that the changes in molar enthalpy are very similar in the acetonitrile and methanol mobile phases. Yet the retention factors for the aza-PAHs differ by nearly an order of magnitude in these mobile phases. From Figure 6.3, it is evident that the difference lies in the intercept of the van't Hoff plot. Again, according to Equation 1.6, there are two possible origins of this difference. The entropy term may be substantially more negative in methanol because of the solvent release from both solute and silanol sites upon binding. A smaller entropy term in acetonitrile would lead to a larger value for the intercept. Alternatively, a change in the phase ratio may arise because of the greater number of free silanol groups in acetonitrile. In methanol, many of the silanol groups may be hydrogen bonded and not available for binding with the solute. The larger phase ratio in acetonitrile would also lead to a larger value for the intercept. As noted previously, it is difficult to discern which of these origins prevails by chromatographic methods alone.

6.3.2.2 Kinetic Behavior

6.3.2.2.1 Rate Constants

Representative values of the rate constants are summarized in Table 6.6.

1-Aminopyrene undergoes much higher rates of transfer than 4-azapyrene, benz[a]acridine, and dibenz[a,j]acridine, which are two to three orders-of-magnitude lower. As in the methanol mobile phase, the rate-limiting step for 1-aminopyrene is the transfer from the acetonitrile mobile phase to the stationary phase. However, the aza-PAHs demonstrate the inverse trend, with the transfer from stationary to mobile phase serving as the rate-limiting step. When compared to the methanol mobile phase, the rate constants in acetonitrile are two to four orders-of-magnitude smaller. The differences in the rate constants result from the increased ability of the N-PAHs to interact with the silica support. As noted previously, the aprotic solvent acetonitrile does not hydrogen bond to the solutes or to the silanol sites as does the protic solvent methanol. Hence, the rate constants from mobile to stationary phase and from stationary to mobile phase are substantially smaller.

6.3.2.2.2 Activation Energy

A representative graph of the logarithm of the rate constant versus the inverse temperature is shown in Figure 6.5. The data for the acetonitrile mobile phase are represented using dashed lines. It should be noted that the data for 1-aminopyrene are not depicted in this graph. The zone profiles for 1-aminopyrene are nearly Gaussian and, as such, exhibit very small values of the asymmetric variance (τ^2). The small values of τ^2 result in calculated values for the rate

Table 6.6 Kinetic data for N-PAHs in acetonitrile mobile phase.

Splits	kms ((S ⁻¹) ⁸	K _{sm} (s ⁻¹) ^a	S-1) a	ΔEst	ΔΕπτ
	303 K	313 K	303 K	313 K	(kcal/mol) ^b	(kcal/mol) ^b
1-Aminopyrene	3.47	3.67	8.2 × 10 ⁻¹	5.9 x 10 ⁻¹	0~	0~
4-Azapyrene	3.9 x 10 ⁻³	1.3 × 10 ⁻²	1.8 x 10 ⁻²	3.6 x 10 ⁻²	23±5	13±3
Benz[a]acridine	2.9 × 10 ⁻³	3.0 × 10 ⁻³	1.3 × 10 ⁻²	1.3 x 10 ⁻²	6 ±3	0~
Dibenz[<i>a,j</i>]acridine	4.1 x 10 ⁻³	2.9 × 10 ⁻³	2.6 × 10 ⁻²	1.6 x 10 ⁻²	2±6	0~

Rate constants from stationary to mobile phase (kms) and from mobile to stationary phase (ksm) calculated at P = 2185 psi

Activation energies from stationary phase to transition state (ΔΕ_{st}) and from mobile phase to transition state (ΔΕ_{mt}) calculated at P = 2185 psi

constants that are highly variable as a function of temperature.

As shown in Figure 6.5, the graph for each N-PAH is linear and the slope is negative. Unlike the graph for the methanol mobile phase, acetonitrile shows correlation coefficients for the linear regression that vary significantly ($R^2 = 0.038 - 0.960$). As such, the reported values should be used only to draw general conclusions. The activation energy is calculated from the slope of this graph, according to Equations 1.15. As shown in Table 6.6, the activation energies are positive for all of the N-PAHs. The activation energy for the transfer from stationary phase to transition state (ΔE_{st}) is generally larger than that from mobile phase to transition state (ΔE_{mt}). These data indicate that it is easier for the solutes to exit the stationary phase than to enter. In spite of the large standard deviations, the activation energy appears to be smallest for 1-aminopyrene, slightly greater for benz[a]acridine and dibenz[a,j]acridine, and greatest for 4-azapyrene.

6.4. CONCLUSIONS

In this study, the thermodynamic and kinetic behavior of N-PAHs was examined in reversed-phase liquid chromatography. The parent PAHs are separated primarily by a partition mechanism with the octadecyl groups, but some minor interaction with the silanol groups can occur through the aromatic (π) system. In methanol mobile phase, the retention factors for the N-PAHs are less than those for the parent PAHs. This is consistent with the partition mechanism, where retention decreases as the polarity of the solute increases. In addition, the trends of retention with ring number and annelation structure are consistent with

the partition mechanism. However, the changes in molar enthalpy for the N-PAHs indicate that adsorption at the silanol groups is more significant than for the parent PAHs. The observed changes reflect the relative basicity of the amine and aza groups, but also indicate that steric effects are important. The more condensed amino- and azapyrenes can diffuse more easily to the silanol groups than the more linear benz[a]acridine and dibenz[a,j]acridine. The importance of adsorption is also reflected in the kinetic rate constants, which are significantly smaller for the NPAHs than for the parent PAHs.

The trends in thermodynamic behavior in the protic solvent methanol become even more pronounced in the aprotic solvent acetonitrile. Methanol is able to hydrogen bond with the NPAH solutes as well as with the silanol groups, thereby reducing their mutual interactions. Acetonitrile is not able to shield interactions in this manner, hence the retention factors for the aza-PAHs are substantially greater than those in methanol. Moreover, the retention factors for the four-ring aza-PAHs are greater than those for the parent PAHs, which suggests that the adsorption mechanism is predominant for these solutes. The changes in molar enthalpy are slightly more negative for these solutes, but not sufficient to account for the large change in retention factor. Hence, we suggest that a significant change in entropy or the phase ratio is responsible for the thermodynamic behavior. The kinetic behavior also reflects the increased role of adsorption, with rate constants that are two to four orders-of-magnitude smaller than those in methanol. This thermodynamic and kinetic information provides a

much clearer description of the retention mechanism of N-PAHs in reversedphase liquid chromatography.

6.5 REFERENCES

- [1] T. Vo-Dinh, Ed., Chemical Analysis of Polycyclic Aromatic Hydrocarbons, John Wiley & Sons, New York, NY, 1988.
- [2] M. Cooke, A.J. Dennis, G.L. Fisher, Eds., Polynuclear Aromatic Hydrocarbons: Physical and Biological Chemistry, Battelle Press, Columbus, OH, 1982.
- [3] R.F. Hertel, G. Rosner, J. Kielhorn, Eds., Selected Non-Heterocyclic Polycyclic Aromatic Hydrocarbons, World Health Organization, Geneva, Switzerland, 1998.
- [4] C.H. Ho, B.R. Clark, M.R. Guerin, B.D. Barkenbus, T.K. Rao, J.L. Epler, Mutat. Res. 85 (1981) 335-345.
- [5] G.M. Seixas, B.M. Andon, P.G. Hollingshead, W.G. Thilly, Mutat. Res. 102 (1982) 201-212.
- [6] A. Matsuoka, K. Shudo, Y. Saito, T. Sofuni, M. Ishidae, Mutat. Res. 102 (1982) 275-283.
- [7] E.A.J. Bleeker, S. Wiegman, P. de Voogt, M. Kraak, H.A. Leslie, E. de Haas, W. Admiraal, Rev. Environ. Contam. Toxic. 173 (2001) 39-83.
- [8] J.M. Schmitter, H. Colin, J.L. Excoffier, P. Arpino, G. Guiochon, Anal. Chem. 54 (1982) 769-772.
- [9] S.C. Ruckmick, R.J. Hurtubise, J. Chromatogr. 321 (1985) 343-352.
- [10] C. Borra, D. Wiesler, M. Novotny, Anal. Chem. 59 (1987) 339-343.
- [11] N. Motohashi, K. Kamata, R. Meyer, Environ. Sci. Technol. 25 (1991) 342-346.
- [12] J.M. Schmitter, I. Ignatiadis, G. Guiochon, J. Chromatogr. 248 (1982) 203-216.
- [13] M.R. Guerin, C.H. Ho, T.K. Rao, B.R. Clark, J.L. Epler, Environ. Res. 23 (1980) 42-53.
- [14] S.G. Wakeham, Environ. Sci. Technol. 13 (1979) 1118-1123.
- [15] H.Y. Chen, M.R. Preston, Environ. Sci. Technol. 32 (1998) 577-583.
- [16] M. Wilhelm, G. Matuschek, A. Kettrup, J. Chromatogr. A 878 (2000) 171-181.

- [18] K. Kamata, N. Motohashi, R. Meyer, Y. Yamamoto, J. Chromatogr. 596 (1992) 233-239.
- [19] K. Kamata, N. Motohashi, J. Chromatogr. 396 (1987) 437-440.
- [20] M. Ashraf-Khorassani, L.T. Taylor, J. Chromatogr. Sci. 26 (1988) 331-336.
- [21] H. Colin, J.M. Schmitter, G. Guiochon, Anal. Chem. 53 (1981) 625-631.
- [22] A.M. Siouffi, M. Righezza, G. Guiochon, J. Chromatogr. 368 (1986) 189-202.
- [23] T.R. Steinheimer, M.G. Ondrus, Anal. Chem. 58 (1986) 1839-1844.
- [24] J.W. Haas, W.F. Joyce, Y.J. Shyu, P.C. Uden, J. Chromatogr. 457 (1988) 215-226.
- [25] K. Kamata, N. Motohashi, J. Chromatogr. 498 (1990) 129-135.
- [26] H. Carlsson, C. Östman, J. Chromatogr. A 715 (1995) 31-39.
- [27] S.B. Howerton, V.L. McGuffin, Anal. Chem. 75 (2003) 3539-3548.
- [28] S.B. Howerton, V.L. McGuffin, J. Chromatogr. A 1030 (2004) 3-12.
- [29] J.H. Hildebrand, R.L. Scott, The Solubility of Nonelectrolytes, 3rd ed., Reinhold Publishing, New York, NY, 1950.
- [30] S.A. Wise, W.J. Bonnett, F.R. Guenther, W.E. May, J. Chromatogr. Sci. 19 (1981) 457-465.
- [31] M.W. Ducey, C.J. Orendorff, J.E. Pemberton, L.C. Sander, Anal. Chem. 74 (2002) 5576-5584.
- [32] M.W. Ducey, C.J. Orendorff, J.E. Pemberton, L.C. Sander, Anal. Chem. 74 (2002) 5585-5592.
- [33] A. Nahum, C. Horvath, J. Chromatogr. 203 (1981) 53-63.
- [34] R.A. Matzner, R.C. Bales, J.E. Pemberton, Appl. Spectrosc. 48 (1994) 1043-1053.
- [35] S.C. Ringwald, J.E. Pemberton, Environ. Sci. Technol. 34 (2000) 259-265.
- [36] D.R. Lide, Handbook of Chemistry and Physics, 71st Ed., CRC Press, Boca Raton, FL, 1990.

- [37] B.N. Woodrow, J.G. Dorsey, Environ. Sci. Technol. 31 (1997) 2812-2820.
- [38] R. Matzner, R.C. Bales, Chemosphere 29 (1994) 1755-1773.
- [39] R. Matzner, R.C. Bales, J. Colloid Interface Sci. 168 (1994) 61-66.

CHAPTER 7

SPECTROSCOPIC STUDY OF NITROGEN-CONTAINING POLYCYCLIC AROMATIC HYDROCARBONS BY FLUORESCENCE QUENCHING

7.1 INTRODUCTION

7.1.1 Nitrogen-Containing Polycyclic Aromatic Hydrocarbons (N-PAHs)

As described in Chapter 6, polycyclic aromatic compounds are well known for their potent biological effects, forming the largest known group of chemical carcinogens and mutagens [1-3]. While much attention has been paid to polycyclic aromatic hydrocarbons (PAHs), comparatively less information is available for nitrogen-containing polycyclic aromatic hydrocarbons (N-PAHs). The N-PAHs fall into two categories: amino-PAHs and aza-PAHs (azaarenes). By another classification scheme, they can also be divided into alternant and nonalternant N-PAHs. Representative alternant N-PAH (1-azapyrene) and nonalternant N-PAH (3-azafluorencene) are shown in Figure 7.1. After labeling every other atom in the aromatic ring system, skipping one atom between, alternant N-PAHs will have no labeled atoms adjacent. Nonalternant N-PAHs will have at least one pair of adjacent labeled or unlabeled atoms [4].

7.1.2 Fluorescence Quenching

Fluorescence is a luminescence technique that is quite suitable for the study of PAHs and N-PAHs because of their high quantum efficiency, which is associated with the delocalized electrons present in conjugated double bonds. While high sensitivity can easily be obtained from fluorescence, high selectivity is not always assured. Synchronous scanning techniques, in which both the

Alternant N-PAH

Nonalternant N-PAH

Figure 7.1 Representative examples of alternant N-PAH and nonalternant N-PAH

excitation and emission monochromators are scanned by maintaining a constant wavelength or energy interval, can provide greater selectivity [5]. However, synchronous scanning may not be sufficient to distinguish structurally similar PAHs and N-PAHs. The use of fluorescence quenchers may significantly increase the selectivity. Fluorescence quenching refers to any process that decreases the fluorescence power of a sample [6,7]. Among the different mechanisms, dynamic quenching is the most useful tool for analytical purposes [3].

In dynamic quenching, an excited-state fluorophore collides and forms a transient complex with a ground-state quencher. This excited-state complex dissociates upon radiative or nonradiative deactivation, leaving both the fluorophore and quencher in the ground state. Dynamic quenching can be described by the Stern-Volmer equation:

$$\frac{P_f^0}{P_f} = 1 + k_d \tau_f^0 C_q = 1 + K_d C_q \tag{7.1}$$

where τ^0_f is the fluorescence lifetime of the fluorophore without quencher, k_d is the bimolecular rate constant, and K_d is the Stern-Volmer constant. A graph of the fluorescence power ratio (P_f^0/P_f) versus the quencher concentration (C_q) is linear, with a slope equal to the Stern-Volmer constant and an intercept of unity. The Stern-Volmer constant is characteristic of each fluorophore-quencher pair and serves as a measure of the quenching efficiency. The ratio of Stern-Volmer constants for two fluorophores with the same quencher, or two quenchers with the same fluorophore, serves as a measure of the selectivity.

Although a large number of quenchers have been identified for polycyclic aromatic compounds, very few have been studied in sufficient depth to permit their routine application. Most of these quenchers are concerned with discrimination between alternant and nonalternant PAHs. These quenchers include nitromethane [8-11], pyridium chloride [12], cetylpyridinium chloride [13], and dodecylpyridinium chloride [14]. Among these quenchers, nitromethane is the most well-known and well-characterized dynamic quencher. After Sawicki et al. first demonstrated that nitromethane, an electron acceptor, could selectively deactivate the fluorescence of alternant PAHs [15], Acree et al. performed systematic studies that elucidated the so-called "nitromethane selective quenching rule" [8-10]. Subsequently, Ogasawara et al. performed a quantitative study to show that the Stern-Volmer constants of nitromethane are 33 - 100 times larger for alternant than nonalternant isomers [11]. Recently, Goodpaster and McGuffin performed an investigation of aliphatic amines as new potential quenchers [16]. Diisopropylamine can quench nonalternant PAHs 15 – 45 times more effectively than their alternant isomers. To date, most of the investigations have been limited to PAHs. For the N-PAHs, only one quencher, nitromethane, has been studied by Acree et al. [4]. But no quenching rule for alternant N-PAH is clearly elucidated, and no quantitative figures have been obtained. In the present study, aliphatic amines will be used to investigate the selective quenching rules applicable to N-PAHs and to evaluate their potential for analytical applications.

7.2 EXPERIMENTAL METHODS

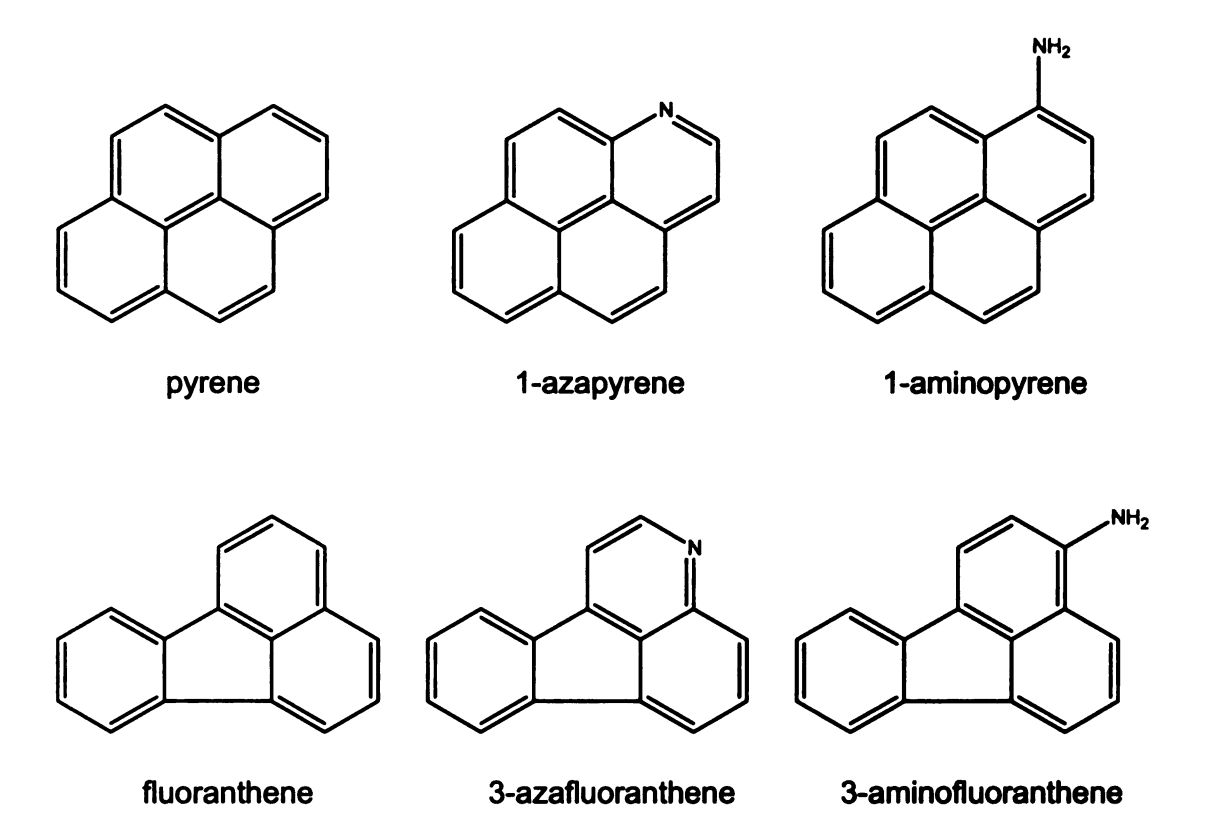
7.2.1 Chemicals

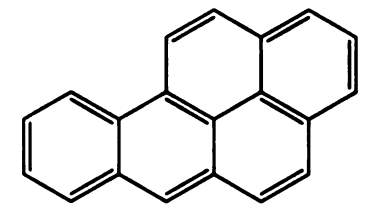
Reagent-grade hexylamine, diisopropylamine, and triethylamine (Aldrich) are used as received. The PAHs, shown in Figure 7.2, include pyrene, 1aminopyrene, fluoranthene, and 3-aminofluoranthene (Aldrich). In addition, 1azapyrene, 4-azapyrene. 3-azafluoranthene. benzo[a]pyrene, 10azabenzo[a]pyrene, benz[a]anthracene, benz[a]acridine, benz[c]acridine, dibenz[a,i]acridine, and dibenz[c,h]acridine are obtained from Institüt für PAH-Forschüng, Greiffenberg, Germany. The PAHs are dissolved in acetonitrile to prepare stock solutions of approximately 1.0 mM concentration. These stock solutions are diluted 100-fold in acetonitrile and mixed with quencher solutions of different concentrations to prepare the sample solutions, which are analyzed with High purity, spectroscopic-grade acetonitrile the system described below. (Burdick and Jackson, Baxter Healthcare) is used to prepare all solutions. No effort was made to remove dissolved oxygen from these solutions. The results of these fluorescence quenching studies are intended for routine practical applications, where scrupulous removal of oxygen may be difficult and the resulting variability in residual oxygen concentration may limit the quantitative accuracy.

7.2.2 Fluorescence Quenching Measurements

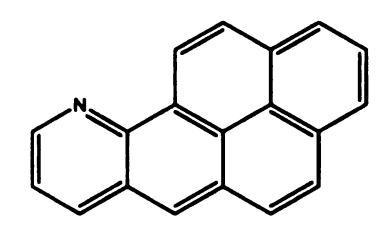
A laser-induced fluorescence spectrometer is used for the determination of quenching constants. Solutions composed of fluorophores and quenchers of different concentrations are introduced to a fused-silica capillary flow cell (75-μm



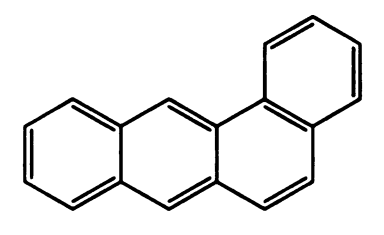




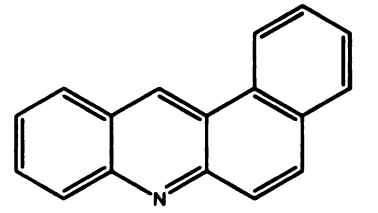
benzo[a]pyrene



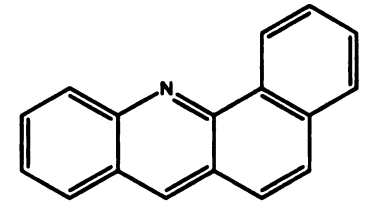
10-aza-benzo[a]pyrene



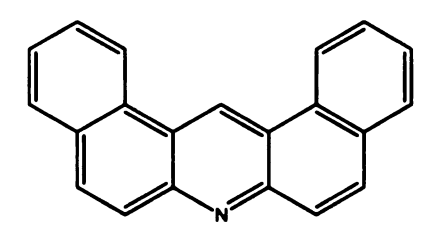
benz[a]anthracene



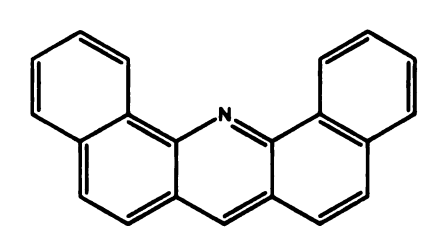
benz[a]acridine



benz[c]acridine



dibenz[a,j]acridine



dibenz[c,h]acridine

4-azapyrene

inner diameter, 375-μm outer diameter, 1.5-m length, Polymicro Technologies) by a gas displacement pump. The capillary flow cell minimizes error arising from primary and secondary absorption effects [17]. A continuous-wave He-Cd laser (Melles Griot, Model 3074-40M, 325 nm, 32 mW) is used as the excitation source. Fluorescence emission is collimated, filtered to remove laser scatter, and then focused onto the entrance slit of a 0.34 m Czerny-Turner monochromator (Instruments SA, Model 340E, 300 groove/mm grating). Fluorescence power is measured by a charge-coupled device (Instruments SA, Model (A)TECCD-2000*800-7, 15-μm pixels), which is cooled and maintained at 233 K. The control of the system and the subsequent data acquisition are achieved by commercially available electronic interfaces (Instrument SA, Model DS1010 and Model CCD 2000) and the associated software (Instruments SA, Spectromax for Windows, version 3.1).

Fluorescence power is measured for an integrated range of wavelengths, rather than a single wavelength, because the relative intensity of the vibronic bonds of PAHs may vary with solvent polarity [18,19]. The wavelength range for different fluorophores is as follows: pyrene (360 – 460 nm), 1-azapyrene (350 – 450 nm), 4-azapyrene (355 – 465 nm), 1-aminopyrene (385 – 530 nm), fluoranthene (380 – 590 nm), 3-azafluoranthene (395 – 595 nm), 3-aminofluoranthene (450 – 600 nm), benzo[a]pyrene (365 – 515 nm), 10-azabenzo[a]pyrene (390 – 550 nm), benz[a]anthracene (365 – 515 nm), benz[a]acridine (370 – 510 nm), benz[a]acridine (370 – 510 nm), dibenz[a,j]acridine (380 – 495 nm), and dibenz[c,h]acridine (380 – 495 nm). The

ratio of fluorescence power with and without quencher is calculated and graphed according to equation 7.1. After linear regression of the fluorescence power ratio with respect to the concentration of quencher, the slope of the graph is determined as the quenching constant (K_d) .

7.2.3 Fluorescence Lifetime Measurements

Fluorescence lifetimes are measured by a time-correlated single photon counting spectrometer [20]. In this system, the second harmonic of a continuous-wave, mode-locked Nd:YAG laser (Quantronix, Model 416) is used to excite a cavity-dumped, synchronously pumped dye laser (Coherent, Model 702-2) at 325 nm. Fluorescence emission is collected and focused on a subtractive double monochromator with a 10-nm bandpass. The emission is detected with a cooled two-stage microchannel plate photomultiplier at 243 K. Single photon counting is performed with commercially available electronic instrumentation (Tennelec, Models TC454, TC864, TC412A, TC525, and PCA-II) and commercially available software (Oxford Instruments, PCAME, Version 2.54).

Fluorescence lifetimes are determined at individual wavelengths corresponding to the emission maximum for each PAH: pyrene (380 nm), 1-azapyrene (375 nm), 1-aminopyrene (428 nm), fluoranthene (464 nm), 3-azafluoranthene (468 nm), and 3-aminofluoranthene (525 nm). Three replicate measurements of the fluorescence time decay are acquired by single photon counting. The data deconvoluted from the instrumental response function (about 35 ps FWHM) are fit by nonlinear regression to a single exponential function to determine the fluorescence lifetime [6].

7.3 RESULTS AND DISCUSSION

Aliphatic amines are dynamic fluorescence quenchers corresponding with their electron-donating ability. They serve as electron donors through the nonbonding electron pair of the nitrogen atom. In this study, aliphatic amines are examined as fluorescence quenchers for fluorophores consisting of PAHs, amino-PAHs, and aza-PAHs.

7.3.1 Effect of Water

During preliminary studies, it was observed that repeated measurements with the same stock solution of triethylamine yielded a continuous decrease of the Stern-Volmer constant. Because amines and polar solvents tend to be hygroscopic, a detailed investigation of the effect of water was warranted. If the primary source of water arises from the amine, then the net concentration of water will vary with the quencher concentration. On the other hand, if the primary source of water arises from the polar solvent, then the net concentration of water will be relatively constant. Both of these effects are examined using the wellinvestigated fluorophore, pyrene (10⁻⁵ M), and the quencher, triethylamine (0.01 - 0.05 M). For the first study, stock solutions of TEA containing 0%, 1%, and 5% (v/v) of water are used to prepare the solutions. The resulting quenching constants are summarized in Table 7.1. With increasing water concentration in the TEA stock solutions, the quenching constants of pyrene and TEA are systematically decreased. For the second study, the water concentrations in the solvent acetonitrile remain constant at 0%, 1%, and 5%. The quenching constants are summarized in Table 7.2. They show the same decreasing trend

with more water contained in the system. In both of these tables, good linearity and intercepts approaching unity are achieved with all quenching constant calculations. These features are indicative of a single quenching mechanism. In order to understand this quenching mechanism, it is important to note that water is not a fluorescence quencher but, according to our results, slightly enhances the quantum yield of pyrene in acetonitrile. However, water can form hydrogen bonds with the amine, comprising neutral complexes, ion pairs, or free ions depending on the dielectric constant of the solvent. These complexes make the nonbonding electrons of the nitrogen atom less accessible for quenching. Thus, the effect of water is to decrease the concentration of the free amine, leading to a decrease in the quenching constant. This is consistent with previous studies by Goodpaster and McGuffin [16], who reported that amines exhibit smaller quenching constants in methanol than in acetonitrile due to the existence of hydrogen bonds. The results of the present study suggest that great care must be taken to control water content in the amines and solvents in order to obtain reproducible and reliable quenching constants. Water may be removed from the amines by distillation with calcium hydride and storage with dry nitrogen.

7.3.2 Effect of Amine Structure

Two representative groups of alternant and nonalternant PAHs and N-PAHs are selected as fluorophores for this study. The alternant group includes pyrene, 1-azapyrene, and 1-aminopyrene. The nonalternant group includes fluoranthene, 3-azafluoranthene, and 3-aminofluoranthene. The corresponding alternant and nonalternant PAHs or N-PAHs have the same molecular formula

Table 7.1 Stern-Volmer constants for pyrene with triethylamine in acetonitrile at room temperature with different water concentration (v/v) in the amine solution.^a

water concentration (v/v)	K _d (M ⁻¹)	intercept	R ²
0%	49.2 ± 0.8	1.08 ± 0.03	0.9992
1%	45 ± 1	1.08 ± 0.05	0.9981
5%	38 ± 2	1.15 ± 0.06	0.9934

 $^{^{\}rm a}$ 10⁻⁵ M pyrene, 0.01 – 0.05 M triethylamine

Table 7.2 Stern-Volmer constants for pyrene with triethylamine in acetonitrile at room temperature with different water concentration (v/v) in the solvent^a.

water concentration (v/v)	K _d (M-1)	intercept	R²
0%	49.2±0.8	1.08±0.03	0.9992
1%	41.0±0.5	1.02±0.02	0.9996
5%	24.3±0.5	1.02±0.02	0.9987

 $^{^{\}rm a}$ 10 $^{\rm -5}$ M pyrene, 0.01 – 0.05 M triethylamine

and the same number of aromatic rings. The fluorescence lifetime (τ^0_f) of each PAH and N-PAH is summarized in Table 7.3. Three aliphatic amines, triethylamine, diisopropylamine, and hexylamine, which have the same molecular weight but different structures, are chosen as quenchers. The Stern-Volmer quenching constants for the two groups of fluorophores by different amines are summarized in Table 7.3. In this table, all of the Stern-Volmer constant calculations show good linearity and intercepts approaching unity. With the information of fluorescence lifetime and Stern-Volmer constants, the bimolecular rate constant for each fluorophore-quencher pair is calculated and is also summarized in Table 7.3.

Comparing the quenching ability of the aliphatic amines, the quenching constants systematically increase from primary to tertiary amine. The same trend is observed for PAHs, aza-PAHs, and amino-PAHs, regardless of their alternant or nonalternant structure. The alkyl group can increase the electron-donating ability of nitrogen. Thus, the greater the number of alkyl groups connected to the nitrogen, the stronger the electron-donating ability, and the higher the Stern-Volmer quenching constant. It is noteworthy that the bimolecular rate constants for the tertiary amine, triethylamine, are approaching the diffusion-limited values ($10^{10} - 10^{11} \text{ M}^{-1} \text{ s}^{-1}$). This implies that almost every collision between the fluorophore and quencher will induce quenching.

Selectivity can be defined as the ratio of quenching constants. In this study, three different selectivities can be evaluated as follows:

$$\alpha_{a} = \frac{K_{d}(aza - PAH)}{K_{d}(amino - PAH)}$$
(7.2)

Table 7.3 Stern-Volmer constants for PAHs and N-PAHs with three aliphatic amines in acetonitrile at room temperature.

Fluorophore	Quencher	K _a (M ⁻¹)	Intercept	R ²	τ ⁰ (ns)	K _d (M ⁻¹ s ⁻¹)	αa	ထို	ဗ
pyrene	triethylamine	49.2±0.8	1.08±0.03	0.9992	14.85	3.31×109		1	
1-azapyrene	triethylamine	110±1	1.02 ± 0.02	9666.0	8.05	1.36×10 ¹⁰	>1100	2.23	
1-aminopyrene	triethylamine	<0.1			4.43				
fluoranthene	triethylamine	215±1	1.05 ± 0.03	0.9998	28.75	7.46×10 ⁹			4.37
3-azafluoranthene	triethylamine	90.2±0.2	0.990±0.003	0.9999	8.71	1.04×10 ¹⁰	006<	0.42	0.82
3-aminofluoranthene	triethylamine	4 0.1			8.78				
pyrene	diisopropylamine	1.76±0.02	1.00±0.01	0.9995	14.85	1.19x10 ⁸			
1-azapyrene	diisopropylamine	47.7±0.6	1.08±0.05	0.9995	8.05	5.93x10 ⁹	>470	27.1	
1-aminopyrene	diisopropylamine	- 0.1			4.43				
fluoranthene	diisopropylamine	19.8±0.2	0.95 ± 0.04	0.9997	28.75	6.89x10 ⁸			11.26
3-azafluoranthene	diisopropylamine	22.7±0.2	1.02±0.01	0.9999	8.71	2.61×10°	>220	1.15	0.48
3-aminofluoranthene	diisopropylamine	<0.1			8.78				
pyrene	hexylamine	* 0.1			14.85				
1-azapyrene	hexylamine	4.02±0.04	1.03±0.01	0.9997	8.05	4.99x108	>40	>40	
1-aminopyrene	hexylamine	4 0.1			4.43				
fluoranthene	hexylamine	1.7±0.2	0.6±0.1	0.9726	28.75	5.91×10 ⁷			>16.7
3-azafluoranthene	hexylamine	3.51±0.06	1.04±0.02	0.9992	8.71	4.03×108	>35	2.10	0.87
3-aminofluoranthene	hexylamine	<0.1			8.78				

$$\alpha_{b} = \frac{K_{d}(aza - PAH)}{K_{d}(PAH)}$$
 (7.3)

$$\alpha_{C} = \frac{K_{d}(\text{nonalternant PAH})}{K_{d}(\text{alternant PAH})}$$
(7.4)

As evident from the Stern-Volmer constants in Table 7.3, aza-PAHs are easily quenched by the aliphatic amines whereas amino-PAHs remain virtually unquenched. The selectivity α_a between aza-PAHs and amino-PAHs is as high as several hundred for diisopropylamine and triethylamine. Even the lowest selectivity α_a for hexylamine is more than thirty-five, which is sufficiently high for discrimination. It is important to note that the fluorescence lifetimes of the aza-PAHs and amino-PAHs are on the same order of magnitude. fluorescence lifetimes will allow more opportunities for collision with the quencher, thus increasing the Stern-Volmer constants according to equation 7.1. But this difference in Stern-Volmer constant is due solely to the physical properties of the fluorophores, which is not the case in the present system. In this system, the difference in Stern-Volmer constant is due to the chemical properties, which influence the bimolecular collision rate between excited-state fluorophore and The high selectivity α_a provides an easy means to discriminate between aza-PAHs and amino-PAHs. While other techniques such as thermionic detection [21] and mass spectrometry can be used to determine whether nitrogen is present, they may fail to reveal whether the nitrogen is within or outside the aromatic ring. On the other hand, some simple organic reactions such as the Hinsberg test or sodium nitroprusside test [38] can differentiate primary, secondary, and tertiary amines, however these methods are not suitable

for complex samples. The fluorescence quenching approach can easily address these difficulties.

Selectivity, α_b , demonstrates the discrimination ability of amines for aza-PAHs compared to that of their corresponding PAHs. It can easily be observed that the selectivity α_b decreases as the quenching constants increase from primary to tertiary amines. The quenching constants for PAHs increase at a much faster rate than those for the aza-PAHs. For the alternant group, the quenching constants for 1-azapyrene are always larger than those of pyrene, which demonstrates the trend that amines can serve as more effective quenchers for alternant aza-PAHs than for PAHs. For the nonalternant group, however, no such trend is obeyed. Triethylamine is a more effective quencher for fluoranthene, whereas diisopropylamine and hexylamine are more effective quenchers for 3-azafluoranthene. However, when the fluorescence lifetimes are taken into account, the bimolecular rate constants (k_d) are always larger for aza-PAHs than for their corresponding PAHs, regardless of alternant or nonalternant character.

Selectivity α_c demonstrates the discrimination capacity of amines for nonalternant polycyclic aromatic compounds (PACs) compared to alternant PACs, including both PAHs and aza-PAHs. The three amines can all serve as more effective quenchers for nonalternant PAHs than alternant PAHs. The selectivity α_c increases from primary to tertiary amines. For the aza-PAHs, however, this trend is not observed. On the contrary, the three amines all serve as more effective quenchers for alternant aza-PAHs. The selectivity α_c is

relatively small and constant. It is important to note that the nonalternant PACs have longer fluorescence lifetimes than do the alternant PACs. For example, the lifetime of the nonalternant PAH, fluoranthene, is approximately two times longer than that of the alternant PAH, pyrene. For the nonalternant and alternant amino-PAHs, 3-aminofluoranthene and 1-aminopyrene, their fluorescence lifetimes also differ by a factor of two. Thus, the selectivities based on bimolecular rate constants for these two groups will be reduced by half. In contrast, there is no significant difference between the lifetimes for nonalternant and alternant aza-PAHs, 3-azafluoranthene and 1-azapyrene. Hence, their selectivity based on bimolecular rate constants will remain the same as that based on Stern-Volmer constants.

7.3.3 Effect of Fluorophore Structure

Due to the consistent trends observed with the alternant PAHs and aza-PAHs, a broader range of these solutes is chosen to investigate the structural effects on fluorescence quenching. Ten solutes constitute the new study, being divided into four groups with varying ring number and annelation structure. Specifically, pyrene, 1-azapyrene, and 4-azapyrene have four aromatic rings arranged in *peri*-condensed structure. Benz[a]anthracene, benz[a]acridine, and benz[c]acridine also have four aromatic rings, but are *ortho*-condensed. Benzo[a]pyrene and 10-azabenzo[a]pyrene have five rings, with one more *ortho*-condensed ring than the pyrene group. Finally, dibenz[a,i]acridine and dibenz[c,h]acridine have five rings, with one more *ortho*-condensed ring than the benz[a]anthracene group. Furthermore, the position of nitrogen within the

aromatic ring is varied within some groups, for example, 1-azapyrene and 4-azapyrene, benz[a]acridine and benz[c]acridine, dibenz[a,j]acridine and dibenz[c,h]acridine. The Stern-Volmer quenching constants for these 10 compounds are measured with diisopropylamine. In general, they show good linearity and an intercept approaching unity. The Stern-Volmer quenching constants and the selectivity α_b , calculated according to equation 7.3, are summarized in Table 7.4.

For each group, larger quenching constants are obtained for aza-PAHs than for their corresponding PAHs, which is demonstrated by a selectivity α_b greater than one. This confirms the general rule shown previously that can be applied to alternant aza-PAHs and alternant PAHs. This rule may help to differentiate between aza-PAHs and PAHs with amine quenchers.

When there are two aza-PAHs in the same group, a close look at the effect of nitrogen position is possible. In the pyrene group, 1-azapyrene and 4-azapyrene have similar quenching constants, which implies that the nitrogen atoms at the 1- and 4-positions show similar electron donor/acceptor ability and similar accessibility. The same trend is observed for benz[a]acridine and benz[c]acridine. In another group, however, dibenz[a,j]acridine has a quenching constant almost two times greater than that of dibenz[c,h]acridine. Although these two nitrogen atoms have similar electron donor/acceptor ability, the nitrogen in dibenz[c,h]acridine is less accessible than that in dibenz[a,j]acridine. Thus, steric hindrance may reduce contact between the fluorophore and quencher.

Table 7.4 Stem-Volmer constants for alternant PAHs and aza-PAHs with diisopropylamine in acetonitrile at room temperature.

Fluorophore	$K_d (M^{-1})$	Intercept	R ²	Selectivity α_b
pyrene	1.76 ± 0.02	1.00 ± 0.01	0.9995	
1-azapyrene	47.7 ± 0.6	1.08 ± 0.05	0.9995	27.10
4-azapyrene	44 ± 1	0.96 ± 0.04	0.998	24.87
benz[a]anthracene	2.1 ± 0.2	0.92 ± 0.05	0.986	
benz[a]acridine	9.4 ± 0.3	1.03 ± 0.02	0.996	4.51
benz[c]acridine	9.6 ± 0.2	1.01 ± 0.01	0.999	4.58
benzo[a]pyrene	1.17 ± 0.04	0.97 ± 0.01	0.996	
10-azabenzo[a]pyrene	1.67 ± 0.03	1.00 ± 0.02	0.999	1.43
dibenz[<i>a,j</i>]acridine	10.42 ± 0.05	1.010 ±	0.9999	
		0.005	2.222	
dibenz[c,h]acridine	6.68 ± 0.08	0.996 ±	0.9997	
discrizio,//jaoridine	0.00 1 0.00	0.006	3.0001	

The effect of ring number on Stern-Volmer constants for PAHs is demonstrated by comparison between pyrene and benzo[a]pyrene. Adding a benzene ring from pyrene to benzo[a]pyrene decreases the Stern-Volmer constant by 33%. For aza-PAHs, the effect of ring number can be demonstrated in two groups. From 1- and 4-azapyrene to 10-azabenzo[a]pyrene, the Stern-Volmer constants decrease dramatically by 96%. This difference might be introduced by the extended ring number, similar to the trend for the parent PAHs, pyrene and benzo[a]pyrene. It might also be related to the effects of steric hindrance, due to reduced accessibility of the nitrogen atom in 10azabenzo[a]pyrene than in 1- or 4-azapyrene. Moreover, the electron donor/acceptor ability might be different depending on the position of the nitrogen atom. The nitrogen atom located within the peri-condensed four-ring system, as 1- or 4-azapyrene, might have stronger electron donor/acceptor ability than the nitrogen atom located in the ortho-condensed benzene ring, as 10azabenzo[a]pyrene. Comparison can also be made between the benz- and dibenz-acridines. Adding a benzene ring from benz[a]acridine to dibenz[a,i]acridine increases the Stern-Volmer constant by about 10%. The accessibility and electron-donating/accepting ability of the nitrogen atom in these two compounds are quite similar. However, adding a benzene ring from benz[c]acridine to dibenz[c,h]acridine decreases the Stern-Volmer constant by about 30%. This decrease in Stern-Volmer constant arises from the reduced accessibility of the nitrogen atom in dibenz[c,h]acridine.

The effect of annelation structure for PAHs can be demonstrated by comparison between pyrene and benz[a]anthracene. The more linear structure of benz[a]anthracene increases the Stern-Volmer constant by 20%. However, for the aza-PAHs, the Stern-Volmer constant decreases dramatically by 80% from the compact structure of 1- and 4-azapyrene to the linear structures of benz[a]acridine and benz[c]acridine. The accessibility of the nitrogen in these four compounds should be similar to each other. However, the nitrogen atom in the peri-condensed pyrene system might have stronger electron donor/acceptor ability than in the ortho-condensed benz[a]anthracene system. In the five-ring by system, the Stern-Volmer constant increases 300% azabenzo[a]pyrene to dibenz[a,j]acridine and dibenz[c,h]acridine, with more linear structures. In this case, the nitrogen atoms are all located in the pericondensed ring and, thus, have similar electron donor/acceptor ability. The more linear structures might increase the Stern-Volmer constants for these N-PAHs, just as for the PAHs pyrene and benz[a]anthracene.

It is helpful to examine whether the observed trends in quenching constants correlate with the gas-phase ionization potential of the fluorophore. The smaller the ionization potential, the more readily the fluorophore can donate rather than accept electrons, which should result in smaller quenching constants. The available information on ionization potentials for selected fluorophores is summarized, together with their quenching constants, in Table 7.5.

For PAHs, the ionization potential data show that benzo[a]pyrene < pyrene < benz[a]anthracene < fluoranthene, which is in agreement with the trends in

Table 7.5 Ionization potentials for the fluorophores (PAHs and N-PAHs).

PAHs and N-PAHs	lonization	Reference	Quenching
	Potential		Constant
pyrene	7.5, 7.41	[23,24]	1.76
fluoranthene	7.9	[25]	19.8
benz[a]anthracene	7.54, 7.43	[23,24]	2.1
benzo[a]pyrene	7.23	[23]	1.17
benz[a]acridine	8.02	[26]	9.4
benz[c]acridine	7.98	[26]	9.6
benzene	9.24	[27]	N/A
pyridine	9.76	[28]	N/A
aniline	7.72	[29]	N/A

fluorescence quenching constants discussed above. For N-PAHs, the information on ionization potential is only available for benz[a]acridine and benz[c]acridine. Their similar ionization potentials are consistent with their similar quenching constants. Meanwhile, both of their ionization potentials are larger than their corresponding PAH, benz[a]anthracene. This is also consistent with the trends for quenching constants.

To investigate the trend in quenching constants for alternant aza-PAH > PAH > amino-PAH, the ionization potentials of benzene, pyridine, and aniline are shown in Table 7.5. Although they are not the fluorophores investigated in this paper, they compose a similar group for comparison with 1-azapyrene, pyrene, and 1-aminopyrene. Aniline has an extremely small ionization potential, which corresponds with the extremely small quenching constant for 1-aminopyrene. Meanwhile, the ionization potential for benzene is smaller than that of pyridine, which also corresponds to a smaller quenching constant for pyrene than that of 1-azapyrene.

However, ionization potential alone cannot fully explain the trends in Stern-Volmer quenching constant. For example, fluoranthene and the benzacridines have similar ionization potential, yet their quenching constants differ by a factor of two. More experimental and theoretical correlations need to be investigated to fully explain these trends.

7.4 CONCLUSIONS

Fluorescence quenching has the potential to become a very practical and useful technique due to its high sensitivity and selectivity. However, its

usefulness is still limited because of the small number of fluorophores and quenchers that have been examined in sufficient detail. In this study, PAHs and N-PAHs as fluorophores and aliphatic amines as quenchers are chosen for investigation. The trends of increased quenching efficiency and decreased selectivity are shown from primary to tertiary amine. Amino-PAHs remain unquenched by aliphatic amines. Alternant aza-PAHs are quenched more efficiently than their corresponding alternant PAHs. These two trends can be very helpful in addressing the difficulty of identifying compounds in complex samples in the future. However, the selectivity of diisopropylamine for some systems in this study is not sufficiently high, which demands further research and development.

- [1] M.L. Lee, M.V. Novotny, K.D. Bartle, Analytical Chemistry of Polycyclic Aromatic Compounds, Academic Press, New York, 1981.
- [2] T. Vo Dinh, Chemical Analysis of Polycyclic Aromatic Compounds, Wiley, New York, 1988.
- [3] V.L. McGuffin, J.V. Goodpaster, in R.A. Meyers (Ed), Encyclopedia of Environmental Analysis and Remediation, Wiley, New York, 1998, p. 3815.
- [4] S.A. Tucker, W.E. Acree, M.J. Tanga, S. Tokita, K. Hiruta, H. Langhals, Appl. Spectrosc. 46 (1992) 229-235.
- [5] G.G. Guilbault, Practical Fluorescence, Marcel Dekker, New York, 1990.
- [6] J.R. Lakowicz, Principles of Fluorescence Spectroscopy, Plenum Press, New York, 1983.
- [7] R. Badley, Fluorescence Spectroscopy, Plenum Press, New York, 1983.
- [8] S.A. Tucker, J.M. Griffin, W.E. Acree, J.C. Fetzer, M. Zander, O. Reiser, A. Meijere, I. Murata, Polycyclic Aromat. Compd. 4 (1994) 141-160.
- [9] S.A. Tucker, J.M. Griffin, W.E. Acree, M.J. Tanga, J.E. Bupp, T.K. Tochimoto, J. Lugtenburg, K. Van Haeringen, J. Cornelisse, P.C. Cheng, L.T. Scott, Polycycl. Aromat. Compd. 4 (1994) 161-172.
- [10] W.E. Acree, S. Pandey, S.A. Tucker, J.C. Fetzer, Polycycl. Aromat. Compd. 12 (1997) 71-123.
- [11] F.K. Ogasawara, Y. Wang, V.L. McGuffin, Appl. Spectrosc. 49 (1995) 1-7.
- [12] C. Mao, S.A. Tucker, J. Chromatogr. A 966 (2002) 53-61.
- [13] S. Pandey, W.E. Acree, J.C. Fetzer, Talanta 45 (1997) 39-45.
- [14] S. Pandey, L.E. Roy, W.E. Acree, J.C. Fetzer, Talanta 48 (1999) 1103-1110.
- [15] E. Sawicki, T.W. Stanley, W.C. Elbert, Talanta 11 (1964) 1431-1439.
- [16] J.V. Goodpaster, V.L. McGuffin, Anal. Chem. 72 (2000) 1072-1077.
- [17] S. Chen, C.E. Evans, V.L. McGuffin, Anal. Chim. Acta 246 (1991) 65-74.
- [18] D.C. Dong, M.A. Winnik, Can. J. Chem. 62 (1984) 2560-2565.

- [19] D.C. Dong, M.A. Winnik, Photochem. Photobiol. 35 (1982) 17-21.
- [20] L. DeWitt, G.J. Blanchard, E. LeGoff, M.E. Benz, J.H. Liao, M.G. Kanatzidis, J. Am. Chem. Soc. 115 (1993) 12158-12164.
- [21] M. Dressler, Selective Gas Chromatography Detectors, Elsevier Science Publishing Co., New York, 1986.
- [22] J.C. Gilbert, S.F. Martin, Experimental Organic Chemistry: A Miniscale and Microscale Approach, 2nd Ed., Saunders, New York, 1998.
- [23] Y. Sakamoto, S. Watanabe, Bull. Chem. Soc. Jpn. 59 (1986) 3033-3038.
- [24] I. A. Shkrob, M. C. Sauer, A. Liu, R. A. Crowell, A. D. Trifunac, J. Phys. Chem. A 102 (1998) 4976-4989.
- [25] Y. Ling, C. Lifshitz, J. Phys. Chem. 99 (1995) 11074-11080.
- [26] W. Xue, D. Zapien, D. Warshawsky, Chem. Res. Toxicol. 12 (1999) 1234-1239.
- [27] R. Billotto, R. J. Levis, J. Phys. Chem. A 103 (1999) 8160-8168.
- [28] P. D. Burrow, A. J. Ashe, D. J. Bellville, K. D. Jordan, J. Amer. Chem. Soc. 104 (1982) 425-429.
- [29] M. A. Smith, J. W. Hager, S. C. Wallace, J. Chem. Phys. 80 (1984) 3097-3105.

CHAPTER 8

CONCLUSIONS AND FUTURE DIRECTIONS

Chiral separations have gained more and more attention over the past twenty years. At present, there are more than 200 chiral stationary phases (CSPs) commercially available for direct chiral separation. But most chiral separations are still accomplished by "trial-and-error" approach. The underlying reason is the uncertainty of the chiral separation mechanism. Thermodynamic and kinetic investigations can provide insight into the retention mechanism and demonstrate how solutes interact with the stationary phase at the molecular level.

8.1 Theoretical simulations

Chapter 2 details the stochastic simulation method to validate models for extracting thermodynamic and kinetic information. Both homogeneous surface and heterogeneous surfaces are simulated. The accuracy was compared between different models and the "true" kinetic method. The reliability for extracting the retention factors follows the order: statistical moment method, exponentially modified Gaussian (EMG) model, Giddings model, and Thomas model. For the extraction of kinetic information, different parameters will influence the relative accuracy of the different methods. With an increase in column length, the rate constants from the statistical moment, Giddings, and Thomas models are constant, while those from the EMG model increase. Decreasing the linear velocity has the same effect as increasing the column length. With a decrease in the stationary-phase diffusion coefficient or a decrease of the interfacial mass transfer coefficient, the rate constants for all

models decrease and the zone profiles become broader with more asymmetry. All models provide reliable extraction of kinetic rate constants with a change in column length, velocity, diffusion coefficient, and mass transfer coefficient. However, the rate constants deviate from the true kinetic data for all models with a change in equilibrium constant in the homogeneous simulations and in all heterogeneous simulations. This deviation may arise from poor fit of the simulation data to the single exponential decay in the true kinetic method.

Based on these results, all of the examined methods yield reasonably accurate values for retention factors and rate constants by comparison to the true kinetic method. However, this comparison was performed under the perfect conditions of a stochastic simulation, i.e., well defined column geometry, well defined interaction sites, no variability in flow rate, temperature, or other parameters, no extra-column contributions, no background or noise, and so on. As such, the stochastic simulation does not provide a realistic and comprehensive consideration of all aspects of this comparison. Only a comparison performed with experimental data can reveal the ability of these different methods to extract retention factors and rate constants under practical conditions, where column and extra-column contributions to broadening and asymmetry are not as well established. The experimental investigation is definitely important for a complete validation of the models.

Although this dissertation validates the different mathematical models for extracting thermodynamic and kinetic information, all the simulations are based on the absorption mechanism. Thus, other possible direction for the stochastic

simulation is to validate different mathematical models with the adsorption mechanism or with a mixed-mode mechanism. Many separation processes are complicated, where one single mechanism is not adequate to explain the separations. A novel simulation method on the adsorption mechanism has been successfully proposed by Dr. Peter Krouskop [1].

8.2 Chiral separations

Chapters 4 and 5 detail the thermodynamic and kinetic investigation of chiral separation with a β -cyclodextrin stationary phase. The EMG model is utilized for all data analysis. Successful chiral separations of coumarin-related compounds are demonstrated. Three different effects are investigated, which include the mobile phase effect (Chapter 4), and the temperature and pressure effects (Chapter 5).

Mobile phase composition is the most important parameter affecting liquid chromatographic separations. In this work, the mobile phase affects the equilibration time, retention time, as well as peak shape. In a preliminary experiment, two-component mobile phases containing only acetonitrile and methanol cannot reach equilibrium even after several weeks. But both acid and amine modifiers shorten the equilibration time greatly from weeks to one day or less. Whereas the acetic acid modifier can increase the linear isotherm range and ensure a Gaussian peak shape, the triethylamine modifier can dramatically decrease the retention time while still enhancing chiral selectivity. In four-component mobile phases, all of the coumarin-based solutes are within their linear isotherm range and give reasonable thermodynamic and kinetic

information. The elution order is strongly dependent on the hydrogen bonding ability between the solutes and the stationary phase. 4-Hydroxycoumarin has the largest retention due to simultaneous interactions at the hydroxyl and carboxyl sites. The chiral solutes are retained less due to steric effects and intramolecular hydrogen bonding. The kinetic rate constants typically decrease The mass transfer kinetics for 4with an increase in retention factor. hydroxycoumarin are much slower than those for the chiral molecules because of the simultaneous interactions. For the chiral solutes, the second enantiomer has a surprisingly higher mass transfer rate than the first enantiomer, although it is more retained. This behavior suggests a difference in the kinetic contributions for chiral and achiral selective sites. The concentration of each component in the four-component mobile phase is varied to observe its individual effects. Methanol can hydrogen bond with the stationary phase, thus decreasing retention and increasing the kinetics for all solutes. Triethylamine decreases retention, but enhances chiral selectivity by interacting with the hydroxyl group of the solutes and with achiral selective sites of the stationary phase. But acetic acid increases retention and reduces chiral selectivity by interacting with the amine and with chiral-selective sites. Both acid and amine modifiers increase adsorption and desorption rate constants. When both acid and amine are present in the mobile phase, they tend to interact with each other and complicate the separation process.

Temperature and pressure effects are usually neglected in liquid chromatographic separations. However, these two parameters showed great

effects in chiral separations in Chapter 5. More detailed thermodynamic and kinetic information are demonstrated. Increasing temperature from 283 K to 303 K decreases the retention for all solutes dramatically. The change in molar enthalpy can be calculated through the slope of the van't Hoff plot. A linear slope indicates a constant change in molar enthalpy over the temperature range. A positive slope indicates a negative change of molar enthalpy. All the solutes exhibit an enthalpically favorable transfer from mobile to stationary phase. 4-Hydroxycoumarin has the largest retention, but the least negative change of molar enthalpy. For the chiral solutes, the trend of their change in molar enthalpy does not always match the trend of their retention. Apparently, the change in molar entropy has an important role in the separation. The second enantiomer has a more negative change in molar enthalpy than the first enantiomer, indicating an enthalpically more favorable process for the second enantiomer. But the second enantiomer does not experience an entropically favorable process in the transfer, which can be seen from the negative chiral difference in molar entropy ($\Delta\Delta$ S). No enthalpy-entropy compensation is observed among all solutes, indicated by the scattered points between logarithm of retention factor versus the change in molar enthalpy, as well as by the different co-elution temperatures (T_{iso}) of all solutes. All the chiral separations are enthalpically controlled processes. Increasing pressure decreases the retention for all solutes. A positive change in molar volume is calculated from the slope of the logarithm of retention versus pressure. The positive change in molar volume indicates no inclusion into the cyclodextrin cavity occurred in this polar-organic mobile phase

composition. As to kinetics, increasing temperature increases kinetic rate constants. Activation energies are positive for chiral solutes, with the second enantiomer having higher activation energy than the first enantiomer.

With the β-cyclodextrin chiral stationary phase, more mobile phase additives can be investigated. Instead of methanol, other organic modifiers such as ethanol, propanol, and isopropanol could be tried; instead of triethylamine, other basic modifiers such as hexylamine, diethylamine and triethanolamine could be tried; instead of acetic acid, other acidic modifiers such as citrate acid could be tried as well. In this dissertation, all of the separations are investigated in the polar-organic mode. Coumarin-related compounds can also be separated in reversed-phase mode as well. Due to the distinct difference in retention mechanism, dramatically different results could be expected with similar studies of the effects of mobile phase, temperature, and pressure. For the system for chiral separation, a circular dichroism detector would facilitate the identification of each enantiomer [2].

β-Cyclodextrin is only one representative type of CSP, other types of CSP could also be investigated in a similar manner. With more systematic research on different types of chiral stationary phase, chiral separation mechanism would not be a mystery any more. More standard guideline procedures could be established and followed. Thus, "trial-and-error" approach could be eliminated and huge amount of resources could be saved.

8.3 Characterization of nitrogen-containing polycyclic aromatic hydrocarbons (N-PAHs)

N-PAHs are a particular group of environmentally toxic polycyclic aromatic hydrocarbons (PAHs) that contain nitrogen. Complete chromatographic (Chapter 6) and spectroscopic characterizations (chapter 7) are carried out in this dissertation.

A series of N-PAHs is separated on an octadecylsilica (ODS) column in methanol as well as in acetonitrile mobile phases. In methanol mobile phase, the retention factors for the N-PAHs are less than those for the parent PAHs, which is consistent with the partition mechanism. In addition, the trends of retention with ring number and annelation structure are also consistent with the partition mechanism. N-PAHs have significantly smaller kinetic rate constants than those of the parent PAHs, indicating the co-existence of an adsorption mechanism. In the aprotic solvent acetonitrile, this adsorption mechanism dominates the separation. The underlying reason is the hydrogen-bonding ability of methanol with the N-PAH solutes as well as with the silanol groups. However, acetonitrile is not able to shield interactions in this manner, hence the retention factors for the aza-PAHs are substantially greater than those in methanol. The changes in molar enthalpy are slightly more negative for these solutes, but not sufficient to account for the large change in retention factor. Hence, a significant change in entropy or the phase ratio must be responsible for the thermodynamic behavior. The kinetic rate constants are two to four orders-of-magnitude smaller than those in methanol. This behavior also reflects the increased role of adsorption. The thermodynamic and kinetic information provides a much clearer description of the retention mechanism of N-PAHs in reversed-phase liquid chromatography. However, further studies with aqueous mobile phases and additives are desirable for more thorough characterization.

Selective fluorescence quenching is demonstrated in Chapter 7 to differentiate PAHs and types of N-PAHs. Aliphatic amines are chosen as selective quenchers. From primary to tertiary amine, the quenching efficiency increases while the selectivity decreases. Amino-PAHs remain unquenched by aliphatic amines. Thus, aliphatic amines are able to differentiate amino-PAHs and aza-PAHs by their dramatically different quenching constants. Also, alternant aza-PAHs are quenched more efficiently than their corresponding alternant PAHs. These two trends can be very helpful in addressing the difficulty of identifying compounds in complex samples in the future. Direct and indirect identification of N-PAHs with liquid chromatographic technique could be applied in a similar manner as reported by Goodpaster and McGuffin [3,4].

8.4 References

- [1] P. Krouskop, Ph.D. Dissertation 2002, Michigan State University
- [2] H. Takahashi, T. Kashima, S. Kimura, N. Muramoto, H. Nakahata, S. Kubo, Y. Shimoyama, M. Kajiwara, H. Echizen, J. Chromatogr. B 701 (1997) 71-80.
- [3] J.V. Goodpaster, V.L. McGuffin, Anal. Chem. 73 (2001) 2004-2011.
- [4] J.V. Goodpaster, S.B. Howerton, V.L. McGuffin, J Forensic Sci. 46 (2001) 1358-1371.

